Title

Technological Improvements in Two-Dimensional Infrared Spectroscopy and Their Applications to Biological Systems

Author

Vinogradov, Ilya Vladimirovich

Publication Date

2019

UNIVERSITY OF CALIFORNIA,
IRVINE

Technological Improvements in Two-Dimensional Infrared Spectroscopy and Their Applications to Biological Systems

DISSERTATION

submitted in partial satisfaction of the requirements
for the degree of

DOCTOR OF PHILOSOPHY

in Chemistry

by

Ilya Vladimirovich Vinogradov

Dissertation Committee:
Professor Nien-Hui Ge, Chair
Professor Vartkess Ara Apkarian
Professor Eric Olaf Potma

2019

DEDICATION

To

my parents and friends,

all those around who offered support,

and all those who will follow

Enjoy!

TABLE OF CONTENTS

LIST OF FIGURES

Page

LIST OF TABLES

Page

ACKNOWLEDGMENTS

I would like to express the deepest appreciation to my committee chair, Professor Nien-Hui Ge for her constant support and patience over the years. Thank you for teaching me the power of persistence. This dissertation would not have been possible otherwise.

I would like to thank my committee members, Professor Vartkess Ara Apkarian and Professor Eric Olaf Potma, for their input and advice over the last several years.

I would like to thank my group members for help in the projects described in this dissertation. First, I would like to acknowledge Dr. Yuan Feng, whom I worked closely with, for Chapters 2 and 3. He was responsible for conceiving the idea for smart referencing and developing the mathematical framework. He was also greatly involved in the theoretical understanding of the pulse shaper, especially with the ray-pulse matrix method. I would like to acknowledge Chenxu (Vincent) Guo and Nina Saki Udagawa, two excellent undergraduate students, who helped with the sample preparation and characterization for Chapter 4. I would like to thank Dr. Hiroaki Maekawa for help in laser maintenance and managing the lab. I would like to thank Dr. Karthick Kumar Somangili Krishnamoorthys, who built the first iteration of the pulse-shaper and 2D IR setup used in this work. I would also like to thank Dr. Sudipta Mukherjee for his helpful input into 2D IR spectroscopy and mid IR pulse shaping.

In addition, a thank you to Professor Christopher Cheatum of The University of Iowa and committee member Professor Vartkess Ara Apkarian for helpful discussion on the models proposed in Chapter 4. I would like to acknowledge Dr. Dima Fishman, director of, and the use of the Laser Spectroscopy Facility at the University of California, Irvine.

Finally, I thank the Optical Society of America for permission to include most of Chapter 2 as part of my dissertation, which was initially published in Optics Express. Financial support was provided by the University of California, Irvine; the U.S. National Science Foundation grants CHE-1310693 and CHE-1013071 and shared instrument support CHE-0802913 and CHE-1414466; the GAANN Fellowship; and C.W. Ackerman Endowed Fellowship.

CURRICULUM VITAE

Ilya Vladimirovich Vinogradov

2013	B.S. in Chemistry, University of Kentucky
2019	Ph.D. in Chemistry, University of California, Irvine

FIELD OF STUDY

Two-Dimensional Infrared Spectroscopy

PUBLICATIONS

Vinogradov, I.; Feng, Y.; Guo, C.; Udagawa, N. S.; Ge, N.-H., Ultrafast Vibrational Dynamics of the Tyrosine Ring Mode. **2018**, To be submitted.

Feng, Y.; Vinogradov I.; Ge, N.-H., Optimized Noise Reduction Scheme for Heterodyne Spectroscopy Using Array Detectors, **2018**. To be submitted.

Feng, Y.; Vinogradov I.; Ge, N.-H., General Noise Suppression Scheme with Reference Detection in Heterodyne Nonlinear Spectroscopy. *Optics Express*, **2017**, 25 (*21*), 26262.

Vinogradov, I., Synthetic Approaches to Organometallic Complexes for Electronics Applications, *Kaleidoscope,* **2011**, *10*, 19.

Vinogradov, I., Organometallic Acene Complexes for Electronics Applications, *Kaleidoscope*, **2010**, *9*, 35.

ABSTRACT OF THE DISSERTATION

Technological Improvements in Two-Dimensional Infrared Spectroscopy and Their Applications to Biological Systems

By

Ilya Vladimirovich Vinogradov

Doctor of Philosophy in Chemistry

University of California, Irvine, 2019

Professor Nien-Hui Ge, Chair

Two-dimensional infrared spectroscopy (2D IR) is a rapidly growing field. Many of the problems studied with this technique, and especially those involving biomolecules, require the detection of very weak signals. To further advance the technique forward, the signal-to-noise ratio needs to be improved. This dissertation details a method for noise reduction, called “smart referencing,” and details several considerations required for increasing the signal when using a pulse shaper. Using these improvements, the ultrafast vibrational dynamics and local environment sensitivity of the tyrosine ring mode in the enkephalin/bicelle system were studied using 2D IR. The 2D IR spectra revealed a new and unusual line-shape distortion for this ring mode. We modeled this distortion with a 3rd order response function formalism and a phenomenological set of master equations to better understand its origin. The 2D IR results also show that the tyrosine ring mode is sensitive to its local environment.

1. INTRODUCTION

Two-dimensional infrared (2D IR) spectroscopy has been used, with great success, to study the structure and dynamics of proteins and peptides.[1,2] Structural insight can be gained by studying the vibrations related to the peptide backbone. These vibrational modes include, but are not limited to, the amide-I and amide-II modes.[3] These vibrational modes can be studied directly to provide information about the protein or peptide secondary structure.[4] This capability exists because the backbone modes oscillate collectively as vibrational excitons, which are sensitive to the long range organization of oscillators.[5] Unfortunately, because the normal mode is delocalized over many coupled oscillators, this method is not useful for site specific information. To overcome this, isotope labeling is often employed. By isotope labeling individual peptide bond's as ^{13}CO or ^{13}C^{18}O, the individual oscillator is significantly red shifted and decoupled from the unlabeled vibrational exciton.[6,7] Several such labels can be simultaneously employed, and their couplings can be extracted to gain residue-specific structural information.[8] Unfortunately, this method is expensive and difficult. Only a few amide-^{13}C isotope labeled amino acids are commercially available, ^{18}O labeling requires an additional exchange step, and their site-specific insertion is usually done by solid-phase peptide synthesis.[7] Therefore, application of this method is limited to peptides or small proteins.

Insight into the biosystem's dynamics can be gained by employing vibrational labels.[9-11] These labels are vibrational chromophores that are sparse within the sample of interest and report on their local environments in a site-specific manner. The labels can be a natural part (including isotope labeled backbone modes) of the protein but are more often included as unnatural amino acids. Usually, the label's transition frequency is used as the spectroscopic reporter because the transition frequency is dependent on local environment parameters such as electric field, field gradient, and hydrogen bonding.[12] In 2D IR spectroscopy, we are interested in extracting how these local environment parameters fluctuate on an ultrafast timescale. To explain how this information is extracted from a 2D spectrum, I will first describe the basic concepts of 2D IR spectroscopy.

1.1 2D IR basics

1.1.1 Pulse Sequence

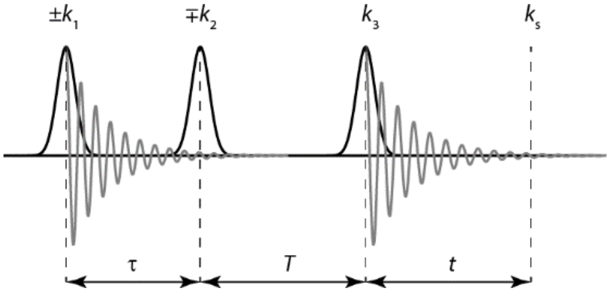

Figure 1. 2D IR pulse sequence

In 2D IR spectroscopy,[5] we use an infrared pulse sequence to generate a nonlinear signal (Figure 1). The first pulse generates a coherence and the second pulse converts that coherence to a population (or interstate coherence). The purpose of this pulse pair can be thought of as labeling a frequency on the ω_τ axis. Finally, after a waiting time T, the third pulse probes the state of the system, which generates the macroscopic polarization which emits along time t. This signal is typically collected by a spectrometer, which generates the frequency axis ω_t. Fourier-transforming over τ generates the ω_τ axis in the 2D IR spectrum.

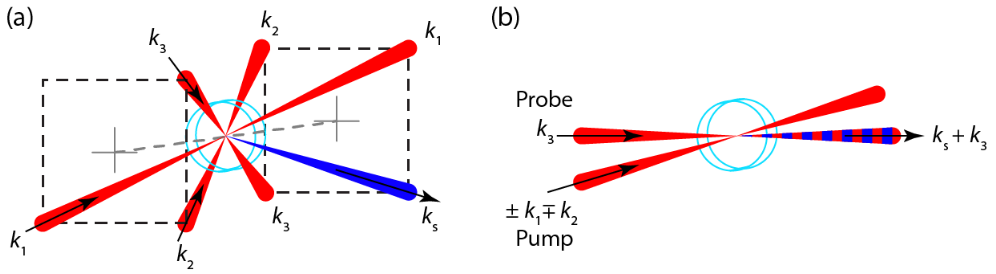

Figure 2. (a) BOX-CARS geometry. (b) Pump-probe geometry.

The macroscopic polarization generated by this pulse sequence does not discriminate between whether the interaction is linear or non-linear. How do we then extract the nonlinear signal of interest? There are a few strategies on how to do this. First, the 2D IR signal depends on the k-vectors of the incoming pulses as $k_{\pm} = \pm k_1 \mp k_2 + k_3$, where k_- is known as the rephasing contribution and k_+ is known as the non-rephasing contribution. These contributions can be extracted by arranging the input beams in the geometry shown in Figure 2(a), so that the macroscopic polarization emits the signal of interest in a direction that is different from any other interaction, linear or non-linear. Note that Figure 2(a) only shows the geometry needed to extract the non-rephasing contribution. The rephasing contribution can be extracted by simply switching the time ordering of k_1 and k_2. The 2D IR signal also contains phase information. To extract this phase information the signal is mixed with a 4th beam called the local oscillator. This type of detection is called heterodyne detection (direct detection of the signal intensity is called homodyne detection). The interference between the signal and LO contains the amplitude and phase information of the signal. This interference can be extracted if a suitable background for the LO is acquired, which is usually done on a shot-by-shot basis through a technique called chopping.

It is also possible to collect 2D IR spectra in a pump-probe geometry, shown in Figure 2(b). In this case, the wavevector components for the two pump pulses cancel and the signal is emitted in the probe direction. This signal is automatically heterodyned with the probe beam. This nonlinear signal is distinguished from the linear signal by subtracting the probe background, which is done on a shot-by-shot basis via chopping or phase cycling. The advantage of this method is that signal collected is purely absorptive (absorptive is the sum of the rephasing and non-rephasing contributions k_- and k_+) and collected with no phase ambiguity—which is difficult in the BOX-CARS geometry.[13] Purely absorptive spectra are advantageous because they usually result in narrower line shapes as compared to the rephasing, non-rephasing, or linear counterparts (although it is sometimes possible to have narrower features in real rephasing and non-rephasing spectra due to the interference between absorptive and dispersive components).[5] Unfortunately, in the pump-probe geometry one loses the ability to independently control the LO and signal strengths, which usually comes at the cost of the signal-to-noise ratio (SNR).

The second strategy involves the temporal phase dependence of the signal on the temporal phase of the input pulses. If the phases of the input pulses can be cycled, certain artifacts, such as scatter of the pump pulses from the sample, can be removed. In the pump-probe geometry, this is often implemented with a pulse shaper, which allows for high phase precision and stability.[14] In addition, the pulse shaper allows for the use of a rotating frame, which can speed up data acquisition. The use of a pulse shaper in the pump-probe geometry is state-of-the art for 2D IR spectroscopy and has led to high-throughput and fully automated 2D IR spectrometers, which are now commercially available.[15] Also, because chopping or phase cycling is done electronically, the pulse shaper can be used with high repetition rate systems, such as a 100 kHz laser.[16-18]

1.1.2 The 2D IR spectrum of a single oscillator

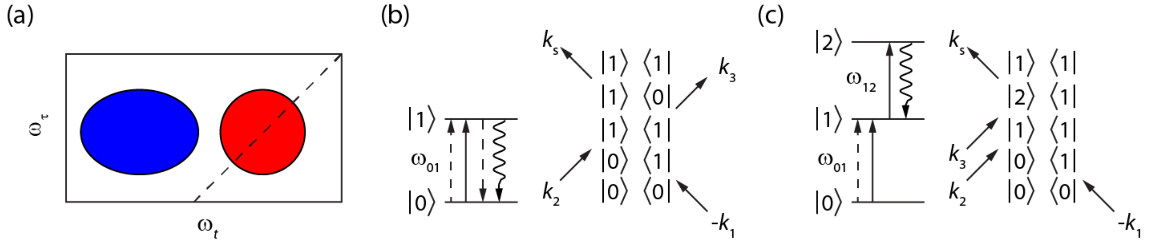

Figure 3. (a) Single-oscillator 2D IR spectrum. (b) Level scheme and Feynman diagram for excited state stimulated emission (red peak). (c) Level scheme and Feynman diagram for excited state absorption (blue peak). Not shown is the ground state bleach contribution, which contributes to the red peak.

Qualitatively, the 2D IR spectrum for a single oscillator is composed of two peaks, as shown in Figure 3(a). The peak on the diagonal has two contributions: the ground state bleach and excited state emission or stimulated emission in Figure 3(b). We will use the convention that this peak is positive because it corresponds to a gain in intensity in the pump probe spectrum. The other peak corresponds to the excited state absorption, shown in Figure 3(c), and is anharmonically shifted because it accesses the overtone transition. Because light is absorbed, by our convention, this peak is negative. Note that anharmonicity is required to generate a 2D IR spectrum and that a purely harmonic oscillator will not generate a spectrum because the positive and negative contributions will cancel.

One of the key advantages of 2D IR spectroscopy is that it generates a photon echo.[5] The photon echo pulse sequence (i.e. rephasing sequence) is capable of distinguishing between homogenous and inhomogeneous contributions to dephasing. This is important because vibrational labels are used as reporters of their local environments, but in many systems the ensemble of labels are in many different environments. The influence of the different environments changes the transition frequency of the label, and the collective ensemble of oscillators leads to inhomogeneous broadening. In the time domain, this causes faster dephasing of the interferogram because the phase of the ensemble of oscillators begins to destructively interfere at longer time τ. The photon echo flips the phase of these oscillators with the second and third pulses with a zero waiting time, which cause the oscillators to rephase or constructively interfere at a later time along t. This is known as the photon echo. Because the rephasing time of the echo depends on the time τ, this manifests as a diagonal broadening in the 2D IR spectrum.

The inclusion of the nonzero waiting time allows for the oscillators to change their environments as a function of T. Because the frequencies of oscillators become more scrambled at longer T, the echo contribution becomes weaker and leads to a rounder 2D lineshape. Another way to think about this is that the pump labels a frequency at ω_τ, and the probe reads out the frequency of the labeled oscillator at ω_t. At short T, the labeled and read-out frequency will be the same. At longer waiting time, the oscillator environment and frequency will change, leading to a different readout frequency for the probe. Because an ensemble of oscillators is being measured and the environment and therefore frequency fluctuations are random, the probe frequency will appear to diffuse away from the initial label position. Assuming the frequency fluctuations are stationary, this is usually modeled in terms of a frequency-frequency correlation function (FFCF).[19] This phenomenon is known as spectral diffusion and is the dynamic observable of interest for many vibrational labels.[20]

There exist several methods to extract the FFCF from the 2D IR spectra.[21] The pump-probe paradigm just described implies that the FFCF can be extracted from the diagonal and off-diagonal widths.[22] It turns out that the slope of the node between the positive and negative peaks, known as the nodal line slope, also reports on the FFCF. The most robust method, though, is the center line slope (CLS) method.[23,24] This method involves finding the diagonal peak maxima of ω_τ slices (ΔOD as a function of ω_τ) and fitting these maxima to a line as a function of ω_τ. With some assumptions, the T-dependent slope of this line is shown to be directly proportional to the FFCF. This is the method I will use in chapter 4 to study the local environment sensitivity of the tyrosine ring mode.

1.2 The 2D IR setup

Figure 4 shows a schematic of the 2D IR setup used in our lab. This setup has several notable features. First, the 2D IR setup is equiped with our new smart referencing algorithm (Chapter 2).[25] Second, the pump double-pulse is generated by a programmable pulse shaper (Chapter 3). Third, we use a telescope to enlarge the probe beam to ensure that the probe focus is tighter than the pump focus, which will help generate the largest signal to probe ratio. This is important for maximizing the SNR. Finally, the setup contains polarization control and can collect the <ZZZZ> and <YYZZ> signal polarizations simultaneously. Although this capability is not extensively used in this dissertation, this capability allows for fast and accurate measurement of rotational dynamics.

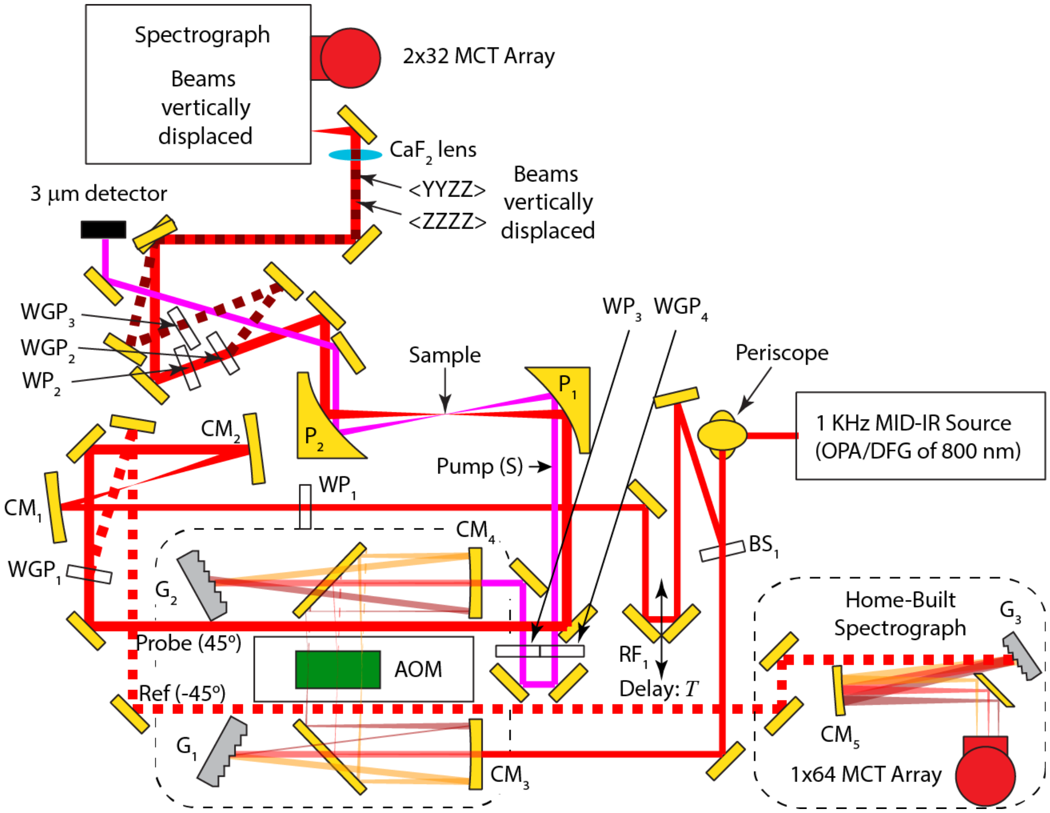

Figure 4. The current state of the 2D IR setup. The beams are labeled as follows. Red: probe; magenta: pump; red-dash: reference. After the sample: red: <ZZZZ>; dark red-dash: <YYZZ>. The optics are labeled as follows. BS: beam splitter; RF: retroreflector; CM: concave mirror; G: grating; WP: ½ waveplate; WGP: wire-grid polarizer; P: parabolic mirror. Boxed in dashed lines are the pulse shaper and the reference spectrograph. This figure is not to scale, but the relative location of all the optics is correct.

The polarization scheme is as follows. First, the probe beam is rotated by a ½-waveplate, WP1, to an arbitrary polarization. The first polarizer, WGP$_1$, is set so that the transmitted beam is linearly polarized at 45^{o} (s + p) at the sample focal spot. The reflected polarization is sent for reference detection. The reason the ½ waveplate rotation is arbitrary is because this waveplate is used to control the relative intensity between the refence and probe beams. The pump is set to be s-polarized by WGP$_2$ so that all polarization components of the pump and probe beams in the focal spot volume are either perfectly orthogonal or parallel to each other. The probe at the focal spot volume has both S and P polarizations. The analyzer (WGP_2) is set to the s-polarization, so that s-polarized light is transmitted and so that p-polarized light is reflected. The s-polarization component is rotated by a ½ waveplate (WP_2) to the p-polarization. A small portion of s-polarized light is also reflected, so an additional polarizer (WGP_3) set to p-polarization is used to improve the extinction of the reflected light. The transmitted light corresponds to the <ZZZZ> signal polarization and reflected light corresponds to the <YYZZ> signal polarization. Note that linear polarization is carefully maintained after the first polarizer by using unprotected gold mirrors until the analyzer to prevent the unwanted generation of elliptical polarizations.[26] Finally, we use a set of vertically-displaced mirrors to direct the beams to cross around 115 mm before a f = 100 mm CaF_2 lens (focal length reported for 588 nm) before the entrance slit. The data is acquired by a 2x32 element MCT dual array from Infrared Associates, Inc. using data acquisition equipment from Infrared Systems Development.

As a reference, I also provide some estimates of the mid IR beam parameters used to acquire the 2D IR data in chapter 4. Our home-built OPA is pumped by 1.2 W of 800 nm light with a FWHM bandwidth of approximately 15 nm. Immediately after the DFG stage, approximately 3 μJ of 6.6 μm mid IR light is generated with a pulse duration estimated at 170 fs. While the 2D IR spectrometer is purged to minimize water vapor absorption, the pulse energy before the pulse shaper is reduced to 1.9 μJ. After the pulse shaper, each pump pulse has an approximate energy of 125 nJ (or 500 nJ total without time delay) at small τ when double pulse falloff is negligible. With good alignment, we can achieve an approximately 150 μm focal spot FWHM for the pump and 75 μm for the probe. This corresponds to a peak intensity of 2.7 GW/cm^2 for each pump pulse at the sample.

1.3 Overview of the Dissertation

2D IR spectroscopy of biomolecules is inherently difficult because low concentrations are usually required to maintain physiological relevance. This requirement poses a serious SNR problem because the signal acquired will be weak. Just by the definition of SNR, there are two ways to approach this problem: either by increasing the signal or reducing the noise. Signal can be increased by using a stronger laser. Because of the pump-probe geometry we use in the setup, the increase in laser power needs to come from the pump because the probe beam intensity must kept within the saturation limit of the detector. The noise can be reduced through a technique called referencing, where the goal is to remove the laser shot-to-shot fluctuations from the measured data.

The remainder of this dissertation will focus on addressing this SNR problem and using the sensitivity that was achieved to study the dynamics of tyrosine ring mode. In Chapter 2, I will present a noise reduction method that reduces the noise to the signal detector noise floor limit. Part of this work has been previously published.[25] A patent is currently pending.[27] Another manuscript is also currently being prepared. In Chapter 3, I will show how to increase the signal by improving the pump intensity and beam quality. This chapter will include a through discussion on the acousto-optic modulator (AOM)-based pulse shaper and is intended to also be used as a reference guide for future students. Finally, in Chapter 4, I will use the improved sensitivity to characterize the local environment sensitivity of the tyrosine ring mode in the enkephalin/bicelle system. The increased sensitivity allowed us to observe unusual vibrational dynamics that cause a line-shape distortion to the otherwise featureless vibrational mode. We examine three possible origins of this line-shape distortion. A manuscript is being prepared for Chapter 4.

2. A General Noise Suppression Scheme with Reference Detection for Heterodyne Nonlinear Spectroscopy

2.1 Introduction

Many optical spectroscopic techniques utilize heterodyne detection where a signal is mixed with a local oscillator (LO) and detected with a square-law photodetector. Heterodyne detection has the benefit of preserving the signal phase information and achieving a high signal-to-noise ratio (SNR) even when the signal is weak. Depending on the role of the LO, optical heterodyne spectroscopy can be divided into two classes.[19] The first class is self-heterodyne spectroscopy, where one excitation beam serves as the LO. This class includes transient absorption/reflection and stimulated Raman scattering, among other techniques. These techniques all employ some form of a pump-probe geometry, where the LO beam is also called the probe beam. The other class uses an external LO which does not excite the sample to generate the signal, as implemented in heterodyne detected four-wave-mixing and sum-frequency generation spectroscopies. Despite the advantages and wide applications of heterodyne detection, the SNR of heterodyne detection is often severely deteriorated by the LO intensity fluctuations. The intensity fluctuation not only introduces random noise that can be averaged out, but also the baseline shift and signal distortion that survive infinite averaging.[28,29] Therefore, noise reduction is a critical issue in heterodyne spectroscopy and the focus of this work.

To reduce noise in heterodyne spectroscopy, previous works often utilize a second photodetector to compensate for the LO intensity fluctuations in two ways: balanced heterodyne detection[30] where both detectors measure the signal and LO (but with a π-phase shift), and reference detection where the second detector only measures the LO.

Reference detection is more versatile in the sense that it can be easily introduced wherever balanced heterodyne detection is applied. Therefore, we will focus on reference detection in this paper.

Previous works on reference detection can be divided into three classes based on the types of detectors used: both signal and reference detectors are single-pixel;[31-35] the signal detector is an array and the reference detector is single-pixel;[29,36,37] and both signal and reference detectors are arrays.[28,34,38-41] To combine the outputs from two detectors, either a subtraction method[31,32,35] or a ratiometric method[28,29,32,33,36,38-42] is used. These are termed as 'conventional methods' to distinguish from the methods described later in this paper. The subtraction method is usually implemented in analog-circuits between two photodetectors before the differential output is digitized. These analog-balanced photodetectors are now commercially available. The ratiometric method is always implemented digitally where both detector outputs are digitized before mathematical divisions are calculated.

Due to its analog implementation, the subtraction method is often used in experiments involving MHz lasers.[31,35] However, the subtraction method requires that the two photodiodes are balanced precisely beforehand. As pointed out previously,[32] slow drift of laser pointing can unbalance the photodiodes. Therefore, the ratiometric method is more popular in kHz lasers even when two matched photodiodes are used. Previous studies showed that the residual laser noise was still much higher than the shot noise limit even with matched photodiodes and careful alignment.[32,33] When detector arrays are employed, the ratiometric method is almost always used because arrays cannot be easily balanced by analog circuits. The simplest approach uses a photodiode output to normalize the array output.[29,36,37] This method assumes that the noise is independent of wavelength, which is not always true, especially for supercontinuum light. More advanced approaches use one array to normalize another array, with examples spanning from UV-visible[28,34,38,42] to mid-IR.[39-41] However, these two arrays and their respective spectrographs (if separate) need to be carefully matched for good performance, which greatly limits the detector choice and can be costly. The requirement of accurate wavelength mapping between the signal and reference arrays also adds extra difficulties for alignment.

In all three classes, it is difficult to suppress noise to the noise floor with conventional methods, especially for detectors with large well depths.[32,33,38,40] Moreover, conventional referencing can introduce additional noise and is only useful when the intensity fluctuations of the light source dominates over other noises.[43] In this chapter, we formulate a two-step reference scheme that circumvents these limitations and further improves the SNR in heterodyne nonlinear spectroscopy. By using a minimization routine and a linear combination of all reference channels, our method can reduce random noise towards the detection limit, ensure the correct convergence of the averaged signal, and is guaranteed to suppress noise. It is versatile for all detector choices and generally applicable for different techniques.

2.2 General analysis of noises in heterodyne spectroscopy

2.2.1 Additive and convolutional noises

We first give a general analysis of noises in heterodyne spectroscopy using the following notation to describe different physical quantities. E and I denote the electric field and intensity of a beam, respectively. They are random variables that can represent any single laser shot and may depend on wavelength (when measured by a detector array). The subscript denotes which beam: LO, Ref, and Pu are the local oscillator, reference, and pump beams, respectively; and Sig is the nonlinear signal from the sample. Both the sample signal and local oscillator are incident on the signal detector, and they are not separable in the self-heterodyne techniques. The total intensity on the signal detector, I_{tot}, is:

$$I_{\mathrm{tot}} = \left(E_{\mathrm{LO}} + E_{\mathrm{Sig}}\right)^2 = I_{\mathrm{LO}} + I_{\mathrm{Sig}} + 2E_{\mathrm{LO}}E_{\mathrm{Sig}} \tag{1}$$

We assume that I_{LO} is much stronger than I_{Sig} throughout this paper, and therefore we will ignore I_{Sig} later. The interference term $2E_{\mathrm{LO}}E_{\mathrm{Sig}}$ contains the sample response we want to extract from heterodyne detection. The exact expression for E_{Sig} depends on the specific techniques employed, but in general it is proportional to the electric fields of all the excitation beams and the sample response.[19] For the sake of simplicity, we will focus on pump-probe, although our methodology is equally applicable to other techniques. In pump-probe, $2E_{\mathrm{LO}}E_{\mathrm{Sig}} \triangleq \chi^{(3)} I_{\mathrm{LO}} I_{\mathrm{Pu}}$ with $\chi^{(3)}$ being the third-order susceptibility.

We further define $\bar{I} \triangleq \langle I \rangle$ and $\delta I \triangleq I - \bar{I}$. Here the brackets indicate the expected (mean) value of a random variable and the δ prefix indicates the deviation of a random variable from its expected value. In heterodyne nonlinear spectroscopy, usually chopping or phase-cycling are used to remove the strong I_{LO} background. In both cases, we use the superscripts * and ′ to denote the two shots in a pair of consecutive shots and define $\Delta I \triangleq I^* - I' = \delta I^* - \delta I'$ as the intensity difference between them. δI and ΔI are related by the variance: $\mathrm{var}(\Delta I) = 2(1 - r) \cdot \mathrm{var}(\delta I)$ where $r \triangleq \mathrm{corr}(I^*, I')$ is the consecutive shot correlation coefficient. With chopping, * refers to pump-on whereas ′ refers to pump-off, and we obtain:

$$\Delta I_{\text{tot}} = \left(E_{\text{LO}}^{*} + E_{\text{Sig}}^{*}\right)^2 - (E'_{\text{LO}})^2 \approx \Delta I_{\text{LO}} + \chi^{(3)} I_{\text{LO}}^{*} I_{\text{Pu}}^{*} \tag{2}$$

With phase-cycling, * refers to zero-phase shift whereas ′ refers to π-phase shift, and we obtain:

$$\Delta I_{\text{tot}} = \left(E_{\text{LO}}^{*} + E_{\text{Sig}}^{*}\right)^2 - \left(E'_{\text{LO}} - E'_{\text{Sig}}\right)^2 \approx \Delta I_{\text{LO}} + \chi^{(3)} (I_{\text{LO}}^{*} I_{\text{Pu}}^{*} + I'_{\text{LO}} I'_{\text{Pu}}) \tag{3}$$

In a perfect world where no noise exists, $\Delta I_{\text{LO}} = 0$ and $I_{\text{LO}}^{*} I_{\text{Pu}}^{*} = I'_{\text{LO}} I'_{\text{Pu}}$. ΔI_{tot} in Eq. (2) and (3) contains only the signal terms. In the real world, both terms contribute to the total noise: the ΔI_{LO} term is independent of the sample response $\chi^{(3)}$, and thus it is additive; the second term is multiplied by $\chi^{(3)}$, and thus it is convolutional (or multiplicative). The two types of noise need to be removed separately. Terms like $I_{\text{LO}} I_{\text{Pu}}$ can be decomposed into:

$$I_{\text{LO}} I_{\text{Pu}} = \bar{I}_{\text{LO}} \bar{I}_{\text{Pu}} \left(1 + \frac{\delta I_{\text{LO}}}{\bar{I}_{\text{LO}}}\right) \left(1 + \frac{\delta I_{\text{Pu}}}{\bar{I}_{\text{Pu}}}\right) \tag{4}$$

This means that the convolutional noise is related to δI of multiple beams, in contrast to the additive noise ΔI_{LO} which is only related to the fluctuation in LO. In many systems of interest where the sample signal is very weak, the additive noise is much larger than the convolutional noise. To see this, we can rearrange Eq. (3) and (4) into:

$$\frac{\Delta I_{\text{tot}}}{\bar{I}_{\text{LO}}} = \overline{\Delta \text{OD}_{\text{e}}} + \frac{\Delta I_{\text{LO}}}{\bar{I}_{\text{LO}}} + \overline{\Delta \text{OD}_{\text{e}}} \left(\frac{\delta I_{\text{LO}}^{*}}{\bar{I}_{\text{LO}}} + \frac{\delta I_{\text{Pu}}^{*}}{\bar{I}_{\text{Pu}}} + \frac{\delta I_{\text{LO}}^{*}}{\bar{I}_{\text{LO}}} \frac{\delta I_{\text{Pu}}^{*}}{\bar{I}_{\text{Pu}}}\right) \tag{5}$$

where $\overline{\Delta \text{OD}_{\text{e}}} \triangleq \chi^{(3)} \bar{I}_{\text{Pu}}$ is the expected value of absorbance change (in e-base) induced by the pump beam. $\overline{\Delta \text{OD}_{\text{e}}}$ is often below 0.01, and can be even lower than 10^{-5}. The second term on the right-hand side of Eq. (5) is the additive noise, and the third term is the convolutional noise. For typical lasers, RMS values of $\Delta I_{\text{LO}}/\bar{I}_{\text{LO}}$, $\delta I_{\text{LO}}^{*}/\bar{I}_{\text{LO}}$ and $\delta I_{\text{Pu}}^{*}/\bar{I}_{\text{Pu}}$ are on the order of 0.2%–2%.[33,34,38,40,43-47] This means that the additive noise is not only orders of magnitude larger than the convolutional noise,[44] but it also can be larger than $\overline{\Delta\mathrm{OD}_\mathrm{e}}$. Therefore, it is most critical to suppress the dominant additive noise.

2.2.2 Characteristics of last Fluctuations

To demonstrate the noise statistics and their suppression, we collected data with our pump-probe 2D IR setup. The schematic of the setup is shown in Figure 5. Ultrafast mid-IR pulses were generated at 1 KHz by an 800-nm pumped OPA/DFG source, [48] and centered at ~6 μm with FWHM ~150 cm^{-1}. The mid-IR beam is split into two: the first beam serves as the source for the LO (probe) and reference beams, and the second beam goes through an acousto-optic modulator (AOM) and acts as the pump beam.[49] The experimental setup was purged to remove atmospheric absorption. Except for Figure 11(a), all data were collected by a liquid nitrogen (LN_2) cooled 2×32-pixel mercury cadmium telluride (MCT) array behind a commercial spectrograph. The top row is designated as the signal detector, and the bottom row as the reference detector. All data for noise analysis were collected with pump off except for Figure 10(a).

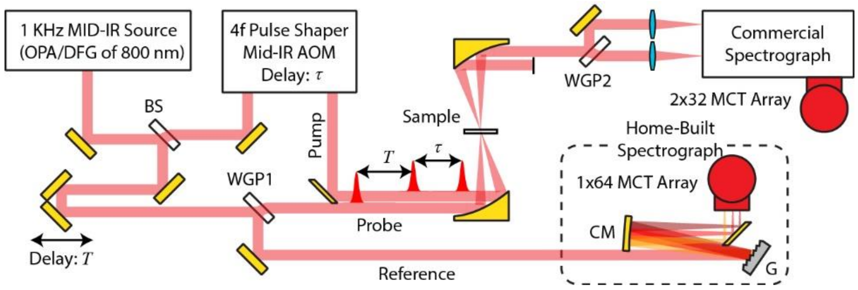

Figure 5. Schematic of our pump-probe 2D IR setup. OPA: optical parametric amplifier; DFG: difference frequency generation; BS: beam splitter; WGP: wire grid polarizer. CM: concave mirror. G: grating. Two spectrographs are unmatched to demonstrate the performance of our reference scheme.

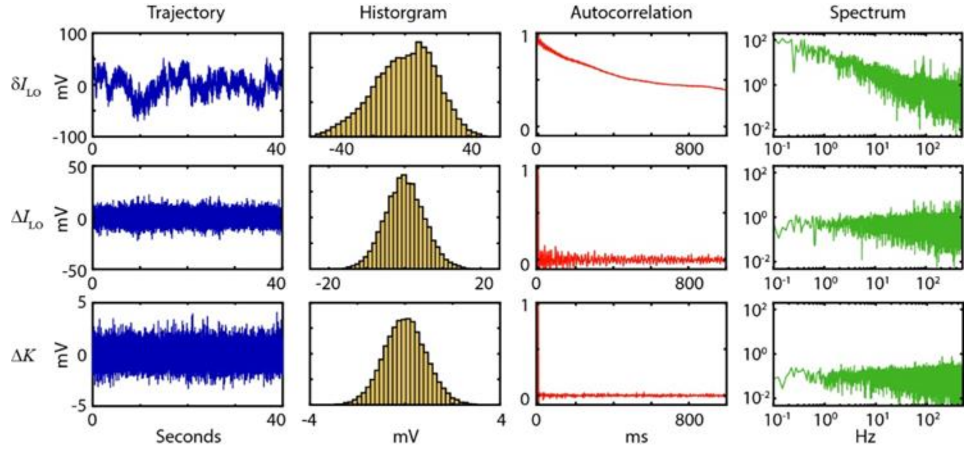

Figure 6. Statistical properties of noise before and after multi-channel referencing. The three rows are δI_{LO}, ΔI_{LO}, and ΔK (see Section 2.3.2) from top to bottom. The four columns are the time trajectories, histograms, autocorrelations, and amplitude spectra from left to right.

The first two rows in Figure 6 show the laser statistical properties taken from the central pixel of the signal array over a 40-second trajectory. δI_{LO} has 40K data points whereas ΔI_{LO} has 20K data points because ΔI is defined for a pair of consecutive shots. δI_{LO} has fluctuations typical for many ultrafast lasers[16,28,29,31-33,45,46] and the histogram shows deviations from a Gaussian distribution. The amplitude spectrum is dominated by 1/f-noise at low frequencies. In contrast, the amplitude spectrum for ΔI_{LO} is almost flat and resembles white noise across the entire frequency range. Its histogram is also very close to a Gaussian distribution. The autocorrelation of ΔI_{LO} exhibits a sharp drop after zero lag followed by small oscillations, which is very different from the decay seen in the autocorrelation of δI_{LO}. We repeated the measurements under many conditions with different 800-nm pump laser intensity/stability and OPA/DFG parameters and found that the basic features of ΔI_{LO} are always stable whereas the behavior of δI_{LO} can vary widely. For example, Figure 6 shows a dataset where the autocorrelation of δI_{LO} decreases very slowly, but it is not always so slow. The operation of chopping and taking the intensity difference between two consecutive shots to obtain ΔI_{LO} is similar to applying a high-pass filter, which removes the low-frequency noise that dominates the δI_{LO} spectrum. Another difference between ΔI_{LO} and δI_{LO} is that they have different correlation coefficients between the corresponding signal and reference pixels, as shown in Figure 7(d). We typically find that $\mathrm{corr}(\Delta I_{\mathrm{LO}}, \Delta I_{\mathrm{Ref}})$ is higher than $\mathrm{corr}(\delta I_{\mathrm{LO}}, \delta I_{\mathrm{Ref}})$ in our system. Without fully accounting for the distinctive statistical properties of ΔI_{LO}, the additive noise cannot be optimally suppressed.

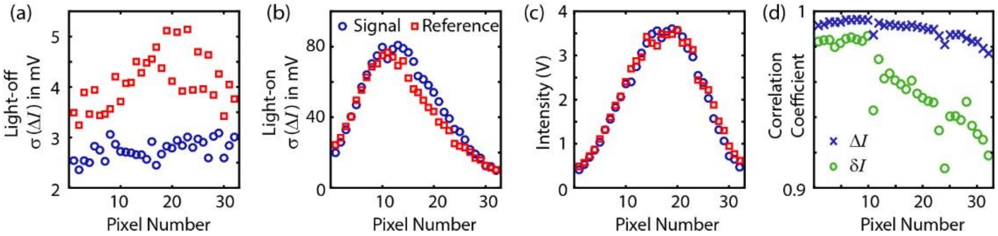

Figure 7. This figure shows the statistics for the dataset in Figure 8, Figure 11, and Figure 12. $\sigma(\Delta \boldsymbol{I})$ with the light off (a) and with the light on (b), and the mean spectrum (c) for the two rows of the 2×32 MCT array. Blue circles are for the signal array and red squares are for the reference array. (d) Correlation coefficients between the corresponding signal and reference pixels. The blue crosses are for $\mathrm{corr}(\Delta I_{\mathrm{LO}}, \Delta I_{\mathrm{Ref}})$, and green circles are for $\mathrm{corr}(\delta I_{\mathrm{LO}}, \delta I_{\mathrm{Ref}})$.

2.2.3 Total noise and detector noise

Before presenting our noise suppression scheme, we will discuss different noise sources. The additive noise ΔI_{LO} can be decomposed as:

$$\sigma(\Delta I_{\mathrm{LO}}) \propto \sqrt{2\left(N_{\mathrm{LO}} + {N_{\mathrm{r}}}^2 + D \cdot t\right) + (N_{\mathrm{LO}} \cdot p_2)^2} \tag{6}$$

where σ means standard deviation throughout this paper. N_{r} is the readout noise (including all electronic and digitization noise). $(D \cdot t)^{1/2}$ is the dark noise with D being the dark current and t being the integration time. $(N_{\mathrm{LO}})^{1/2}$ is the photon shot noise from the LO (except for amplitude-squeezed light[50]). All three noise terms are counted by the number of electrons. Ideally, they are uncorrelated with one another. $(N_{\mathrm{LO}} + N_{\mathrm{r}}{}^2 + D \cdot t)^{1/2}$ is the noise floor, and $(N_{\mathrm{r}}{}^2 + D \cdot t)^{1/2}$ is the detector noise which can be measured by blocking the light. The factor of 2 before the parentheses in Eq. (6) accounts for the fact that ΔI is defined for a pair of consecutive shots, but is not included when reporting the detector SNR. For our dual-row MCT array, the full-well capacity is $\sim 10^9$ electrons in the linear response range, and the best dynamic range is ~ 2800 (although the detector noise level of MCT detectors drifts frequently). This gives an estimated $(N_{\mathrm{r}}{}^2 + D \cdot t)^{1/2} \sim 3.6\times10^5$ electrons which is more than 11 times the maximal $(N_{\mathrm{LO}})^{1/2}$ possible, making photon shot noise negligible. Therefore, the SNR of MCT detectors is limited by the detector noise. The SNR may be limited by photon shot noise for other types of detectors, especially for many sensitive CCD and CMOS arrays. The $(N_{\mathrm{LO}} \cdot p_2)$ term represents the contribution of LO intensity fluctuation with p_2 being a measure of the fractional intensity change between two consecutive shots, and it is the only referenceable common-mode noise shared by both the signal and reference detectors. Because the $(N_{\mathrm{LO}} \cdot p_2)^2$ term is quadratically scaled with N_{LO}, it can dominate and severely degrade the SNR of heterodyne detection when the LO intensity is high. For detectors with large well depths, it is beneficial to work with a high LO intensity to exploit the high detector SNR,[40,44,45] and thus good noise suppression is especially needed for this case.

2.3 Suppression of additive ΔI_{LO} noise

2.3.1 Derivation of the single-channel method

We begin with an arbitrary single-reference-channel method where each signal channel is referenced by only one reference channel. Here "arbitrary" means that this can be one photodiode referenced by another photodiode, an array pixel referenced by a photodiode, or an array pixel referenced by another array pixel. To our best knowledge, this already generalizes the referencing methods previously covered in the literature.

First, we propose an extended ratiometric method that introduces two free parameters d_{LO} and d_{Ref} as an ansatz, and define $k_{\mathrm{LO}} \triangleq \bar{I}_{\mathrm{LO}} + d_{\mathrm{LO}}$, $k_{\mathrm{Ref}} \triangleq \bar{I}_{\mathrm{Ref}} + d_{\mathrm{Ref}}$.

$$J \overset{\mathrm{def}}{=} \frac{\left(\bar{I}_{\mathrm{LO}} + d_{\mathrm{LO}}\right) + \delta I_{\mathrm{LO}}}{\left(\bar{I}_{\mathrm{Ref}} + d_{\mathrm{Ref}}\right) + \delta I_{\mathrm{Ref}}}\left(\bar{I}_{\mathrm{Ref}} + d_{\mathrm{Ref}}\right) \approx k_{\mathrm{LO}} + \left(\delta I_{\mathrm{LO}} - \frac{k_{\mathrm{LO}}}{k_{\mathrm{Ref}}} \cdot \delta I_{\mathrm{Ref}}\right) \tag{7}$$

When $d_{\mathrm{LO}} = d_{\mathrm{Ref}} = 0$, Eq. (7) reduces to the conventional ratiometric method and J becomes the LO intensity after referencing. In the approximation of Eq. (7), we assume $\delta I_{\mathrm{Ref}}/k_{\mathrm{Ref}} \ll 1$. In the case of conventional ratiometric method, this approximation requires that the relative intensity fluctuation $\delta I_{\mathrm{Ref}}/\bar{I}_{\mathrm{Ref}}$ is small. However, we will show below that this approximation can always be justified by choosing appropriate values for d_{LO} and d_{Ref} in our extended ratiometric method. Now taking the difference between a pair of consecutive shots:

$$\Delta J = J^{*} - J' = \Delta I_{\mathrm{LO}} - \frac{k_{\mathrm{LO}}}{k_{\mathrm{Ref}}} \cdot \Delta I_{\mathrm{Ref}} \tag{8}$$

ΔJ can be considered as residual ΔI_{LO} noise after referencing and needs to be minimized with respect to the free parameters. Because the expected values of both ΔI_{LO} and ΔI_{Ref} are zero, the expected value of ΔJ is also zero for any value of $k_{\mathrm{LO}}/k_{\mathrm{Ref}}$. To minimize a random variable with a zero mean, we just need to minimize its variance with respective to the free parameters:

$$\frac{\partial\,\mathrm{var}(\Delta J)}{\partial k_{\mathrm{Ref}}} = 0 \qquad \frac{\partial\,\mathrm{var}(\Delta J)}{\partial k_{\mathrm{LO}}} = 0 \tag{9}$$

Both equations yield the same result:

$$\frac{k_{\mathrm{LO}}}{k_{\mathrm{Ref}}} = \frac{\mathrm{cov}(\Delta I_{\mathrm{LO}}, \Delta I_{\mathrm{Ref}})}{\mathrm{var}(\Delta I_{\mathrm{Ref}})} = R \cdot \frac{\sigma(\Delta I_{\mathrm{LO}})}{\sigma(\Delta I_{\mathrm{Ref}})} \tag{10}$$

where $\mathrm{cov}(\Delta I_{\mathrm{LO}}, \Delta I_{\mathrm{Ref}})$ is the covariance and $R = \mathrm{corr}(\Delta I_{\mathrm{LO}}, \Delta I_{\mathrm{Ref}})$ is the correlation coefficient between ΔI_{LO} and ΔI_{Ref}. The minimized residual noise is:

$$\mathrm{var}_{\mathrm{min}}(\Delta J) = (1 - R^2) \cdot \mathrm{var}(\Delta I_{\mathrm{LO}}) \tag{11}$$

Because Eq. (10) only imposes a constraint on the ratio, we can adjust d_{LO} and d_{Ref} while keeping $k_{\mathrm{LO}}/k_{\mathrm{Ref}}$ constant without changing the result in Eq. (11). In fact, d_{LO} and d_{Ref} can be set to be arbitrarily large so that $\delta I_{\mathrm{Ref}}/k_{\mathrm{Ref}} \ll 1$ is always justified for Eq. (7).

Next, we propose an extended subtraction method which introduces one free parameter b as an ansatz:

$$K \overset{\mathrm{def}}{=} I_{\mathrm{LO}} - b \cdot I_{\mathrm{Ref}} \tag{12}$$

When $b = \bar{I}_{\mathrm{LO}}/\bar{I}_{\mathrm{Ref}}$, Eq. (12) reduces to the conventional subtraction method and K can be considered as the differential output of analog-balanced photodetectors. Now taking the difference between a pair of consecutive shots:

$$\Delta K = \Delta I_{\mathrm{LO}} - b \cdot \Delta I_{\mathrm{Ref}} \tag{13}$$

ΔK is the residual noise after referencing, and it is also zero mean for any value of b. Minimizing the variance of ΔK with respect to b yields similar results to Eq. (10) and (11):

$$b = \frac{\mathrm{cov}(\Delta I_{\mathrm{LO}}, \Delta I_{\mathrm{Ref}})}{\mathrm{var}(\Delta I_{\mathrm{Ref}})} = R \cdot \frac{\sigma(\Delta I_{\mathrm{LO}})}{\sigma(\Delta I_{\mathrm{Ref}})} \tag{14}$$

$$\mathrm{var}_{\min}(\Delta K) = (1 - R^2) \cdot \mathrm{var}(\Delta I_{\mathrm{LO}}) \tag{15}$$

This is not surprising given the similarity between Eq. (8) and Eq. (13). When both are minimized, ΔK is exactly the same as ΔJ (in the very large k_{LO} and k_{Ref} limit) although K and J are different. Intuitively, b or $k_{\mathrm{LO}}/k_{\mathrm{Ref}}$ optimally scales the reference channel ΔI fluctuations to the signal channel ΔI fluctuations when either parameter is found by simple linear regression. In the subsequent sections we will focus on the extended subtraction method.

In our method, the effects of uncorrelated noises are explicitly considered because b is calculated from $\mathrm{cov}(\Delta I_{\mathrm{LO}}, \Delta I_{\mathrm{Ref}})$ and $\mathrm{var}(\Delta I_{\mathrm{Ref}})$ rather than mean intensities $\bar{I}_{\mathrm{LO}}$ and $\bar{I}_{\mathrm{Ref}}$ which average out the noises. This guarantees that our method always suppresses the noise more effectively than the conventional methods. To demonstrate this intuitively, consider a case where perfectly matched signal and reference detectors detect the same light intensities so that $\bar{I}_{\mathrm{LO}} = \bar{I}_{\mathrm{Ref}}$ and $\mathrm{var}(\Delta I_{\mathrm{LO}}) = \mathrm{var}(\Delta I_{\mathrm{Ref}})$. With conventional methods, taking the variance of Eq. (13) and (8) under the condition of $b = 1$ and $k_{\mathrm{LO}}/k_{\mathrm{Ref}} = 1$, respectively, leads to $\mathrm{var}(\Delta K) = \mathrm{var}(\Delta J) = 2(1 - R)\,\mathrm{var}(\Delta I_{\mathrm{LO}})$. From Eq. (6), R is always less than 1 due to the presence of uncorrelated noises, which leads to $(1 - R^2) < 2(1 - R)$. This means that the residual noise in our method is always lower than that of conventional methods. Sometimes the $(N_{\mathrm{LO}} \cdot p_2)^2$ term in Eq. (6) is so small that the uncorrelated detector noises constitute a major noise source for $\sigma(\Delta I_{\mathrm{LO}})$ and R is well below 1. This occurs when the laser is stable or the light intensity is weak. When $R < 0.5$, the conventional methods will increase the noise level after referencing. In contrast, our method always reduces noise even for anti-correlation, which is guaranteed by the non-negative R^2. The above comparison considers the best-case scenario in the conventional methods. In more realistic situations where two detectors cannot be perfectly matched, the conventional methods will perform even worse.

Moreover, by treating the statistics of ΔI_{LO} directly, the referencing performance in Eq. (15) does not explicitly contain the consecutive shot correlation r. Another important feature is that because of the linear form in Eq. (13) and $\langle \Delta I_{\mathrm{LO}} \rangle = \langle \Delta I_{\mathrm{Ref}} \rangle = 0$, our method does not introduce any baseline shift or signal distortion even when the light intensity fluctuates a lot.

2.3.2 Combining multiple reference channels

As shown in Eq. (15), the performance of our referencing method only depends on the correlation coefficient R. When using an array as reference, the reference pixel does not need to detect the same wavelength as the signal pixel nor need to be a physical pixel. Below we will show that it is possible to linearly combine all physical reference pixels into an optimal virtual reference pixel which maximizes R.

Figure 8(a) shows the spectral correlation map for ΔI_{LO} in the signal array, $\mathrm{corr}(\Delta I_{\mathrm{LO}}, \Delta I_{\mathrm{LO}})$. It is clear that ΔI_{LO} on different pixels is most correlated when their wavelengths are close, and the correlation decreases with increasing wavelength difference. This feature of spectral correlation is quite typical for femtosecond lasers,[38] but it may also be more complex depending on the nature of the light source.[28] In Figure 8(a), the spectral correlation map between the signal array and the reference array, $\mathrm{corr}(\Delta I_{\mathrm{LO}}, \Delta I_{\mathrm{Ref}})$, also shows similar features. This means that multiple pixels in the reference array contain information about the intensity fluctuations of a single pixel in the signal array. It is therefore possible to find a linear combination of these reference pixels that will give a higher correlation with the signal pixel than any single reference pixel. Following Eq. (13), we write:

$$\Delta\boldsymbol{K}(i) = \Delta\boldsymbol{I}_{\mathbf{LO}}(i) - \Delta\boldsymbol{I}_{\mathbf{Ref}}\,\boldsymbol{\beta}_i \tag{16}$$

assuming that the signal array has m pixels and reference array has n pixels, $\Delta\boldsymbol{K}$ and $\Delta\boldsymbol{I}_{\mathbf{LO}}$ are random row vectors with m components, and $\Delta\boldsymbol{I}_{\mathbf{Ref}}$ is a random row vector with n components. $\Delta\boldsymbol{K}(i)$ and $\Delta\boldsymbol{I}_{\mathbf{LO}}(i)$ are ΔK and ΔI_{LO} for the i^{th} signal pixel, respectively, and $\Delta\boldsymbol{I}_{\mathbf{Ref}}(j)$ is ΔI_{Ref} for the j^{th} reference pixel. $\boldsymbol{\beta}_i$ is a column vector with n components, and its j^{th} component represents the contribution of $\Delta\boldsymbol{I}_{\mathbf{Ref}}(j)$ to the i^{th} virtual reference pixel. Since the expected value of $\Delta\boldsymbol{K}(i)$ is zero for any $\boldsymbol{\beta}_i$, the variance of the $\Delta\boldsymbol{K}(i)$ can be minimized by ordinary least squares. A closed-form expression for $\boldsymbol{\beta}_i$ exists:

$$\boldsymbol{\beta}_i = \langle \Delta\boldsymbol{I}_{\mathbf{Ref}}{}^{T} \Delta\boldsymbol{I}_{\mathbf{Ref}} \rangle^{-1} \langle \Delta\boldsymbol{I}_{\mathbf{Ref}}{}^{T} \Delta\boldsymbol{I}_{\mathbf{LO}}(i) \rangle \tag{17}$$

where the brackets indicate evaluating the expected values of random variables. For the single-reference-channel case, $\boldsymbol{\beta}_i$ reduces back to b in Eq. (14). Combining all m signal pixels, Eq. (17) can be written as a concise matrix expression:

$$\boldsymbol{B} = \langle \Delta\boldsymbol{I}_{\mathbf{Ref}}{}^{T} \Delta\boldsymbol{I}_{\mathbf{Ref}} \rangle^{-1} \langle \Delta\boldsymbol{I}_{\mathbf{Ref}}{}^{T} \Delta\boldsymbol{I}_{\mathbf{LO}} \rangle = \mathrm{cov}(\Delta\boldsymbol{I}_{\mathbf{Ref}})^{-1}\,\mathrm{cov}(\Delta\boldsymbol{I}_{\mathbf{Ref}}, \Delta\boldsymbol{I}_{\mathbf{LO}}) \tag{18}$$

where $\boldsymbol{B} = (\boldsymbol{\beta}_1, \boldsymbol{\beta}_2, \ldots, \boldsymbol{\beta}_i, \ldots, \boldsymbol{\beta}_m)$ is a $n \times m$ matrix. The 2nd equality in Eq. (18) utilizes the fact that the expected values of $\Delta\boldsymbol{I}_{\mathbf{Ref}}$ and $\Delta\boldsymbol{I}_{\mathbf{LO}}$ are zero vectors. The matrix $\mathrm{cov}(\Delta\boldsymbol{I}_{\mathbf{Ref}})$ is positive-definite because the detector noises are always linearly independent between different pixels. Therefore, matrix inversion can be robustly and efficiently computed by the Cholesky decomposition, even when the reference array has many pixels. Inserting Eq. (17) back into Eq. (16), we get the residual noise after multi-channel referencing:

$$\frac{\mathrm{var}_{\min}\big(\Delta\boldsymbol{K}(i)\big)}{\mathrm{var}\big(\Delta\boldsymbol{I}_{\mathbf{LO}}(i)\big)} = 1 - \frac{\mathrm{cov}(\Delta\boldsymbol{I}_{\mathbf{LO}}(i), \Delta\boldsymbol{I}_{\mathbf{Ref}})\,\mathrm{cov}(\Delta\boldsymbol{I}_{\mathbf{Ref}})^{-1}\,\mathrm{cov}\big(\Delta\boldsymbol{I}_{\mathbf{Ref}}, \Delta\boldsymbol{I}_{\mathbf{LO}}(i)\big)}{\mathrm{var}\big(\Delta\boldsymbol{I}_{\mathbf{LO}}(i)\big)} \tag{19}$$

The quotient on the right-hand side of Eq. (19) is a generalization of R^2 in Eq. (15). It is also non-negative, which guarantees that multi-channel referencing will not increase the noise level.

The third row of Figure 6 illustrates the statistics of residual additive noise after multi-channel referencing with a virtual pixel that linearly combines all 32 physical reference pixels. The autocorrelation is almost flat around zero after the initial drop, which resembles that of ideal white noise. Compared with ΔI_{LO}, the histogram of ΔK has a much narrower distribution, and the amplitude spectrum is lowered by about 10 dB.

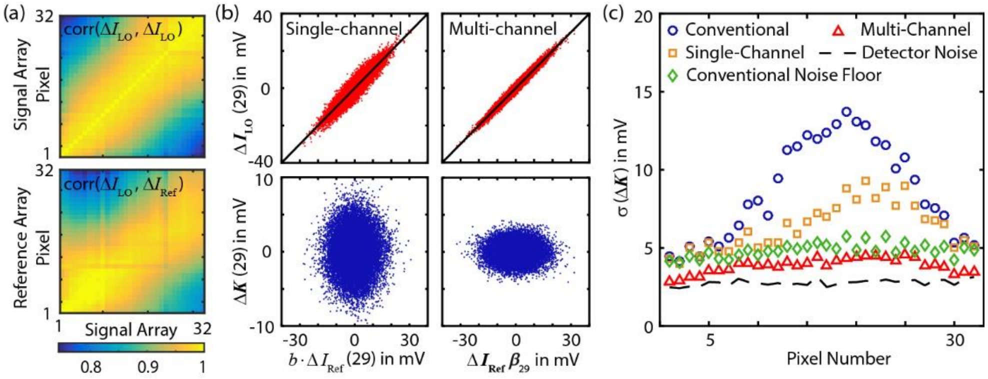

Figure 8. (a) Spectral correlation of ΔI between pixels within the signal array (top) and between the signal and reference arrays (bottom). (b) Scatter plot of a trajectory with 10K data points to show the relationship between the 29th signal pixel and the 29th physical or virtual reference pixels. The left column is for the single-channel method in Eq. (13). The right column is for the multi-channel method in Eq. (16). The coefficient b and column vector $\boldsymbol{\beta}_{29}$ were optimized based on Eq. (14) and (17), respectively. The black line in the top row is $y = x$, which is the best linear least-squares fit of the data. (c) Performance of different reference methods as measured by $\sigma(\Delta\boldsymbol{K})$. The blue circles, orange squares, and red triangles show the results from the conventional ratiometric, our single-channel and multi-channel reference method, respectively. The green diamonds show the total noise floor in the conventional methods, and the black dashed line shows the detector noise of the signal array only. Raw data statistics are shown in Figure 7.

Compared with the single-channel method, noise suppression is more effective with the multi-channel method. Figure 8(b) shows that the virtual reference pixel provides a better prediction of ΔI_{LO} with much less scattered residual noise ΔK than the physical reference pixel. The correlation coefficient R is 0.935 in the single-channel method and is optimized to 0.988 in the multi-channel method, resulting in an additional noise reduction of 2.3 times. The noise suppression follows the predicted $(1-R^2)^{1/2}$ dependence from Eq. (15) and (19), where $\sigma(\Delta \boldsymbol{K})$ drops steeply when R approaches 1. For pixels that measure the spectrum edge with low light intensity, the uncorrelated detector noises will lower R so that single-channel referencing is not as effective. Multi-channel referencing, however, can maximize R by utilizing the spectral correlation between different wavelengths.

Figure 8(c) illustrates how close each method can push the residual noise $\sigma(\Delta \boldsymbol{K})$ toward the noise floor. For the 13th signal pixel, which is the noisiest in this dataset, the conventional ratiometric, our single- and multi-channel referencing methods suppress the noise by a factor of 7.2, 12.2 and 19.6, respectively. In the conventional methods, the total noise floor contains detector noises from both signal and reference pixels and can be approximated by the root-sum-square of both contributions.[43] The residual noise after conventional referencing is still well above the conventional noise floor, indicating that the theoretical limit cannot be achieved in practice. In contrast, our multi-channel method brings the residual noise below the conventional noise floor, and only $\sim$38% higher than the detector noise of signal array. This means that there is a different noise floor limit for the new method (discussed below in Section 2.5.1). Using multi-channel referencing, the best achievable $\sigma(\Delta K/I_{\mathrm{LO}})$ before averaging is lower than $1/1400$ with MCT detectors working in the linear range, or $1/2000$ in the nonlinear range (see Section 2.5.3). This corresponds to a RMS noise level below 10 μOD (OD is the absorbance in 10-base) after averaging over 500 pairs of laser shots (1 second).

2.3.3 Implementation methods

In the above discussion, we collected all the LO spectra without the nonlinear signal (pump blocked) and calculated $\boldsymbol{B}$. In real data collection, the LO is mixed with the nonlinear signal and hence $\boldsymbol{B}$ needs to be estimated. One natural idea is to insert a small amount of blank shots without signal (pump is blocked but other conditions are the same) and estimate $\boldsymbol{B}$ based on these shots. Accordingly, shots that contain signal are called signal shots. There are many ways to distribute blank shots with the only requirement that at least two consecutive blank shots are inserted between signal shots to satisfy the definition of ΔI. We will consider two special cases while keeping the total number (percentage) of blank shots the same. In the fully-aggregated case, all the blank shots are collected together in one segment of data acquisition period. In the fully-dispersed case, only one blank-shot pair is inserted at a time, and the blank-shot pairs are distributed evenly among the signal shots. $\boldsymbol{B}$ is estimated after all the blank shots are collected. To characterize the quality of the estimation for $\boldsymbol{B}$, we define a quality factor q:

$$q = \left\langle \frac{\sigma(\Delta \boldsymbol{K}) \text{ based on the estimated } \boldsymbol{B} \text{ from blank shots}}{\sigma(\Delta \boldsymbol{K}) \text{ based on the optimal } \boldsymbol{B} \text{ from all shots}} \right\rangle \tag{20}$$

The brackets indicate the quadratic mean of all pixels. By definition, q is always larger than 1. The closer q is to 1, the better the estimation.

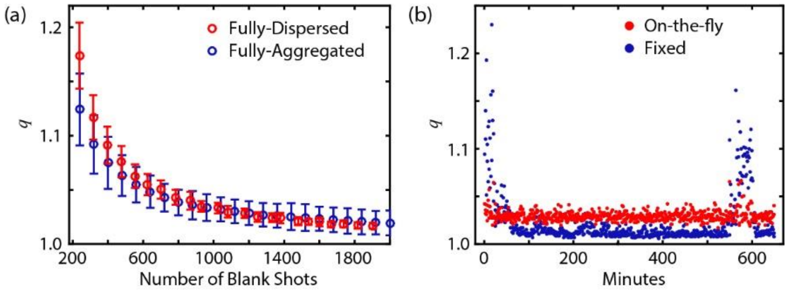

Figure 9. (a) Convergence of the q factor as a function of the number of blank shots. Red is for the fully-aggregated case, and blue is for the fully-dispersed case. (b) Long-term stability of the q factor as a function of time. Red is using a fixed $\boldsymbol{B}$ estimated from a single dataset, whereas blue is using $\boldsymbol{B}$ refreshed on-the-fly.

To evaluate the number of blank shots needed and the convergence of $\boldsymbol{B}$ estimation toward the optimal $\boldsymbol{B}$, we saved 100 datasets each of 40K total shots. For each dataset, we assigned a certain number of blank shots and calculated the corresponding estimated $\boldsymbol{B}$ and q. **Figure 9**(a) plots the mean value and standard deviation of q over the 100 datasets versus the number of blank shots, with the blank shots distributions being either fully-aggregated or fully-dispersed. For both distributions, q decreases rapidly at the beginning, reaching around 1.03 with only 1000 blank shots or 2.5% of the total shots. Further convergence is much slower and may be unnecessary considering the extra time cost of collecting more blank shots. Note that these numbers are validated with our MCT array which has only 32 pixels for reference detection. For a reference detector that has many more pixels, such as a CCD/CMOS array, the number of blank shots should be much higher than the number of pixels so that $\boldsymbol{B}$ estimation is an overdetermined problem. Figure 9(a) also shows that the fully-aggregated case gives a lower q than the fully-dispersed case when the number of blank shots is low. This trend is reversed with more blank shots. The former behavior is because the fully-aggregated case generates $(n-1)$ consecutive pairs from n blank shots, whereas the fully-dispersed case only generates $n/2$ pairs. With more consecutive pairs, $\boldsymbol{B}$ estimation is more accurate, especially when the number of blank shots is low. However, the fully-aggregated blank shots are not as representative of the statistical feature of the whole dataset as the fully-dispersed blank shots. This explains why the fully-dispersed case gives a lower q for larger numbers of blank shots. Furthermore, the fully-dispersed case also gives much smaller standard deviations, and hence the performance is more robust across different datasets. On the other hand, the fully-aggregated distribution has the advantage of early convergence and can be easily implemented in any experimental setups by simply blocking the pump (or signal) beams manually or with a motorized optical shutter. The fully-dispersed distribution generally requires a fast modulator like an AOM to arbitrarily control the percentage of blank shots, although it can also be achieved by a modified mechanical chopper wheel. Depending on the specific experimental details, such as the number of reference pixels and the laser repetition rate, it is possible to design another distribution of blank shots that combines the benefits of both cases.

To check the long-term stability of $\boldsymbol{B}$ estimation, we saved a dataset of 8000 shots (which takes 8 seconds) every minute over a period of about 11 hours. Immediately before the data collection began and after about 9 hours into the process, we refilled the MCT array with LN_2 to introduce an external disturbance. We calculated the q factor by estimating $\boldsymbol{B}$ in two ways: first, by using the whole 8000 shots taken at 300 min and applying this fixed $\boldsymbol{B}$ to each dataset; and second, by using the first 800 shots in each dataset and applying the "on-the-fly" $\boldsymbol{B}$ to the entire 8000 shots of that dataset. Figure 9(b) shows the q factor as a function of time. The fixed $\boldsymbol{B}$ estimation works quite well during the period without external disturbance. The q is about 1.01, lower than that of "on-the-fly" estimation because more blanks shots are included in the estimation. The fixed $\boldsymbol{B}$ performance is less satisfactory when the MCT array was refilled with LN_2. In comparison, the "on-the-fly" method has a steadier performance even when LN_2 was added. Depending on the types of detectors and stability of lasers, both the fixed and "on-the-fly" estimation methods can find their applications. Essentially, our method digitally post-balances arbitrary detectors with a small additional cost of time. Unlike those analog-balanced photodiodes with fixed balancing settings, our method can compensate for slow drifts of system during data collection when $\boldsymbol{B}$ is refreshed periodically.

Another question is whether or not $\boldsymbol{B}$ has to be refreshed when scanning some experimental parameters, such as the T delay (transient absorption), the τ delay (photo echo), the wavelength (hole-burning), and the polarization state of excitation beams. In Eq. (18), $\boldsymbol{B}$ depends on the LO and reference beams but not on the sample signal. Therefore, $\boldsymbol{B}$ has to be refreshed only when the intensity/spectrum of the LO or reference beams are changed in a parameter scan. Most parameter scans, including the ones stated above, do not change the LO or reference beams, and therefore a new $\boldsymbol{B}$ is not required. One exception is when the position of a heterogeneous sample is scanned in a pump-probe experiment. In experiments like the heterodyne photo echo, where the LO and reference beams do not pass through the sample, a new $\boldsymbol{B}$ is not required even when the sample position is scanned.

After $\boldsymbol{B}$ is estimated from the blank shots using Eq. (18), the additive noise in the signal shots is then removed by calculating Eq. (21). The involved matrix operations can be efficiently calculated in real time even for high-repetition-rate systems.[16,17,43]

$$\boldsymbol{S} \overset{\text{def}}{=} \Delta \boldsymbol{I}_{\mathbf{tot}} - \Delta \boldsymbol{I}_{\mathbf{Ref}}\, \boldsymbol{B} \tag{21}$$

To illustrate the effect of proper referencing, Figure 10(a) shows a sample scan over the coherence time τ in a 2D IR experiment. The sample was a solution of N-methylacetamide (NMA-d) in deuterated water with a 5 mOD amide-I peak in the FTIR spectrum. The traces come from the same dataset processed with three different referencing methods, and they are shown without applying any smoothing. A fully-aggregated blank shot distribution was adopted for the multi-channel referencing. Compared with the traces without referencing and with the conventional ratiometric referencing, our multi-channel referencing significantly improves the SNR. We typically observe a 10-30 times improvement over no referencing in our system.

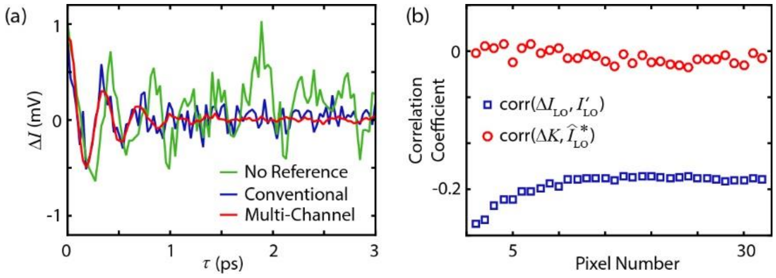

Figure 10. (a) Traces of the τ scan in a 2D IR experiment of NMA-d/D₂O. Performance of multi-channel referencing (red) compared with conventional ratiometric referencing (blue) and no referencing (green). Convolutional noise is not removed yet. (b) The correlation coefficient between ΔI_{LO} and I'_{LO} (blue square) and between ΔK and $\hat{I}^{*}_{\mathrm{LO}}$ (red circle).

Sometimes linear combinations (such as subtraction, average, and FFT) of data from different signal pixels or from multiple signal detectors (like balanced heterodyne detection) are needed. Our reference scheme is fully compatible with these operations. It can be easily shown that Eq. (18) and (21) are still the optimal solutions to additive noise suppression for combined pixels, as long as the equations are applied before linear combinations.

2.4 Suppressing convolutional noises

The next step is to suppress the convolutional noise. Combing Eq. (2), (16) and (21), the heterodyned signal for the i^{th} signal pixel in pump-probe experiments with chopping becomes:

$$\boldsymbol{S}(i) = \Delta\boldsymbol{K}(i) + \chi^{(3)} I_{\text{LO}}^{*} I_{\text{Pu}}^{*}(i) \tag{22}$$

As shown in Eq. (4), we can remove the intensity fluctuations in $I_{\text{LO}}^{*} I_{\text{Pu}}^{*}$ by dividing by $[1 + (\delta I/\bar{I})]$ for both beams. For phase-cycling in Eq. (3), the expression is more complex because it contains $(I_{\text{LO}}^{*} I_{\text{Pu}}^{*} + I_{\text{LO}}' I_{\text{Pu}}')$ involving both consecutive shots. For other techniques in general, we can remove the fluctuation by dividing the expression by $[1 + (\delta I/\bar{I})]^{1/2}$ for LO and each occurrence of field-matter interaction of the excitation beams. For the excitation beams derived from the same source as the LO, their intensity fluctuation is tracked by the reference detector. Otherwise, the intensity fluctuation of each excitation beam can be monitored individually by a photodetector. In principle, the convolutional noises need to be factored out from the correct version of Eq. (22) for different techniques in a shot-to-shot basis. Otherwise, the spectrum will be distorted even with infinite averaging due to non-zero correlation between the intensities of different beams (e.g. the third term in the parenthesis of Eq. (5), as discussed previously.[29] In reality, we found that signal distortion is usually negligible compared with other noise terms within reasonable averaging time. We also took the red trace in Figure 10(a) and further removed the convolutional noise and did not notice observable differences. This is consistent with our earlier analysis in Section 2.2.1 that the convolutional noise is orders of magnitude smaller than the additive noise in pump-probe spectroscopy.

Although our reference detector is an array, we usually sum over all its pixels and use the result to factor out LO intensity fluctuation. We found that this simple method is sufficient for our purpose. It also avoids the numeric instability problem if some pixels give near zero intensity. However, sometimes the LO intensity on every signal pixel is needed if the intensity fluctuations at different wavelengths are very different. This information can be reconstructed by the same $\boldsymbol{B}$ in Eq. (18) utilizing reference detectors which can have different numbers of pixels. For experiments using chopping, the LO spectrum of the pumped shot can be reconstructed from the un-pumped shot as:

$$\hat{\boldsymbol{I}}_{\mathbf{LO}}^{*} \stackrel{\text{def}}{=} \boldsymbol{I}_{\mathbf{LO}}^{\prime} + \Delta\boldsymbol{I}_{\mathbf{Ref}}\,\boldsymbol{B} \tag{23}$$

Here the hat ^ symbol denotes the reconstructed intensity. From Eq. (16), the reconstruction error is $\boldsymbol{I}_{\mathbf{LO}}^{*} - \hat{\boldsymbol{I}}_{\mathbf{LO}}^{*} = \Delta\boldsymbol{K}$. For experiments using phase-cycling, $(\boldsymbol{I}_{\mathbf{LO}}^{*} + \boldsymbol{I}_{\mathbf{LO}}^{\prime})$ can often be approximated by $(\boldsymbol{I}_{\mathbf{tot}}^{*} + \boldsymbol{I}_{\mathbf{tot}}^{\prime})$ because the $E_{\mathrm{LO}}E_{\mathrm{Sig}}$ terms with opposite phase cancel each other, except for when strong background signals remain. With this approximation, the LO spectrum can be reconstructed as:

$$\hat{\boldsymbol{I}}_{\mathbf{LO}}^{*} \stackrel{\text{def}}{=} (\boldsymbol{I}_{\mathbf{tot}}^{*} + \boldsymbol{I}_{\mathbf{tot}}^{\prime} + \Delta\boldsymbol{I}_{\mathbf{Ref}}\,\boldsymbol{B})/2 \qquad \hat{\boldsymbol{I}}_{\mathbf{LO}}^{\prime} \stackrel{\text{def}}{=} (\boldsymbol{I}_{\mathbf{tot}}^{*} + \boldsymbol{I}_{\mathbf{tot}}^{\prime} - \Delta\boldsymbol{I}_{\mathbf{Ref}}\,\boldsymbol{B})/2 \tag{24}$$

with reconstruction errors being $\boldsymbol{I}_{\mathbf{LO}}^{*} - \hat{\boldsymbol{I}}_{\mathbf{LO}}^{*} = \Delta\boldsymbol{K}/2$ and $\boldsymbol{I}_{\mathbf{LO}}^{\prime} - \hat{\boldsymbol{I}}_{\mathbf{LO}}^{\prime} = -\Delta\boldsymbol{K}/2$. As already shown in Figure 8(c), $\Delta\boldsymbol{K}$ is very small, which means that Eq. (23) and (24) can reconstruct LO spectra with high accuracy.

When dividing Eq. (22) by the $[1 + (\delta I/\bar{I})]^{1/2}$ terms to suppress convolutional noise, the residual additive noise $\Delta\boldsymbol{K}$ is also divided by these factors. While $\Delta\boldsymbol{K}$ is zero-mean, the quotient is not necessarily zero-mean. In fact, the baseline of a pump-probe spectrum without referencing, $\langle \Delta I_{\mathrm{LO}}/I'_{\mathrm{LO}} \rangle$, is not zero[29] although $\langle \Delta I_{\mathrm{LO}} \rangle$ is zero, which is due to their nonzero $\mathrm{corr}(\Delta I, I') = -[(1-r)/2]^{1/2}$. Furthermore, this correlation can have wavelength-dependence as shown in Figure 10(b). This leads to a wavelength-dependent baseline shift, especially when a supercontinuum probe is used.[28] In comparison, $\mathrm{corr}\left(\Delta K, \hat{I}^{*}_{\mathrm{LO}}\right)$ with $\hat{I}^{*}_{\mathrm{LO}}$ reconstructed from Eq. (23), is basically zero as shown in Figure 10(b). This guarantees that the baseline of pump-probe spectra with our reference scheme, $\langle \Delta \boldsymbol{K}/\hat{\boldsymbol{I}}^{*}_{\mathbf{LO}} \rangle$, converges to zero. When the referencing performance described by Eq. (19) is very good, $\Delta \boldsymbol{K}$ is virtually uncorrelated with the intensity fluctuation of any beam because it mainly contains uncorrelated detector noise and photon shot noise. In summary, our reference scheme does not introduce baseline shift and signal distortion in the step of convolutional noise suppression.

2.5 Discussion

2.5.1 Referencing with a different number of pixels

With the concept of virtual reference pixels, the signal and reference detection no longer need to be matched because there is no requirement for pixel wavelength mapping. To test this, we used a 1×64 pixel MCT array as an additional reference detector. It has different pixel size, responsivity and electronics from those of the 2x32 array, and was placed behind a home-built spectrograph (see Figure 5). Figure 11(a) shows $\sigma(\Delta \boldsymbol{K})$ of the signal array after referencing with different arrays. While referencing with the 32 pixels on the bottom reference array is already effective, referencing with the 1×64 pixel array performs even better. This is clear evidence that matched detectors are not necessary in our scheme. Moreover, referencing with a combination of 96 pixels from both arrays further improves the performance compared to referencing with individual arrays. This is because the combination of multiple arrays increases the degrees of freedom and enables better minimization in Eq. (17). Therefore, a major advantage of our method over the conventional methods is that including more reference pixels helps to further reduce noise instead of introducing additional noise.

The residual noise after 96-pixel referencing is on the same level as the detector noise of the signal array. This shows that, with complete referencing, the lowest possible residual noise level is the noise floor of the signal array only, which has not been realized before (to the best of our knowledge). This theoretical limit is even lower than that of analog-balanced photodetectors, where the photon shot noise and dark noise of the reference photodiode will add to the total noise floor.

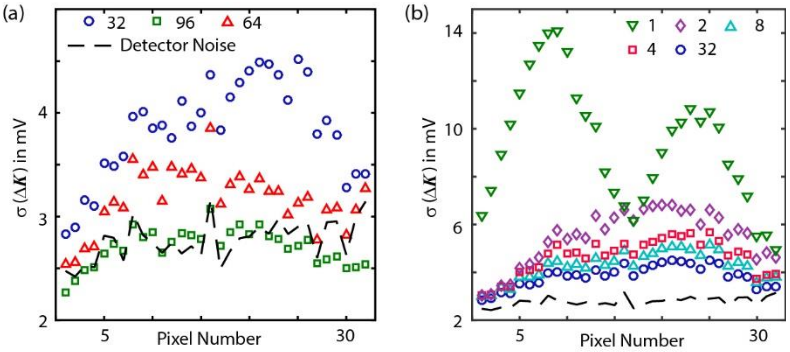

Figure 11. (a) Residual noise after referencing with a 32-pixel array (blue circles), an unmatched 64-pixel array (red triangles), and a combined 96-pixel array composed of the 32- and 64-pixel array (green squares). The detector noise of the signal array is shown as the dashed line in both panels. Because the detector noises of our signal and reference arrays were partially correlated, some pixels on the green-square curve show residual noise slightly below the detector noise. (b) Dependence of residual noise on the number of reference pixels (indicated in the legend). The number of reference pixels was reduced from 32 to 8, 4, 2, and 1 by digitally binning over 4, 8, 16, and 32 adjacent pixels, respectively, and re-calculating $\boldsymbol{B}$ for each case. The blue-circle curve in (a) and (b) are the same as the red-triangle curve in Figure 8(c).

To explore the effect of reducing the number of reference pixels, we digitally binned the data from adjacent reference pixels. The results are shown in Figure 11(b). As expected, full 32-pixel referencing gives the best noise suppression, yet the performance of 4-pixel referencing is already reasonably good. The small improvement over a large increase in the number of pixels suggests that most of the pixels in the reference array are providing largely redundant information. We believe that this redundancy is common in various detection systems, although the amount of redundancy depends on the total number of reference pixels and characteristics of light source. A reference array with less pixels is preferable when the per-pixel cost of the detector is high, especially in the near-IR and mid-IR range. Less reference pixels may also be preferable when the LO is not intense so that only a small portion of the energy can be used for reference detection without sacrificing the SNR on the signal detector.[43] For this case, one way to achieve good referencing is to use the same type of detectors for signal and reference detection, but to reduce the number of reference pixels by using a much less dispersive spectrograph to give a similar light intensity on the signal and reference pixels.

2.5.2 Effect of detector SNR on the noise floor

In this section we explore the effect of detector SNR on reference performance. Because our MCT arrays have relatively high SNRs, we can simulate detectors with lower SNRs by adding different amounts of noise to the raw data before referencing. This also provides a simulation for detectors in other spectral range, like CCD and CMOS arrays which typically have lower SNRs. Two different patterns of noises were added to simulate two types of detectors where either detector noise $(N_{\mathrm{r}}{}^{2} + D \cdot t)^{1/2}$ or photon shot noise $(N_{\mathrm{LO}})^{1/2}$ dominates the noise floor. Both noises are white Gaussian noises with zero means, but they have different pixel dependencies because photon shots noise depends on the intensity.

Figure 12(a) shows the residual noise after increasing the detector noise in the signal array to l multiples of the original level, and Figure 12(b) shows results for increasing the detector noise in the reference array. The statistics of the raw data measured with light off and on, respectively, are plotted in Figure 7(a) and Figure 7(b). When the original dataset was taken, the highest detector SNR was $\sim$2100 (1400) for the signal (reference) array. Increasing the detector noise level by 8 times reduces the highest SNR to $\sim$260 (170), which are typical values for many CCD and CMOS arrays. Figure 12(c) and Figure 12(d) show the residual noise after adding l multiples of photon shot noise to the signal and reference arrays, respectively. Because photon shot noise on our MCT detector is negligible (Section 2.2.3), we simulated its effect by generating uncorrelated white noise and scaling it proportionally to the square root of the mean intensity in Figure 7(c). To compare directly with Figure 12(a) and Figure 12(b), the amount of photon shot noise is defined as “8 multiples” when adding it reduces the highest SNR of the signal (reference) array to $\sim$260 (170). Other multiples are scaled accordingly.

When the noises are added to the signal array as shown in Figure 12(a) and Figure 12(c), the residual noise level increases almost linearly with the multiples. The pixel dependence of residual noises also reflects the type of noises added: almost flat for detector noise, and proportional to the square root of the mean intensity for photon shot noise. This means that the added noise directly enters into the residual noise, which is expected because referencing cannot remove the uncorrelated noises. On the contrary, the noise added to the reference array does not directly enter into the residual noise as shown in Figure 12(b) and Figure 12(d). The pixel dependence of $\sigma(\Delta\boldsymbol{K})$ is not flat when detector noise is added. Instead it loosely follows the pixel dependence of $\sigma(\Delta\boldsymbol{I})$ shown in Figure 7(b). This behavior can be understood from Eq. (15) and (19), where the effect of noise in the reference array is transmitted to $\Delta\boldsymbol{K}$ through R^2. Increasing the noise floor of the reference array reduces R^2, and hence degrades the referencing performance. The pixel dependence in Figure 12(b) and Figure 12(d) comes from the unsuppressed laser noise rather than the added white noise. $\sigma(\Delta\boldsymbol{K})$ in Figure 12(d) is lower than that in Figure 12(b) because the added photon shot noise is lower than the added detector noise (of the same multiples) outside the central pixels.

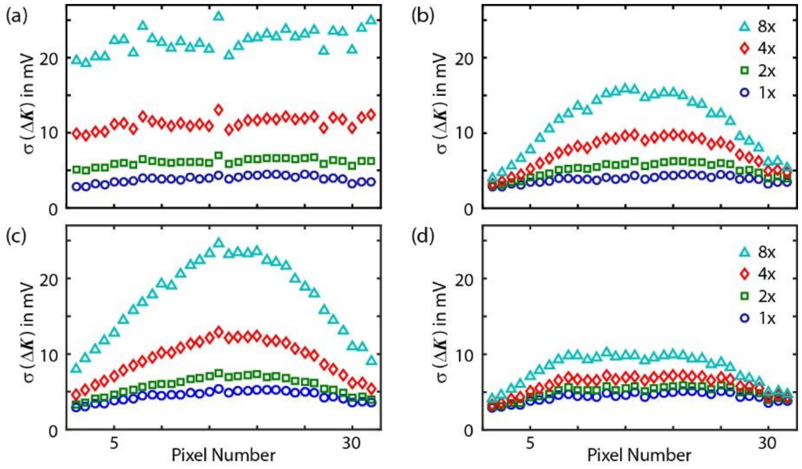

Figure 12. Effect of detector SNR on referencing performance. The legend indicates the multiples (l) of noise included. (a) Adding detector noise to the signal array; (b) adding detector noise to the reference array. Because the original data already contains one part of detector noise, the added detector noise is scaled by $(l^2 - 1)^{1/2}$. (c) Adding photon shot noise to the signal array; and (d) adding photon shot noise to the reference array.

In addition, $\sigma(\Delta\boldsymbol{K})$ in both Figure 12(b) and Figure 12(d) is much lower than its counterparts in Figure 12(a) and Figure 12(c), and the advantage is even larger when the multiples are higher. This means that reducing the SNR of the reference array does not deteriorate the referencing performance as severely as reducing the SNR of the signal array. This is because the performance of our reference scheme is related to the effective SNR of virtual reference pixels, which is higher than the SNR of physical reference pixels. The extent of gain in effective SNR from linear combination of multi-channels depends on factors like the reference pixel count and the spectral correlation pattern between different wavelengths. In terms of detector choices, this means that it is more important to use high SNR detectors for signal detection. For reference detection, good referencing can be achieved by using detectors with either high pixel SNR or large pixel number. In the example of 96-pixel referencing, it is realized by including more pixels. In the example of less-pixel referencing, binning over adjacent pixels increases the effective SNR of resulting pixels, which partially compensates for the effect of less pixels.

2.5.3 Non-linearity of detectors

The pixels in an array detector can have significant non-uniform responsivity. More generally, the detector response is not linear against light intensity, and the non-linearity also varies across pixels. Most applications utilize detectors only in the linear range for simplicity. However, sometimes it is preferable to exploit the nonlinear range for better SNR.[51] For example, our MCT array has about twice the maximum SNR in the nonlinear range compared with the linear range, as shown in Figure 13(b).

For our MCT array, the response is nonlinear when a low gain setting is used as shown in Figure 13(a). We usually fit the calibration curve with a rational function $I = f(x) = P(x)/Q(x)$ where x is the detector readout, $P(x)$ is a quadratic or cubic polynomial, and $Q(x)$ is a linear polynomial. $f(x)$ is different for every pixel in the array, and it also depends on the spectral range and on the position where the light is focused on the pixel.

This makes frequent re-calibration necessary, which is very time consuming. With conventional methods, $f(x)$ for both the signal and reference detectors must be accurately calibrated before the referencing step. With our referencing method, no $f(x)$ is needed for the additive noise suppression step. Equation (18) and Eq. (21) can be directly evaluated using the detector readout x, instead of the calibrated intensity I. The two equations can be applied to the nonlinear response because the calculation of $\boldsymbol{B}$ only involves terms representing small fluctuations around zero where the linear approximation is sufficient locally. We found that this method works well in the nonlinear response range with intensity fluctuation up to 10% (data not shown).

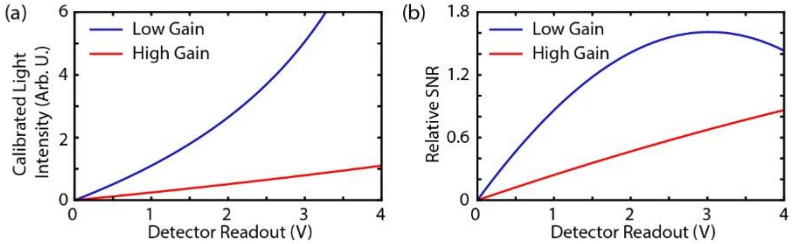

Figure 13. Characteristics of one pixel from our MCT arrays. The detector has adjustable gain settings corresponding to different full-well capacities. (a) Calibration curves for detector responsivity. (b) Relative SNR as a function of detector outputs. Red (blue) is for high (low) gain where the response is linear (nonlinear).

To further remove the convolutional noise from the LO fluctuation, only $f(x)$ for the signal array is needed. The resulting $\boldsymbol{S}$ from Eq. (21) is calibrated by multiplying with the derivative $f'(x)$ which can be evaluated either at x of the pumped shot, or at mean x (the difference is negligible). When $f(x)$ is a rational function, $f'(x)$ is also a rational function which can be calculated analytically. The convolutional noise is then factored out from the calibrated $\boldsymbol{S}$ as described in Section 2.4 using the calibrated LO intensity. If the signal array is used in the linear range and the reference array is used in the nonlinear range, no calibration curves are needed and the higher SNR in the reference array can be exploited to achieve better referencing.

2.5.4 Extension of the ΔI definition and $\boldsymbol{B}$ estimation

In earlier sections, ΔI is defined as the intensity difference between two consecutive shots. This convenient definition is based on the fact that most chopping and phase cycling patterns are simply cycled by two shots. However, there exist complex scenarios that involve more than two shots. For example, in some dual-color pump-probe experiments, the signal is proportional to the difference between the 1st and 3rd shots. In some phase-cycling patterns, the signal is extracted by taking the difference between the 1st shot and the mean of the 2nd and 3rd shots. Another scenario is when the detector pixel integrates several (n) light pulses before readout. This method is often used when the readout rate is slow compared to the laser repetition rate, or a single laser pulse is not intense enough to saturate the detector pixel. In this case, the signal is extracted by taking the difference in total energy between two consecutive groups of n laser pulses. In any of the above cases, the ΔI term should be defined according to the specific chopping, phase-cycling pattern, or detector readout mode.

For these complex scenarios, the corresponding $\boldsymbol{B}$ can be calculated from Eq. (18) by consistently defining ΔI for both the signal shots and the blank shots. We have validated this on our experimental setup and found it works well, although the residual noise marginally increased compared to the case of consecutive shots. However, such a consistent ΔI definition makes the implementation of blank shots more complex (especially for the fully-dispersed distribution) since it requires inserting different numbers of consecutive blank shots for different ΔI definitions. While this is not really an issue when a programmable optical modulator is available, it is almost impossible when a mechanical chopper is used.

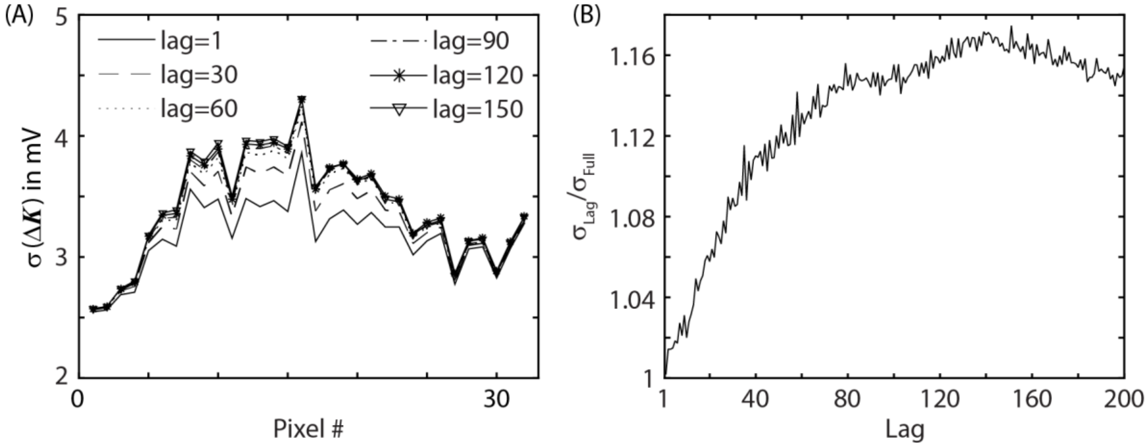

Figure 14. Effect on reference performance with different lag. Lag = n is defined for the shot pair difference, Δ, between the current and nth consecutive shot. First $\boldsymbol{B}$ is calculated from shot pair difference with a given lag. Then this $\boldsymbol{B}$ estimate is used to calculate $\sigma(\Delta\boldsymbol{K})$ for the normal consecutive shot difference. Note that lag = 1 corresponds to $\boldsymbol{B}$ calculation for the normal consecutive shot case (i.e. full referencing). In the chopping case, lag = 2 corresponds to referencing with the chopped shots only. (a) $\sigma(\Delta\boldsymbol{K})$ of the mid IR spectrum with $\boldsymbol{B}$ estimated with different lags. The 1x64 MCT array is used as the reference detector, and top array of the 2x32 MCT as the signal detector. (b) Reference performance for pixel 15 in (a) as a function of lag. σ_{Lag} is $\sigma(\Delta\boldsymbol{K})$ as defined in (a), and σ_{Full} is $\sigma(\Delta\boldsymbol{K})$ with lag = 1.

As a convenient alternative, we found that $\boldsymbol{B}$ can be estimated by inconsistently defining ΔI for the blank shots and the signal shots with a negligible loss of performance. Consider a situation where we still want to reduce the ΔI between consecutive shots but estimate $\boldsymbol{B}$ based on ΔI of two shots with a given lag (lag=1 means normal consecutive shots). Figure 14 demonstrates the loss of performance as the lag becomes large. Figure 14(a) shows there is a sudden increase of residual noises from lag=1 to lag=30, but then the residual noises increase mildly. This trend is even clearer in Figure 14(b). We used a similarly defined q as in Eq. (20) to quantify the performance loss. When lag=1, q is exactly

1. From lag=1 to lag=2, q jumps to 1.015. It then increases with steady slope until roughly lag=40 and tops off around lag=150. This loss of performance is expected since more low frequency fluctuations enter into $\boldsymbol{B}$ estimation with larger lag, while we are trying to suppress the ΔI noise between consecutive shots. However, q remains within 1.05 until around lag=20, which means that the referencing performance is reasonably good. Realistically lag=20 is very uncommon because most chopping or phase cycling patterns only involve smaller number of consecutive shots, like 2-8. The q is even closer to 1 with smaller lag, although the number will depend on the specific experimental conditions, especially laser repetition rate. For kilohertz laser systems, this kind of feature should be typical.

For pump-probe experiments utilizing normal chopping, every other shot is a blank shot. Now we can confidently use all the blanks shots to estimate $\boldsymbol{B}$ with lag=2 and apply $\boldsymbol{B}$ to signals shots with lag=1. This method is very robust and does not require the insertion of additional blank shots. For more complex chopping patterns, $\boldsymbol{B}$ can be similarly estimated without any modification to the data collection scheme. For phase cycling, a small percentage of additional blank shots are still necessary since there were no blank shots initially.

2.6 UV-Vis and near-IR wavelength with Silicon-based detectors

2.6.1 Reference performance of high-pixel count cameras

In this section we demonstrate our referencing method with Si-based CMOS array detectors for UV-Vis (white light continuum) and near-IR (femtosecond 800 nm, FWHM ~15 nm) wavelengths. These detectors and light sources have several key differences from the MCT detectors and mid-IR light source discussed in the previous section, even though the referencing method remains the same. First, Si-based detector arrays typically have many more pixels than MCT detectors, which allows us to demonstrate all the advantages discussed in section 2.5.1. Second, Si-based detectors have lower full-well capacity and dark noise than detectors, which gives a different noise floor (as discussed in section 2.5.2). Finally, we demonstrate reference detection with a visible light source with a complex spectral correlation.

A schematic of the setup used to collect the 800 nm and white light continuum data in this section is shown in Figure 15. To collect data, we use two unmatched home-built spectrographs with CMOS arrays: a high well-depth detector, the Hamamatsu S10453-1024, as a signal array with 1024 pixels and a low well-depth detector, the Hamamatsu S11639-01, as a reference array with 2048 pixels. The spectrographs are designed to provide a similar spectral range for both detectors. The probe (reference) spectrograph uses a f = 250 mm (300 mm) concave mirror. For both spectrographs, a pair of 1800 g/mm and 300 g/mm gratings were used for the 800 nm light and white light continuum, respectively. The ratio of total light intensity entering the signal/reference spectrographs is approximately 21:1 for the 800 nm light. The 800 nm light is used directly from a Ti:Sapphire regenerative amplifier, while the white light continuum is generated by focusing ~1 μJ of 800 nm onto a sapphire window and collimating the outgoing continuum.

The temporal statistics for both the 800 nm and white light continuum light source show features similar to the mid-IR statistics shown in Figure 6. Figure 16(a) and Figure 16(b) show the spectral correlation of $\Delta \boldsymbol{I}$ between pixels between the signal and reference arrays. The complex spectral correlation for the white light continuum in Figure 16(b) likely arises from interference patterns of multifilament generation. The corresponding spectra are shown in Figure 16(c) for 800 nm and Figure 16(d) for the white light continuum. The intensity of both light sources on both detectors was around 90% of saturation.

Figure 17 shows the reference performance for both light sources. All data sets used 60k shots from both detectors and 30k shot pairs to calculate $\boldsymbol{B}$. For the 800 nm case in Figure 17(a), the LO noise is reduced to the noise floor limit of the signal detector, which is dominated by photon shot noise. The SNR for the 800 nm data is approximately 850 for a shot pair. For the white light continuum, the reduced LO noise is close to the noise floor limit near the spectrum edge (where the intensity is highest) and corresponds to a maximum SNR of ~700. Figure 17 demonstrates that satisfactory noise suppression can be achieved by utilizing only 5% of the energy for reference detection.

Figure 18 shows the reference performance for the white light continuum when the low well-depth detector is used as the signal detector and the high well-depth detector is used as the reference detector. Although the LO noise is reduced to the noise floor limit, the maximum detector SNR is much lower at approximately 280. This clearly demonstrates the advantage of using a high well-depth detector as the signal detector, even when the LO noise is not fully suppressed to the noise floor limit.

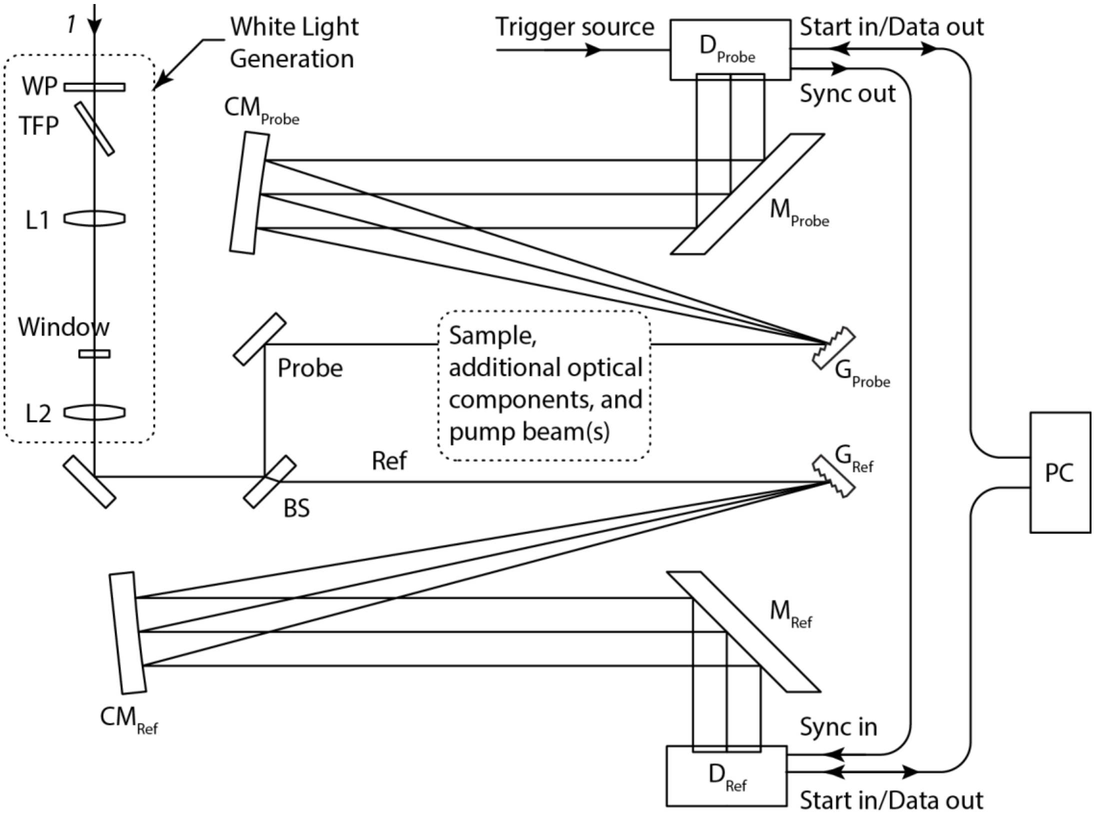

Figure 15. A schematic of the setup used to collect visible and near-IR reference data. The input beam 1 is derived from a femtosecond pulsed 1 kHz 800 nm light source. An optional white light generation stage is used to generate the white light continuum data set with a sapphire window, and is composed of a waveplate (WP), thin film polarizer (TFP), f=125 mm concave lens (L1), a 3 mm thick sapphire window (Window), and a f = 50 mm collimating lens (L2). The outgoing light is split by a 90% beam splitter, BS, into the probe (90%, also the LO) and reference beam (10%), which are then detected by the home-built spectrographs. The camera D_{Probe} is triggered by an external trigger source that is synchronized to beam 1. Upon a start command from the computer, PC, D_{Probe} generates a sync out trigger for every shot collected, which is used to trigger D_{Ref} (after D_{Ref} has received a start command from PC).

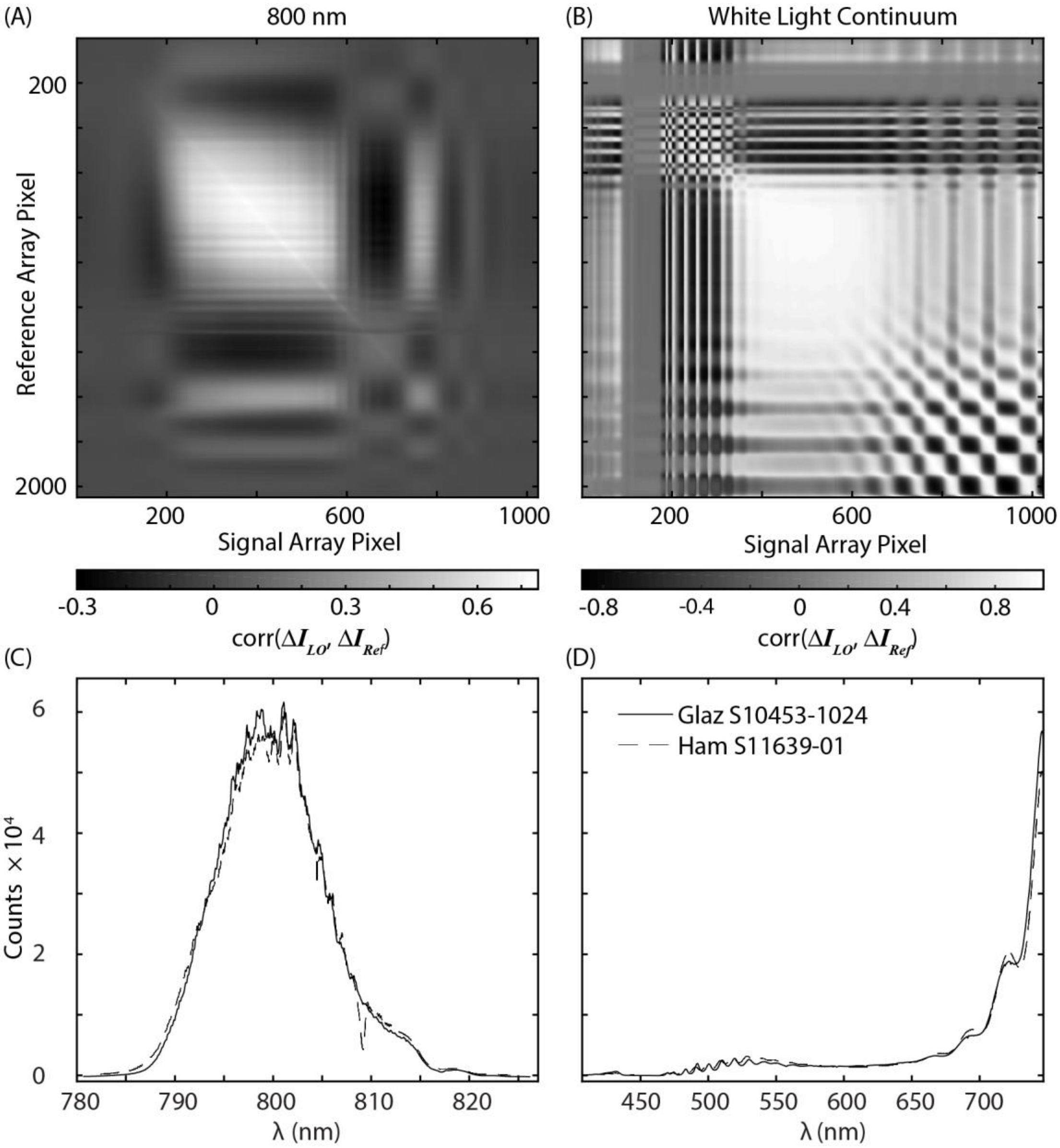

Figure 16. Spectral correlation of $\Delta \boldsymbol{I}$ between pixels within signal and reference arrays: 800 nm light in (a) and the white light continuum in (b) with corresponding spectra in (c) and (d). S11639-01 is used as the reference and has 2048 pixels. S10453-1024 is the signal detector with 1024 pixels. Both detectors are 16-bit with a maximum count of 65536. Note that the pixel numbering between the signal and reference detectors is flipped. Panel (c) and (d) share the same legend.

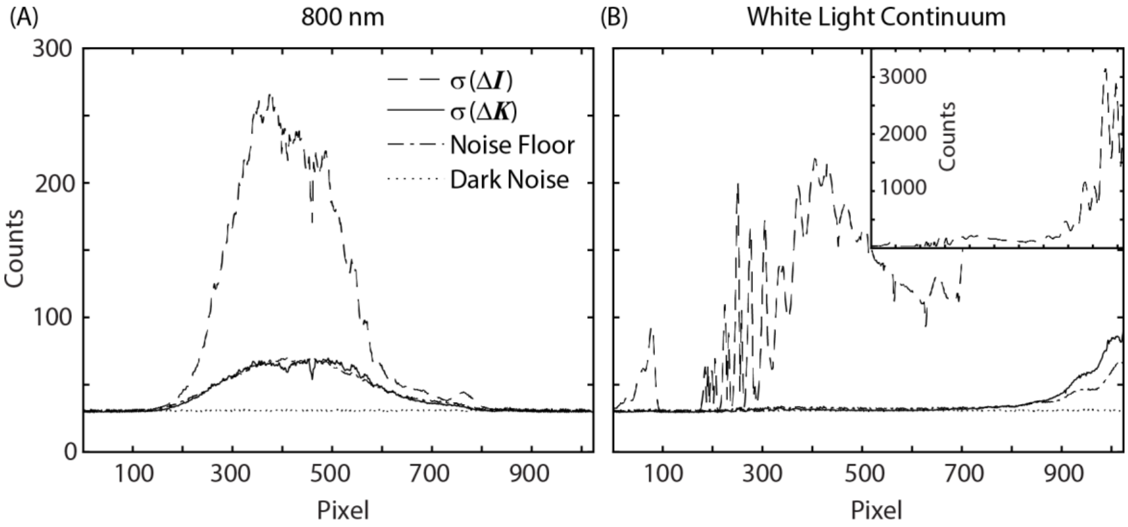

Figure 17. Reference performance for the 800 nm light data set in (a) and the white light continuum data set in (b). The inset in (b) shows $\sigma(\Delta \boldsymbol{I})$ with a scaled y-axis. The noise floor is calculated from the RMS sum (of a shot pair) of the dark noise and photon shot noise assuming a 2 Me$^-$ full-well capacity for the signal detector. Note that the noise floor largely overlaps with the $\Delta \boldsymbol{K}$ line, indicating that the reference performance is down to the noise floor limit. S10453-1024 is the signal detector and S11639-01 is the reference detector. Both panels share the same legend.

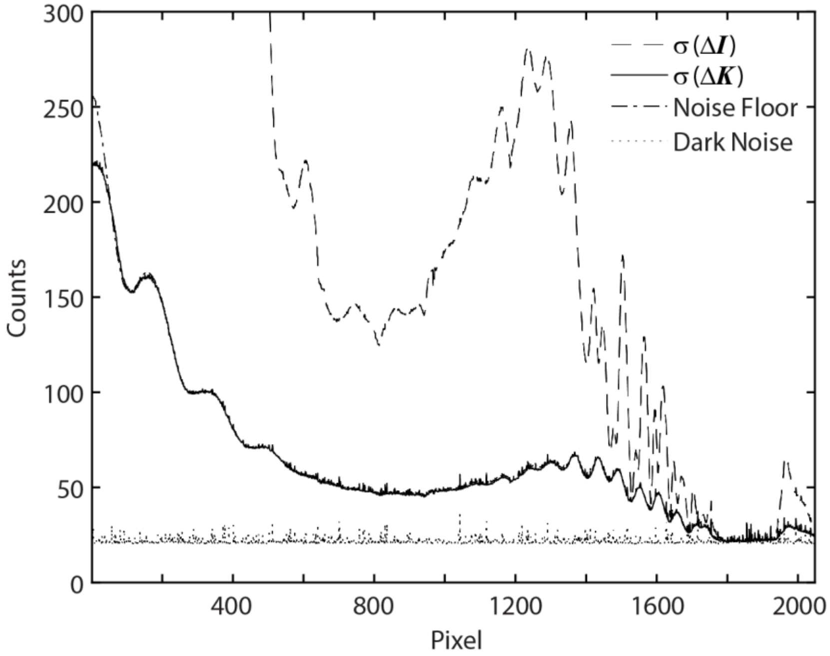

Figure 18. Reference performance of the white light continuum data, but with the S11639-01 as the signal detector and S10453-1024 as the reference detector. The noise floor is calculated the same way as in Figure 17, but with the an assumed full-well capacity of 100 ke$^-$. The noise floor largely overlaps with the $\Delta\boldsymbol{K}$ line, indicating that the reference performance is down to the noise floor limit. Note that the noise floor limit is higher for S11639-01 (lower SNR), as compared to S10453-1024 in Figure 17 (higher SNR).

2.6.2 Reference pixel data compression

The introduction of high-pixel count reference detectors comes with the following costs: first, $\boldsymbol{B}$ calculation becomes computationally expensive and second, not enough blank shots can be collected for a robust $\boldsymbol{B}$ estimation with small percentage of blank shots and within reasonable time. These problems are easily mitigated because the different reference channels contain largely redundant information and may therefore be compressed into less reference channels. This is done through an extended definition of the reference channels:

$$\Delta \boldsymbol{I}_{\mathbf{Ref}}^{\boldsymbol{ext}} \stackrel{\text{def}}{=} \Delta \boldsymbol{I}_{\mathbf{Ref}} \, \boldsymbol{C} \tag{25}$$

where $\boldsymbol{C}$ is a $n \times p$ matrix ($p < n$) that takes a linear combination of the original n reference channels of $\Delta \boldsymbol{I}_{\boldsymbol{Ref}}$ and maps them into p compressed reference channels, $\Delta \boldsymbol{I}_{\boldsymbol{Ref}}^{\boldsymbol{ext}}$, of reduced dimensionality. $\Delta \boldsymbol{I}_{\boldsymbol{Ref}}^{\boldsymbol{ext}}$ is then used in eq. (18) and (21).

Examples of reference pixel data compression include, but are not limited to, binning and principal component analysis (PCA). These two methods demonstrate two different cases of data compression: the pixel binning case is computationally simple (and may be implemented in hardware), while the PCA case provides data compression that is more representative of the uncompressed data. In the case of pixel binning, $\boldsymbol{C}$ corresponds to a matrix that averages neighboring pixels. The number of neighboring pixels binned does not necessarily have to be uniform across the detector array. For the PCA case, $\boldsymbol{C}$ corresponds to a matrix that is composed of the first p loadings for the original reference data set ($\Delta \boldsymbol{I}_{\boldsymbol{Ref}}$). The number of effective pixels is therefore the number of principal components used.

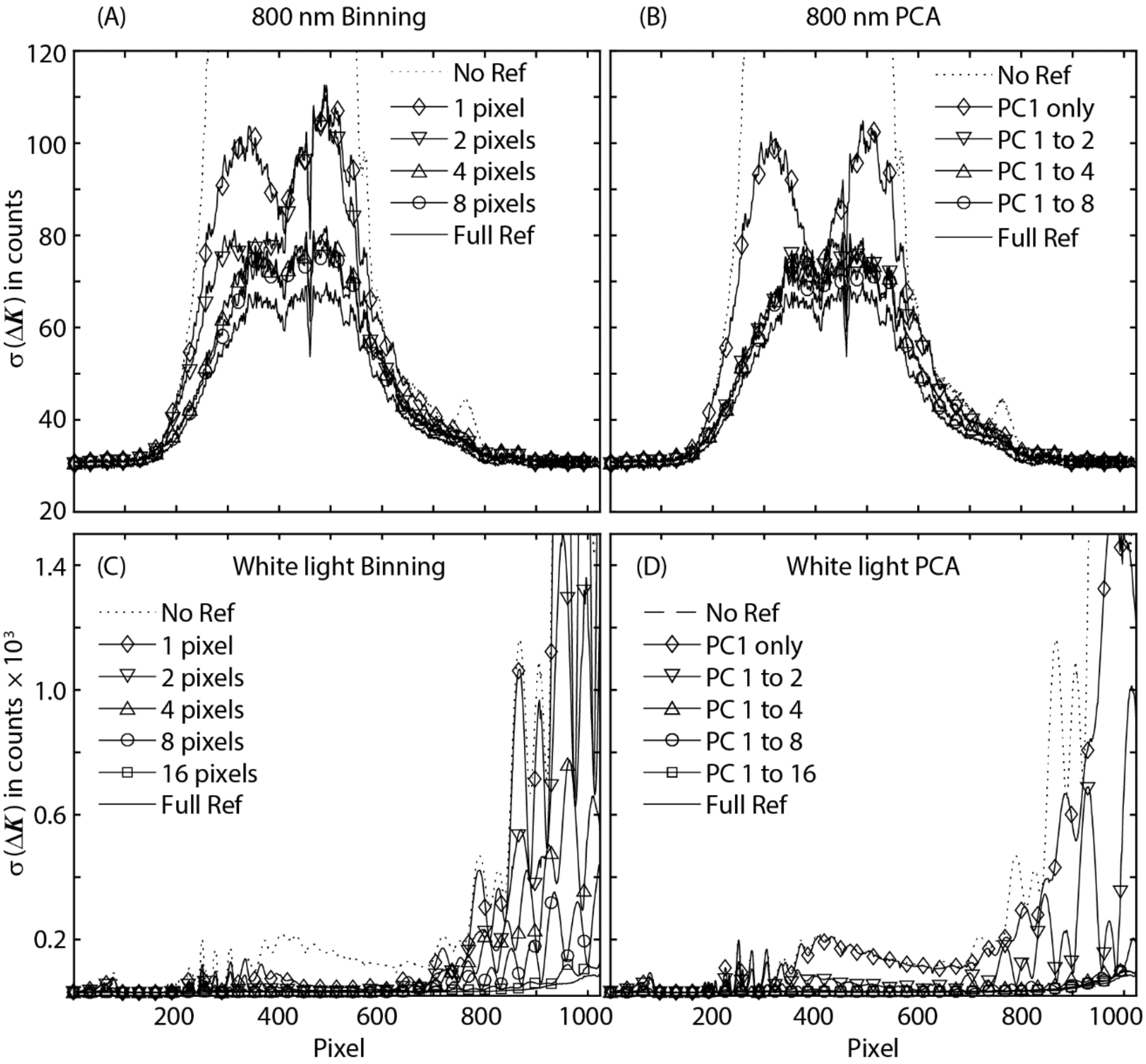

Figure 19. The effect of reference data compression on reference performance, $\sigma(\Delta \boldsymbol{K})$, measured in counts. In the left column, (a) and (c), the data compression corresponds to binning neighboring pixels. The data corresponds to the number of combined pixels left after binning. In the right column, (b) and (d), data compression corresponds to a linear combination of pixels as found by PCA. The number, n, of compressed pixels corresponds to the first n principal components.

We demonstrate the results of the two cases in Figure 19 for the 800 nm light and white light continuum, which have very different reference channel correlation statistics. In Figure 19(a) and Figure 19(b) we show the effects of binning and PCA for the 800 nm data set. Similar to the mid-IR case shown in Figure 11(b), compressing reference data down to one pixel (diamond) shows some improvement, but the $\Delta\boldsymbol{K}$ noise is still far above the noise floor. Note that the solid lines show the performance of full referencing, or referencing without data compression, which is close to the noise floor. In the two-pixel case (upside-down triangle), PCA shows some improvement over binning. With more pixels, both methods quickly converge, with PCA always slightly outperforming binning. In general, the use of PCA is not warranted when the reference channel correlation (not shown but is similar to Figure 16(a)) is relatively simple.

The case is quite different for the white light continuum, Figure 19(c) and Figure 19(d), which contains interference from multiple filaments and has a very complex reference channel correlation (not shown, but is similar to Figure 16(b))). With one compressed pixel (diamonds), the two methods perform relatively poorly. The binning case can effectively reduce $\Delta\boldsymbol{K}$ noise where the reference channel correlation remains simple (in the middle of the spectrum) but fails completely at the edges of the spectrum. PCA reduces $\Delta\boldsymbol{K}$ noise at the edges even for one pixel but fails in the middle of the spectrum. With two compressed pixels (upside down triangle), PCA shows a significant improvement, while binning shows a small improvement at the spectrum edge. With four compressed pixels (right-side up triangle), the PCA performance converges to the performance seen with full referencing (solid line). Meanwhile binning shows some additional improvement near the spectrum edge but is still far from converged. This shows that, even with the complex spectral correlation, the noise information in the reference channels can be effectively compressed down to four pixels via PCA. The small number of effective pixels makes it possible to refresh $\boldsymbol{B}$ frequently, which is important in applications like pump-probe and 2D-IR microscopy.

We conclude this section by noting that the exact method used for calculating $\boldsymbol{C}$ depends on the properties of the light source. Like $\boldsymbol{B}$ estimation in section 2.3.2, $\boldsymbol{C}$ can also be periodically refreshed (e.g. in the case of PCA), although it does not have to be refreshed as often as $\boldsymbol{B}$. Unlike with $\boldsymbol{B}$ estimation, $\boldsymbol{C}$ is usually calculated from only the reference channel data. This means that all shots in $\Delta\boldsymbol{I}_{\mathbf{Ref}}$ can be used to calculate $\boldsymbol{C}$, not just the blank shots, even when $\boldsymbol{C}$ is refreshed on-the-fly.

2.6.3 Reference pixel data expansion

In some cases (discussed below) it is also preferable to expand the effective number of reference pixels by reference pixel data expansion. This method extends the $\Delta\boldsymbol{I}_{\mathbf{Ref}}$ definition as a concatenated row vector composed of $\Delta\boldsymbol{I}_{\mathbf{Ref}}$ and any higher order polynomial cross terms:

$$\Delta\boldsymbol{I}_{\mathbf{Ref}}^{\boldsymbol{exp}} \stackrel{\text{def}}{=} \left(\Delta\boldsymbol{I}_{\mathbf{Ref}}, \Delta\boldsymbol{I}_{\mathbf{Ref}}^{(2)}, \Delta\boldsymbol{I}_{\mathbf{Ref}}^{(3)}, \dots\right) \tag{26}$$

Here, $\Delta\boldsymbol{I}_{\mathbf{Ref}}^{(2)}$ is any row vector composed of quadratic polynomial cross terms, explicitly written as $\Delta\boldsymbol{I}_{\mathbf{Ref}}^{(2)} = \Delta\{\boldsymbol{I}_{\mathbf{Ref}}(i) \cdot \boldsymbol{I}_{\mathbf{Ref}}(j)\}$. Similarly, $\Delta\boldsymbol{I}_{\mathbf{Ref}}^{(3)}$ is any row vector composed of cubic polynomial cross terms, explicitly written as $\Delta\boldsymbol{I}_{\mathbf{Ref}}^{(3)} = \Delta\{\boldsymbol{I}_{\mathbf{Ref}}(i) \cdot \boldsymbol{I}_{\mathbf{Ref}}(j) \cdot \boldsymbol{I}_{\mathbf{Ref}}(k)\}$ for $k \geq j \geq i$ up to the n^{th} reference pixel. Any such higher order polynomial cross term can be included. It should be noted that all these terms are still zero-mean, so no background distortion is introduced when including them. Because $\Delta\boldsymbol{I}_{\mathbf{Ref}}^{\boldsymbol{exp}}$ is composed of many more additional terms, it may be necessary to reduce its dimensionality before $\boldsymbol{B}$ calculation. This reduction can be achieved by compressing Eq. (26) via Eq. (25).

This method is useful in cases where the normal $\Delta\boldsymbol{I}_{\mathbf{Ref}}$ do not achieve satisfactory performance. These cases include, but are not limited to, when the reference detector has high level of nonlinearity, the signal is detected after a frequency conversion stage, or the reference channel count is too small. In **Figure 20**, we show that reference pixel data expansion can provide approximately two times increase in SNR for a data set that is unusually noisy and is referenced with too few pixels.

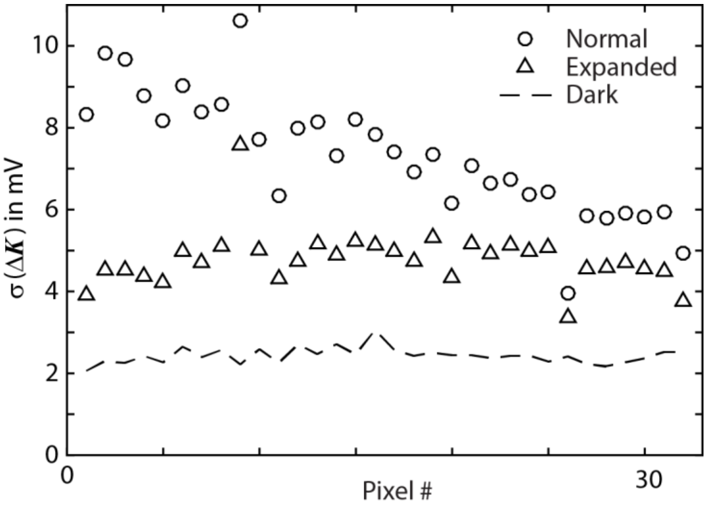

Figure 20. Refence performance improvement with pixel data expansion over normal multi-channel referencing. The expanded reference data set contains all 32 first order pixels that the normal reference data set has as well as the full set of 528 2nd order polynomial combinations. In this data set, the signal array is the top array of a 2x32 MCT detector, and the reference is the bottom array. This data set has an average (over all signal pixels) $\sigma(\Delta \boldsymbol{I})$ of 217 mV for 10k data points.

2.7 Summary and conclusions

We have devised a general reference scheme for noise suppression in heterodyne nonlinear spectroscopy. Upon recognizing that there are both additive and convolutional noises, we formulated a two-step process to remove them sequentially. To remove the dominant additive noise, we begin with an arbitrary single-reference-channel method that encompasses the conventional methods as special cases. The idea is generalized in the multi-reference-channel method to linearly combine all physical reference pixels into virtual pixels to utilize the correlation between different spectral components. Because a minimization routine is used to predict $\Delta \boldsymbol{I}$ on the signal detector using the reference detector, the additive noise is optimally suppressed with theoretically guaranteed better performance over the conventional methods. Practical implementation of this method only requires adding a small fraction of extra blank shots. The convolutional noise is then removed straightforwardly in the second step by factoring out the intensity fluctuations of all involved beams. The two-step referencing does not introduce any baseline shift and signal distortion. It provides a unified treatment for nonlinear spectroscopic techniques of different orders under different configurations, no matter whether they are self-heterodyne or have an external LO or use chopping or phase cycling.

Applying our reference scheme to existing experimental systems can greatly enhance their performance. We achieved 10-30 times noise reduction and a 10 μOD RMS noise level with 1-second averaging for MCT arrays and 20 μOD RMS noise level with 1 second averaging for the CMOS array with 800 nm light. While the numbers depend on the specific detection system, in general the residual noise level is not sensitive to the original noise level because the measurement sensitivity is pushed toward the detection limit. Our method is especially advantageous when a detector array is used for reference, which is validated with, but not limited to, MCT arrays and Si-based CMOS arrays. Because there is no requirement for wavelength mapping and spectral resolution, the reference array can be easily aligned, similar to aligning a photodiode, without sacrificing the ability to track wavelength-dependent fluctuations. The new algorithm enables the use of unmatched reference detection systems, which could significantly reduce the experimental cost if detectors with less pixels or home-built compact spectrographs are employed.

Because our reference scheme effectively decouples the final SNR from the stability of light sources, one can afford greater flexibility in experimental designs than previously possible. Light sources that exhibit higher fluctuations but may have broader spectra or stronger intensities can be used, such as a multi-filament supercontinuum probe. Depending on how much LO power is available, the well depths and pixel numbers of both signal and reference detectors can be scaled to fulfill the objective SNR. We hope that this work will further advance the applications of heterodyne nonlinear spectroscopy to systems with weak signals, such as measuring higher order responses from very dilute samples.

3. Mid IR Pulse Shaping

Pulse shaping is a very mature field that has been developing for the past 40+ years. Several thorough reviews are available on the subject.[52-54] The goal in pulse shaping is to be able to controllably generate any arbitrary pulse shape, with programmable control over special profile, polarization,[55,56] amplitude, and phase.[49] For our purposes, we use an acousto-optic modulator (AOM)-based pulse shaper in a 4f zero-dispersion geometry[57,58] to generate a double pulse with controllable phase and delay for the pump in 2D IR spectroscopy. Several good reviews also exist on mid IR pulse shaping.[7,14,15] In this chapter, I will summarize my experience and new insights gained into the mid IR AOM-based pulse shaper. This chapter is largely meant to introduce the reader to key pulse shaping concepts and describe the optical behavior of each shaper component and how it affects the output.

3.1 Basic operating principles

The 4f zero-dispersion line is composed of a pair of gratings and concave mirrors separated by the focal length of the concave mirror, f (Figure 21). The separation between the two concave mirrors is $2f$. The grating/concaves mirror acts to Fourier-transform the pulse's field, so that a mask placed at the Fourier plane can modulate the pulse directly in the frequency domain. This is done by first dispersing the beam via a grating and focusing the individual frequency components by the concave mirror. The concave mirror also makes individual frequency components parallel.

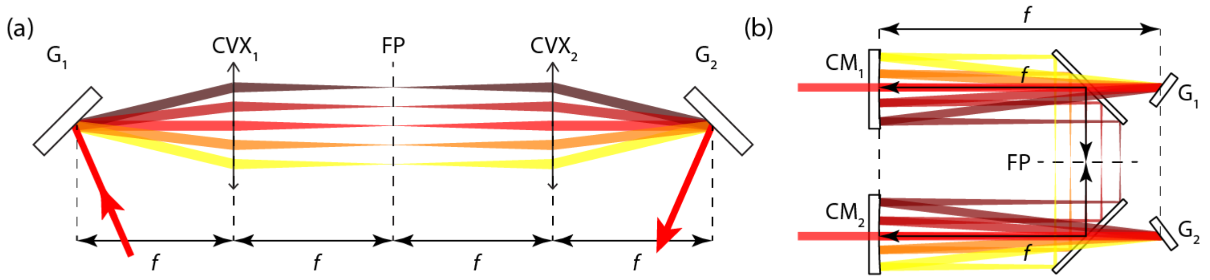

Figure 21. (a) A generic 4f zero-dispersion line. (b) The 4f zero-dispersion line in the folded Littrow configuration with reflective optics. G_1 and G_2 are gratings that disperse and compress a broadband pulse. CVX_1 and CVX_2 are convex lenses and CM_1 and CM_2 are concave mirrors. The focusing optic maps and focuses the angularly dispersed beam onto and the Fourier plane (FP), while the second focusing optic maps the FP back to an angle into G_2.

For an AOM-based pulse shaper, an AOM is inserted at the Fourier plane. The AOM is controlled by an arbitrary waveform generator (AWG) which is synchronized and clocked to the laser for phase stability. The AWG generates a waveform which is converted into an acoustic wave. This acoustic wave generates a periodic modulation of the acoustic medium's index of refraction, which acts as a phase grating for the incoming light.[59] For pulsed light, this phase grating appears stationary because of the orders-of-magnitude difference between the optical and acoustic velocities inside acoustic medium. The interaction of the incoming light field and acoustic field can be thought of as a parametric interaction. [59] In the Bragg's regime, where the interaction length between the light and acoustic fields is long, only the first order diffracted field is significant. Therefore, the in the acoustic medium the output field has wavevector $\boldsymbol{k}_{out} = \boldsymbol{k}_{in} + \boldsymbol{k}_a$, where $\boldsymbol{k}_a$ is the wavevector for the acoustic wave and $\boldsymbol{k}_{in}$ is the wavevector of the input light field.

Assuming that $\boldsymbol{k}_a$ is parallel to the AOM surface, the phase matching condition is satisfied when $\boldsymbol{k}_{in}$ is at the Bragg's angle with respect to the surface normal:

$$\sin\theta_{\mathrm{Bragg}} = \frac{\lambda_0 f_{\mathrm{CW}}}{2v_{\mathrm{Ge}}} \approx \theta_{\mathrm{Bragg}} \tag{27}$$

where λ_0 is input field's vacuum wavelength, f_{CW} is the frequency of the acoustic waveform, and v_{Ge} is the acoustic velocity in the acoustic medium, in our case germanium. The approximation shown is made because this angle is usually on the order of a few degrees. The outgoing field is deflected by an angle of $2\theta_{Bragg}$ compared to the input field direction. Mismatch from this angle comes at a diffraction efficiency cost (see section 3.1.3), although the AOM we use is relatively tolerant to Bragg's angle mismatch.

As will be shown in the later sections, the physical mode of operation of the AOM-based 4f pulse shaper depends on the AOM's ability to amplitude and phase modulate the input field at the Fourier plane. Amplitude shaping is done by changing the amplitude of the acoustic wave, which in turn affects the diffraction efficiency of any given optical frequency component. Phase modulation is done by changing the instantaneous frequency of the acoustic waveform for any given frequency of light. This corresponds to a change in the phase matching condition (i.e. Bragg's angle), which deflects the output field at a different angle. The second concave mirror maps this angle to a horizontal position on the second grating. Because the grating is tilted, a path length difference is introduced, which corresponds to a delay, or phase buildup, of the individual frequency component.

3.1.1 Acoustic Waveform Mask for the Double Pulse

Given the description of a 4f AOM-based pulse shaper, what should the waveform mask look like to be able to generate a double pulse? The waveform mask can be derived phenomenologically. First, assume that there exists a linear transfer function, $H(\omega)$, that represents the pulse shaper. This function will map an input field (in the frequency domain) to an output field, and can be written as:

$$\tilde{E}_{out}(\omega) = \widetilde{H}(\omega) \times \tilde{E}_{\mathrm{in}}(\omega) \tag{28}$$

Because this function is linear, the pulse shaper can only introduce linear amplitude or a phase modulation. For ideal double pulse generation with delay τ (e.g. in a Michaelson interferometer), the transfer function will take the form of:[53]

$$\widetilde{H}(\omega) = \frac{1}{2}\left(1 + e^{i\omega\tau}\right) \tag{29}$$

This can be verified by defining a Gaussian input field envelope in both the time and frequency domain, which are related by a Fourier transform:

$$E_{\mathrm{in}}(t) = A_t \exp\left(-\frac{t^2}{2\Delta t^2}\right) \tag{30}$$

$$\tilde{E}_{\mathrm{in}}(\omega) = A_\omega \exp\left(-\frac{\omega^2}{2\Delta\omega^2}\right) \tag{31}$$

$$\tilde{E}_{\mathrm{in}}(\omega) = F.T.\{E_{\mathrm{in}}(t)\} = \frac{1}{2\pi} \int_{-\infty}^{\infty} e^{i\omega t} E_{\mathrm{in}}(t) dt \tag{32}$$

Solving for $\tilde{E}_{out}(\omega)$ using the double-pulse $\widetilde{H}(\omega)$ defined in Eq. 29 and Fourier transforming back gives:

$$E_{\mathrm{out}}(t) = \frac{1}{2}\left(E_{\mathrm{in}}(t) + E_{\mathrm{in}}(t-\tau)\right) \tag{33}$$

This confirms that the transfer function does in fact give a double pulse. The transfer function can also be formulated in the time domain, where the output field is found by convoluting the transfer function with the input field. For double pulse generation, the time-domain transfer function is a pair of delta functions, with one delayed by τ (note that we drop the normalization factor):

$$H(t) = \frac{1}{2}\big(\delta(t) + \delta(t-\tau)\big) \tag{34}$$

It is also convenient to have control over the phase of each pulse for phase cycling. This is usually done in terms of a constant relative phase ϕ_{rel}, which defines the phase between the two pulses in the double pulse, and a constant absolute phase ϕ_{abs}, which defines the phase between the pump and probe pulse:

$$\widetilde{H}(\omega) = \frac{1}{2}\big(1 + e^{i(\omega\tau + \phi_{\mathrm{rel}})}\big) \cdot e^{i\phi_{\mathrm{abs}}} \tag{35}$$

Phase cycling is useful because it can be used to help remove pump-probe scatter (via ϕ_{abs}) and it can be used to differentiate between signal and artifacts, such as the 2DIR signal (signal of interest) and transient absorption signal induced by each pump pulse (artifact), as well as some higher order signal harmonics caused by nonlinearity of the AOM acoustic mask (via ϕ_{rel}).[14]

In addition, we can correct for phase errors caused by chirp. Chirp is defined by expanding the phase about a central frequency ω_0. The 2nd order term, group delay dispersion (GDD), and third order term, third order dispersion (TOD), are typically included as:[7]

$$\phi_{\mathrm{chirp}}(\omega) = \frac{1}{2}GDD \cdot (\omega - \omega_0)^2 + \frac{1}{6}TOD \cdot (\omega - \omega_0)^3 \tag{36}$$

This is added to the transfer function as an additional phase term:

$$\widetilde{H}(\omega) = \frac{1}{2}\left(1 + e^{i(\omega\tau + \phi_{\mathrm{rel}})}\right) \cdot e^{i\left(\phi_{\mathrm{abs}} + \phi_{\mathrm{chirp}}(\omega)\right)} \tag{37}$$

The chirp parameters are typically found by first focusing the pulse shaper output into a frequency-doubling crystal or window such as $AgGaS_2$ or ZnSe. The chirp parameters are then scanned to maximize the frequency-doubled output. As an example, the pulse shaper can be used to compensate for chirp introduced by propagating through a thick slab of material. To verify the chirp compensation, we measured the GDD chirp compensation parameter with and without the pulse propagating through 8 mm of CaF_2. CaF_2 at 6 μm has a group velocity dispersion (GVD) of -1113 fs^2/mm, which gives a total GDD of -8904 fs^2.[60,61] The pulse shaper had a GDD compensation parameter of 1.268×10^5 fs^2 before addition of the CaF_2 and 1.118×10^5 fs^2 after addition of CaF_2. This gives a difference of -8260 fs^2, which is in good agreement with the first value.

The acoustic mask, $M(t_{\mathrm{RF}})$, can be directly related to the transfer function $\widetilde{H}(\omega)$ because the first grating and concave mirror act to Fourier-transform the input time-domain field $E_{\mathrm{in}}(t)$ to $\tilde{E}_{\mathrm{in}}(\omega)$ at the Fourier plane. At the Fourier plane, the mask acts as $\widetilde{H}(\omega)$ and linearly operates on $\tilde{E}_{\mathrm{in}}(\omega)$ to generate $\tilde{E}_{out}(\omega)$, which is Fourier transformed back into $E_{\mathrm{out}}(t)$ in the time-domain by the second grating and concave mirror. Therefore, one only needs to be able to find the relationship, $\omega(t_{\mathrm{RF}})$, between the optical frequency and acoustic waveform delay. In addition, the AOM requires a carrier frequency, $\omega_{\mathrm{CW}} = 2\pi f_{\mathrm{CW}}$, so that it can diffract the input beam. Finally, the acoustic mask is real-valued and has a value between zero and one. The acoustic mask can then be written as:

$$M(t_{\mathrm{RF}}) = \frac{1}{2}\left(1 + Re\left\{\widetilde{H}\left(\omega(t_{\mathrm{RF}})\right) \cdot e^{i\omega_{\mathrm{CW}} \cdot t_{\mathrm{RF}}}\right\}\right) \tag{38}$$

Finding the function $\omega(t_{\mathrm{RF}})$ is known as AOM calibration.[58] The calibration procedure is done by generating an acoustic mask that generates a time-domain comb. The comb spacing is chosen so that comb maxima coincide with the maxima of the carrier wave. This is necessary because the comb needs to have a frequency-domain component that coincides with f_{CW}. For f_{CW} = 75 MHz, the comb spacing needs to be an integer multiple of the carrier wave period of 13.3 ns. In addition, arbitrary waveform generators (AWGs) can only generate masks at discrete time points at a fixed interval, whose spacing is determined by the clock frequency of the AWG. For our system, the clock frequency is 1 GHz, which corresponds to a minimum time spacing of 1 ns. Therefore, the minimum allowable comb spacing is 3 periods, or 40 ns. The comb mask is then defined as:

$$M_{\mathrm{Comb}}(t_{\mathrm{RF}}) = \begin{cases} 1 & t_{\mathrm{RF}} = n \cdot m \cdot 40 \text{ ns} \\ 0 & t_{\mathrm{RF}} \neq n \cdot m \cdot 40 \text{ ns} \end{cases} \tag{39}$$

where n is any positive integer and m is a positive integer comb spacing multiplier so that the comb is not too dense. The output from the shaper is a frequency comb that has a frequency spacing which is determined by $\omega(n \cdot m \cdot 40 \text{ ns})$. This frequency comb is then sent into a spectrometer and the wavelengths of each comb maxima are recorded as a function of t_{RF}. The data is typically fit to a second order polynomial, $\lambda(t_{\mathrm{RF}})$, which is used to find $\omega(t_{\mathrm{RF}}) = 2\pi c/\lambda(t_{\mathrm{RF}})$. The reason the data is fit to a second order polynomial is because the dispersion generated by the grating is not perfectly linear.

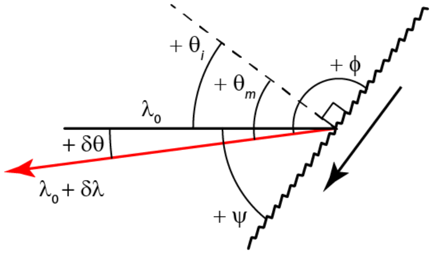

Figure 22. Definitions for grating angles used throughout this chapter. The grating is drawn in the Littrow configuration. The solid black line is the undispersed input beam. The black arrow represents the grating blaze direction.

For the purpose of providing definitions for later sections, we will finish this section by deriving the dispersion at the AOM surface in some detail. In the Littrow configuration, the dispersion can be found using the grating equation:

$$d(\sin\theta_i + \sin\theta_m) = m\lambda \tag{40}$$

where d is the grating groove period, θ_i is input beam angle with respect to the grating normal and θ_m is the m^{th} diffraction order's angle with respect to the grating normal, defined in the same direction as θ_i. Figure 22 defines all the grating angles for the Littrow configuration. In the Littrow configuration, $\theta_i = \theta_m$ for a center wavelength λ_0, which gives for the 1st diffraction order:

$$\theta_i = \sin^{-1}\left(\frac{\lambda_0}{2d}\right) \tag{41}$$

$$\theta_m = \sin^{-1}\left(\frac{2\lambda - \lambda_0}{2d}\right) \tag{42}$$

The dispersion introduced by the grating and concave mirror of focal length f can be defined in terms of the angle difference, which is introduced by a corresponding wavelength difference $\delta\lambda = \lambda - \lambda_0$:

$$D_l(\delta\lambda) = f \cdot D_a(\delta\lambda) = f \cdot \tan(\theta_m - \theta_i) \tag{43}$$

where $D_l(\delta\lambda)$ is the linear dispersion and $D_a(\delta\lambda)$ is the angular dispersion. Expanding up to the second order in terms of $\delta\lambda$ yields the series:

$$D_l(\delta\lambda) = f \cdot D_a^{(1)}\delta\lambda + f \cdot D_a^{(2)}\delta\lambda^2 + \mathcal{O}(\delta\lambda^3) \tag{44}$$

The first order linear dispersion term is given by:

$$D_l^{(1)} = f \cdot D_a^{(1)} = \frac{2f}{d}\left(4 - \frac{{\lambda_0}^2}{d^2}\right)^{-\frac{1}{2}} = \frac{2f}{\lambda_0}\tan(\theta_i) \tag{45}$$

The second order correction is small, but not negligible if the pulse is very broadband:

$$D_l^{(2)} = -\frac{2f \cdot \lambda_0}{d^3}\left(4 - \frac{{\lambda_0}^2}{d^2}\right)^{-\frac{3}{2}} = -\frac{2f}{{\lambda_0}^2}\tan^3(\theta_i) \tag{46}$$

As an example, the typical mid IR configuration of a 200 grooves/mm grating, f = 200 mm, and λ_0 = 6 μm gives $D^{(1)}$ = 50 mm/μm and $D^{(2)}$ = 4.7 mm/μm^2.

3.1.2 Pulse Shaper Instrument Response Function

One of the limits of the pulse-shaper is the maximum double pulse delay that can be generated. This limit, in turn, determines the pump frequency resolution in the 2D IR measurement. In reality, the delayed pulse falls off smoothly (known as double pulse falloff, the origins of which will be discussed in the next section) and can be thought of as a window function that is applied to a sample's response. In the frequency domain, this window function corresponds to convolution of ω_τ with the pump's instrument response function. This is important because, in the next chapter, we will discuss 2D IR spectra of a relatively narrow oscillator. Therefore, we attempt to measure this response function and use it to deconvolute the 2D data to help improve our pump-axis resolution.

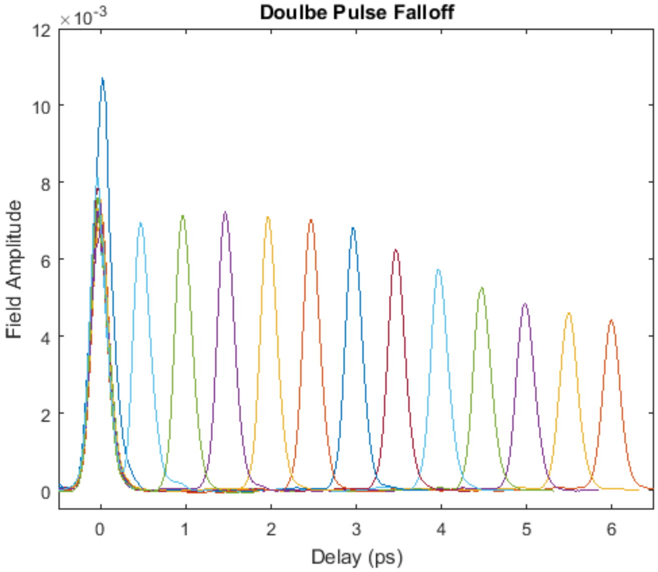

Figure 23. The cross-correlation of pump double pulse with delay tau and a probe beam in a ZnSe window. The data was collected for a chirp-corrected 6 um pump with the f_{CW} = 73 MHz and a 200 g/mm grating. The x-axis delay is the cross-correlation delay and was generated with a delay stage. Note the initial rise in the delayed pulse field amplitude and subsequent falloff.

We have devised several methods to measure this response function. The first method (Figure 23) shows the cross correlation between the pump and a probe pulse measured by frequency doubling in a ZnSe window. This clearly shows the generation of transform limited double pulses and the double pulse fall-off in the time domain. Unfortunately, this measurement cannot be done routinely because it is a difficult measurement to perform. The second method (not shown) shows the integrated frequency-domain field amplitude of a single pulse with delay τ. This method is usually performed by measuring the pump output immediately after the pulse shaper using a pyroelectric detector. Finally, the third method (Figure 24) measures the double pulse generation using a spectrometer. This is a routine measurement already performed for correcting a small ω_τ calibration error of 1-2 cm^{-1}.

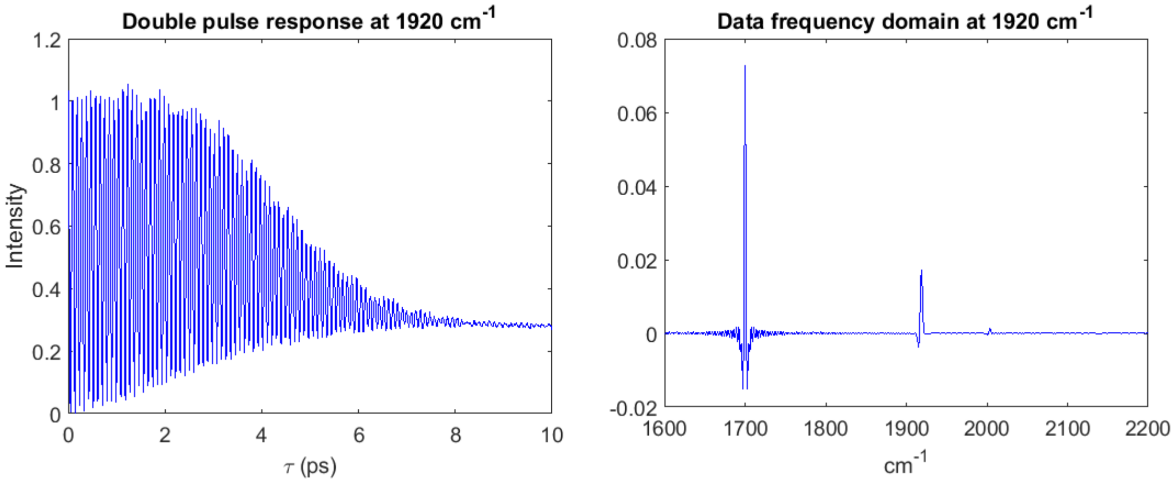

Figure 24. The double pulse tau-delay interferogram as measured by a spectrometer at 1920 cm^{-1} in (a) the time domain and (b) the frequency domain (real part). Note the presence of the folded-over higher harmonic distortion present at 2000 cm^{-1}. The data was measured for a 5 µm pump with a 200 g/mm grating with f_{CW} = 70 MHz. A rotating frame of 1700 cm^{-1} was also used.[14,62]

For the third method, the spectrometer measured intensity can be written as:

$$I(\omega,\tau) = |E_1(\omega) + E_2(\omega,\tau)|^2 = I_1(\omega) + I_2(\omega,\tau) + 2|E_1(\omega)||E_2(\omega,\tau)|\cos(\omega\tau) \tag{47}$$

To recover the double pulse falloff, we postulate that there exists a response function $R(\omega,\tau)$ which satisfies $E_2(\omega,\tau) = R(\omega,\tau)\cdot E_1(\omega)$. Eq. 47 can then be written as:

$$I(\omega,\tau) = I_1(\omega)\cdot(1 + 2R(\omega,\tau)\cos(\omega\tau) + R(\omega,\tau)^2) \tag{48}$$

From this equation, $R(\omega,\tau)$ can be extracted by first assuming that at τ = 0 ps, $E_1(\omega) = E_2(\omega,\tau)$, or that $R(\omega,0) = 1$. Assuming the un-delayed pulse, $E_1(\omega)$, does not decay with τ, we can say that $I(\omega,0) = 4\cdot I_1(\omega)$. These assumptions give:

$$2\cdot R(\omega,\tau)\cos(\omega\tau) + R(\omega,\tau)^2 = \frac{4\cdot I(\omega,\tau)}{I(\omega,0)} - 1 \tag{49}$$

It is probably safe to assume that the instrument response function, $R(\omega,\tau)$, is slowly varying in τ. Therefore, highly oscillatory contributions from $I(\omega,\tau)$ and from

$R(\omega,\tau)\cos(\omega\tau)$ can be filtered out by convolution with a suitable filter $F(\tau)$. Using the approximation that $F(\tau) \otimes (R(\omega,\tau)\cos(\omega\tau)) \approx 0$, the double pulse falloff is given by:

$$R(\omega,\tau) = \sqrt{F(\tau) \otimes \left(\frac{4 \cdot I(\omega,\tau)}{I(\omega,0)} - 1\right)} \tag{50}$$

One may also try a filter centered at frequency ω to directly extract $R(\omega,\tau)$. Unfortunately, our treatment excludes the spectrometer response function, which is convoluted with $I(\omega,\tau)$ along ω and causes a faster decay for the $R(\omega,\tau)\cos(\omega\tau)$ term compared to terms that vary slowly along ω. This response function represents the spectrometer resolution, which for our MCT detector is limited by the pixel size. One can in principle also extract the spectrometer's response function by comparing the $R(\omega,\tau)$ extracted with a zero-frequency filter and with a filter centered at ω.

The procedure of recovering $R(\omega,\tau)$ is shown in Figure 25. As a comparison, we generated a single pulse with a delay τ and plotted its corresponding $R(\omega,\tau)^2$ relative to its undelayed intensity, shown in (color). Clearly, the single pulse trace and the $R(\omega,\tau)^2$ trace are very similar. The small difference may be due to nonlinearities in the transducer that generates the acoustic waveform in the AOM. The difference may also be due to a failure in the assumption that E_1 is independent of τ. Therefore, we will use the single pulse trace as our deconvolution function, $R(\omega,\tau)$.

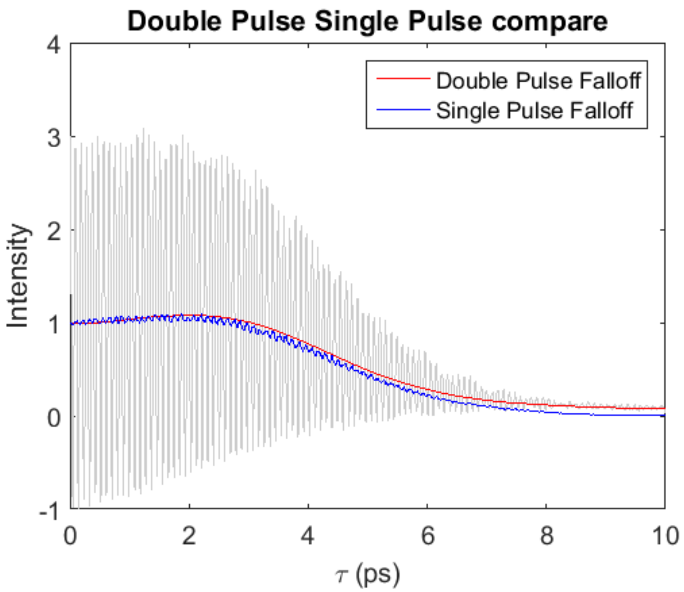

Figure 25. The procedure for extracting the double-pulse falloff for the interferogram in Figure 24. In light gray is shown the result from Eq. 49. The red curve shows the result after convolution with a Gaussian with σ = 0.25 ps $(R(\omega,\tau)^2$ as calculated by Eq. 50). As a comparison, the single pulse falloff is shown in blue, which is measured directly.

3.1.3 Double Pulse Falloff

There are at least three physical origins for double pulse falloff. First, the AOM resolution is limited at the Fourier-plane because of the finite beam waist of the focused laser.[54] Second, as a delay is introduced, the waveform's acoustic frequency increases, which causes an increase in Bragg's angle mismatch.[63] This Bragg's angle mismatch comes at the cost of a lower diffraction efficiency for the AOM. Finally, acoustic frequencies that are detuned from 75 MHz also suffer an amplitude loss at the transducer stage. We will briefly consider each of these effects and show that these origins are related the RF bandwidth of the acoustic mask. The RF bandwidth should be minimized for the best pulse shaper resolution.

The first origin of falloff, the effect of the finite beam waist, can be calculated by convoluting the waveform mask, $M(t_{\mathrm{RF}})$, with a Gaussian whose width is equal to $1/\sqrt{2}$ times the beam waist radius, which if the beam is correctly focused at the Fourier plane is w_0. This corresponds to the convolution with the horizontal intensity profile of any given frequency component.[64] A functional form can be derived by assuming the calibration law, $\omega(t_{\mathrm{RF}})$, is linear with a slope D_ω (in reality $\omega(t_{\mathrm{RF}})$ is approximately quadratic). By performing the convolution on the mask's corresponding transfer function, $\widetilde{H}(\omega(t_{\mathrm{RF}}))$, one finds that the delayed pulse has the following falloff function:

$$R(\tau) = \exp\left(-\frac{(D_\omega\, w_0 \cdot \tau)^2}{8{v_{\mathrm{Ge}}}^2}\right) \tag{51}$$

where this function, due to the linearity assumption, is independent of optical frequency. This function represents a gaussian whose width is related to the inverse of the beam waist at the Fourier plane. This means that when the beam focus at the Fourier plane is worse (or is defocused), the falloff is faster. This phenomenon can also be thought in terms of the RF bandwidth of the acoustic mask. The finite beam size acts to "smear" any complex features in the mask. These features become more rapidly varying with longer delay τ and require a larger RF bandwidth to sustain. The exact dependence between delay and RF bandwidth will be explained in more detail shortly.

The second origin of falloff is related to the Bragg's angle mismatch introduced by the acoustic mask. The change in Bragg's angle is the physical method for introducing a delay in the pulse. The second concave mirror maps the angle to a new horizontal position on the second grating, which introduces an additional pathlength for the delayed pulse because the grating is tilted. The Bragg's angle mismatch is best thought of in terms of the instantaneous frequency of the acoustic mask, which can be defined by rewriting Eq. 38 as:

$$M(t_{\mathrm{RF}}) = \frac{1}{2}\left(\cos\left(\phi_2(t_{\mathrm{RF}})\right) + \cos\left(\phi_1(t_{\mathrm{RF}})\right)\right) \tag{52}$$

Here, $\phi_1(t_{\mathrm{RF}})$ and $\phi_2(t_{\mathrm{RF}})$ are the time-dependent phases that correspond to the un-delayed and delayed pulses, respectively. Ignoring constant phase factors, these can be written as:

$$\phi_1(t_{\mathrm{RF}}) = \omega_{\mathrm{CW}} \cdot t_{\mathrm{RF}} + \phi_{\mathrm{chirp}}\left(\omega(t_{\mathrm{RF}})\right) \tag{53}$$

$$\phi_2(t_{\mathrm{RF}}) = \omega_{\mathrm{CW}} \cdot t_{\mathrm{RF}} + \phi_{\mathrm{chirp}}\left(\omega(t_{\mathrm{RF}})\right) + \omega(t_{\mathrm{RF}}) \cdot \tau \tag{54}$$

The instantaneous frequency of each waveform is then given by $d\phi(t_{\mathrm{RF}})/dt_{\mathrm{RF}}$, which gives:

$$\frac{d\phi_1(t_{\mathrm{RF}})}{dt_{\mathrm{RF}}} = \omega_{\mathrm{CW}} + \frac{d\phi_{\mathrm{chirp}}\left(\omega(t_{\mathrm{RF}})\right)}{dt_{\mathrm{RF}}} \tag{55}$$

$$\frac{d\phi_2(t_{\mathrm{RF}})}{dt_{\mathrm{RF}}} = \omega_{\mathrm{CW}} + \frac{d\phi_{\mathrm{chirp}}\left(\omega(t_{\mathrm{RF}})\right)}{dt_{\mathrm{RF}}} + \frac{d\omega(t_{\mathrm{RF}})}{dt_{\mathrm{RF}}} \cdot \tau \tag{56}$$

Equation 56 shows that the instantaneous frequency offset from the carrier wave is linearly proportional to the delay, τ. The term $d\omega(t_{\mathrm{RF}})/dt_{\mathrm{RF}}$ depends on the calibration law, which is approximately quadratic.

The instantaneous frequency of the delayed pulse is plotted in Figure 26 for several delays. the instantaneous frequency increases with longer delay, thereby increasing the Bragg's angle mismatch, which causes a loss in diffraction efficiency. The AOM throughput due to a change in instantaneous frequency, δf_{CW}, at constant Bragg's angle can be written as:[63]

$$I_1(P, \delta f_{\mathrm{CW}}) = A_1 \sin^2\left(A_2 \cdot P^{1/2}\right) \cdot \mathrm{sinc}^2\left(A_3 \cdot \frac{\delta f_{\mathrm{CW}}}{f_{\mathrm{CW}}} \cdot \left(1 + \frac{\delta f_{\mathrm{CW}}}{f_{\mathrm{CW}}}\right)\right) \tag{57}$$

where A_1, A_2, and A_3 are prefactors that depend on the acoustic medium and the AOM's geometric parameters such as acoustic divergence and interaction length, and where P is the acoustic power. Assuming the acoustic power is constant, the diffraction efficiency falloff due to changes in instantaneous frequency has a sinc^2 functional form. Note that the falloff is also asymmetric with respect to δf_{CW}, which provides slightly slower falloff for negative delays.

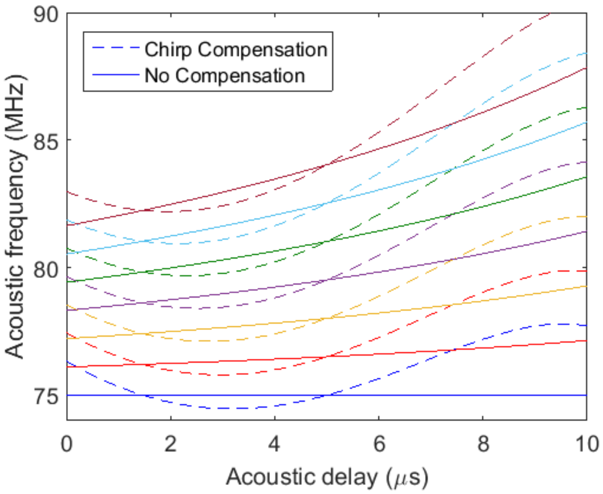

Figure 26. The instantaneous frequency of the acoustic waveform for several τ delays (0-6 ps, spaced in 1 ps) without chirp compensation (solid line) and with chirp compensation (dashed line). The data is for the pulse shaper parameters used in Figure 24.

When experimentally measuring the throughput of an un-delayed pulse the measured intensity falls off rapidly as a function of carrier wave frequency, as is shown in Figure 27(a). This falloff is far faster than the AOM efficiency falloff predicted by Eq. 57 for just Bragg's angle mismatch (Figure 27(b)). We found that when the correct Bragg's angle is recovered by alignment, the throughput is not recovered. This means that the acoustic power in the AOM is also a function of carrier wave frequency—i.e. the acoustic transducer has significant RF frequency dependence, which leads to the unexpected throughput loss.

This power loss is likely caused by transducer impedance mismatch, which is briefly discussed in the acousto-optic devices review by Chang with several useful references throughout.[59] This fact leads to the third source of double pulse falloff.

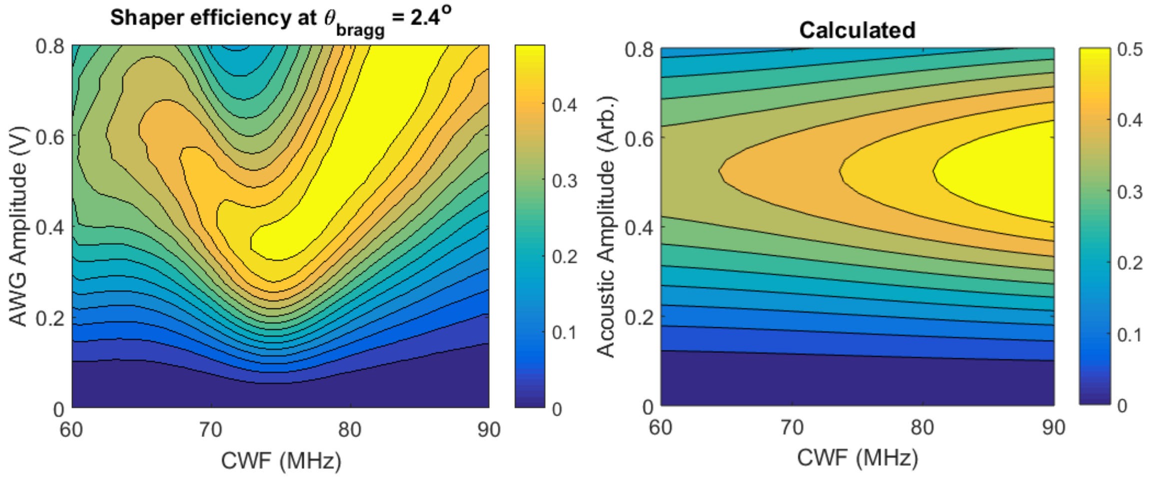

Figure 27. The pulse shaper throughput as a function of AWG waveform amplitude and f_{CW} when (a) measured experimentally and (b) calculated (approximately) by Eq. 57. Parameters used: A_1 = 0.55, A_2 = 3, A_3 = 2.5. The Bragg's angle is intentionally mismatched, giving the highest throughput at 105 MHz. Note the calculated data lacks the distinct 'V' shape present in the experimental data. The data was acquired for a 4.4 μm pump with a 200 g/mm grating.

All three of these sources lead to the effective attenuation of the first cosine component in Eq. 52 because this term has a higher instantaneous frequency compared to the second term, which corresponds to the un-delayed pulse. This means that minimizing the acoustic bandwidth is crucial to improving the pump resolution along ω_τ. In addition, the acoustic masks that are used should be roughly centered around 75 MHz due to the frequency response of the transducer. This implies the following procedure to maximize the AOM throughput and pump resolution: first, estimate the dephasing rate along τ for the sample of interest. Second, assuming that the AOM is calibrated, set the AOM carrier wave frequency so that the single pulse throughput, a good approximation for $R(\omega, \tau)$, is maximized near the oscillator's dephasing $1/e$ time. Then, perform all necessary experimental setup, including chirp compensation (the chirp parameters change with different carrier wave frequency). Finally, after collecting data, deconvolve the data along the pump dimension with $R(\omega, \tau)$. For simplicity, it was assumed that $R(\omega, \tau)$ is frequency independent. This procedure was also used for collecting all the 2D data shown in the next chapter.

Finally, another source that increases the acoustic bandwidth, and thereby contributing to double pulse falloff, is chirp compensation, which adds an additional quadratic and cubic phase (shown in Figure 26 as dashed lines). In the next sections we will show that insertion of the pulse shaper adds a significant amount of chirp, which needs to be compensated. We will also show that most of this chirp can be compensated passively by using the 4f geometry as a pulse compressor, thereby conserving precious acoustic bandwidth.

3.1.4 Sources of Chirp and Their Compensation

The zero-dispersion line, by design, does not introduce any chirp into the output pulse, which is shown explicitly in section 3.2.2. The addition of the AOM, on the other hand, introduces several sources of chirp. These sources include: the material dispersion of the acoustic medium, in our case 20.5 mm of Ge, which introduces a group delay dispersion (GDD) of $1.38\text{x}10^4$ fs^2 for 6 µm;[61,65] and the pathlength difference introduced by the acousto-optic phase matching condition. The second source can be further decomposed into: (1) the path length difference introduced by the Bragg's angle for the center wavelength and (2) the angular dispersion introduced by the Bragg's angle mismatch for wavelengths detuned from the central wavelength. Both sources (1) and (2) have clear geometric origins.

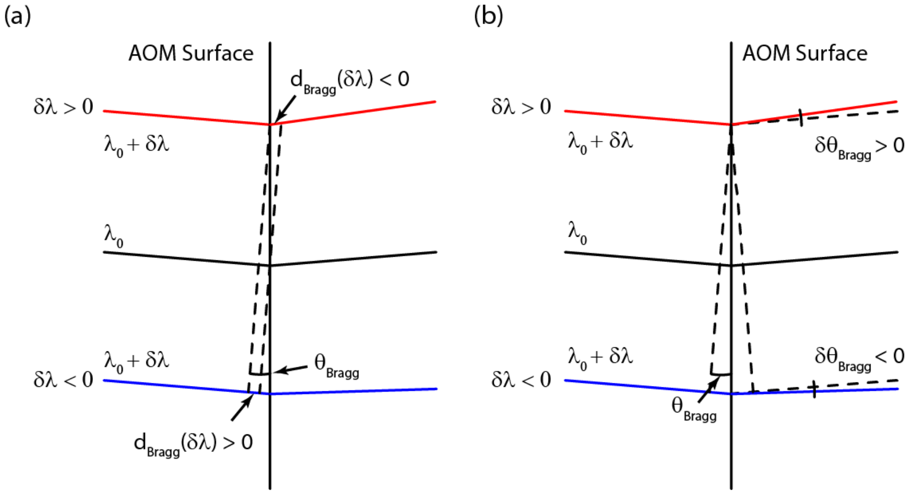

Figure 28. (a) The path length difference introduced due to the Bragg's angle. (b) The additional angular dispersion introduced due to Bragg's angle mismatch (exaggerated for illustration). Note that the acoustic medium is 20.5 mm thick but is drawn as a thin line (AOM Surface) for simplicity.

The first source contributing to the path length difference is summarized in Figure 28a. For the first half of the pulse shaper, the broadband pulse is dispersed by a grating. The individual wavelengths, or rays, are made parallel by the concave mirror and are focused onto the Fourier-plane. At the Fourier-plane all rays have the same pathlength. Because these rays must hit the AOM at the Bragg's angle, rays with shorter wavelength must travel a longer distance $d_{\mathrm{Bragg}}(\delta\lambda)$ before hitting the AOM surface. Within the paraxial approximation and with linear dispersion $D_l^{(1)}$ from Eq. 45, the additional pathlength difference is given by:

$$d_{\mathrm{Bragg}}(\delta\lambda) = -2D_l^{(1)}\delta\lambda \cdot \theta_{\mathrm{Bragg}} \tag{58}$$

A factor of two is included because the 1st order diffracted rays also exit the AOM at the Bragg's angle.

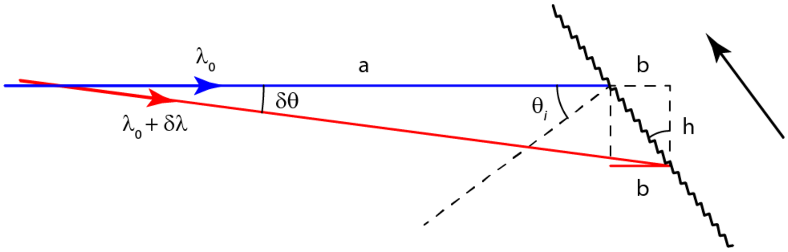

Figure 29. A geometric representation on how the grating introduces a path length difference for two different wavelengths. Moving the grating by distance a introduces an additional path length of $2b$ as well as a horizontal displacement of h. The black arrow represents the grating blaze direction.

This path length difference can be compensated by moving the second grating by a distance Δ_{Bragg}. When the grating is moved, individual rays no longer cross at the original grating position, as is shown in Figure 29. This introduces an additional delay to the ray because the grating is tilted. Because the angle $\delta\theta = \theta_m - \theta_i$ is small (see Figure 22 for grating angle definitions), the additional path length is approximately given by $2b$, where b is given by:

$$b = a \cdot \frac{\tan\theta_i \tan\delta\theta}{1 - \tan\theta_i \tan\delta\theta} \tag{59}$$

Expanding in terms of $\delta\theta$ gives:

$$b = a \cdot \tan(\theta_i)\, \delta\theta + a \cdot \tan^2(\theta_i)\, \delta\theta^2 + \mathcal{O}(\delta\theta^3) \tag{60}$$

Terms with $\delta\theta^2$ and higher order are small but can have a significant impact if the pulse duration is very short by introducing high order chirp. Note that the maximum value of $\delta\theta$ is limited by the AOM aperture and focal length instead of being determined by the pulse bandwidth. These higher order distortions are taken care of with AOM calibration and chirp compensation (section 3.1.1). Taking the first order term and plugging in $\delta\theta = D_a^{(1)}\delta\lambda$, the grating's ability to introduce a path length difference $d(\delta\lambda)$ by adding an additional distance Δ is given by:

$$\frac{d(\delta\lambda)}{\Delta} = \frac{4\delta\lambda}{\lambda_0}\tan^2(\theta_i) \tag{61}$$

Therefore, to compensate for the first source of path length difference, the second grating must be moved by:

$$\Delta_{\mathrm{Bragg}} = f \cdot \theta_{\mathrm{Bragg}} \cot\theta_i \tag{62}$$

Note that moving the grating to compensate for the path length difference comes at the cost of introducing spatial chirp, $s(\delta\lambda)$, which is derived assuming $d(\delta\lambda) \ll \Delta$:

$$\frac{s(\delta\lambda)}{\Delta} = D_a^{(1)}\delta\lambda = \frac{2\delta\lambda}{\lambda_0}\tan(\theta_i) \tag{63}$$

If temporal chirp is suppressed by moving the pulse shaper by Δ_{Bragg}, the dispersion introduced is:

$$\frac{ds}{d(\delta\lambda)} = \frac{2 \cdot f \cdot \theta_{\mathrm{Bragg}}}{\lambda_0} = \frac{f \cdot f_{\mathrm{CW}}}{v_{\mathrm{Ge}}} \tag{64}$$

This important result indicates that the spatial chirp introduced by the pulse shaper is dependent only on the geometric parameters of the pulse shaper, i.e. the focal length of the concave mirrors and the acoustic parameters of the AOM. This dependence is a type of spatio-temporal coupling.[53,66] Such coupling means that spatial chirp in the AOM 4f pulse shaper is fundamentally unavoidable, although a double-pass designs is capable of reversing spatial chirp to some extent.[67]

The second source of path length difference is subtler in origin, but equally significant. The AOM is usually aligned to match the center wavelength's Bragg's angle, but because the AOM surface is flat, rays with wavelengths that deviate from the central wavelength have a Bragg's angle deviation:

$$\delta\theta_{\text{Bragg}} = \frac{\delta\lambda \cdot f_{\text{CW}}}{2v_{\text{Ge}}} \tag{65}$$

As shown in Figure 28(b), this deviation introduces a significant angular dispersion of $2\delta\theta_{\text{Bragg}}/\delta\lambda$ for the AOM's 1st diffracted order. The deviation of any ray is then mapped back to the 2nd grating accordingly, but the rays instead recombine at an additional distance of Δ_{Angular}. This distance can be found by using the ABCD ray-transfer method, with a reference ray following the path of λ_0. The ray of interest has an offset of $D^{(1)}\delta\lambda$ and angle deviation of $2\delta\theta_{\text{Bragg}}$. Propagating this ray through a distance f, a concave mirror with focal length f, and finally a distance $f + \Delta_{\text{Angular}}$ yields:

$$\begin{pmatrix} -\Delta_{\text{Angular}}/f & f \\ -\frac{1}{f} & 0 \end{pmatrix} \cdot \begin{pmatrix} f \cdot D_a^{(1)}\delta\lambda \\ 2\delta\theta_{\text{Bragg}} \end{pmatrix} = \begin{pmatrix} 2f \cdot \delta\theta_{\text{Bragg}} - \Delta_{\text{Angular}} \cdot D_a^{(1)}\delta\lambda \\ -D_a^{(1)}\delta\lambda \end{pmatrix} \tag{66}$$

All rays recombine at a point where the 1st element is equal to zero. Solving forΔ_{Angular} yields:

$$\Delta_{\text{Angular}} = \frac{2f \cdot \delta\theta_{\text{Bragg}}}{D_a^{(1)}\delta\lambda} = \frac{f \cdot f_{\text{CW}}}{v_{\text{Ge}} \cdot D_a^{(1)}} \tag{67}$$

Two important conclusions can be drawn from this result. First, this source of path length difference does not introduce spatial chirp, which differentiates this path length difference source from the other two sources. Alternatively, this result can be thought of as the angular dispersion introduces an amount of spatial and temporal chirp which is perfectly compensated for when moving the grating by a distance Δ_{Angular}. Second, any angular dispersion introduced by Bragg's angle mismatch does not generate angular dispersion in the output pulse because the ray's output angle, $-D_a^{(1)}\delta\lambda$ (R.H.S. of eq. 67), has no dependence on $\delta\theta_{\text{Bragg}}$ and is matched to the grating's angular dispersion.

To summarize, temporal chirp is introduced into the zero-dispersion line by addition of the AOM. Temporal chirp, which originates from the material dispersion from the AOM, the Bragg's angle, and angular dispersion introduced by Bragg's angle mismatch, can be compensated by moving the second grating by a distance:

$$\Delta_{\text{Tot}} = \Delta_{\text{Ge}} + \Delta_{\text{Bragg}} + \Delta_{\text{Angular}} \tag{68}$$

In addition, moving the second grating introduces spatial chirp, where only the distance $\Delta_{\text{Ge}} + \Delta_{\text{Bragg}}$ contributes. As an example, using the pulse shaper parameters introduced in the previous sections, the distances needed to compensate the introduced chirp are $\Delta_{\text{Ge}} =$ 0.58 mm , $\Delta_{\text{Bragg}} = 10.9$ mm, $\Delta_{\text{Angular}} = 10.8$ mm, for a total distance of $\Delta_{\text{tot}} = 22.3$ mm. Δ_{Ge} was calculated by dividing the GDD for 20.5 mm of Ge by the GVD of the pulse shaper, which is $2.39\text{x}10^4$ fs^2/mm (see section 3.2.2). Δ_{tot} is a significant deviation from the original f = 200 mm 4f geometry! In the next section, we will show how these geometric results naturally come out of a more general 1st order ray-transfer treatment of the pulse shaper.

3.2 The Ray-pulse Matrix

Additional insight into the 4f geometry can be gained through a more rigorous 1st order treatment of pulse propagation through the optical system. This treatment is known as the ray-pulse matrix method and is an extension of the ABCD ray-transfer matrix method to dispersive systems.[68-70] The method is constructed, within the paraxial approximation, from a transform-limited reference pulse propagating along the optical axis for any optical system. Deviations from this reference pulse are then considered in a transverse plane. The possible deviations in the transverse plane are displacement, angle, time of arrival, and Hertzian frequency, which are denoted by x, θ, t, and f, respectively. There must exist a transfer function that can transform between any two given two transverse planes, P_{in} and P_{out}:

$$P_{\text{out}}(x,\theta,t,f) = T\{P_{\text{in}}(x,\theta,t,f)\} \tag{69}$$

Assuming that the deviations are sufficiently small, the transfer function can be expanded and truncated to 1st order. Because we chose to write the formulism in terms of deviations from the reference pulse, there are no 0th order terms. In matrix notation this can be written as:[68]

$$\begin{pmatrix} x \\ \theta \\ t \\ f \end{pmatrix}_{\text{out}} = \begin{pmatrix} \dfrac{\partial x_{\text{out}}}{\partial x_{\text{in}}} & \dfrac{\partial x_{\text{out}}}{\partial \theta_{\text{in}}} & 0 & \dfrac{\partial x_{\text{out}}}{\partial f_{\text{in}}} \\ \dfrac{\partial \theta_{\text{out}}}{\partial x_{\text{in}}} & \dfrac{\partial \theta_{\text{out}}}{\partial \theta_{\text{in}}} & 0 & \dfrac{\partial \theta_{\text{out}}}{\partial f_{\text{in}}} \\ \dfrac{\partial t_{\text{out}}}{\partial x_{\text{in}}} & \dfrac{\partial t_{\text{out}}}{\partial \theta_{\text{in}}} & 1 & \dfrac{\partial t_{\text{out}}}{\partial f_{\text{in}}} \\ 0 & 0 & 0 & 1 \end{pmatrix} \begin{pmatrix} x \\ \theta \\ t \\ f \end{pmatrix}_{\text{in}} \tag{70}$$

In this form, the bottom row is written to preserve the frequency of the pulse because the optical components do not change the pulse frequency. Similarly, any action of these optical components also does not depend on the arrival time of the pulse, which sets most of the third column derivatives to zero.

Several of the matrix elements have direct physical meanings. For example, the upper left 2x2 submatrix corresponds to the familiar ABCD matrix used in the previous sections. In addition, the matrix elements $\partial t_{\text{out}}/\partial f_{\text{in}}$ and $\partial x_{\text{out}}/\partial f_{\text{in}}$ corresponds temporal and spatial chirp respectively. Below, we will apply this formalism specifically to the Littrow configuration for the 4f pulse shaper and extract several useful and simple algebraic relations for these terms. Note that the 4f zero-dispersion line has already been analyzed using the ray-pulse matrix formalism.[71] Therefore, we will skip most derivation and focus on the results specific to the Littrow configuration.

3.2.1 Ray-Pulse Analysis of the 4f Geometry

Just like in the ABCD ray-transfer matrix formulism, an optical system's total transfer function can be constructed from the individual optical component's transfer functions. This is intuitive because the previous component's output transverse plane acts as an input for the next optical component. This implies the following method of nested transfer functions, where T_i is the i^{th} optical component's transfer function:

$$P_{\text{out}}(x,\theta,t,f) = T_i\left\{\dots\left\{T_2\left\{T_1\{P_{\text{in}}(x,\theta,t,f)\}\right\}\right\}\right\} \tag{71}$$

When expanded to 1st order, each transfer function becomes a matrix operator, called a ray-pulse matrix:

$$\boldsymbol{p}_{\text{out}} = \boldsymbol{T}_i \cdot \boldsymbol{T}_{i-1} \cdots \boldsymbol{T}_2 \cdot \boldsymbol{T}_1 \cdot \boldsymbol{p}_{\text{in}} \tag{72}$$

The individual operators can be combined and rewritten in terms of a total ray-pulse matrix:

$$\boldsymbol{M} = \boldsymbol{T}_i \cdot \boldsymbol{T}_{i-1} \cdots \boldsymbol{T}_2 \cdot \boldsymbol{T}_1 \tag{73}$$

The ray-pulse matrices, $\boldsymbol{T}_i$, have been derived for most optical components.[68] For the 4f pulse shaper, we are interested in the ray-pulse matrix for propagation through free space, diffraction from a grating, and reflection from a concave mirror.

First, we will write down the ray-pulse matrix for free propagation through a non-dispersive medium:

$$\boldsymbol{T}_i = \begin{pmatrix} 1 & f+\Delta_i & 0 & 0 \\ 0 & 1 & 0 & 0 \\ 0 & 0 & 1 & 0 \\ 0 & 0 & 0 & 1 \end{pmatrix} \tag{74}$$

where f is the focal length of the pulse shaper concave mirrors and Δ_i is an additional distance introduced through either misalignment or for chirp compensation. For a concave mirror of focal length f, the ray-pulse matrix is:

$$\boldsymbol{F} = \begin{pmatrix} 1 & 0 & 0 & 0 \\ -\dfrac{1}{f} & 1 & 0 & 0 \\ 0 & 0 & 1 & 0 \\ 0 & 0 & 0 & 1 \end{pmatrix} \tag{75}$$

Note that for these two matrices are similar to their ABCD counterparts and do not have off-diagonal elements that couple t or f with x or θ. This is because these operations do not introduce dispersion into the pulse—meaning that the pulse remains transform limited.

The gratings, on the other hand, do introduce dispersion into the pulse. For the first grating:

$$\boldsymbol{G}_1 = \begin{pmatrix} -\dfrac{\sin\phi}{\sin\psi} & 0 & 0 & 0 \\ 0 & -\dfrac{\sin\psi}{\sin\phi} & 0 & \dfrac{\cos\phi - \cos\psi}{f_0 \sin\phi} \\ \dfrac{\cos\psi - \cos\phi}{c\sin\psi} & 0 & 1 & 0 \\ 0 & 0 & 0 & 1 \end{pmatrix} \tag{76}$$

where c is the speed of light, f_0 is the central Hertzian frequency of the pulse, and ψ and ϕ are the incident and reflected angles with respect to the *grating surface*, as is shown in Figure 22.[68] Care must be taken when defining these angles because the grating equation in Eq. 40 is defined in terms of angles with respect to the grating normal. The input grating angle ψ is therefore written as:

$$\psi = \frac{\pi}{2} - \sin^{-1}\left(\frac{\lambda_0}{2d}\right) \tag{77}$$

The reflected pulse, with wavelength $\lambda_0 + \delta\lambda$, has its first order diffraction at:

$$\phi = \frac{\pi}{2} + \sin^{-1}\left(\frac{2\delta\lambda + \lambda_0}{2d}\right) \tag{78}$$

The second grating, $\boldsymbol{G}_2$, recombines the dispersed pulse, which is the opposite of the first grating. Therefore, $\boldsymbol{G}_2$ is like the $\boldsymbol{G}_1$ except that the definitions ψ and ϕ are interchanged.

Combining all the elements, the total ray-pulse matrix for the 4f system becomes:

$$\boldsymbol{M}_{4\mathrm{f}} = \boldsymbol{G}_2 \cdot \boldsymbol{T}_4 \cdot \boldsymbol{F} \cdot \boldsymbol{T}_3 \cdot \boldsymbol{T}_2 \cdot \boldsymbol{F} \cdot \boldsymbol{T}_1 \cdot \boldsymbol{G}_1 \tag{79}$$

The total system matrix, $\boldsymbol{M}_{4\mathrm{f}}$**,** is given by:

$$\begin{pmatrix} \frac{\Delta_{2,3}\Delta_4}{f^2} - 1 & \frac{\left(\Delta_m - f^2\Delta_{1,4}\right)\sin^2\psi}{f^2\sin^2\phi} & 0 & \frac{\left(f^2\Delta_{1,4} - \Delta_m\right)F_{\phi\psi}\sin\psi}{f^2 f_0 \sin^2\phi} \\ \frac{\Delta_{2,3}\sin^2\phi}{f^2\sin^2\psi} & \frac{\Delta_1\Delta_{2,3}}{f^2} - 1 & 0 & \frac{\Delta_1\Delta_{2,3}F_{\psi\phi}}{f^2 f_0 \sin\psi} \\ \frac{\Delta_{2,3}\Delta_4 F_{\psi\phi}}{cf^2\sin\psi} & \frac{\left(f^2\Delta_{1,4} - \Delta_m\right)F_{\phi\psi}\sin\psi}{cf^2\sin^2\phi} & 1 & \frac{\left(\Delta_m - f^2\Delta_{1,4}\right)(\cot\phi - \cos\psi\csc\phi)^2}{cf^2 f_0} \\ 0 & 0 & 0 & 1 \end{pmatrix} \tag{80}$$

where $F_{AB} = \cos A - \cos B$, $\Delta_{2,3} = \Delta_2 + \Delta_3$, $\Delta_m = \Delta_1\Delta_{2,3}\Delta_4$, and $\Delta_{1,4} = \Delta_1 + \Delta_4$.

3.2.2 Spatio-Temporal Coupling

The element corresponding to temporal chirp is given by:

$$\frac{\partial t_{\mathrm{out}}}{\partial f_{\mathrm{in}}} = \left(\frac{\Delta_m}{f^2} - \Delta_{1,4}\right) \cdot \frac{(\cot\phi - \cos\psi\csc\phi)^2}{cf_0} \tag{81}$$

$\Delta_{1,4}$ corresponds to the total grating displacement. Note that the Δ_m term is negligible compared to $\Delta_{1,4}$ because the distance misalignments are small compared to the focal lengths, i.e. $f^2 \gg \Delta_m$. This important approximation, which will be discussed in more detail later, can also be made for the other matrix elements in $\boldsymbol{M}_{4\mathrm{f}}$, meaning that the individual grating offsets are not important. Instead, it is the total grating offset distance that is critical for chirp compensation and leads to the introduction of spatio-temporal distortions.

Making this approximation and plugging in the definitions for ψ and ϕ yields:

$$\frac{\partial t_{\text{out}}}{\partial f_{\text{in}}} \approx -\frac{4\Delta_{1,4}}{cf_0} \cdot \frac{(\lambda_0 + \delta\lambda)^2}{4d^2 - (\lambda_0 + 2\delta\lambda)^2} \tag{82}$$

To extract the group velocity dispersion (GVD_f), we expand in terms of $\delta\lambda$ to yield:

$$\frac{\partial t_{\text{out}}}{\partial f_{\text{in}}} = \Delta_{1,4} \cdot \text{GVD}_f^{(0)} + \Delta_{1,4} \cdot \text{GVD}_f^{(1)} \delta\lambda + \Delta_{1,4} \cdot \mathcal{O}(\delta\lambda^2) \tag{83}$$

$$\text{GVD}_f^{(0)} = \frac{4}{cf_0} \cdot \frac{{\lambda_0}^2}{\left({\lambda_0}^2 - 4d^2\right)} = -\frac{4}{cf_0} \tan^2 \theta_i \tag{84}$$

$$\text{GVD}_f^{(1)} = -\frac{8}{cf_0} \cdot \frac{\left({\lambda_0}^3 + 4d^2\lambda_0\right)}{\left({\lambda_0}^2 - 4d^2\right)^2} \tag{85}$$

Higher order dispersions are also generated by the higher order terms and can be pre-compensated for by the methods described in section 3.1.1. Note that the ray-pulse matrix was derived in terms of Hertzian frequency, whereas GVD is usually reported as derivative with respect to angular frequency. Therefore, we are off by a factor of $(2\pi)^{-1}$:

$$\text{GVD}_\omega = \frac{\partial t_{\text{out}}}{\partial \omega_{\text{in}}} = \frac{\partial t_{\text{out}}}{2\pi \cdot \partial f_{\text{in}}} = -\frac{2}{\pi \cdot cf_0} \tan^2 \theta_i = -\frac{4}{c\omega_0} \tan^2 \theta_i \tag{86}$$

As an example, the pulse shaper in the configuration described in section 3.1.1gives a calculated value of GVD_ω = -2.39x10^4 fs^2/mm. Using the procedure for chirp compensation described in section 3.1.1 (by frequency doubling the pulse shaper output in a ZnSe window), we measured the GDD_ω chirp compensation parameter for several values of $\Delta_{1,4}$ as shown in Figure 30. The slope gives a value for GVD_ω of 2.21x10^4 fs^2/mm, which is in good agreement with the calculated value. Note the sign difference, which correctly indicates that the acoustic mask adds chirp to compensate chirp introduced by moving the second grating.

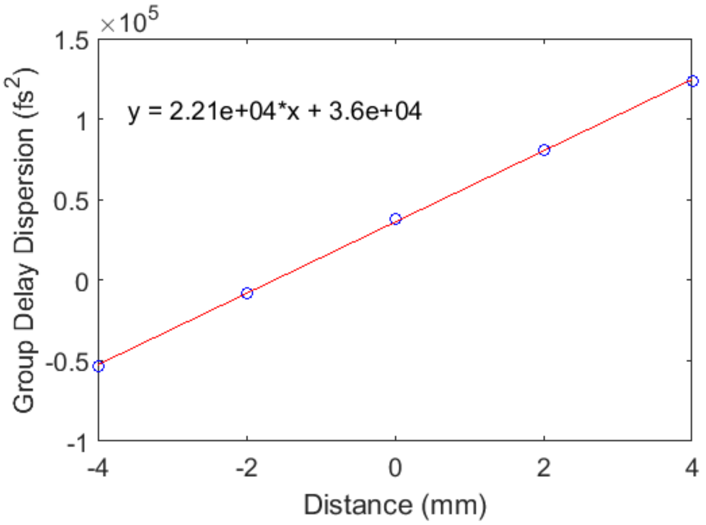

Figure 30. Measured GDD values as a function of grating distance. The slope gives the compensating ability of the pulse shaper, i.e. the GVD.

It is more practical to use Eq. 84 to predict the necessary grating offset required to compensate the geometric pathlength differences introduced by inserting the AOM and using the 1st order diffracted beam (see section 3.1.4). The grating's ability to compensate for the pathlength difference for a given $\delta\lambda$ is:

$$\frac{d(\delta\lambda)}{\Delta_{1,4}} = \mathrm{GVD}_f^{(0)} \cdot c\delta f = -\mathrm{GVD}_f^{(0)} \frac{c^2\delta\lambda}{{\lambda_0}^2} = \frac{4\delta\lambda}{\lambda_0}\tan^2\theta_i \tag{87}$$

This equation is the same as the geometrically derived result in Eq. 61, verifying that our initial analysis was correct.

Spatial chirp can be derived in an analogous fashion. Applying the same approximations used earlier, the matrix element for spatial chirp is given by:

$$\frac{\partial x_{\text{out}}}{\partial f_{\text{in}}} = \left(\Delta_{1,4} - \frac{\Delta_m}{f^2}\right) \cdot \frac{(\cos\phi - \cos\psi)\sin\psi}{f_0 \sin^2\phi} \approx \Delta_{1,4} \cdot \frac{(\cos\phi - \cos\psi)\sin\psi}{f_0 \sin^2\phi} \tag{88}$$

Including the definitions for the grating angles and expanding around $\delta\lambda$ and only including the 0th order term:

$$\frac{\partial x_{\text{out}}}{\partial f_{\text{in}}} = \Delta_{1,4} \cdot \text{SC}_f^{(0)} + \Delta_{1,4} \cdot \text{SC}_f^{(1)} \delta\lambda + \Delta_{1,4} \cdot \mathcal{O}(\delta\lambda^2) \tag{89}$$

$$\text{SC}_f^{(0)} = -\frac{2}{f_0} \tan(\theta_i) \tag{90}$$

The ray horizontal displacement, as a function of $\delta\lambda$, is given by:

$$\frac{s(\delta\lambda)}{\Delta_{1,4}} = \text{SC}_f^{(0)} \delta f = -\text{SC}_f^{(0)} \cdot \frac{c\delta\lambda}{{\lambda_0}^2} = \frac{2\delta\lambda}{\lambda_0} \tan(\theta_i) \tag{91}$$

This equation equivalent to the geometrically derived result in Eq. 63, except that now spatial chirp is defined in terms of the total grating distance, instead of only the second grating's distance.

The final term of interest is the angular chirp, which determines the output angle as a function of frequency:

$$\frac{\partial \theta_{\text{out}}}{\partial f_{\text{in}}} = \frac{\Delta_1 \Delta_{2,3} (\cos\psi - \cos\phi)}{f^2 f_0 \sin\psi} = \frac{\Delta_1 \Delta_{2,3}}{c f^2} (\lambda_0 + \delta\lambda) \cdot \tan\theta_i \tag{92}$$

Note that the angular chirp is linear in $\delta\lambda$, suggesting that the output angular dispersion is quadratic in wavelength. Eq. 92 shows that the angular chirp depends, intuitively, on the distance between the two concave mirrors. In addition, the distance between the first grating and first concave mirror is also important, suggesting that moving the first grating to compensate from Bragg's angle mismatch may make the system more susceptible to angular chirp. Ignoring the quadratic contribution, the angular dispersion can be found for any frequency component by multiplying by δf, which was defined as an offset frequency from f_0. In terms of $\delta\lambda$, this gives

$$\theta_{\text{out}}(\delta\lambda) = \frac{\delta\lambda}{\lambda_0} \cdot \frac{\Delta_1 \Delta_{2,3}}{f^2} \tan\theta_i \tag{93}$$

As an example, the angular dispersion introduced is 0.16 mrad (full angle) in the configuration described previously for a 1 μm bandwidth centered around 6 μm with the first grating displacement of 5 mm and the concave mirror displacement of 10 mm. A 10 mm misalignment is large but possible considering the difficulty of collimating a mid IR beam. The angular dispersion introduced, on the other hand, is very small.

Unfortunately, this analysis assumes that the pulse shaper input beam is perfectly collimated, which is generally not the case. Angular chirp is an especially important parameter because it directly affects the focal spot size at the sample. In the next section we will consider the effects of the input beam collimation and angular chirp on the focus quality.

3.3 Geometric Ray-Tracing Analysis

As mentioned, the analysis in the previous section did not consider the effect of beam collimation. Beam profile measurements suggest that pump can have an elliptical focus at the sample position even though all optics are spherical (except the parabola before the sample). We find that the best focus often has a 1:2.7 aspect ratio, with the elongation always being horizontal. Spatial chirp can make a beam appear slightly elliptical, but the beam should still be able to focus tightly. To gain more insight into the source of the elliptical focus, I wrote and ran a custom 3D geometric ray-tracing simulation for the 4f pulse shaper and parabola. This raytracing method also goes beyond the paraxial approximation, meaning that higher order aberrations are also included, although they are not significant.

Ray tracing is performed by generating an ensemble of random rays and propagating the rays through space. Just like in the ray-pulse method, the rays parametrically keep track of their duration, spatial position, direction, and frequency. Because the paraxial approximation in not made, this ray tracing method cannot be written in a matrix form. Instead of using transverse planes, I use an iterative method to propagate rays to a surface and calculate the new ray direction, which will be summarized below. Throughout this section, I will use a subscript notation to keep track of rays and iterations through different optical surfaces. For example, a ray of wavelength λ_j and with position $\vec{\boldsymbol{q}}_{jk}$ is propagated in the direction $\vec{\boldsymbol{p}}_{jk}$ for a duration t_{jk} by:

$$\vec{\boldsymbol{q}}_{j,k+1} = \vec{\boldsymbol{q}}_{jk} + \vec{\boldsymbol{p}}_{jk} \cdot t_{jk} \tag{94}$$

The subscript k keeps track of the number of ray propagations and j keeps track of which ray. In practice, these operations are simultaneously performed for the j rays and the vectors $\vec{\boldsymbol{q}}_{jk}$ and $\vec{\boldsymbol{p}}_{jk}$ are stored as $3 \times j \times k$ arrays.

The ray tracing algorithm can be summarized as follows. Starting with a given ray's position and direction, the intersection between the ray and a surface is calculated using Eq. 94 and an equation for the surface of interest. This calculation yields the time t_{mn} that it takes to reach the surface. The ray's next position, $\vec{\boldsymbol{q}}_{j,k+1}$, which is the intersection point between the ray and the surface, is calculated by plugging the time t_{mn} back into Eq. 94. The surface's normal is calculated at this point and is used to reflect or diffract the ray, which generates the next direction, $\vec{\boldsymbol{p}}_{j,k+1}$. This is done in a numerically efficient manner for all rays using MATLAB array functions such as bsxfun(), which allows for the implicit expansion of array. After all ray operations are performed, the j^{th} ray's total propagation time is calculated by summing over the k-dimension in t_{jk}.

There are five types of surfaces that the ray interacts with in this simulation: a concave mirror (sphere), off-axis parabola (paraboloid), flat mirror (plane), grating (plane), and AOM (plane). The first surface we will consider is a spherical mirror. The vector equation for a spherical surface is (the paraboloid is handled in a similar way):

$$|\vec{\boldsymbol{r}} - \vec{\boldsymbol{r}}_0| = 2f \tag{95}$$

where $\vec{\boldsymbol{r}}$ is a position vector (x, y, z), $\vec{\boldsymbol{r}}_0$ is the center of the sphere, and f is the focal length of the concave mirror. The intersection time between the sphere and a ray (Eq. 94) is given by:

$$t_{jk} = \frac{1}{2}\left(-b \pm \sqrt{b^2 - 4c}\right) \tag{96}$$

where $b = 2\left(\vec{\boldsymbol{q}}_{jk} - \vec{\boldsymbol{r}}_0\right) \cdot \vec{\boldsymbol{p}}_{jk}$ and $c = \left|\vec{\boldsymbol{q}}_{jk} - \boldsymbol{r}_0\right|^2 - 4f^2$. Care must be taken to choose the solution with positive t_{jk} to ensure forward propagation of the ray. The intersection point $\vec{\boldsymbol{q}}_{j,k+1}$ is then calculated by Eq. 94. The normalized surface normal is calculated at the intersection point by the derivative at the surface:

$$\vec{\boldsymbol{n}}_m = \frac{\left(\vec{\boldsymbol{q}}_{j,k+1} - \vec{\boldsymbol{r}}_0\right)}{\left|\vec{\boldsymbol{q}}_{j,k+1} - \vec{\boldsymbol{r}}_0\right|} \tag{97}$$

The reflection is then calculated as:

$$\vec{\boldsymbol{p}}_{j,k+1} = \vec{\boldsymbol{p}}_{jk} - 2\vec{\boldsymbol{n}}_j\left(\vec{\boldsymbol{n}}_j \cdot \vec{\boldsymbol{p}}_{jk}\right) \tag{98}$$

A similar procedure is followed for reflections from planar surfaces, where the plane is directly defined by the surface normal:

$$\vec{\boldsymbol{n}} \cdot (\vec{\boldsymbol{r}} - \vec{\boldsymbol{r}}_0) = 0 \tag{99}$$

In practice, the normal is generated by rotating a reference normal vector into the direction of the desired optic using rotation matrices. For example, the rotation of the steering mirror SM$_1$ for Bragg's angle matching is done by rotating a vector $\vec{\boldsymbol{n}}_0 = (-1, 0, -1)$, which corresponds to a 45° mirror pointing in the $-XZ$ direction, by half the Bragg's angle along the Y-axis:

$$\vec{\boldsymbol{n}} = \begin{pmatrix} \cos\theta_{\mathrm{Bragg}} & 0 & \sin\theta_{\mathrm{Bragg}} \\ 0 & 1 & 0 \\ -\sin\theta_{\mathrm{Bragg}} & 0 & \cos\theta_{\mathrm{Bragg}} \end{pmatrix} \cdot \vec{\boldsymbol{n}}_0 \tag{100}$$

The intersection time for a planar surface is calculated by:

$$t_{jk} = \frac{\vec{\boldsymbol{n}} \cdot (\vec{\boldsymbol{r}}_0 - \vec{\boldsymbol{q}}_{jk})}{\vec{\boldsymbol{n}} \cdot \vec{\boldsymbol{p}}_{jk}} \tag{101}$$

The new positions and directions of the ray, $\vec{\boldsymbol{q}}_{j,k+1}$ and $\vec{\boldsymbol{p}}_{j,k+1}$ are then calculated using the previously described method.

Diffraction from a grating represents a special case of planar reflection. Because our pulse shaper is in the Littrow geometry, the grating is tilted vertically to allow the beam to clear the 45° steering mirrors. Because the beam is not in the same plane as the groove periodicity, the normal grating equation cannot be used. Instead, we calculate the diffracted beam's wavevector using conical diffraction. [72] To do this, we must first rotate our XYZ beam coordinate frame into the UVW grating coordinate frame. This can be achieved by using a coordinate transformation matrix that is constructed from the grating normal and groove propagation direction. The grating normal is constructed by first defining and normalizing a grating surface normal $(0,\ g\ , -1)$ with downward tilt, where $g = -0.5 \times \Delta h/f$ is the downward tilt component of the grating and Δh is the beam height change (e.g. 25.4 mm). This vector is then rotated along the Y-axis by the grating angle to generate a vector $\vec{\boldsymbol{w}}$. An analogous vector $\vec{\boldsymbol{u}}$ represents the grating groove period direction and is constructed by rotating an initial vector $(-1, 0, 0)$ by the grating angle. Finally, a third orthogonal vector $\vec{\boldsymbol{v}} = \vec{\boldsymbol{u}} \times \vec{\boldsymbol{w}}$ is also calculated. Note that the second grating is physically flipped (i.e. rotated 180° along its normal), meaning that its initial groove period vector is $(+1, 0, 0)$. The unitary coordinate transformation matrix is given by concatenating the vectors, $\boldsymbol{M} = (\vec{\boldsymbol{u}} \quad \vec{\boldsymbol{v}} \quad \vec{\boldsymbol{w}})$.

Conical diffraction is calculated using the vector grating equation:[72]

$$\vec{\boldsymbol{k}}_{s,m} = \vec{\boldsymbol{k}}_{s,i} + \frac{2\pi m}{d}\vec{\boldsymbol{u}} \tag{102}$$

here $\vec{\boldsymbol{k}}_{s,i}$ is the grating surface component of the incident wavevector (i.e. incident wavevector's projection onto the UV plane), $\vec{\boldsymbol{k}}_{s,m}$ is the m^{th} order diffracted wavevector with grating period d. Note that this is written in the grating coordinate frame, so $\vec{\boldsymbol{u}}$ should be understood as the unit vector $(1, 0, 0)$. The W component of the diffracted wavevector is calculated to reflect the ray and preserve the wavevector norm: $|\vec{\boldsymbol{k}}_m| = 2\pi/\lambda$. Finally, the diffracted wavevector is transformed back into the XYZ coordinate frame:

$$\vec{\boldsymbol{p}}_{j,k+1} = \frac{\boldsymbol{M} \cdot \vec{\boldsymbol{k}}_m}{|\vec{\boldsymbol{k}}_m|} \tag{103}$$

First order diffraction from the AOM is also treated with this conical diffraction method.

Figure 31 summarizes the key dimensions, coordinates, and adjustable parameters in this simulation. The input beam size, defined by the standard deviation of a Gaussian intensity profile, is σ = 1 mm and divergence is normally set to zero, but is adjustable. The shaper focal length is set to 200 mm, with the distances from the ideal 4f position of the optics being denoted in an absolute coordinate frame as ΔCM_1, ΔCM_2, ΔG_1, and ΔG_2 (as opposed to the relative coordinate frame, Δ_1, Δ_2, Δ_3, and Δ_4 used in the previous sections, which defines the relative distance between two optics or transverse planes). The steering mirrors are located half way (100 mm) between the AOM and the ideal concave mirror position. They are adjusted to match the Bragg's angle ($\theta_{Bragg} = 1.95^o$) for the central pulse wavelength for which the beam profile measurements were made (λ = 5 μm). The steering mirrors have adjustable angle parameter δSM_1 and δSM_2, which mimics our alignment procedure. The gratings have a downward tilt which is fixed at 25.4 mm/200 mm. The grating angles are set for the pulse central wavelength, $\theta G_1 = 30^o$ and $\theta G_2 = -30^o$. The second grating has an adjustable parameter $\delta\theta G_2$ Finally, after propagation through the 4f pulse shaper, the rays are propagated a total distance of 500 mm to the parabola (Figure 32). In the next section, the parabola focus is analyzed by the ray's intersection with a plane that is offset from the ideal focal point.

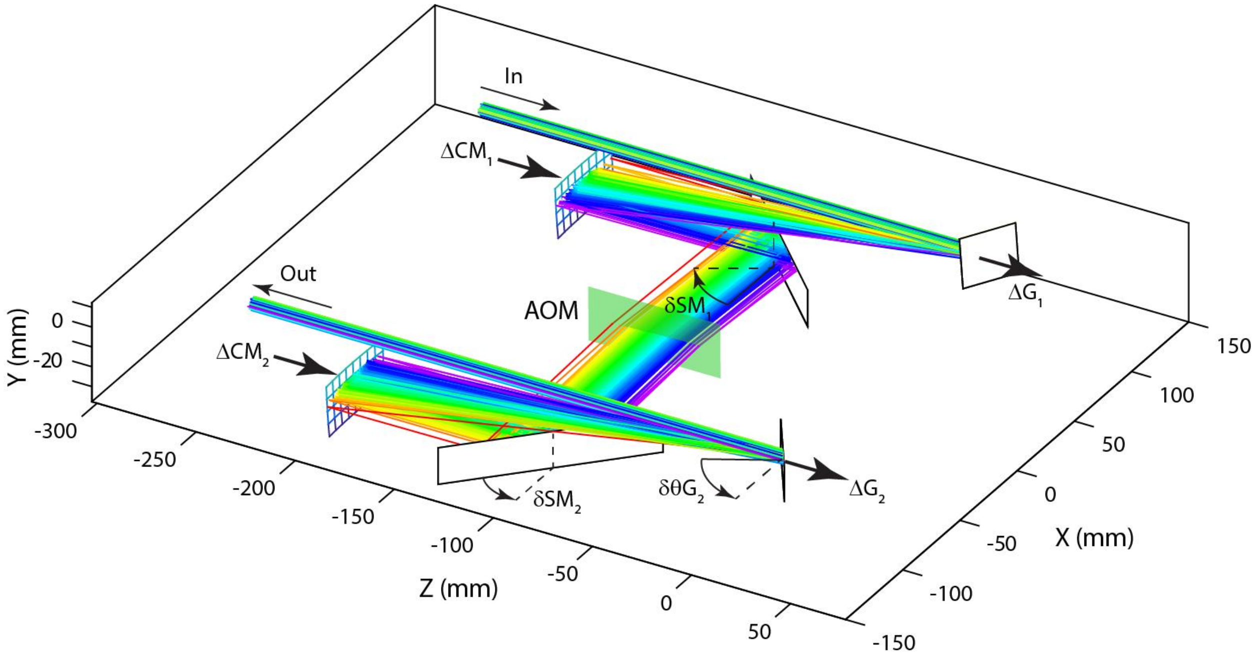

Figure 31. Parameter definitions for the pulse shaper used in the ray-tracing simulation.

3.3.1 Misalignment into the Parabola

In this section, I will discuss the results from the ray tracing simulation. First, I will discuss the effects of focus on parabola misalignment and show that the astigmatism introduced, although significant, is unable to reproduce the 1:2.7 pump focus aspect ratio.

Next, I will discuss the pulse shaper. As a check, the ray tracing simulation results will be compared to the linear theory developed in section 3.2. Finally, I will present how different misalignments affect the focus after the parabola.

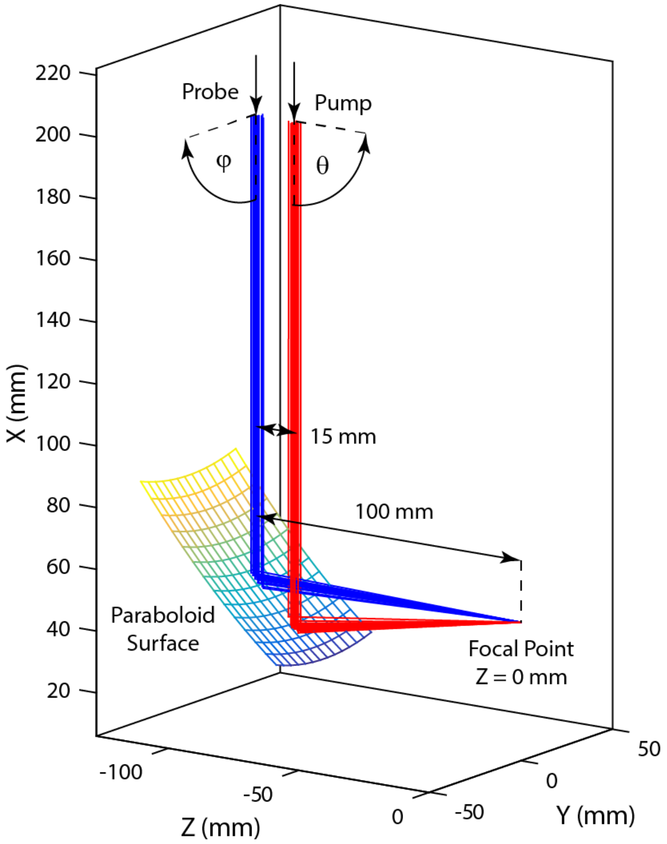

Figure 32. Definitions of distances and angles for the parabola used in the ray-tracing simulation.

The 90° off-axis parabola used in the 2DIR setup has an effective focal length of 101.6 mm. As shown in Figure 32, the probe beam typically enters parallel to the optical axis and is therefore deflected by 90°. The pump beam is typically offset by 15 mm, and therefore has a steeper deflection angle. It is well known that if the input beam is not parallel to the optical axis, the off-axis parabola generates an astigmatic focus. Table 1 qualitatively summarizes what the pump beam focus looks like for different misalignments. To summarize, horizontal misalignments generate horizontal or vertical astigmatic features, while vertical misalignments generate astigmatic features rotated by approximately 45°. Both increase the size of the circle of least confusion at the focus with larger beam deviation.

Table 1. Qualitative summary of the pump beam focus for different misalignments into the parabola. Angles are defined in Figure 32.

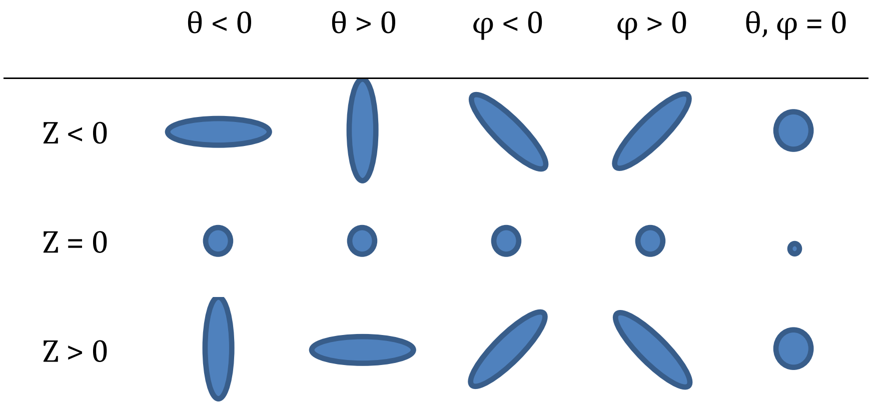

A more quantitative understanding of the effect of misalignment on the parabola focus is possible by propagating a Gaussian spatial distribution of rays through the parabola. Around the focus, the generated astigmatism can be characterized by standard deviation of maximum spread at the two astigmatic focal points and at the circle of least confusion (medial focus). Figure 33 show the effects of horizontal and vertical misalignment on the astigmatism. The Z-axis deviations of the astigmatic focal points and circle of least confusion is shown in Figure 34. Also, for vertical misalignment, the rotational deviation from 45° is shown in Figure 35. Note that this simulation is performed for rays, as opposed to a wavefront. Therefore, the results may significantly underestimate the true beam size, especially close to the focus. In practice, our ideal beam focal size (reported as standard deviation for comparison purposes, $\sigma = 0.36w$) is 31 μm ($w = 86$ μm) for the probe, with an input diameter of 1.7 mm ($w = 4.7$ mm) for 6 μm light. In principle, it is possible to estimate the amount of misalignment by measuring the locations of the astigmatic focal points.

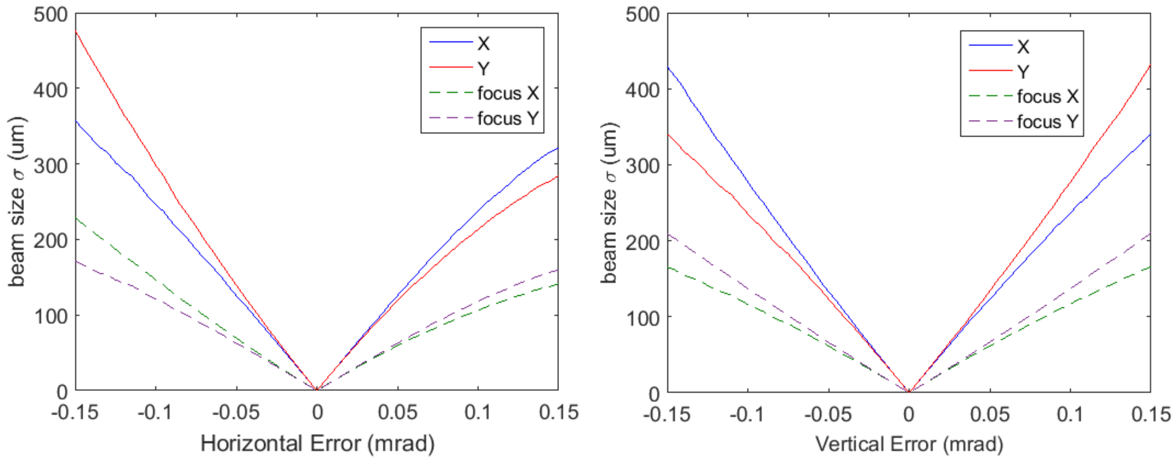

Figure 33. Characterization of the astigmatism generated with (a) horizontal and (b) vertical misalignment of the pump beam into the parabola. The X and Y lines give the beam size in the corresponding astigmatic plane. The focus X and focus Y give the X and Y beam sizes for the circle of least confusion. Note that with vertical misalignment, the astigmatism is rotated by approximately 45º.

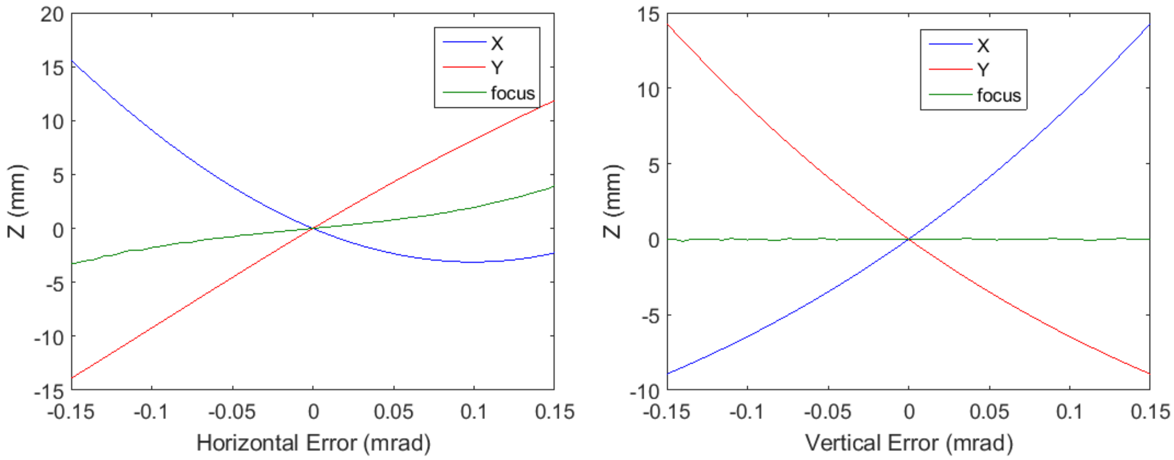

Figure 34. The Z-positions for the X and Y astigmatic planes and circle of least confusion for (a) horizontal misalignment and (b) vertical misalignment.

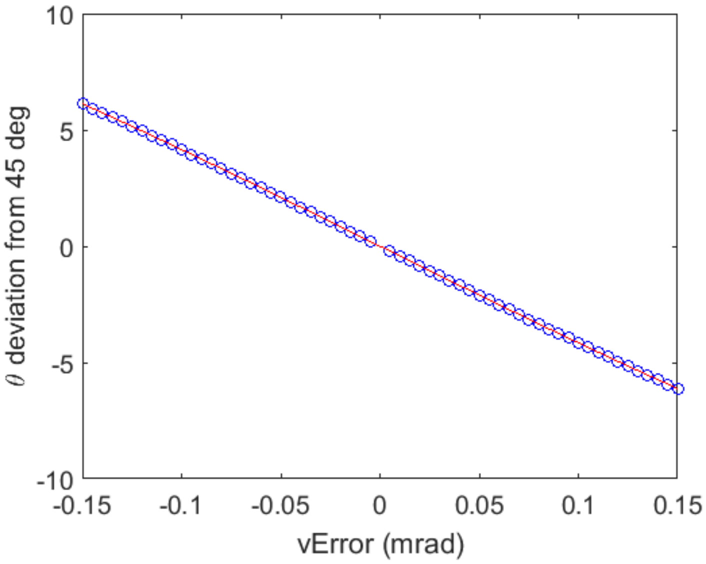

Figure 35. Rotational deviation of the astigmatism generated for vertical misalignment.

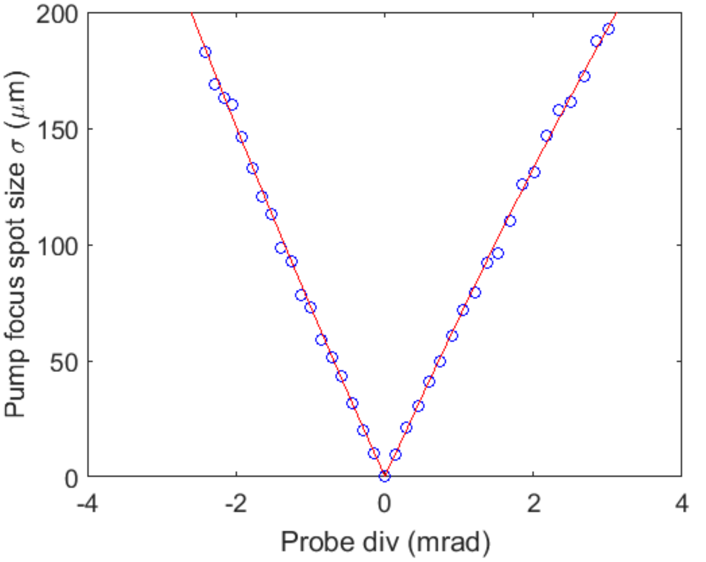

Figure 36. The pump focus spot size for a given probe divergence as found by the pump-probe overlap procedure described in the main text.

A large amount misalignment error can be considered as a full knob turn on a typical 1” 100 TPI actuated mirror mount (such as Newport Ultima U100). This corresponds to a beam deviation of approximately 13 mrad or 0.76^{o}. As a comparison, the sensitivity (0.5x beam deviation angle) of such mirror mounts is on the order of a few arcseconds (3.8 arcseconds for the U100). Based on our results, pump beam misalignments of 30 to 40 mrad or 1.7° to 2.3° would be required to achieve an approximately 1:2.7 aspect ratio for an astigmatic focus. Therefore, pump misalignment into the parabola is unlikely to be the sole source of 1:2.7 aspect ratio of the pump focus.

It is possible that a combination of poor probe beam collimation and the resulting pump-probe overlap can induce a large pump misalignment in to the parabola. This would be caused by the procedure used to find the pump-probe overlap. Briefly, the optimal probe focus is found by maximizing the probe throughput through a 100 µm diameter pinhole. The pump angle into the parabola is then adjusted, using a mirror mount 200 mm away) to maximize its throughput through the pinhole. If the probe is poorly collimated, it will focus away from the parabola's focal point. To recover the overlap, the pump will be slightly misaligned so that pump and probe beams cross at the probe's focal point. This procedure was repeated using the ray-tracing simulation with the results shown in Figure 36. A probe divergence of 1.4 mrad is required to recover a 1:2.7 aspect ratio, assuming a minimum pump focus of $\sigma = 35$ µm along the vertical direction.

Given the telescope design after the DFG stage of our OPA and the alignment procedure developed, the beam divergence is likely around 1 mrad. Briefly, a strongly diverging mid IR (mid IR $w_0 = 0.40$ mm, λ = 5 µm) is generated from focusing signal and idler which is collimated by a concave mirror pair ($R_1 = 100$ mm, $R_2 = 150$ mm) 18 inches away. The collimation procedure involves minimizing the beam size at the shaper grating, which is 3.8 m away. This procedure yields a beam which has $w = 2.4$ mm ($w_0 = 1.7$ mm), which gives a divergence of 0.94 mrad. This number is less than the divergence required to cause the measured aspect ratio. Note that the probe also has an additional telescope to increase its size by 1.5x, therefore it is possible that its divergence is quite off.

3.3.2 Misalignment of the Pulse Shaper

Another possible source for the 1:2.7 pump aspect ratio is misalignment in the pulse shaper. In this section we will consider a few common pulse shaper/pump beam alignment procedures and their effects on the parabola focus. These procedures include: (1) the use of the concave mirror distances for beam collimation, (2) adjusting the gratings for chirp compensation, (3) adjusting the 1st steering mirrors for Bragg's angle compensation, and (4) adjusting the 2nd steering mirror and 2nd grating angle to recover the pump alignment. The adjusted parameters in this section were summarized in Figure 31. Based on the analysis from the previous sections, it is expected that only the first alignment procedure, adjusting the concave mirror distances, can introduce the mentioned beam distortions.

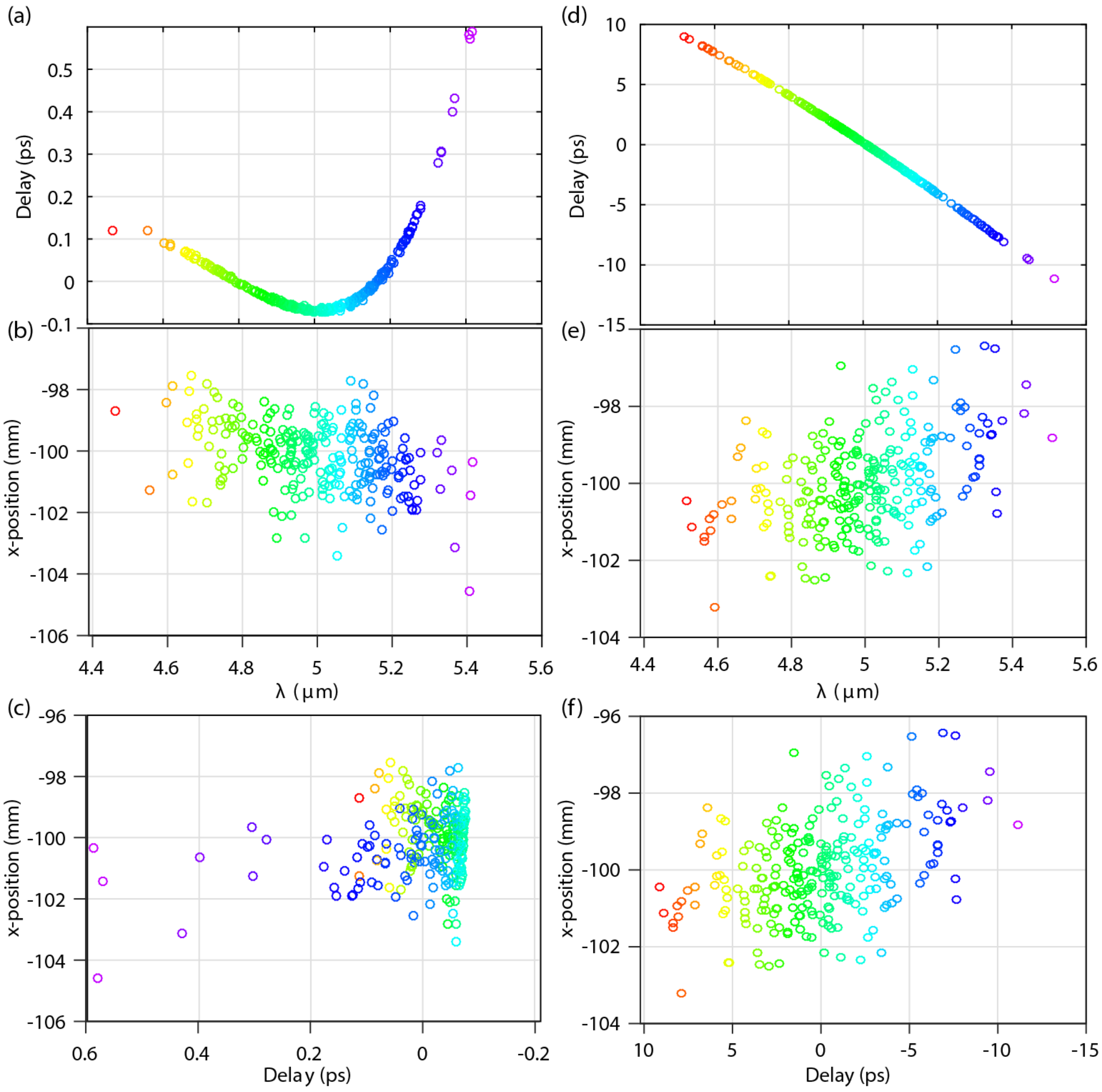

Figure 37. Chirp ray tracing results. Panels (a) through (c) are for an ideally compressed 5 μm pulse with a 200 g/mm grating. Panels (d) through (f) are for the pulse shaper output at the ideal 4f alignment. Panels (a) and (d) show the temporal chirp in the pulse. Linear components correspond to GDD, quadratic to TOD, cubic to 4th order dispersion, etc. Panels (b) and (e) show the presence of spatial chirp. Note that in (e) spatial chirp is present even though the pulse shaper is at the ideal alignment because of the introduction of angular dispersion due to Bragg's angle mismatch. Panels (c) and (f) show the projection of the pulse onto the x (mm)-z (ps) plane. Panel (c) shows a nearly compressed pulse with some trailing rays due to TOD. Note that there is a slight pulse-front tilt present. Panel (f) shows a strongly chirped pulse, which also has a pulse front tilt.

To verify the ray-tracing simulation, Figure 37 shows the chirp of the pulse propagated through the pulse shaper. When the grating distances are set to ΔG_1 = 5.9 mm, ΔG_2 = 17.7 mm), the slope of the delay vs. wavelength near 6 μm is nearly zero, which represents GDD. If the grating distances are set to the ideal 4f position (ΔG_1 = 0, ΔG_2 = 0), then there is substantial temporal chirp present along with some spatial chirp. Note that in both cases there is a significant contribution from higher order chirp.

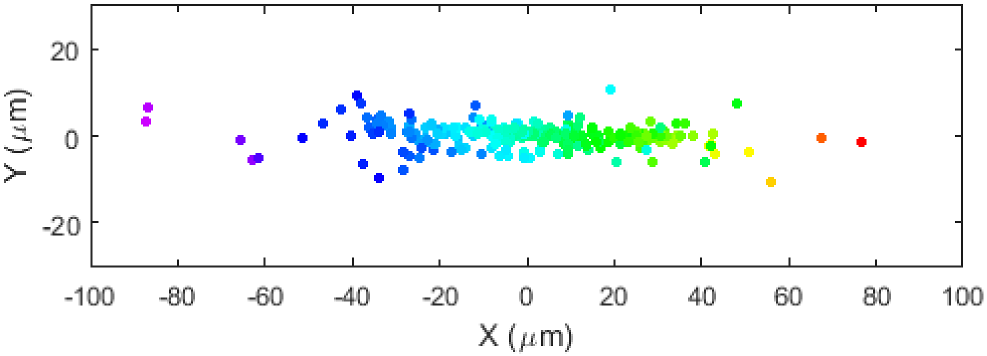

Figure 38. A typical focus generated with pulse shaper misalignment. Note that the Y-direction is focused but the X direction is dispersed. This was generated with a correctly aligned pulse shaper but with an input beam with 1 mrad divergence. This focal spot is 4.1 mm past the true parabola focus.

The first alignment procedure involves collimating the pump via the two concave mirror distances. In practice this is a very inaccurate procedure because of the limited space in our setup and the difficulty in directly collimating a low-powered mid IR beam. Instead, we usually rely on the initial HeNe alignment of the 4f pulse shaper for the correct concave mirror distances. Therefore, it is possible that the concave mirror distances may be off by several millimeters. Figure 38 shows the typical focal spot generated with a concave mirror misalignment or with correct concave mirror alignment but with a diverging input beam. Notice that the focal spot is chromatically dispersed horizontally. In the following figures, the focus spot size is measured as the standard deviation of the horizontal width at the tightest vertical focus as a function of different pulse shaper alignment parameters.

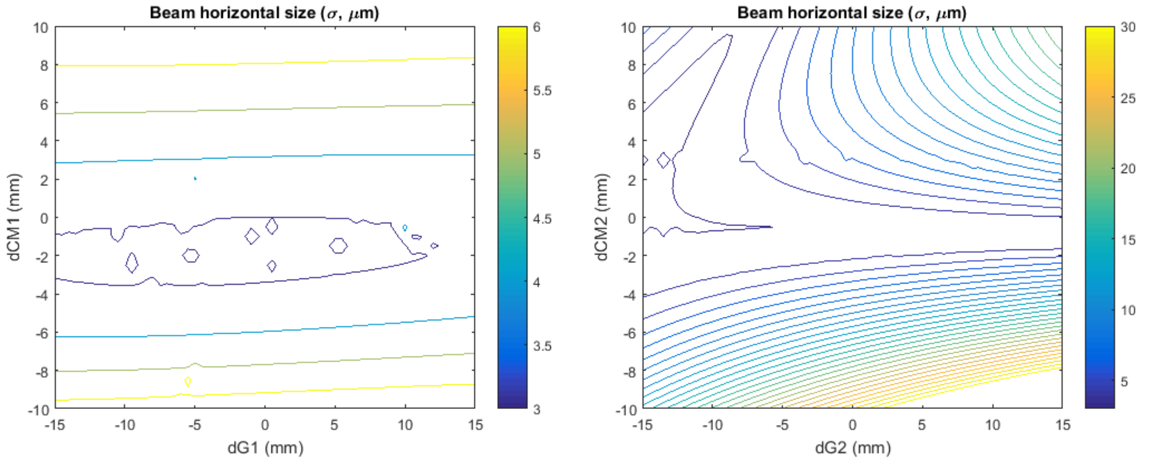

Figure 39. The horizontal beam size at tightest vertical focus when moving (a) the first grating and first concave mirror and (b) the second grating and second concave mirror. The noise is caused by numerical error because the ray-tracing method is not robust against division by very small numbers. Zero represents the compressed alignment in Figure 37.

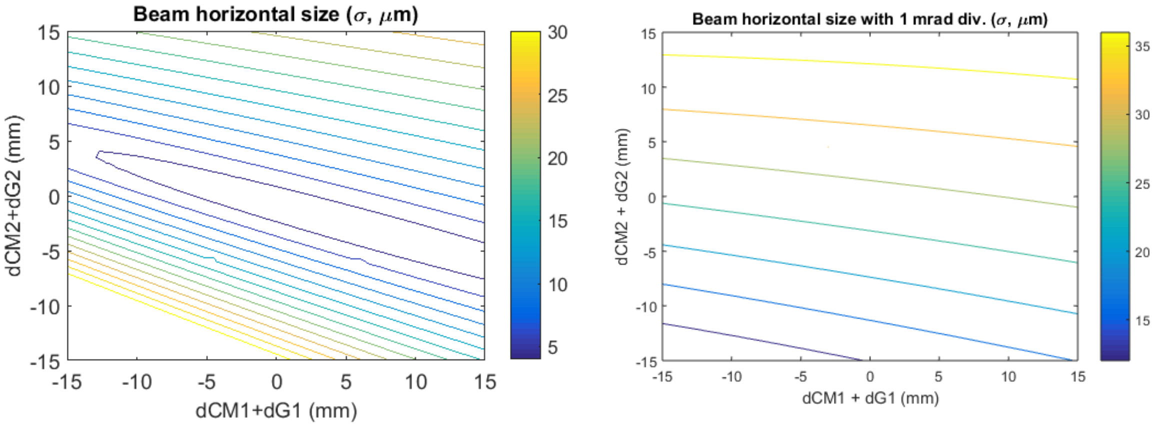

Figure 40. The horizontal beam size at tightest vertical focus when moving (a) the first grating and first concave mirror together vs. the second grating and second concave mirror together. Panel (b) is the same as (a) except the input beam has a 1 mrad divergence. Zero represents the compressed alignment used in Figure 37.

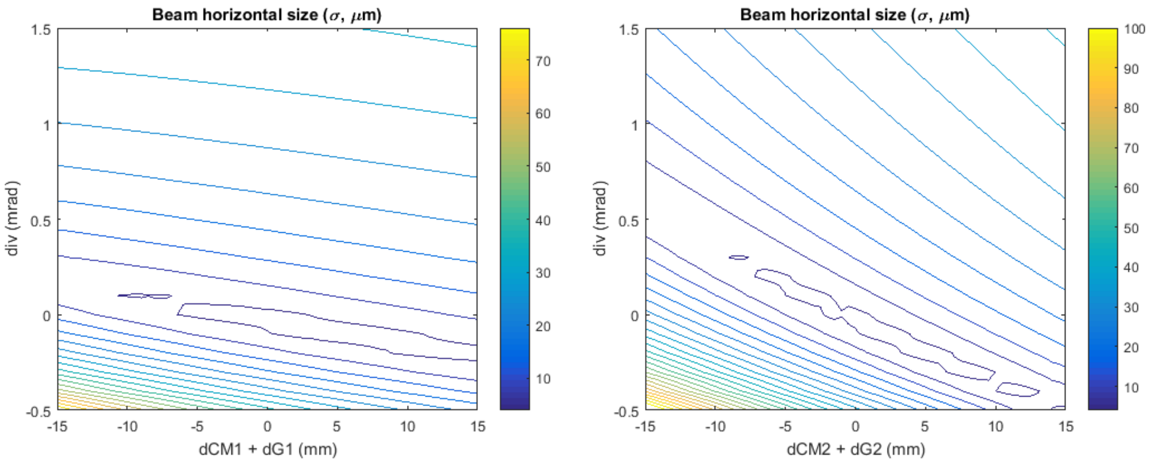

Figure 41. The horizontal beam size at tightest vertical focus when changing the input beam divergence and (a) moving the first grating and concave mirror together and (b) moving the second grating and concave mirror together. Zero represents the compressed alignment used in Figure 37.

Figure 39(a) shows the effect of moving the first grating and first concave mirrors. Moving the grating, as expected, has a minimal effect on the focal spot size. Moving the concave mirror, on the other hand, leads to a larger horizontal beam size. Figure 39(b), where the second grating and concave mirror are moved together, shows a similar result. Figure 40(a) shows the beam size when the concave mirror and corresponding grating is moved together (ΔCM_1 and ΔG_1 have the same value and ΔCM_2 and ΔG_2 have the same value) so that the chirp compensation remains constant. This figure shows that increasing the distance of one optic pair while decreasing the distance of the other optic pair can partially compensate for the other.

So far, we have only considered the effects of misalignments on a collimated input beam. If the input beam has a significant divergence, the effects of misalignment are slightly different. Typically, any divergence would be compensated by moving the concave mirrors and second gratings together to keep the pulse compressed. The results are shown in

Figure 41. In both cases, a converging beam causes a significant chromatic dispersion at the focus, which cannot be easily compensated by the concave mirrors. Figure 41(b) shows that the second concave mirror is more capable of compensating for poor collimation. A diverging beam causes a less severe focus distortion but can still cause a poor focus if not corrected for by the concave mirrors. Given the input mid-IR collimation described in the previous section, it is likely that this effect is a contributor toward the observed aspect ratio. As an example, Figure 40(b) shows the concave mirror's ability to compensate a 1 mrad divergence. The concave mirrors are unable to compensate this divergence and the horizontal beam size remains quite large at the focus.

The generation of the chromatic dispersion at the focus can be thought of as a mismatch between the angular dispersion and beam divergence, as is shown in Figure 42. This results in two focal planes after any focusing optic such as a lens: the beam divergence plane and the angular dispersion plane (note that for a parabola only one focal point is defined). A tight focus can only be generated when these two focal planes overlap. This has profound consequences for the alignment of the shaper—even though the angular chirp introduced may be small, if it is not matched to the output beam divergence then the output beam will focus poorly. Because the pulse shaper does not introduce significant angular chirp, the concave mirrors mostly compensate for beam divergence. Finally, the beam divergence, spatial chirp, and angular chirp are all coupled in the sense that they all effect the apparent divergence, linear dispersion, and angular dispersion of the beam after the pulse shaper. Therefore, if this work is published, the terms used qualitatively in this analysis will require more precise definitions, likely in terms of the ray-pulse matrix analysis used in earlier sections.

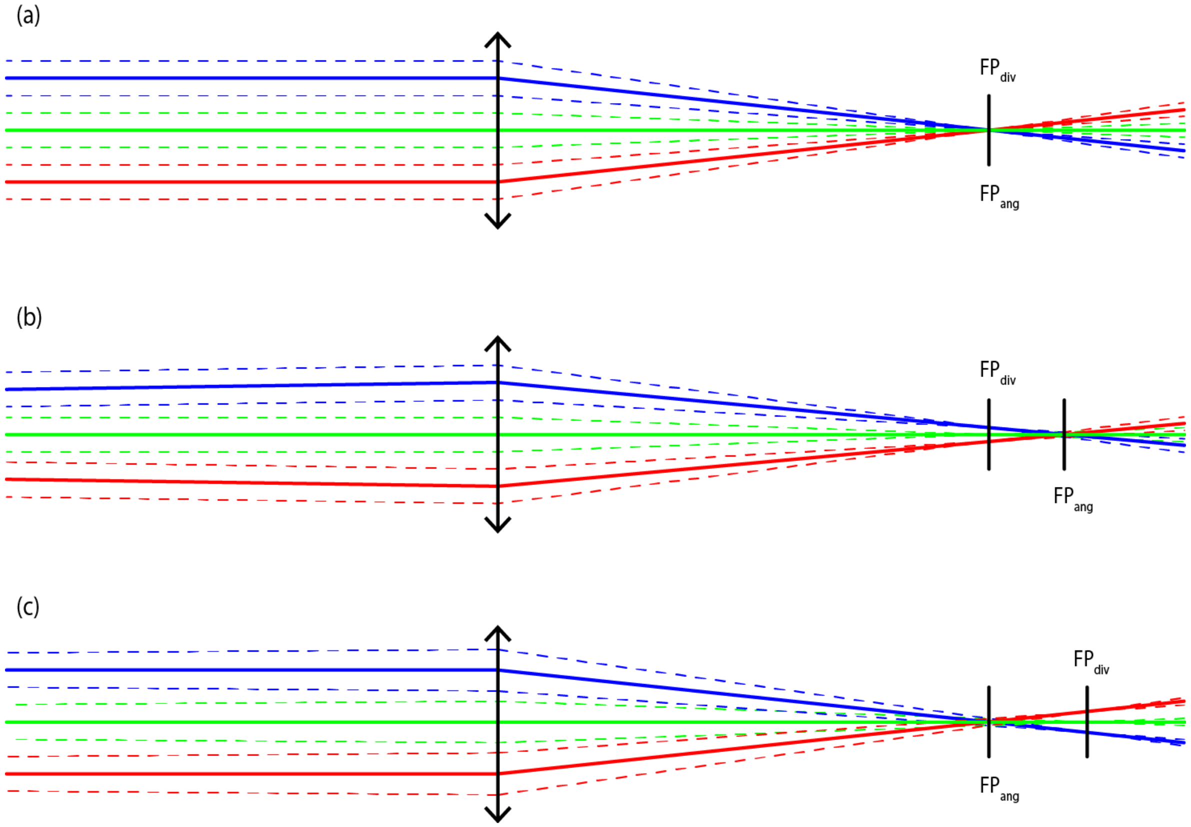

Figure 42. A ray diagram representation of the angular dispersion focal plane (FP$_{ang}$) and beam divergence focal plane (FP$_{div}$) for a linearly dispersed (caused by spatial chirp) beam. Panel (a) shows the ideal condition, when the beam divergence and angular dispersion are both zero. In this case, both focal planes coincide. This case occurs anytime the beam divergence and angular dispersion are matched. Panel (b) shows when the beam divergence is zero but the angular dispersion non-zero. In this case, FP$_{div}$ is at the ideal focus and FP$_{div}$ is after the ideal focus. This can lead to the observed focal spot. Panel (c) shows when the angular dispersion is zero but the divergence is positive. In this case, FP$_{ang}$ is at the ideal focus and FP$_{div}$ is after the ideal focus. This case represents the result in Figure 38.

The next three procedures do not introduce as a significant focus spot distortion. Figure 43 shows the effect of changing the 2nd grating distance and compensating the offset with the first, so that the output pulse remains mostly compressed. Over a 40 mm range, the focal spot size is relatively insensitive (Gaussian beam waist would be minimum σ = 30 μm). Therefore, at least from the perspective of focal spot size, it is safe to use any of the two gratings for chirp compensation. This further implies that the procedure for the passive correction of Bragg's angle mismatch is okay (see section 3.2.2). Similarly, errors in Bragg's angle determination, as measured by misalignment of the first steering mirror and recovery with the second steering mirror, do not introduce a significant increase in focal spot size (Figure 44(a)). The last common alignment procedure is to make the HeNe tracer and pump beam colinear. The two degrees of freedom we use are the 2nd steering mirror and 2nd grating angles to control for horizontal position and horizontal direction. As shown in Figure 44(b), this procedure is safe in terms of focus spot size, although it can introduce a slight pump frequency error for double pulse generation.

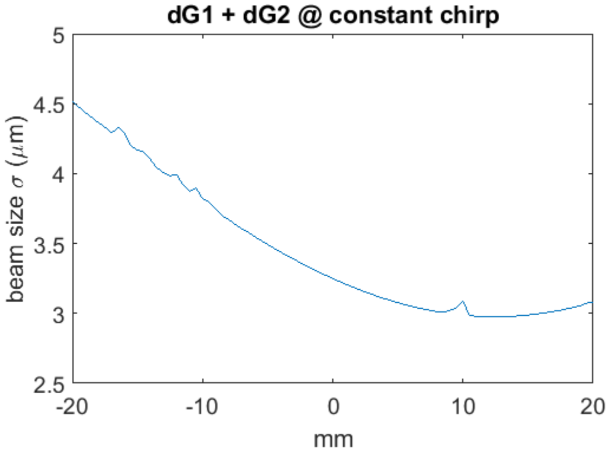

Figure 43. The horizontal beam size at tightest vertical focus when moving the second grating and recovering the displacement by the first grating to keep the chirp compensation constant. The noise is caused by numerical error because the ray-tracing method is not robust against division by very small numbers. Zero represents compressed the alignment used in Figure 37.

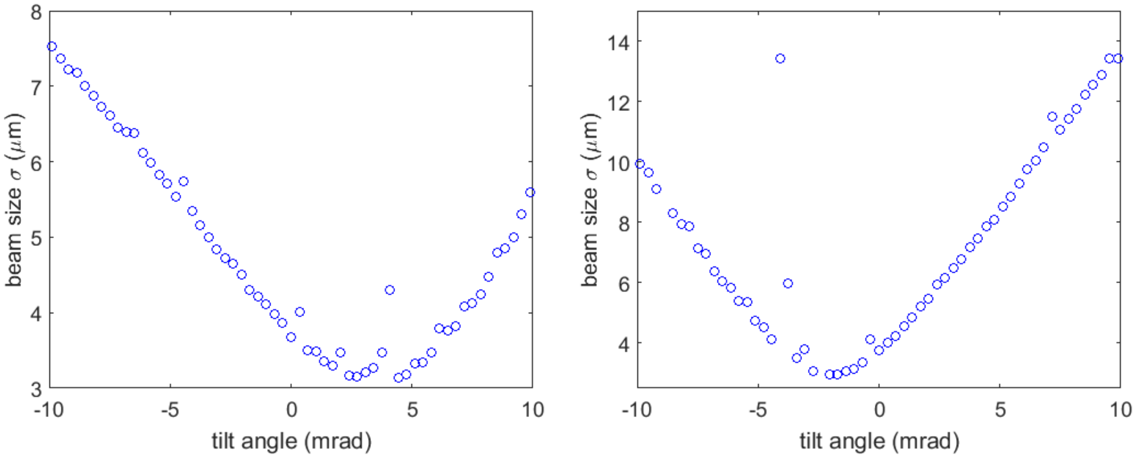

Figure 44. The horizontal beam size at tightest vertical focus when: (a) tilting the first steering mirror and recovering with the second steering mirror; (b) tilting the second steering mirror and recovering with the second grating angle. The noise is caused by numerical error because the ray-tracing method is not robust against division by very small numbers. Zero represents the compressed alignment used in Figure 37.

To conclude, there are only two reasonable sources of misalignment that can cause the 1:2.7 aspect ratio for the pump focus. Both sources come from incorrect beam collimation into the 2DIR setup. The first source is caused by the procedure used to find pump-probe overlap: because the probe focus is not at the true parabola focus, the pump beam is horizontally misaligned into the parabola. This induces a severe astigmatism into the pump focus. The second source comes from incorrect collimation into the pulse shaper, which causes a mismatch between angular chirp and beam divergence. This in turn leads to a chromatically dispersed pump focus. Individually, both misalignments need to be quite severe to cause the measured pump focus aspect ratio. Therefore, the observed pump focus is likely a combination of both misalignments.

3.4 Conclusions

To conclude this chapter, I will summarize the key insights from this chapter and list possible future directions. The key insights are:

1. Frequency-dependent delays (i.e. phase modulation) are generated at the second grating. The AOM generates phase modulation by changing the Bragg's angle of the output frequency-component, which then gets mapped to a horizontal position on the second grating via the second concave mirror. Because the grating is tilted, a horizontal position induces a delay.
2. It is critical to conserve acoustic bandwidth in the AOM. Although the AOM is tolerant to a certain frequency range, deviation from this range leads to a loss of throughput and causes double-pulse falloff. This is the limit for the pump frequency resolution in the 2D experiment. Acoustic bandwidth use can be minimized by maximizing the linear dispersion at the AOM.
3. The AOM introduces a large amount of chirp through the acoustic medium's GDD, the Bragg's angle, and Bragg's angle mismatch. Most of this chirp can be compensated passively by using the 4f geometry as a pulse compressor.
4. Bragg's angle mismatch and its resulting angular dispersion can be compensated passively by moving the first grating by $1/2\Delta_{\mathrm{Angular}}$. The resulting angular dispersion has no effect on the output pulse's angular dispersion when correctly compensated for. For broadband pulses, I recommend this method over active matching[73] in order to conserve acoustic bandwidth.
5. Temporal chirp can be compensated either by only the first, only the second, or both gratings simultaneously without the introduction of other 1st order distortions into

the output pulse. It is the total grating offset that is important. This suggests that the passive Bragg's angle matching method in the previous method is safe.

6. Spatial chirp and temporal chirp are inherently coupled in the 4f geometry pulse shaper because of the first insight. The output pump beam will always have spatial chirp, although it can be reduced by choosing a shorter focal length for the 4f geometry.
7. Angular chirp introduced by the 4f geometry is small.
8. For the parabola: the probe beam must be carefully collimated, otherwise the pump beam may have an astigmatic focus when overlapped with the probe.
9. For the pulse shaper: the pump beam must be carefully collimated, otherwise there will be a mismatch between angular dispersion and beam divergence after the pulse shaper. This will cause a horizontal chromatic dispersion at the focus, which will cause the focus to be elliptical.

Finally, the question remains: what's next? There are two directions that lead to publications. First, characterization of double pulse falloff could be useful in cases where high pump-frequency resolution is important. This would require a better understanding of the acoustic-frequency acoustic power-dependence of the AOM throughput. In addition, the power dependence is non-linear, which generates several higher harmonics in the double pulse. These are largely eliminated by using the AOM in the linear power regime (at the cost of the throughput), through phase cycling, and Fourier filtering. It would be interesting to be able to pre-compensate the acoustic waveform to correct for these effects, which may allow the AOM to be used in its nonlinear regime. This may allow for a pulse shaper throughput up to 50 %. Typical throughputs used in experiment are on the order of 30-40 % or less. A stronger pump will be beneficial for a stronger signal.

The second direction involves completing the characterization of the pump focus. Ideally, the ray-pulse method used in section 3.2 would be expanded to include the pump focus. A linear mathematical formulism would generate simple equations that could aid in alignment and could generate additional insights. It would also be interesting to extend this to Gaussian beam optics. More careful beam profile measurements as a function of shaper alignment parameters are needed to confirm the theory and simulation used in the previous sections. This is motivated by the fact that having a tight pump focus is critical toward maximizing the signal.

4. The Ultrafast Vibrational Dynamics of the Tyrosine Ring Mode

4.1 Introduction

Vibrational labels are a ubiquitous tool for studying the local environments of many different systems, spanning from biosystems such as proteins and peptides[10-12,74] to energy-related systems such as ionic liquids[75-80]. In 1D IR, vibrational labels are often used to measure local electric fields via the vibrational stark effect.[12,81,82] In 2D IR, this idea is extended to measure local electric field fluctuations on picosecond timescales, thereby providing ultrafast dynamic information about their environments.[11] Vibrational labels have provided detailed information on peptide/protein folding events, local viscosity,[83-85] and lipid dynamics.[86-88]

For a vibrational label to be useful, it must satisfy the following criteria. First, the label should appear in a clear IR window, away from strongly absorbing solvent modes and solute modes, such as C-H stretching and the amide modes. The label must be sensitive to its local environment and would ideally have a straightforward correlation between its environment and frequency shift. For studies involving biomolecules, the label should have a sufficiently strong absorption cross-section to allow access to biologically relevant concentrations of the micromolar scale.[74,89-94] For complex biomolecules such as proteins, it should also be easy to synthetically introduce vibrational labels, which is often done so as synthetically modified amino acids.[95-101] Finally, these labels should also not significantly perturb the structure or dynamics of the protein system; that is, they should only act as probes. The last two points are satisfied by a class of vibrational labels called "natural labels." Natural labels are amino acid side chains that naturally occur in a peptide or protein that have a strong absorption cross section and appear in a clean region of the IR spectrum. One example, which we have studied previously,[102] is the tyrosine ring mode at 1515-1517 cm^{-1}.[102-104] In this chapter, we further explore the sensitivity of the tyrosine ring mode to its local environment with our recent advances in noise reduction.

To further test the sensitivity of the tyrosine ring mode on its local environment, we revisit the enkephalin system.[102,105] Briefly, enkephalins are endogenous opioid peptides whose binding to the opioid receptors is catalyzed by a lipid membrane.[106] These peptides remain largely unfolded in buffer, adopting only transient random coil conformations.[107-109] This conformational change allows for the peptide to bind to the opioid receptor, where binding-site specificity is determined by the relative positioning and orientation of the tyrosine and phenylalanine side-chains.[110-113] For example, a synthetic enkephalin mimic is morphine, where the positioning of a phenol and phenyl ring is locked.[114,115] Marcotte et al. have shown that the conformational distribution and insertion of the peptide can be modulated by doping the bilayers' surface with different headgroups (Figure 45).[110] The authors suggested that the main effect comes from the bilayer packing and surface charge, where highly packed bilayers and negatively charged headgroups cause the peptide to be less inserted.

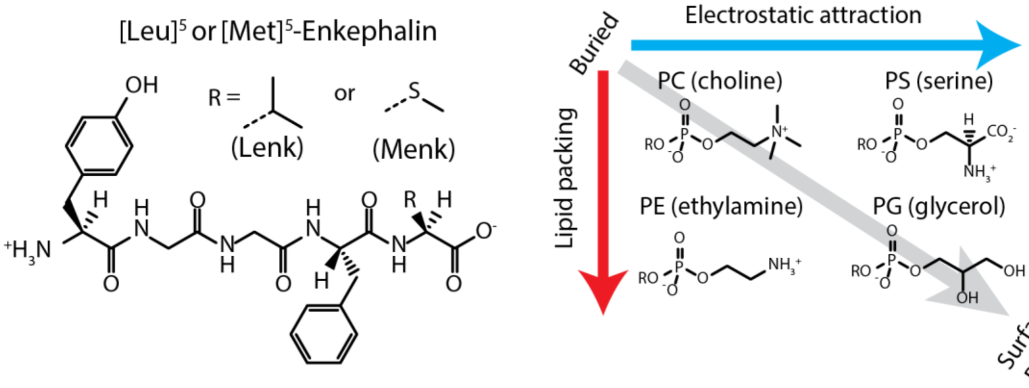

Figure 45. Graphical abstract for this chapter. On the left is the structure of enkephalin. On the right is the expected behavior of the peptides in different bicelle conditions with different headgroup doping.

In this work, we show that the tyrosine ring mode reports on its local environment even when the bilayer surface is doped with only 10% of a different headgroup. More significantly, we found that this sensitivity is hidden under complex relaxation dynamics that cause a significant distortion in the 2D line-shape. We propose that the ring mode undergoes efficient energy relaxation to a nearby dark-state and suggest three models to explain the spectra, two of which can explain the line-shape distortion. We conclude with showing what effects these three models have on extracting the frequency-frequency correlation function, which is the dynamic parameter of interest.

4.2 Results

To gain insight into the sensitivity of the tyrosine ring mode to its local environment, we performed FTIR and 2D IR measurements on Leu-enkephalin (Lenk) and Met-enkephalin (Menk) in a pD 7 D_2O phosphate buffer and a variety of membrane conditions. The membrane conditions were prepared by doping 3:1 DMPC/DHPC bicelles (1,2-dimyristoyl-*sn*-glycero-3-phosphocholine/1,2-dihexanoyl-*sn*-glycero-3-phosphocholine) with 10% of PC (phosphatidylcholine, no doping), PG (phosphatidylglycerol), PE (phosphatidylethanolamine), and PS (phosphatidylserine) headgroups (Figure 45). The doping was performed by replacing the DMPC with DMPG, DMPE or DMPS before preparing the bicelles. See SI for more detail.

4.2.1 FTIR:

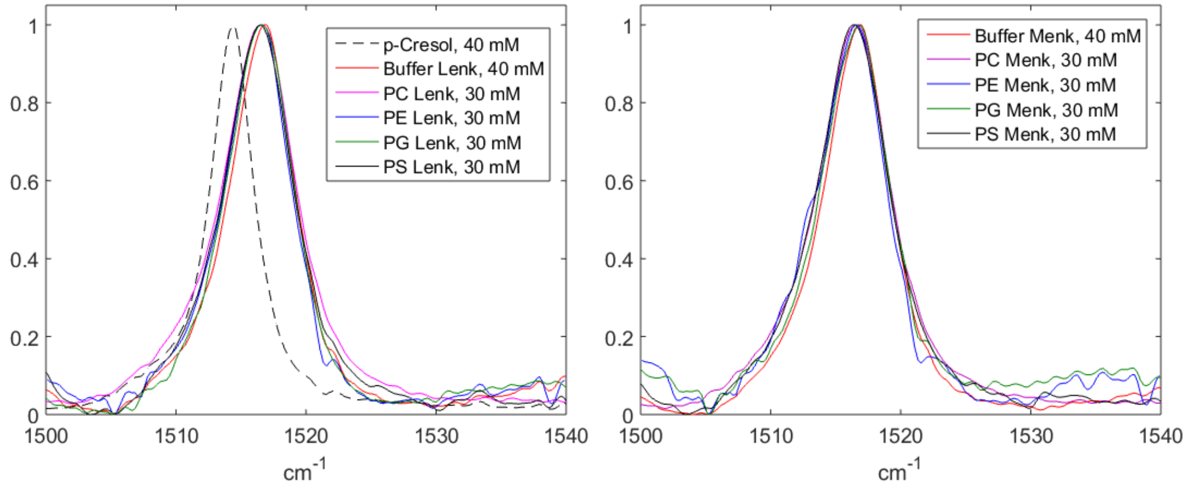

Figure 46. FTIR data comparing (a) Lenk, on the left, and (b) Menk, on the right, in different bicelle conditions.

We first performed FTIR measurements for both Lenk and Menk in the various membrane conditions and in pD 7 phosphate buffer, and for p-cresol in pD 7 phosphate buffer (Figure 46) For p-cresol in pD 11 phosphate buffer and DMSO see Chapter 5. p-Cresol exhibits an approximately 2 cm^{-1} redshift compared to the peptides. The ring mode in the peptides does not show a significant solvatochromatic shift, which is consistent with other work on this ring mode.[102-104] The most prominent feature is an asymmetric line shape, with a longer tail on the red-side of the spectrum. This asymmetry is present in all spectra acquired of the ring mode and has been observed in other aromatic vibrational probes.[116] We believe that this asymmetry is most likely caused by vibrational hot-bands: thermally-populated low frequency modes that are anharmonically coupled to the observed ring mode.

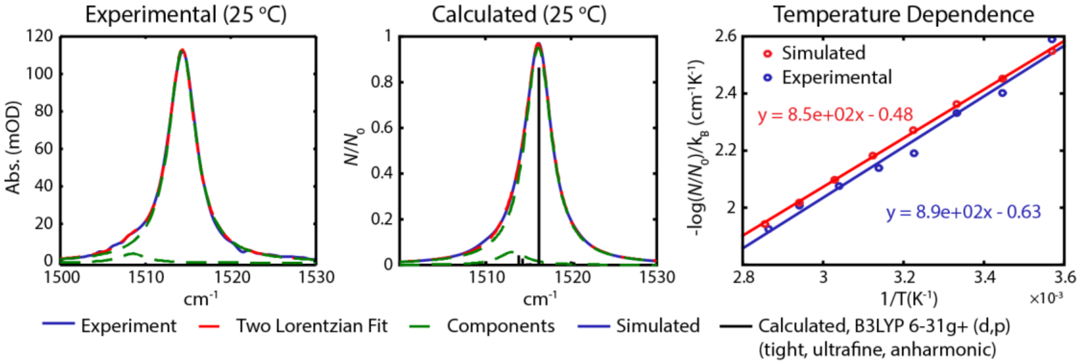

Figure 47. Temperature-dependent FTIR results of p-cresol. (a) Experimental, left. (b) Calculated, middle. (c) Temperature-dependent plot comparing the experimental and calculated results, right.

To test this hypothesis, we performed temperature dependent FTIR on p-cresol in pure D_2O and anharmonic DFT calculations (B3LYP 6-31g+ (d,p)) for p-cresol-OD in vacuo using Gaussian 03.[117] The results are shown in Figure 47. Temperature dependent FTIR spectra were acquired in approximately 10° increments from 7 to 76 °C. After subtracting the temperature-dependent solvent background, we fit the asymmetric lineshape to the sum of two Lorentzians of equal width, as shown in Figure 47(a). The amplitudes of these two Lorentzians represents the relative populations of “cold” and red-shifted “hot” p-cresol molecules. As shown in Figure 47(c), we fit the relative population of the hot-band to the Boltzmann factor, $I_{Hot}/I_{Total} = e^{-\omega/k_B T}$, as a function of inverse temperature $-k_B \log(I_{Hot}/I_{Total}) = \omega/T$. The fit suggests that the coupled low frequency mode is at approximately 880 cm^{-1}.

We found that linear fit also had a large intercept, which is unphysical according to our model. This intercept suggests that there may be contributions from multiple low-frequency modes. We found a similar slope and intercept when repeating the same fitting procedure with temperature-dependent spectra simulated from the anharmonic DFT calculations (Figure 47(b)). The anharmonic shifts from the DFT calculations suggest that at least three coupled ring modes significantly contribute to the shoulder in the FTIR spectrum.

4.2.2 2D IR:

We performed pump-probe 2D IR measurements in order to gain more insight into the sensitivity of the tyrosine ring mode to its local environment (see SI for experimental and data processing details). The data was collected using a pump-probe geometry with the pump double-pulse delay generated with an AOM-based pulse shaper, as described in the previous chapters. The pump-probe delay was scanned to 10 ps in variable steps for the 2D IR spectra. Probe laser fluctuations were removed using our recently developed multi-channel "smart referencing" algorithm.[25] After the referencing algorithm, data was Fourier-transformed (using a discrete Fourier-transform) along the pump delay, τ, and used without any further processing or interpolation. The data shown in this work is of the <ZZZZ> polarization, although our setup collects both <YYZZ> and <ZZZZ> spectra simultaneously. We performed all 2D IR measurements immediately after taking the FTIR of the previously described samples.

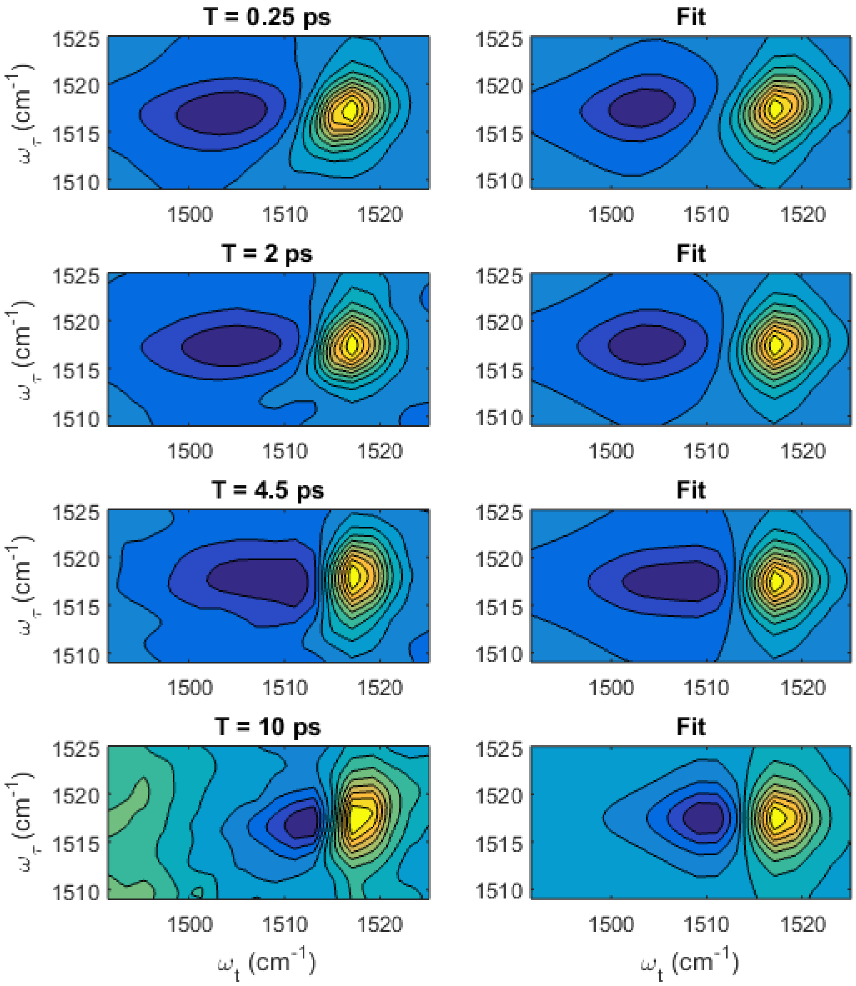

Figure 48. 2D IR spectra of Lenk in PC bicelles. (a) On the left is the experimental data. (b) On the right is the response function fit.

In Figure 48, we show 2D IR data that is representative for all measurements performed (see SI for all data). At $T < 0.5$ ps, all the 2D IR spectra resemble typical single oscillator spectra, where the peptide spectra are inhomogeneously broadened. At longer waiting time, there is a distinct blue-shift along ω_t in the frequency of the $v = 1 \rightarrow 2$ transition. This shift has been previously attributed to intramolecular energy redistribution (IVR): ultrafast energy relaxation to an anharmonically coupled dark state.[116,118-122]

The new shifted peak, which is also observable in the pump-probe spectra, represents the probe excitation from a dark state to a combination band between the dark and bright states. Therefore, the shift is the manifestation of the decay of the bright overtone transition and the growth of the combination band transition.

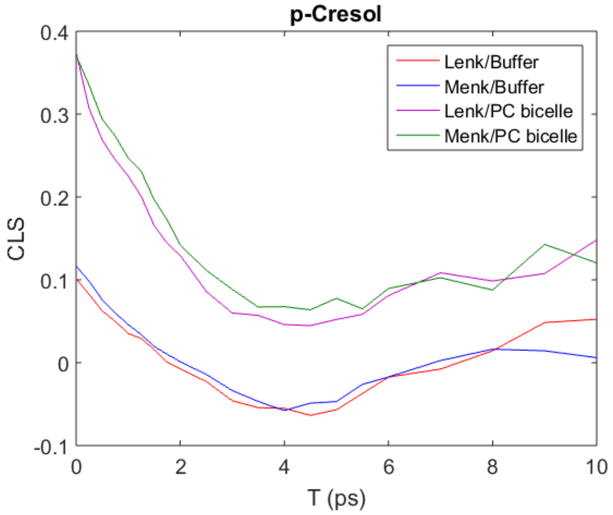

Figure 49. CLS data for Lenk and Menk in buffer and PC bicelles.

One popular procedure that is used to extract the dynamic observable of interest (the FFCF) is the center-line-slope method (CLS).[23,24] Briefly, this method takes slices of the fundamental transition along ω_t as a function of ω_τ, extracts the maximum point for each slice, and fits a line through the points. The slope ($d\omega_t/d\omega_\tau$) as a function of T has been shown to be proportional to the FFCF within certain limits.[23] The advantage of this method is that the FFCF estimation is more robust compared to a full response function fit because the number of free fitting parameters is smaller. Unfortunately, the CLS method is highly susceptible to systematic error that can be introduced by complex lineshapes or experimental noise. As an example, Figure **49** shows a representative sample of CLS plots as a function of waiting-time which all exhibit a prominent dip around 4-5 ps (see SI for all plots). Therefore, we were unable to directly use the CLS method to extract the FFCF.

4.3 Modeling the 2D IR Spectra

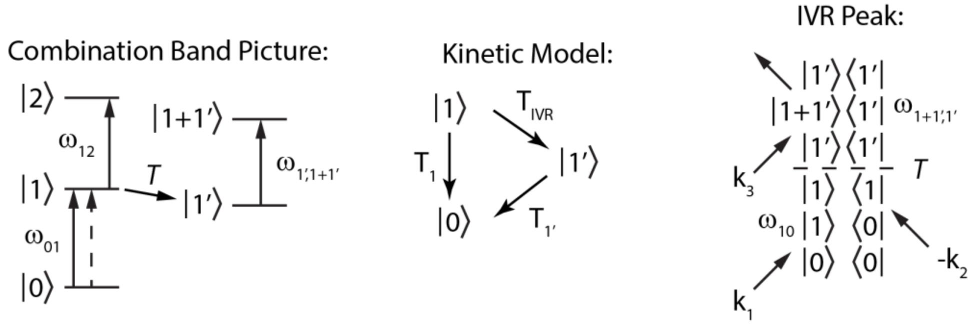

Figure 50. Summary of the IVR model. (a) The combination band picture. (b) The kinetic model describing population relaxation. (c) The Feynman diagram that corresponds to the non-rephasing IVR peak.

To gain more insight into the dynamics, we performed a global 3rd order response function fit that includes a kinetic model for IVR during the population evolution period. The full details of this fit are outlined in the SI. We summarize diagrammatically the key features in Figure 50. The model consists of a 5-level system that includes the $v = 0$, $v = 1$, and $v = 2$ tyrosine ring mode states, as shown in Figure 50(a). Irreversible energy transfer is allowed between the $v = 1$ and a dark state, $v = 1'$, which can be further excited to the combination band $v = 1 + 1'$. All population relaxation dynamics are modeled using a kinetic model shown in Figure 50(b). The model does not include reorientation dynamics because the peptide's rotational correlation function decays much more slowly compared to the vibrational lifetime of the ring mode (see SI). Spectral diffusion is included in the model using the second-order cumulant expansion and with the model FFCF:[102]

$$C(t) = \gamma_0 + \Delta\omega_{\mathrm{Inh}}{}^2 + \Delta\omega_1{}^2 e^{-\frac{t}{\tau_1}} \tag{104}$$

where $\Delta\omega_{\mathrm{Inh}}$ is the static inhomogeneity, $\Delta\omega_1$ is the magnitude of frequency fluctuations in the spectral diffusion, τ_1 is the timescale of spectra diffusion, and $\gamma_0 = 2\delta(t)/T_2^*$ is the pure dephasing contribution.

To calculate the 2D IR spectrum, we first calculate all the rephasing and non-rephasing response functions as a function of τ, t, T. The analytical form of these response functions has been tabulated elsewhere.[5] Figure 50(c) shows one of the Feynman diagrams that involve energy transfer during T. The sum of these pathways is then Fourier-transformed (using a discrete Fourier-transform) directly to the calibrated experimental ω_τ and ω_t frequencies. We use a nonlinear least-squares fitting procedure that fits the 3rd frequency-domain response functions directly to the 2D IR data (see SI for more detail).

We found that the fit reproduces the 2D IR, pump-probe spectra, and FTIR spectra quite well, but the fitted parameters are not robust due to overparameterization. If we repeat the CLS method on the simulated 2D spectra from fitting, we find that resulting waiting-time dependence cannot reproduce the prominent dip. Using this procedure, we also found that the extracted FFCF correctly reproduces the input parameters (up to a scaling factor). Therefore, the prominent dip in the CLS does not directly come from the energy transfer during the population period.

Upon closer inspection, the 2D data shows an unusual line-shape distortion that occurs at T = 4.5 ps. The apparent result of this distortion is the red-shifting of the new IVR peak along ω_τ as a function of T. This distortion appears, to various extents, in all data acquired for the tyrosine ring mode. The feature is also present in the p-cresol anion, where the ring mode is red-shifted by 14 cm^{-1} in the linear IR (see SI). Therefore, the distortion is unlikely to be caused by noise (either random or static) or instrumental error because of its repeatability.

We consider three models that may explain this line-shape distortion: (1) population exchange with hot states, (2) frequency-dependent IVR rate, and (3) fast reversible coherence transfer between the bright and dark states. The first model does not introduce this line-shape distortion but does reproduce several subtle features of the 2DIR spectra. The second model recovers the effect of the line-shape distortion but requires a static inhomogeneity that is not present in all samples. The third model also recovers the line-shape distortion but introduces additional distortions that are not immediately apparent in the data. In the following section, we discuss each model in detail and show their effects on the CLS.

4.3.1 Population exchange with hot-bands

The first model, population exchange with hot-bands, is motivated by the fact that the hot-band shoulder present in the FTIR should also be present in the 2DIR spectra. Assuming transition dipole and dephasing of the hot and cold bands to be the same, the peak intensity ratio in both the 2DIR and FTIR will be approximately the same and depend on relative populations determined by the Boltzmann factor. Therefore, we expect, from the FTIR fit, a ~5% contribution at room temperature. Furthermore, we expect that the hot population will exchange with the cold population on a 2DIR accessible timescale,[123,124] which will lead to cross peaks that will interfere with the overtone and IVR combination peaks.

We implement this model by adding the kinetic model described in Figure 51 to the response function fit in the previous section. The resulting kinetic model for the population evolution period, T, includes the irreversible IVR decay detailed in Figure 50 plus reversible exchange to corresponding hot states for all three cold populations. The forward (cold to hot) and backward (hot to cold) exchange rate ratio is determined by the steady state population ratio between the hot and cold state, which is equal to the Boltzmann factor. The forward exchange rate is left as a free parameter. Finally, we assume that the energy fluctuations in all populations generated remain fully-correlated during any population exchange.

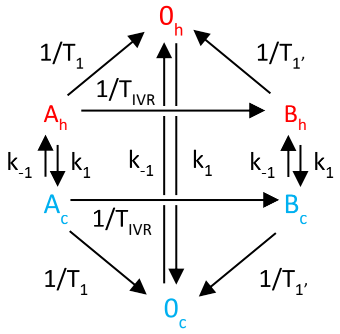

Figure 51. Kinetic scheme for the hot band exchange model. State A represents the first excited state of the tyrosine ring mode. State B represents the dark state. State 0 represents the ground state. Red states are hot and blue states are cold.

Given the assumptions made, the 2DIR spectra are straightforward to calculate, even though an analytical expression for the kinetic model cannot be derived. First, in our model the pump can be thought of as generating a non-equilibrium population of transition dipole-allowed states. The kinetic model then describes how each non-equilibrium population decays back to equilibrium as a function of T (see SI). Therefore, we implement the kinetic model as a T-dependent transfer matrix, $\boldsymbol{M}(T)$, that maps pump-generated populations to populations that the probe acts on. The pump (probe) is represented as a matrix where each row (column) represents a discretized function τ (t) that is summed over, for a given population, the half of the Feynman diagrams before (after) T-evolution. Finally, because we assume all oscillators have fully correlated FFCFs, we multiply the response function by the exponential of the line shape function. The full computational detail of this method is given in the SI.

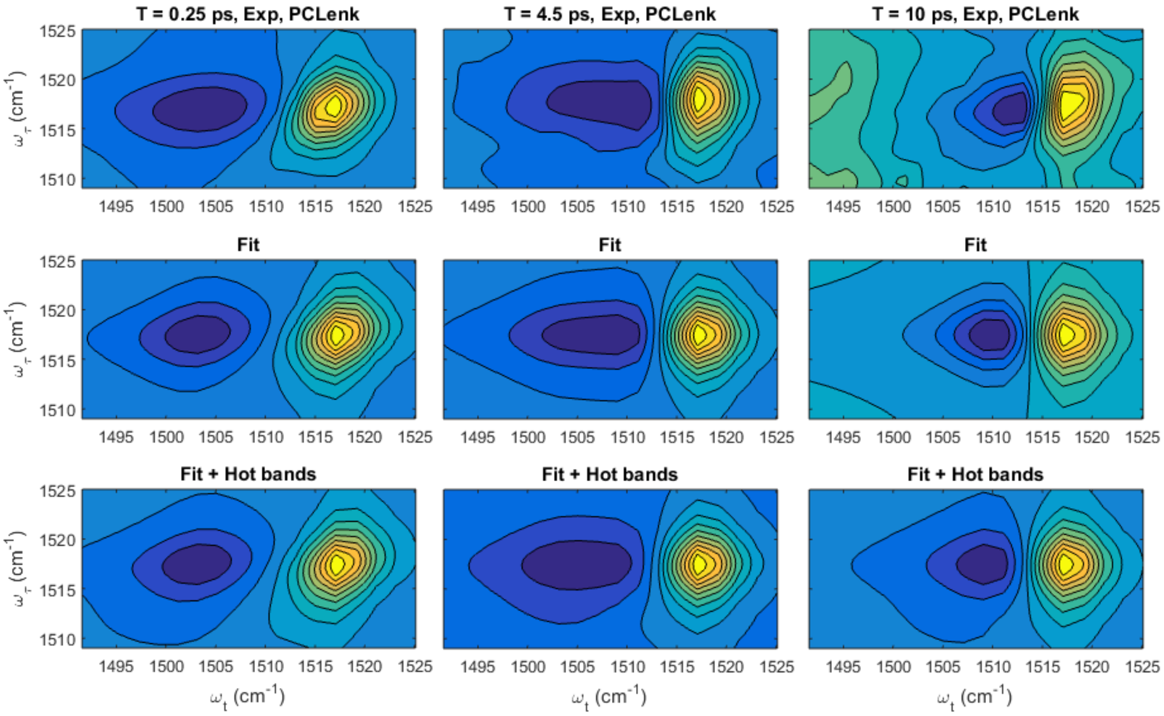

Figure 52. Comparison of the hot band model (3rd row), with the response function fit (2nd row) and the experimental data (1st row) for Lenk in PC bicelles.

The hot band population exchange model generates several new subtle features in the simulated 2DIR spectrum (Figure 52). First, the fundamental transition now exhibits a red-side shoulder which is due to the hot band peak. Second, this tail persists at long T, slightly altering the peak shape. Finally, due to population exchange and the cancelation with the IVR peak, the fundamental and overtone peaks have a slight additional broadening along ω_τ. We note that this model cannot reproduce the line-shape distortion because the hot-band populations are too small.

4.3.2 Local environment-dependent IVR model

The local environment-dependent IVR model involves the reconstruction of the line-shape distortion by the interference of two or more populations with different IVR rates. In this model, the relaxation dynamics depend on the local environment. The populations may have different relaxation dynamics with little frequency shift because of the ring mode's weak vibrational solvatochromism. For example, p-cresol in DMSO and D_2O have only a 2 cm^{-1} shift but significantly different relaxation rates. p-Cresol in DMSO shows a 1.6x faster relaxation rate compared to p-cresol in D_2O/pD 7 buffer, which is evidenced by the greater line-width and the faster pump-probe dynamics (see SI). Furthermore, the response function fit suggests that, in DMSO, energy transfer to the dark state is a significant contributor to relaxation, which is evident in the 2D IR spectra by the rapid growth of the IVR peak. Therefore, we believe that such a model is possible, and we provide further comment on possible physical origins in the discussion.

We construct this model by approximating local environment inhomogeneity with two populations with their $v = 0 \rightarrow 1$ frequency separated by 2.5 cm^{-1}. The framework for this model is the same as the population exchange response-function model, but with two key differences: first, the ratio of the two populations is assumed to be 1:1, and therefore the forward and backward exchange rates between them are the same if they undergo chemical exchange; and second, the red-shifted population has a significantly faster IVR rate. The results of the simulated 2DIR spectra are summarized in Figure 53. The line-shape distortion is well-reproduced in the case of no exchange (bottom row) between the two populations (i.e. static inhomogeneity), which is typical for peptides in bicelles.

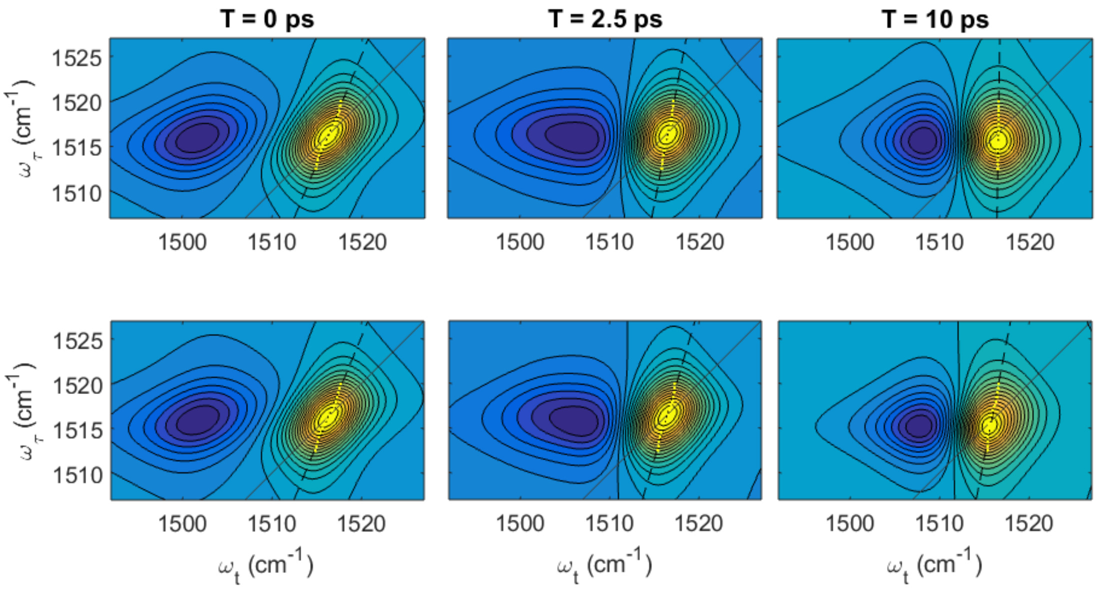

Figure 53. Simulated 2D IR spectra based on the frequency-dependent IVR model with chemical exchange (top) and without chemical exchange (bottom). Peak-slice maxima are shown as yellow dots and the CLS is shown is a dashed black line.

Including population exchange allows for this model to mimic spectra dominated by spectral diffusion without much static inhomogeneity (Figure 53, top row), including the peptide in buffer and the p-cresol anion in D_2O. The caveat is that the addition of exchange generates cross peaks that diminish the line-shape distortion. Therefore, a faster energy transfer rate is required for the lower-frequency mode to compensate for the exchange. We note that a faster energy transfer rate should, in principle, lead to faster dephasing, but we do not consider the effect of IVR on dephasing in this model.

4.3.3 Fast reversible coherence transfer between bright and dark states

So far, we have only considered the effect of energy transfer during the population evolution period. It is also possible to generate a similar line-shape distortion by including coherence transfer to the dark state. In this case, the line-shape distortion is caused by the interference of inter-state coherences generated between the bright and dark states. The advantage of such a model is that it does not require local environment inhomogeneity with very different relaxation rates.

To include coherence transfer, we propagate the density matrix directly using a phenomenological set of rate equations based on Redfield theory following a procedure described by Khali et al.,[125] but with the exclusion of rotational dynamics. The procedure consists of two main parts: (1) propagation of the density matrix via the master equation and (2) operating on the density matrix with the transition dipole operator. The density matrix is propagated in Liouville space via the master equation:

$$\dot{\rho} = (\Gamma + i\omega)\rho \tag{105}$$

where ρ is the density matrix in Liouville space, Γ is the tetradic Redfield tensor in matrix form, and ω is a diagonal matrix of transition frequencies. In the Markovian limit, the Redfield tensor is time-independent and can be thought of as a kinetic model between different diagonal elements and between different off-diagonal elements of the density matrix.[125] In this limit, the solution to the time propagator can be written directly, assuming $t \geq 0$:

$$\mathcal{G}(t) = e^{(\Gamma + i\omega)t} \tag{106}$$

The 2D IR spectrum is calculated in the time domain via step (2) by iteratively operating with the transition dipole superoperator, $\mathcal{V}_{ij,mn} = V_{jm}\delta_{kn} - V_{kn}\delta_{jm}$,[19] and time propagator $\mathcal{G}(t)$. The transition dipole operator, V, is a matrix of the magnitudes of transition dipole moments for all allowed and forbidden transitions (if the transition is forbidden, the matrix element is zero). The response function is calculated by:

$$R(t, T, \tau) \propto \langle\langle V(\mathcal{G}(t)\mathcal{V}\mathcal{G}(T)\mathcal{V}\mathcal{G}(\tau)\mathcal{V})\rho_0\rangle\rangle \tag{107}$$

where $\langle\langle \ldots \rangle\rangle$ represents the trace over the density matrix and where ρ_0 is a vector representing the equilibrium density matrix. For our model, ρ_0 has the element corresponding to the ground state population set to 1 while all other elements set to zero. The final V represents the transition dipole operator acting from the left. As written, Eq. 107 represents all possible interactions with the light field, integrated over all directions. To extract the components that contribute to the 2D IR signal, one must keep track of the phase-matching in the transition dipole operator. To do this, we partition $\mathcal{V}$ into $\mathcal{V}^+$ and $\mathcal{V}^-$, which correspond to interactions with fields of wavevector $+k$ and $-k$, respectively. The rephasing and non-rephasing response functions are then calculate separately:

$$R_R(t,T,\tau) \propto \langle\langle V^-(\mathcal{G}(t)\mathcal{V}^+\mathcal{G}(T)\mathcal{V}^+\mathcal{G}(\tau)\mathcal{V}^-)\rho_0\rangle\rangle \tag{108}$$

$$R_{NR}(t,T,\tau) \propto \langle\langle V^-(\mathcal{G}(t)\mathcal{V}^+\mathcal{G}(T)\mathcal{V}^-\mathcal{G}(\tau)\mathcal{V}^+)\rho_0\rangle\rangle \tag{109}$$

Finally, the two response functions are Fourier-transformed and added in the usual way to get the absorptive spectra. This greatly simplified form of the calculation is possible because we do not consider rotational dynamics. As a result, we do not need to keep track of any coordinate frame for the transition dipole operators so that all transitions can be considered simultaneously.

Using the diagram notation introduced by Khali et al.,[125] Figure 54(a) summarizes the key parameters used in the model. Any transition directly involving the dark state will have matrix element value of zero for the transition dipole operator. Therefore, any coherence involving the dark state directly will not be observable. This means that the coherence transfer needs to be reversible in order to be observable, otherwise it will not be distinguishable from dephasing.

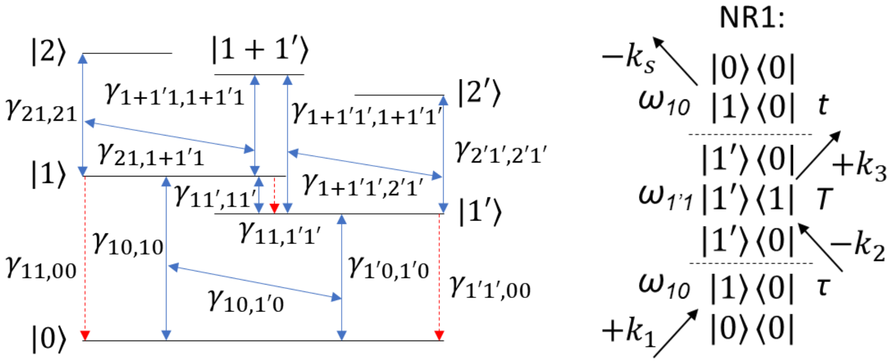

Figure 54. (Left) A level scheme diagram showing all the energy transfer processes in the simulation. Blue up and down arrows represent dephasing of a coherence. Blue diagonal arrows represent coherence transfer. Red dashed arrows represent population transfer. (Right) A Feynman diagram showing one of the possible coherence transfer pathways.

When coherence transfer to the dark state is included, several new features appear in both the 1D IR and 2D IR spectra. For the 1D IR spectra two features appear: first, the apparent transition frequency of the mode redshifts because of motional narrowing; second, a prominent dip appears at the frequency of the dark state. These two effects can be directly explained in the time-domain. At short *t*, the coherent oscillator |1><0| transfers to the dark state |1’><0|, which oscillates at a lower frequency. Therefore, when the coherence is transferred back, it is done so with a phase lag. The interference between the unlagged and phase lagged oscillators causes the line-shape distortion. Intuitively, the presence of the dark state slows down the bright oscillator (this causes the red-shift) and phase-lag leads to destructive interference between the oscillators, which causes the dip.

The 2D IR spectrum has additional features that reproduce the line-shape distortion present in experimental data (Figure 55). Careful analysis of the different possible Liouville pathways reveals that only two pathways contribute to T-dependent dynamics (Figure 55(c)). Both pathways generate an interstate coherence between the bright and dark states. These pathways are closely related to cross-peaks that lie on the diagonal which are generated in the case of two coupled oscillators by non-rephasing pathways. The frequency domain equivalent is analogous to a non-rephasing 2D Lorentzian that cycles through its phase at the frequency difference between the bright and dark. The line-shape distortion in the experimental data can be reproduced when the dephasing of the interstate coherence is long enough to include only a single oscillation.

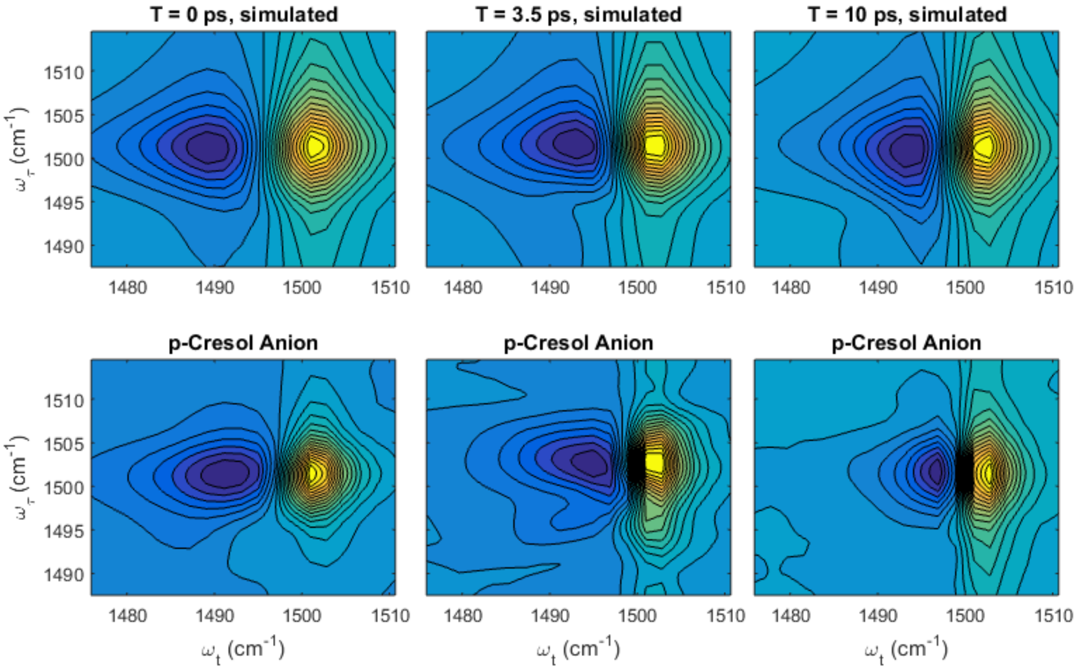

Figure 55. Simulated 2D IR spectra with the coherence transfer model (top). Experimental 2D IR spectra of the p-cresol anion in pD 11 buffer (bottom).

With this model, several new distortions that are not present in the experimental data are introduced. First, the red-side dip that is present in the 1D spectrum is also present in the 2D spectra, while our experimental data shows a shoulder. The addition of hot-bands to the model is not sufficient to recover the shoulder in this case. Second, the nodal line-slope is negative at short T, while the experimental data has a positive slope. It is possible that the addition of spectral diffusion may overcome this distortion. Given these distortions, we believe that, although coherence transfer may be present, it is not a significant contributor to the experimentally observed line-shape distortion.

4.4 Discussion

4.4.1 Many coupled ring modes

The presence of multiple hot-bands in the FTIR spectra suggest that the tyrosine side-chain potential energy surface is composed of several mechanically coupled ring modes, which is also supported by DFT calculation. This network of coupled ring modes, and their combination bands, likely provide efficient relaxation channels for vibrational energy. This is evident in the 2DIR spectra as a T-dependent anharmonicity, where the $v = 1$ vibrationally excited state population relaxes to a dark state that is likely composed of a combination of lower energy ring modes. The fact that this feature is present in both p-cresol and in Lenk and Menk in a variety of environments strongly suggest that this feature is directly related to the ring.

For the initial energy relaxation to satisfy detailed balance, the ratio of the backward and forward rates must be proportional to the Boltzmann factor. Our experimental data shows an irreversible energy transfer where the overtone peak decays fully as the IVR peak grows in. This irreversibility can either be accomplished by having a dark state energy substantially lower than the bright state, or by having a bath of many coupled dark states. In the first case, the energy difference between the bright and dark state needs to be >> $k_B T$, but the bath is unlikely to readily accept such a large amount of energy, unless it involves a discrete solvent molecular mode.[126] Therefore, the first case will likely have a slow relaxation rate.

We believe the second case is more likely because our DFT calculations indicate that there are many coupled low-frequency modes that involve the ring and their frequency separation from the ring mode is within the available solvent DOS. Figure 56 shows a possible dominant relaxation channel based on this picture. Here the IVR peak represents a vibrationally hot ring and the "dark state" is instead a thermal reservoir of many modes delocalized over the ring. It follows that the decay of the IVR peak represents the vibrational cooling of the ring. When energy is dissipated away from the coupled ring modes into states that are not coupled with the fundamental transition (i.e. the solvent or uncoupled solute modes), the IVR peak attains a zero-frequency shift. The IVR peak then destructively interferes with the bleach contribution, thereby causing the decay of the remaining peaks.

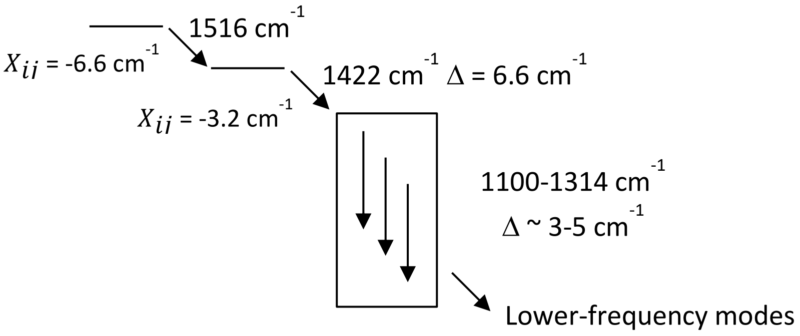

Figure 56. Figure showing the level scheme diagram for p-cresol based on the DFT calculations. X_{ij} and Δ are anharmonic couplings and anharmonic frequency shifts, respectively.

4.4.2 Physical origin of frequency-dependent IVR model

The faster growth of the IVR peak in DMSO, as compared to D_2O, clearly shows that the IVR rate can be local-environment dependent. Because the molecular vibrational state energies and their anharmonicities are unlikely to be changed significantly in weakly interacting solvents, the relaxation rate is likely to be related to the solvent's ability to accept the ring mode's vibrational energy. The solvent can accept vibrational energy either through its internal vibrations or through its low-frequency phonon-like vibrations.[126,127] For the case of internal vibrations, DMSO is more likely to facilitate energy transfer because it has more low-frequency internal vibrations as compared to D_2O.[128,129] Neat DMSO has several intermolecular modes around 300 cm^{-1} which match the energy difference between the bright mode and a set of coupled modes between 1100-1200 cm^{-1} (see DFT results in SI).

For the case of low-frequency vibrations, intuition says that p-cresol in D_2O should show a faster relaxation because of its higher DOS in the 100 cm^{-1} range.[129] These modes would facilitate the relaxation pathway to the 1400 cm^{-1} mode shown in Figure 56, but the opposite is observed (see pump-probe results in SI). One explanation is that the hydrophobic effect limits the available DOS (i.e. when solvent/solute coupling is considered) that can act as energy acceptors. The hydrophobic effect has been previously been implicated in explaining the unusual solvent dependence on bandwidth observed for the tyrosine ring mode.[103] One possible microscopic explanation for this hydrophobic effect is that water forms a more-ordered cage around the ring (i.e. the Iceberg model),[130] limiting the motions of the water molecules in the solvation shell.[131] We speculate that this limited motion can limit the forces felt by the ring, which may lower the coupling-DOS product needed for relaxation.

Indeed, MD simulations suggest that the first hydration shell around benzene has a significant ordering of the water molecules, with hydrogen bonding to the faces of benzene.[132,133] Because this hydrogen bond is relatively weak and has an entropic driving force for formation,[134] the librational and translational motions of water at the benzene faces are faster compared to those of bulk water.[135] The equatorial region of benzene, on the other hand, displays a more hydrophobic character and ab initio molecular dynamics simulations suggest slower water dynamics. [135] We believe that similar dynamics exist in our system because the pi-H-bond has also been identified in tyrosine.[136]

4.4.3 Physical origin of the coherence transfer model

The picture just described makes it difficult to rationalize the coherence transfer model because of the following features. First, coherence transfer requires a dark state that is close in energy. To be able to reproduce the dip in the CLS spectra, the interstate coherence must oscillate with a period of approximately 9 ps. Therefore, the dark state must be redshifted by approximately 3.7 cm^{-1}. Our calculations do not predict any Fermi-resonances. It is possible that the dark state is composed of a combination of three or more modes, making it possible that such a state could exist, although the corresponding higher-order couplings are probably weak. Second, the coupling between the bright and dark state needs to be strong enough to allow for fast reversible coherence transfer. Given the near-degeneracy of the proposed states, this may be possible, although one would also expect some amount of mode and transition dipole mixing. Including a small transition dipole for the dark state in the coherence transfer model does not generate a shoulder that can compensate for the red-side dip predicted by the model. Third, the coherence transfer process must be sufficiently fast to allow for a significant peak interference. In our model, the coherence transfer process is 1.3x faster than population transfer. Although the fitting by Khalil et al. suggests that coherence transfer can be much faster than population transfer,[125] subsequent work by Baiz et al. shows, from a microscopic model involving force correlation functions, that this is unlikely.[137] Finally, there is a discrepancy between the fact that coherence transfer needs to be reversible, while population transfer needs to appear irreversible. Resolving this discrepancy would require that the interferences generated by coherence transfer are distinct from the IVR peak and involve different states. Therefore, we think that the coherence transfer model is unlikely.

We note that, in the coherence transfer model, it is the generation of the interstate coherence and its interference with diagonal peaks that lead to the line-shape distortion. Coherence transfer is only a method of generating the interstate coherence. It is possible that other processes exist that can generate an interstate coherence. For example, if there are two coupled state (such as a Fermi-resonance), then the cross-peaks between the two states (at short T) would be generated by an interstate coherence and would therefore oscillate. This cross-peak can, in turn, lead to the peak distortion involved. In this case, this additional state still needs to be within approximately 4 cm^{-1} of the bright state and is still distinct from the processes involving the IVR peak (although this additional state may facilitate relaxation).

4.4.4 Model effect on CLS

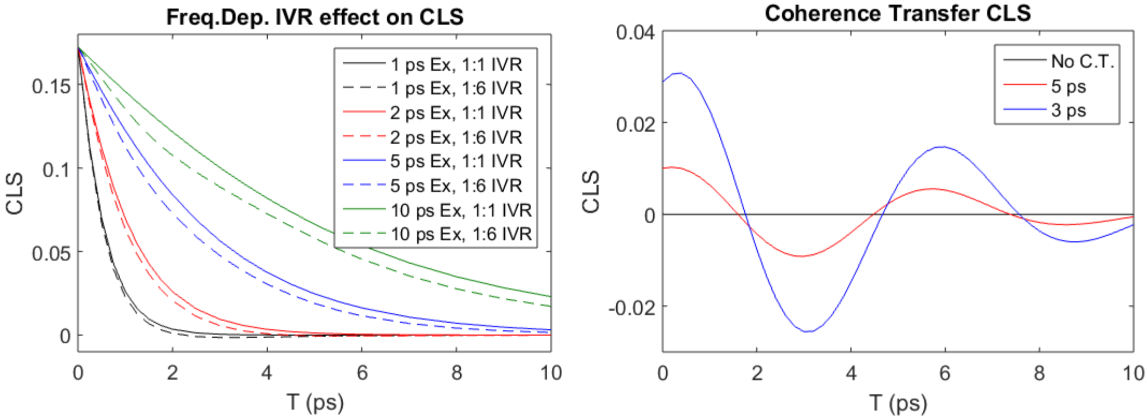

Figure 57. (a) The effect of the frequency-dependent IVR model, left; and (b) the coherence transfer model, right, on the CLS. Note that the coherence transfer model does include static inhomogeneity or spectral diffusion, which causes the no coherence transfer line to be flat.

Finally, we consider how each of these models effect the CLS. In Figure 57, we show the CLS results from each model and compare it against the same model with the process of interest turned off. The presence of hot bands (not shown) does not significantly perturb the CLS. On the other hand, in Figure 57(a), the presence of frequency-dependent IVR does significantly perturb the CLS. The line-shape distortion introduced by the frequency-dependent IVR is only present when the peak is inhomogenously broadened. If spectral diffusion is present, the line-shape distortion and its effect on the CLS is diminished at longer T. This result is intuitive considering that in spectral diffusion the oscillator's frequency becomes uncorrelated: at long T, the correlation between IVR rate and the local environment is lost. We also note that the distortion is stronger when the ratio between fast and slow energy transfers is larger.

Although a distortion is present for the frequency-dependent IVR model, it does not completely reproduce the dip feature present in the experimental data. A much stronger perturbation is introduced with the coherence transfer model Figure 57(b). The presence of an interstate coherence generates an oscillatory feature in the CLS. The oscillation's period corresponds to that of the interstate coherence. The amplitude of the oscillation is related to the amplitude of the interstate coherence, which is determined by the rate of coherence transfer. The dephasing of the oscillation is also related to the dephasing of the interstate coherence.

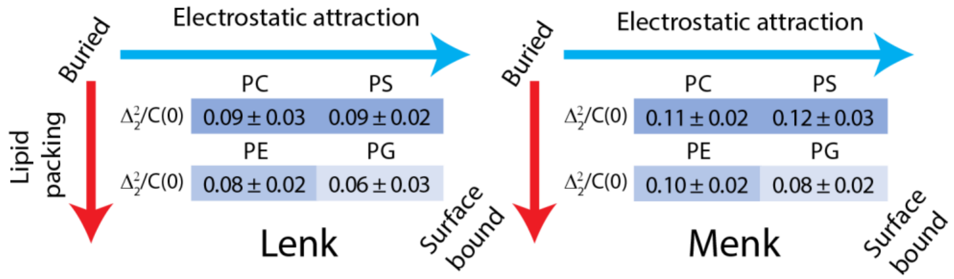

Figure 58. Graphical summary of the CLS static inhomogeneity for (a) Lenk and (b) Menk with a color scheme to show the trend. See SI for full fits and fit parameters.

Given the effects of both models on the CLS, the most reliable fitting parameter is the static inhomogeneity. To see if any trend exists in the CLS data, we fit the data to a single underdamped oscillation plus an offset:

$$C(t) \propto {\Delta_1}^2 + {\Delta_2}^2 \cdot \cos\left(\frac{2\pi t}{\tau_1}\right) \cdot e^{-\frac{t}{\tau_2}} \tag{110}$$

The results are summarized in Figure 58. The full fitting details and full set of fit parameters are given in SI. The fitting parameter for the static inhomogeneity does show a trend that is consistent with our initial hypothesis: charged and packed lipid surfaces result in less static inhomogeneity. We previously attributed a larger static inhomogeneity to a larger conformational distribution of the peptide because the peptide conformations exchange on a timescale much slower than picoseconds. Simulations by Marcotte, et al.

suggest that a surface-bound peptide will have less conformational distribution compared to a buried peptide.[111]

4.5 Conclusion

In this work we studied the ultrafast vibrational dynamics of the tyrosine ring mode at long T, up to 10 ps. Our results show that the tyrosine ring mode exhibits rich relaxation dynamics that involve fast vibrational relaxation to one or more dark states. The ring mode also exhibits some sensitivity to its local environment. Quantitative analysis was complicated by the presence of a line-shape distortion related to vibrational relaxation. We proposed and discussed two models that could explain some features of the line-shape distortion: a local-environment dependent IVR rate model and a coherence transfer model. Given these distortions, a qualitative analysis was still possible. In the enkephalin system studied in this work, the local environment sensitivity was manifest in the mode's static inhomogeneity, which we attributed to the amount of conformational heterogeneity present in different bicelles.

As the sensitivity of 2D IR is pushed to its limit, new features will be observable in the spectra. Ideally, these new features would provide a better understanding of a system's dynamics and the system's interaction with its local environment. Recent examples that highlights this point include the identification of a hydrogen-bond sensitive Fermi-resonance[121] or the hydrogen-bond sensitive vibrational relaxation rate.[138] The use and identification of such new features in 2D IR spectroscopy will require a more solid theoretical underpinning. This will likely involve the development of better methods to model vibrational potential energy surfaces, identification of dark states and vibrational relaxation pathways (which may be facilitated with continuum 2D IR), and the development of simulation protocols that can accurately and efficiently model a local-environment’s effect on the potential energy surface.

5. Supporting Information for Chapter 4

5.1 Sample preparation

We followed the sample preparation protocol described previously.[102] The doped bicelles were prepared by replacing 10% of DMPC with the desired lipid. The doped bicelle was then prepared normally. Bicelles were prepared in batches and kept just above freezing until their measurement time. Bicelles were not kept for longer than two weeks. When the instrument was ready, the bicelles solution was split into two aliquots. One aliquot was mixed with the peptide, while the second aliquot was diluted with D_2O so that both aliquots had the same lipid concentration. Menk was introduced into the bicelle in the same manner as Lenk. Both aliquots were thermally cycled one more time. FTIR spectra was taken for both the peptide-containing aliquot and peptide-free aliquot. Pump probe and 2D data acquisition was started immediately after the FTIR spectra were taken. The peptide-free aliquot was used as a background for the FTIR and the pump-probe.

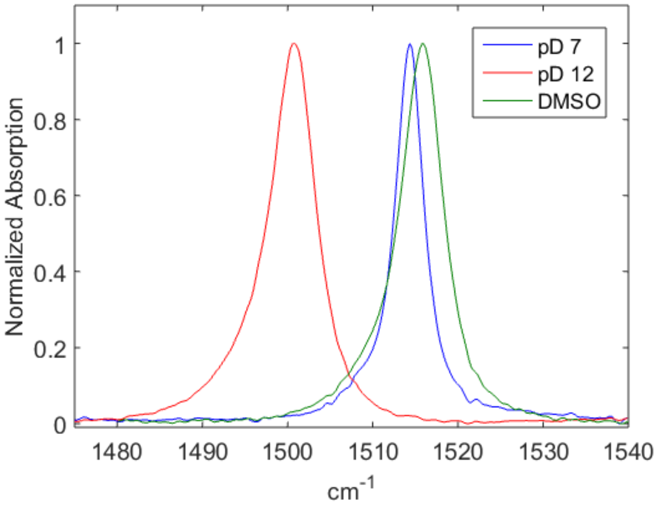

Figure 59. FTIR data for p-cresol.

The FTIR data was processed by first subtracting a water-line-reference spectrum, and then performing background subtraction and baseline correction simultaneously. To do this, we used an algorithm known as asymmetric least squares[139] and performed the subtraction in a 100 cm^{-1} range surrounding tyrosine ring mode. This directly yielded an undistorted baseline and background free IR line shape for the tyrosine ring mode. In addition, the FTIR data for p-cresol is shown in **Figure 59**.

5.2 DFT results

Figure 60 provides a brief summary of our DFT (B3LYP 6-31g+ (d,p)) results on p-cresol-OD in vacuo. The upper triangle in the plot represents anharmonic frequency shift between two anharmonically coupled modes. The lower triangle is the X_{ij} matrix as output by Gaussian 03.[117] The tyrosine ring mode is labeled in the figure. The corresponding transition frequencies are shown in **Table 2**.

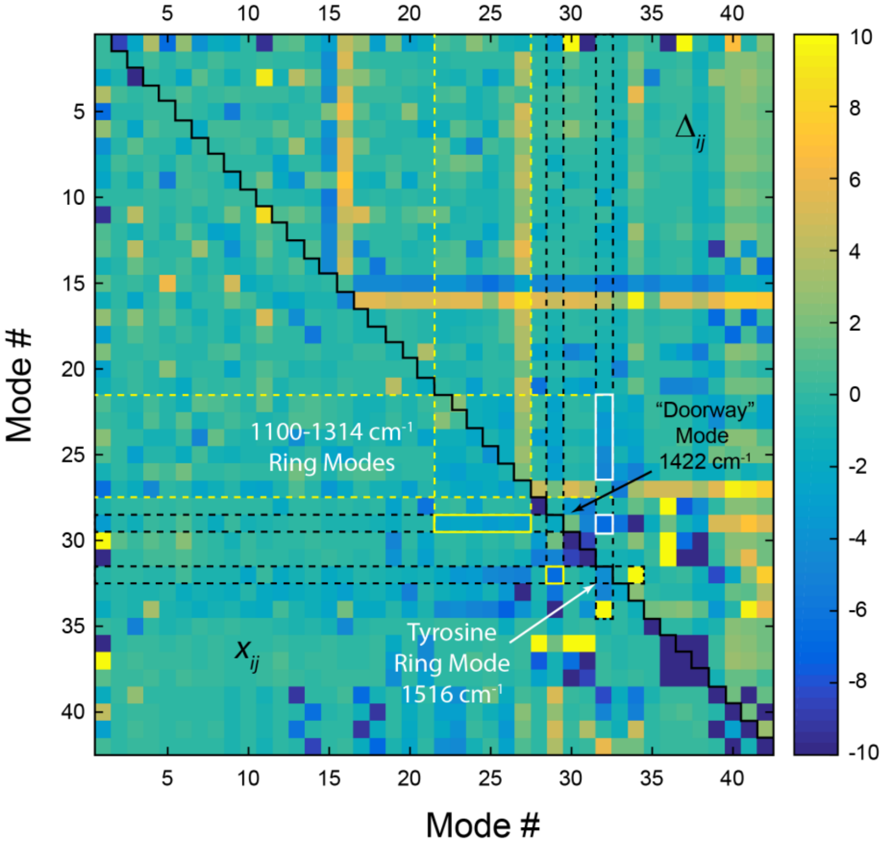

Figure 60. Anharmonic frequency shifts (Δ_{ij}) and anharmonic couplings (X_{ij}) for all normal modes in p-cresol-OD. The color bar is in the unit of cm^{-1}.

Table 2. Harmonic and anharmonic frequencies for all normal modes in p-cresol-OD. Energies given in cm^{-1}.

	Harmonic	Anharmonic	Assignment		Harmonic	Anharmonic	Assignment
1	23.4	-114.6	Me rotation	22	1135.6	1121.8	Ring C-H wag (asym.)
2	143	136.1	Me/ring/OD stretch	23	1197.8	1180.1	Ring C-H wag (sym.)
3	235.9	208.1	CCOD dihedral	24	1231.1	1204.4	Methyl-C stretch
4	300.5	303.7	Me/ring/OD bend	25	1277.1	1249.7	C-O stretch
5	331.3	326.5	Me/ring/OD bend	26	1336.4	1314.2	Ring C-H wag
6	410.1	409.1	Me/ring/OD bend	27	1346.8	1308.5	Ring C-C bending
7	421.6	412.8	Ring dihedral	28	1422	1389.7	Ring C-H wag
8	462	457.9	COCOD dihedral	29	1451.7	1422.2	Ring C-H wag
9	514.9	500.7	Ring dihedral	30	1490.9	1463.2	Methyl wag
10	655	647.7	Ring bend	31	1503.2	1459.4	Methyl wag
11	696.4	708.7	Ring dihedral	32	1550.4	1516.3	Ring bend and C-H wag
12	740	730.1	CC/CO stretch	33	1632.1	1592.5	Ring C-C stretch
13	812.5	797.6	C-H dihedral	34	1664.9	1626.6	Ring C-C stretch
14	835	819	C-H dihedral	35	2787.8	2685.6	O-D stretch
15	847.1	845.2	C-H dihedral	36	3031.5	2947.9	Methyl C-H stretch
16	923.7	896.7	COH bend	37	3083.8	2952.1	Methyl C-H stretch
17	932.9	919	C-H dihedral	38	3113.6	2973.1	Methyl C-H stretch
18	966.9	946.4	C-H bend	39	3161.5	3019.8	Ring C-H stretch
19	1008	993.4	Methyl bend	40	3172.7	3032.8	Ring C-H stretch
20	1030.2	1014.5	Ring bend (sym.)	41	3182.7	3049.3	Ring C-H stretch
21	1062.2	1042.8	Methyl wag	42	3208.1	3077.3	Ring C-H stretch

5.3 Pump-probe data

We also collected polarization-resolved pump-probe data for all samples. **Figure 61** and **Figure 62** show the lifetimes collected as <ZZZZ>+2<YYZZ> with our polarization resolved 2D IR spectrometer. One may fit the peaks to decaying exponentials to extract the vibrational lifetimes. Note that the fundamental transition will experience double exponential behavior because of the contribution from the excited state decay and ground state bleach (i.e. lifetime of the IVR peak). To improve the robustness of the fit, the overtone peak was first fit to a single exponential (right side of the figures). The time constant of this exponential represents the lifetime of the first excited state, including the IVR contribution. The fundamental peak was then fit to two exponentials (left side of the figures), one of which had the time constant fixed to that of the overtone peak. The functional form of the fit function is:

$$f(T) = A_1 e^{-\frac{T}{\tau_1}} + A_2 e^{-\frac{T}{\tau_2}} \tag{111}$$

The fit results are summarized in Table 3. The longer time constant represents the decay of the bleach, which coincides with the decay of the IVR peak.

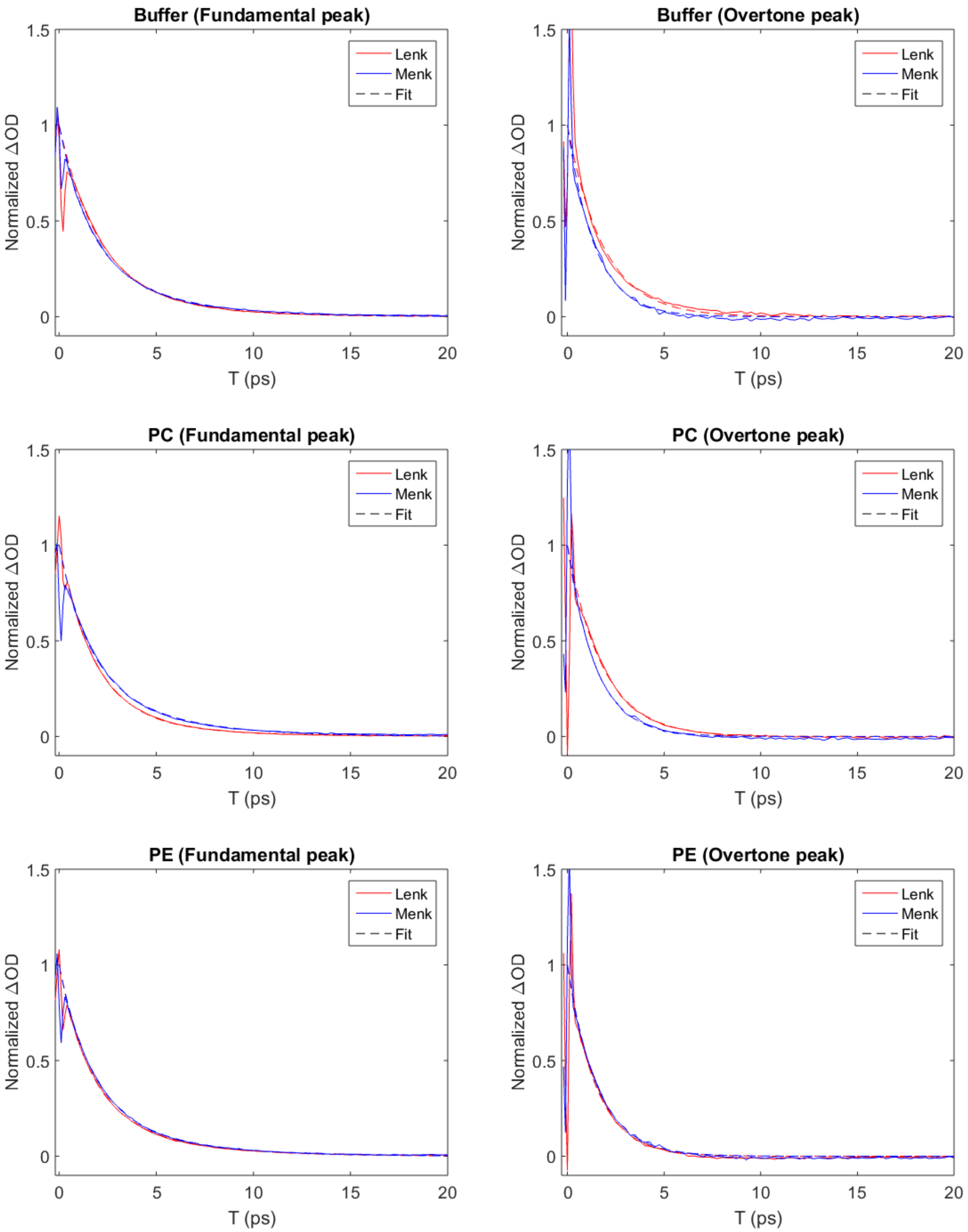

Figure 61. Part 1 of the pump probe data for Lenk and Menk in different conditions. The fundamental peak was at 1517 cm^{-1} and overtone peak at 1505 cm^{-1}.

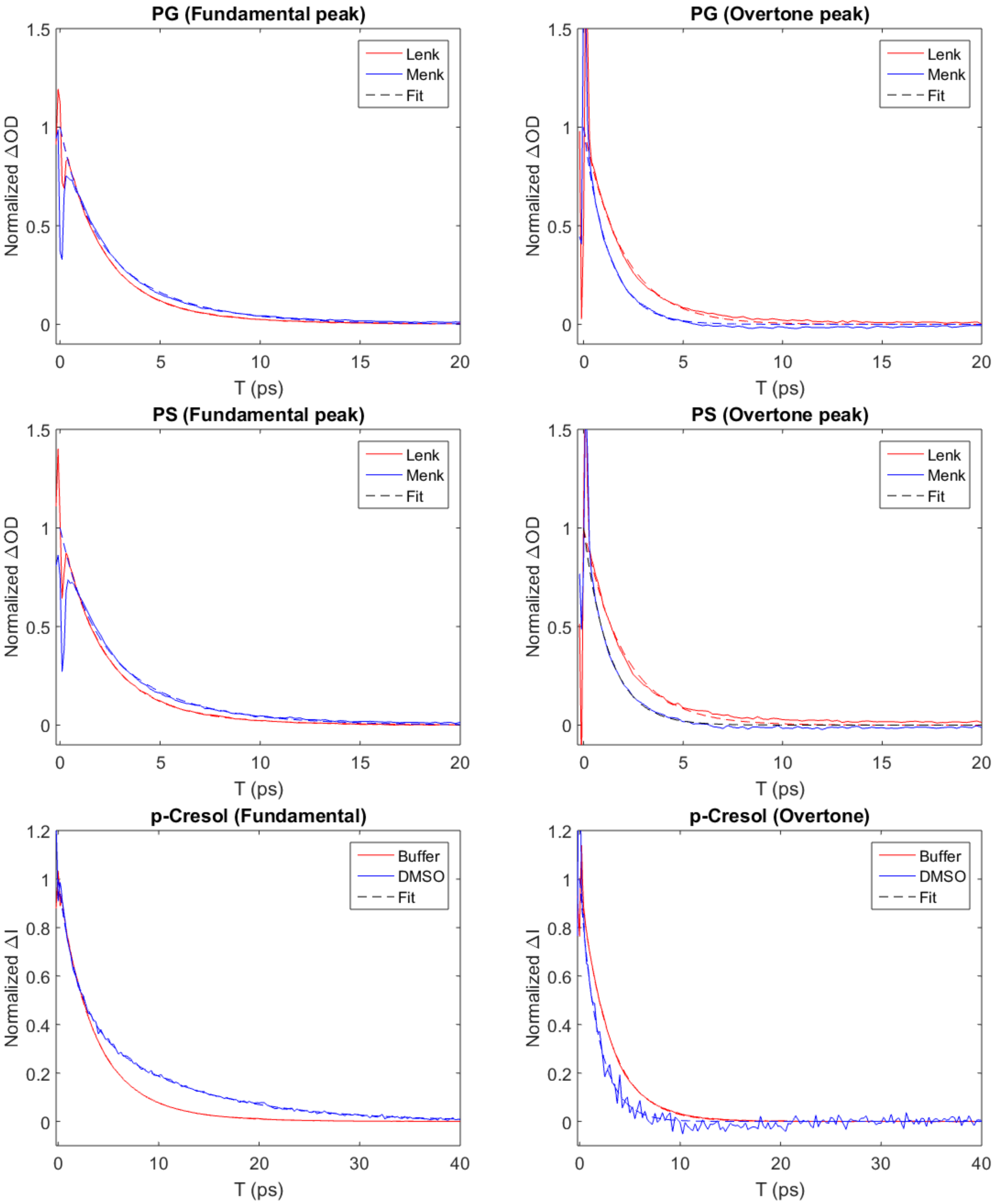

Figure 62. Part 2 of the pump probe data for Lenk, Menk, and p-cresol in different conditions. The traces shown are at 1517 cm^{-1} for the fundamental and 1505 cm^{-1} for the overtone for Lenk and Menk. For p-cresol in buffer, the fundamental and overtone traces are at 1515 cm^{-1} and 1503 cm^{-1}, respectively. For p-cresol in DMSO, the traces are at 1517 cm^{-1} and 1500 cm^{-1}.

Table 3. Double exponential fit parameters used in the pump probe data.

		A_1/A_2	τ_1 (ps)	τ_2 (ps)
Lenk	Buffer	2.5	1.9	3.9
	PC	2	1.5	4
	PG	6.9	2	4.9
	PE	1.5	1.5	4
	PS	0.7	1.3	3.8
Menk	Buffer	10.3	1.8	5.8
	PC	7.8	2	5.6
	PG	1.5	1.4	3.9
	PE	1.9	1.5	4.1
	PS	0.7	1.3	3.8
p-Cresol	Buffer	1.7	2.8	5.4
	DMSO	1.1	1.8	10.3

5.4 Reorientation dynamics:

Figure 63 shows the vibrational anisotropy for p-cresol in D_2O/Buffer. The decay happens with a time constant of approximately 8 ps with an offset of 0.27. The vibrational lifetime is less than 3 ps for all samples. Because p-cresol is the smallest molecule we measured, we do not expect that anisotropy effects will be significant in the 2D data of the peptides.

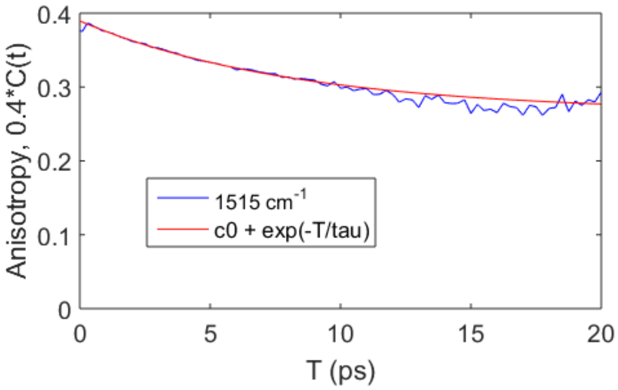

Figure 63. Pump-probe vibrational anisotropy of p-cresol measured at 1515 cm^{-1}.

5.5 2D IR Response Function Fitting

Spectral fitting is performed by using MATLAB's non-linear least squares optimization function, lsqnonlin. Due to the overparameterization of the model, we tried to use an iterative procedure to fit the 2D IR, pump-probe and FTIR spectra to the same parameter set. This idea has its roots on the fact that different measurements have better representations of different information. Unfortunately, the pump-probe data suffers from a strong background signal from the solvent, bicelles, and peptide. This background signal dephases quickly, so it is not as prominent in the 2D spectra. Therefore, we only show the fits from the 2D IR spectra (Figure 64 through Figure 74, Lenk in PC bicelles is shown in the main text). The parameters are summarized in **Table 2**. Note that for several parameters, there are sometimes extreme changes between samples even though the fits are visually okay. We attribute this to overparameterization.

In addition, we also include the following two considerations. First, there can be multiple minima present in the fitting parameters. We use the MultiStart class in MATLAB to overcome this issue. This set of functions generates multiple initial guesses, each of which are minimized using the nonlinear least squares procedure. This method ensures, at least for our data set, that a global minimum is always found. Note that if each run consistently finds different local minima, it is likely the least squares convergence criteria is not tight enough, and we adjust the convergence criteria when this situation occurs. Second, we include a 0.8 cm^{-1} frequency correction for the pump axis which is related to a small pump double pulse delay generation error.[7]

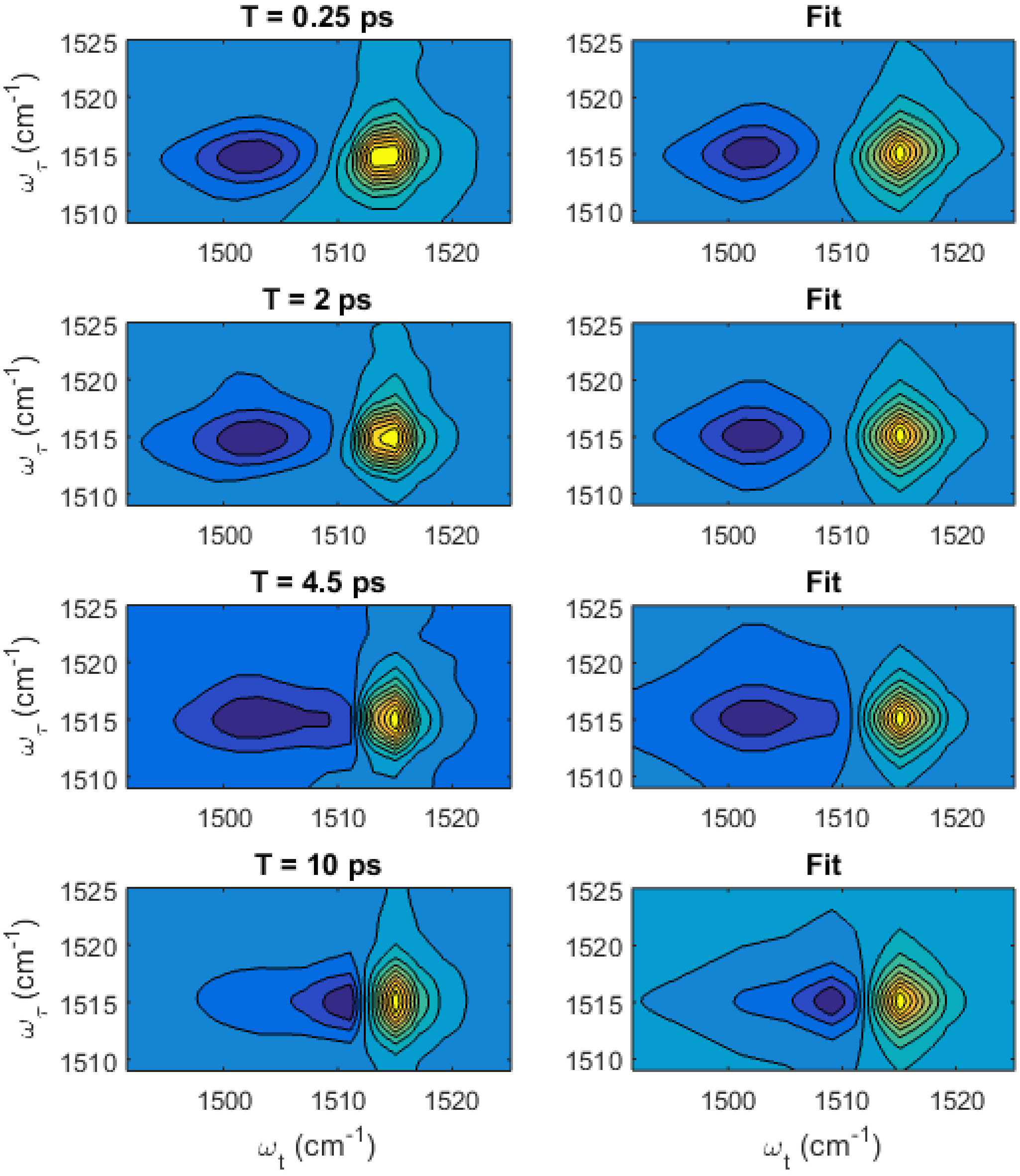

Figure 64. 2D IR spectra of p-cresol in pD 7 phosphate buffer

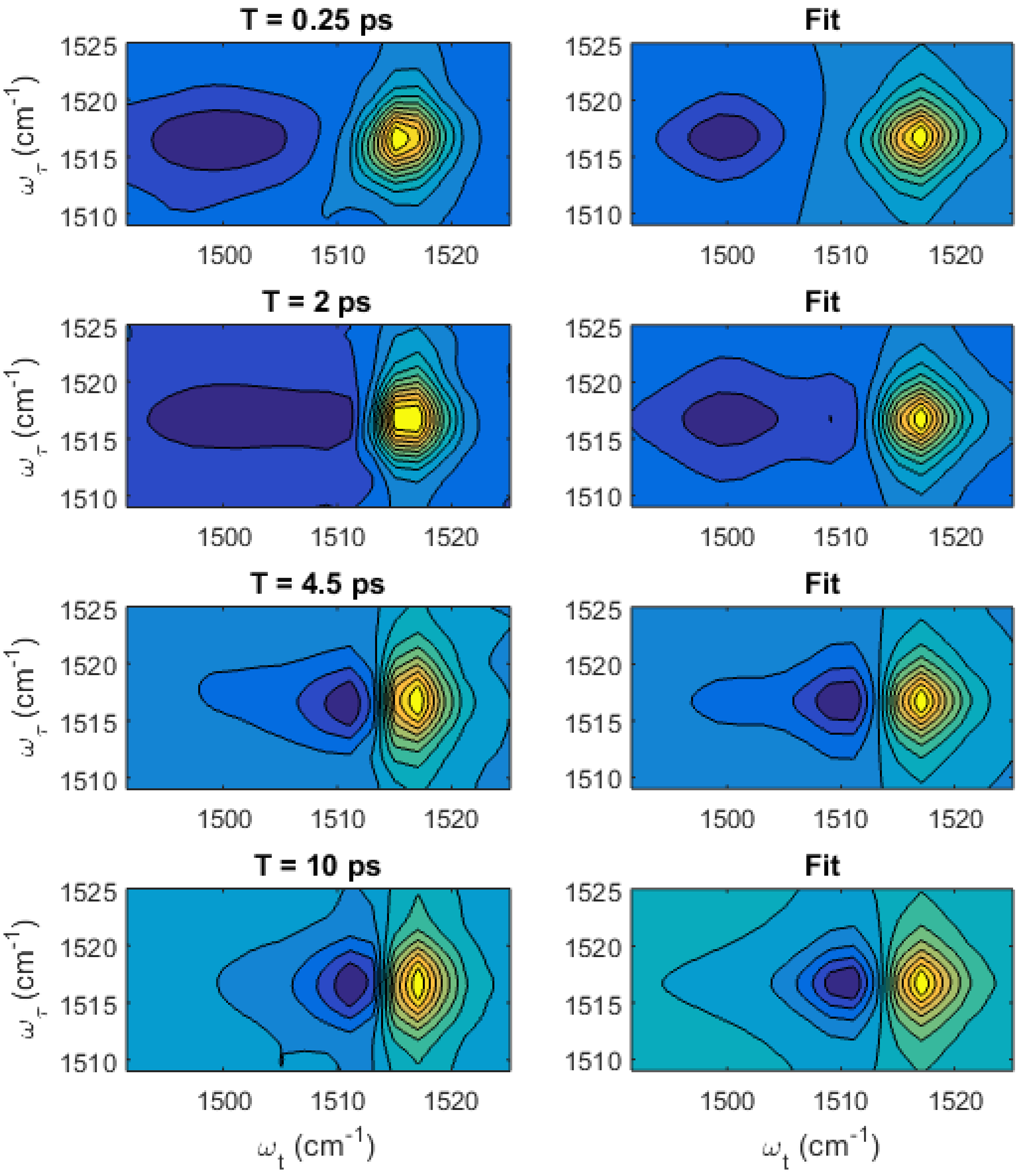

Figure 65. 2D IR spectra of p-cresol in DMSO

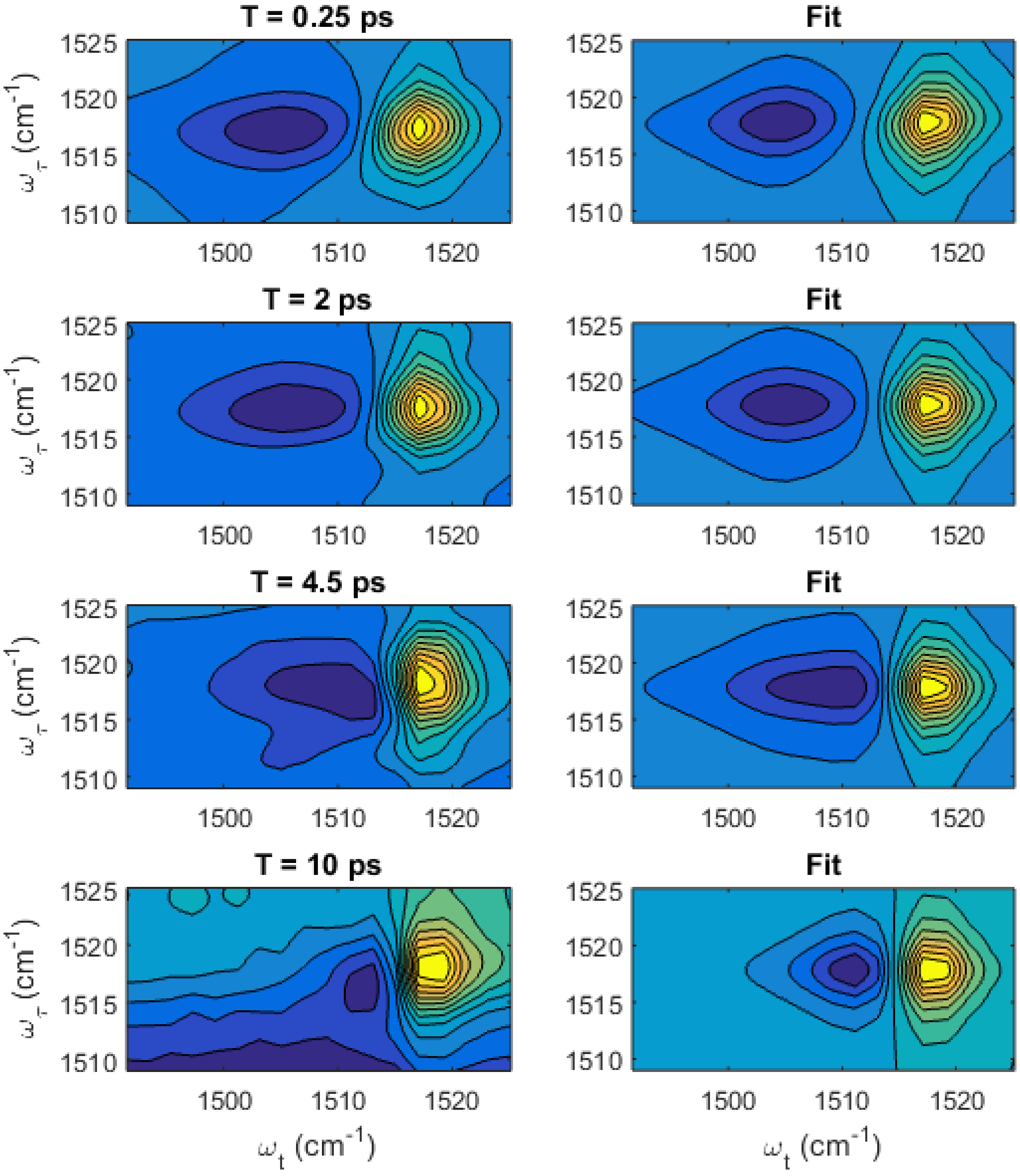

Figure 66. 2D IR spectra of Lenk in pD 7 phosphate buffer

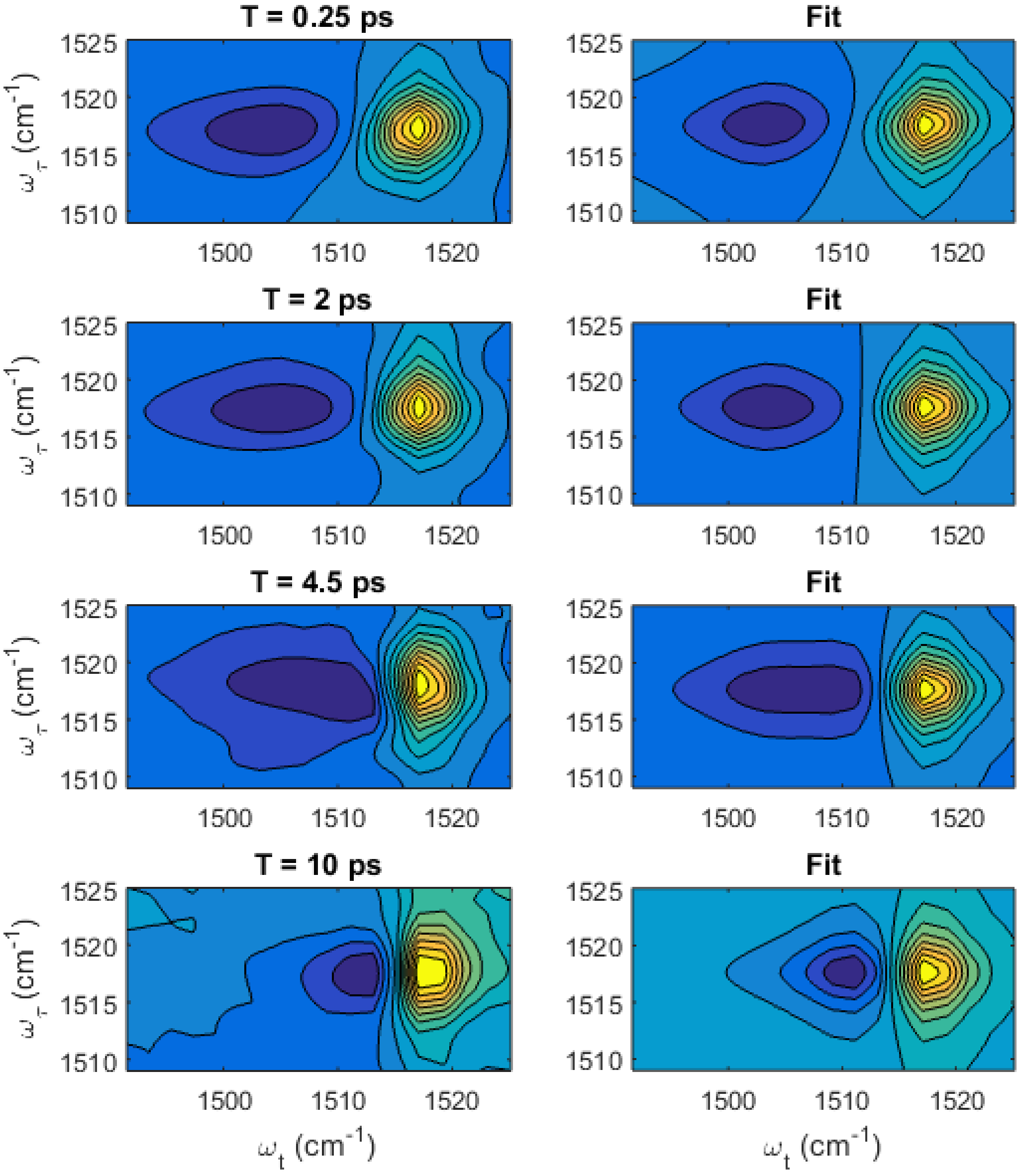

Figure 67. 2D IR spectra of Menk in pD 7 phosphate buffer

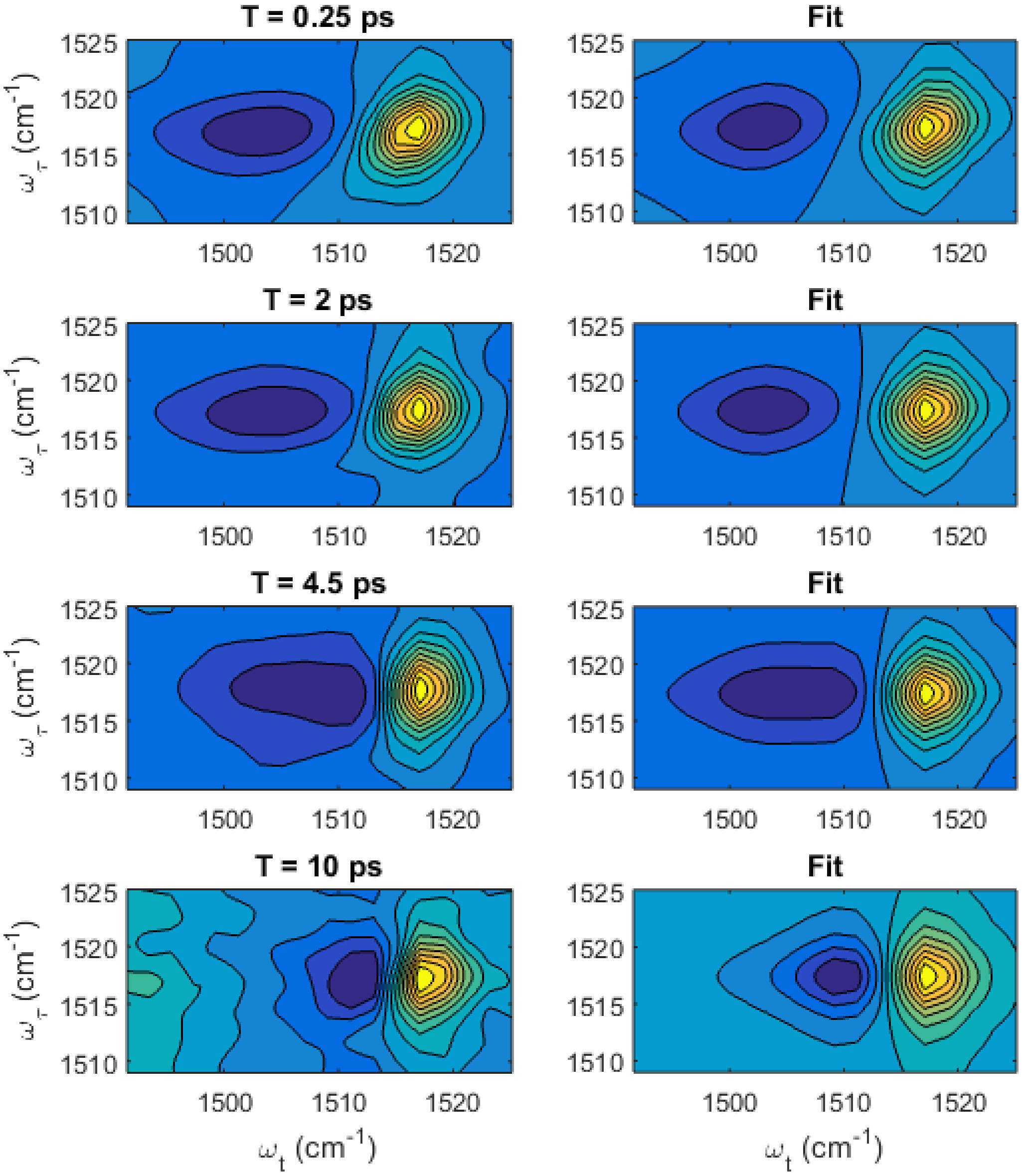

Figure 68. 2D IR spectra of Menk in PC bicelles.

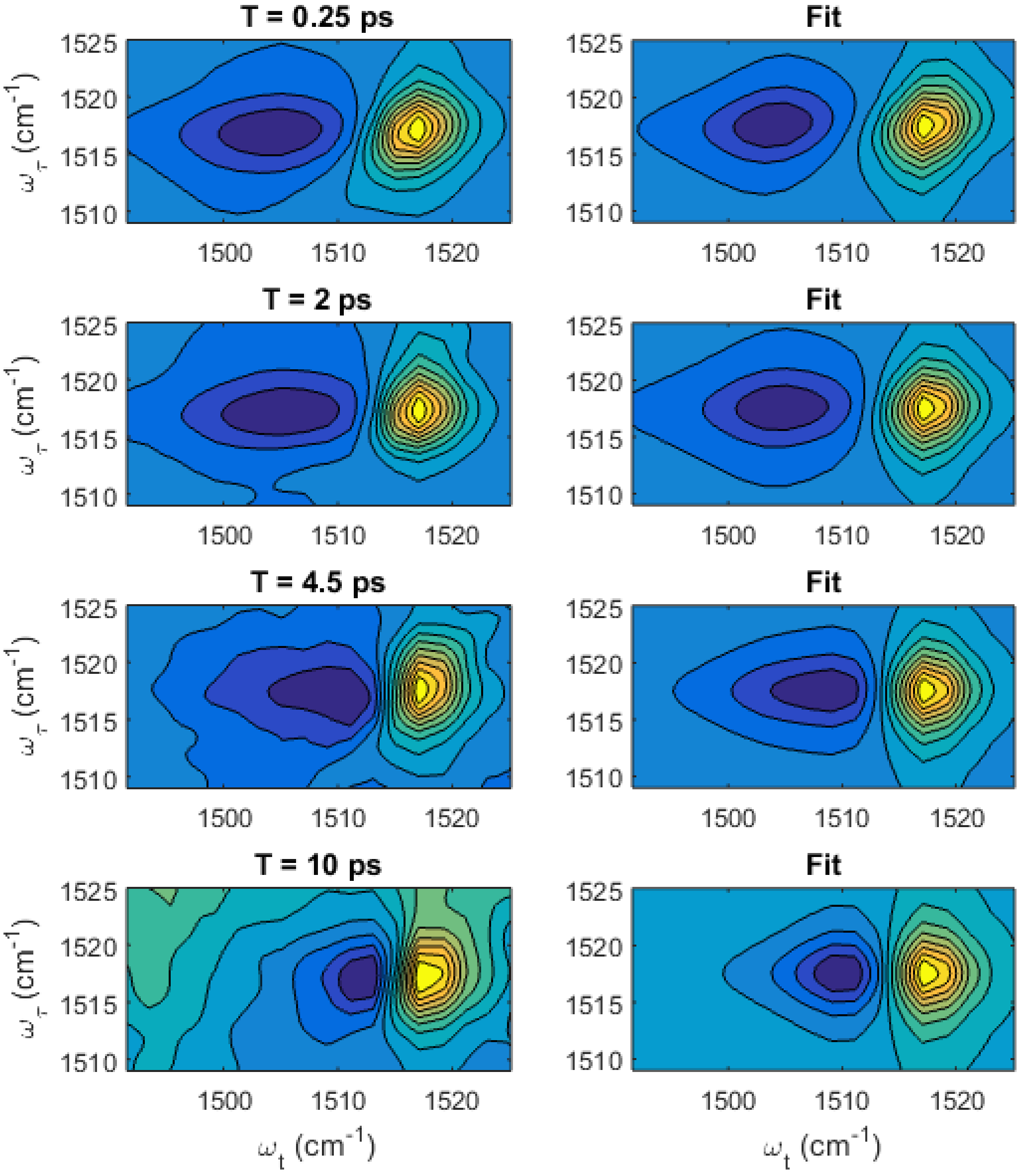

Figure 69. 2D IR spectra of Lenk in PE bicelles.

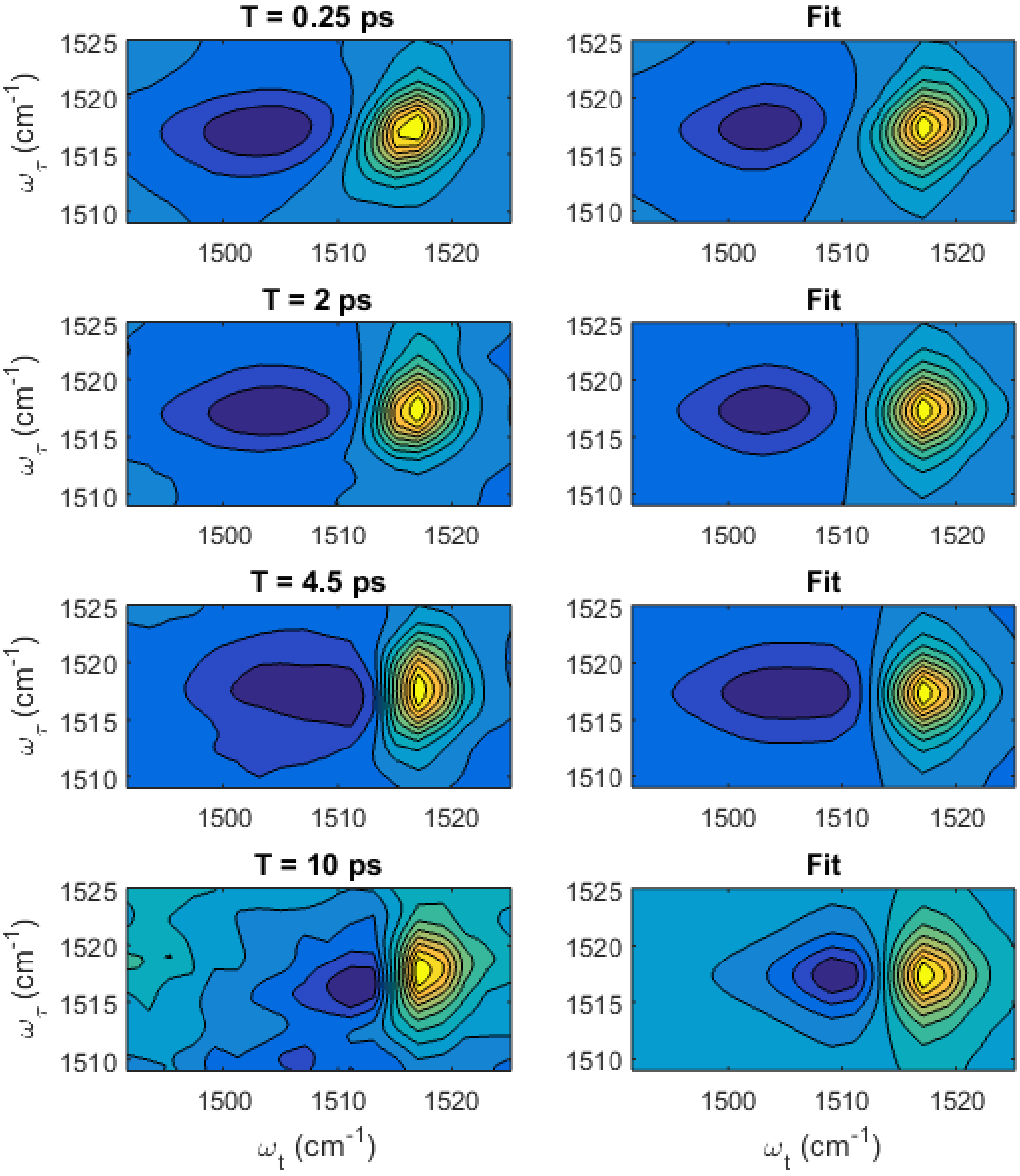

Figure 70. 2D IR spectra of Menk in PE bicelles.

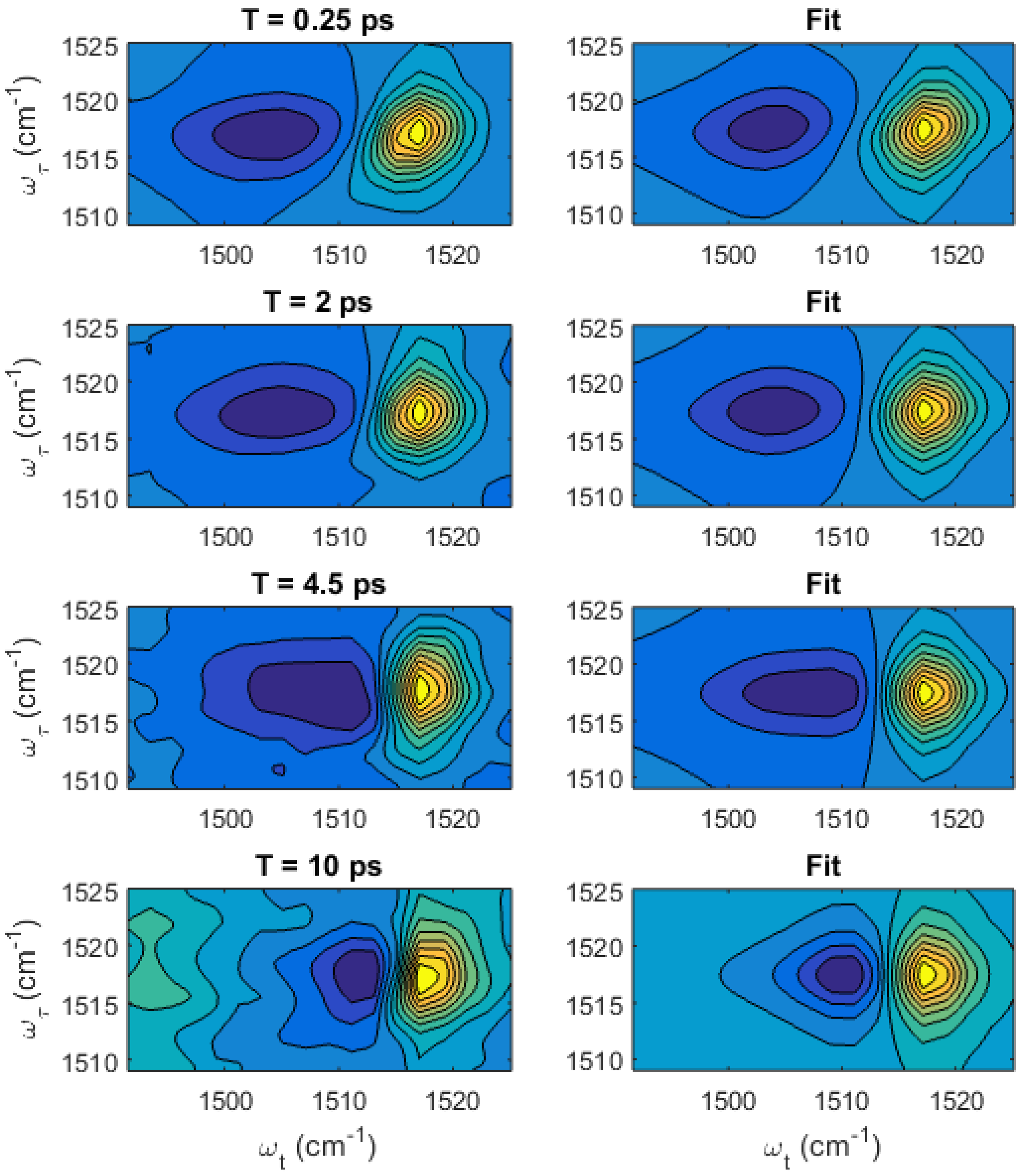

Figure 71. 2D IR spectra of Lenk in PG bicelles.

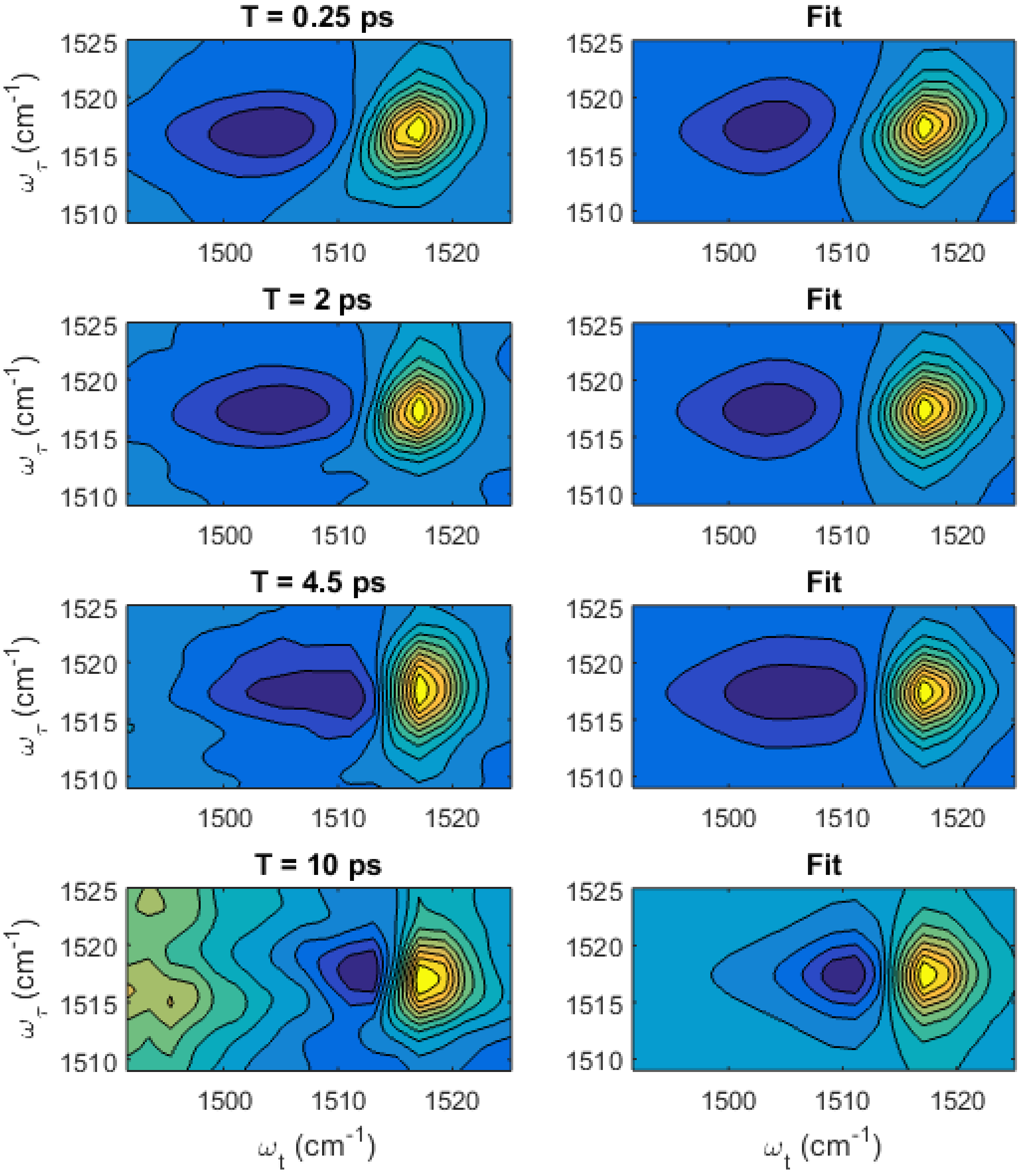

Figure 72. 2D IR spectra of Menk in PG bicelles.

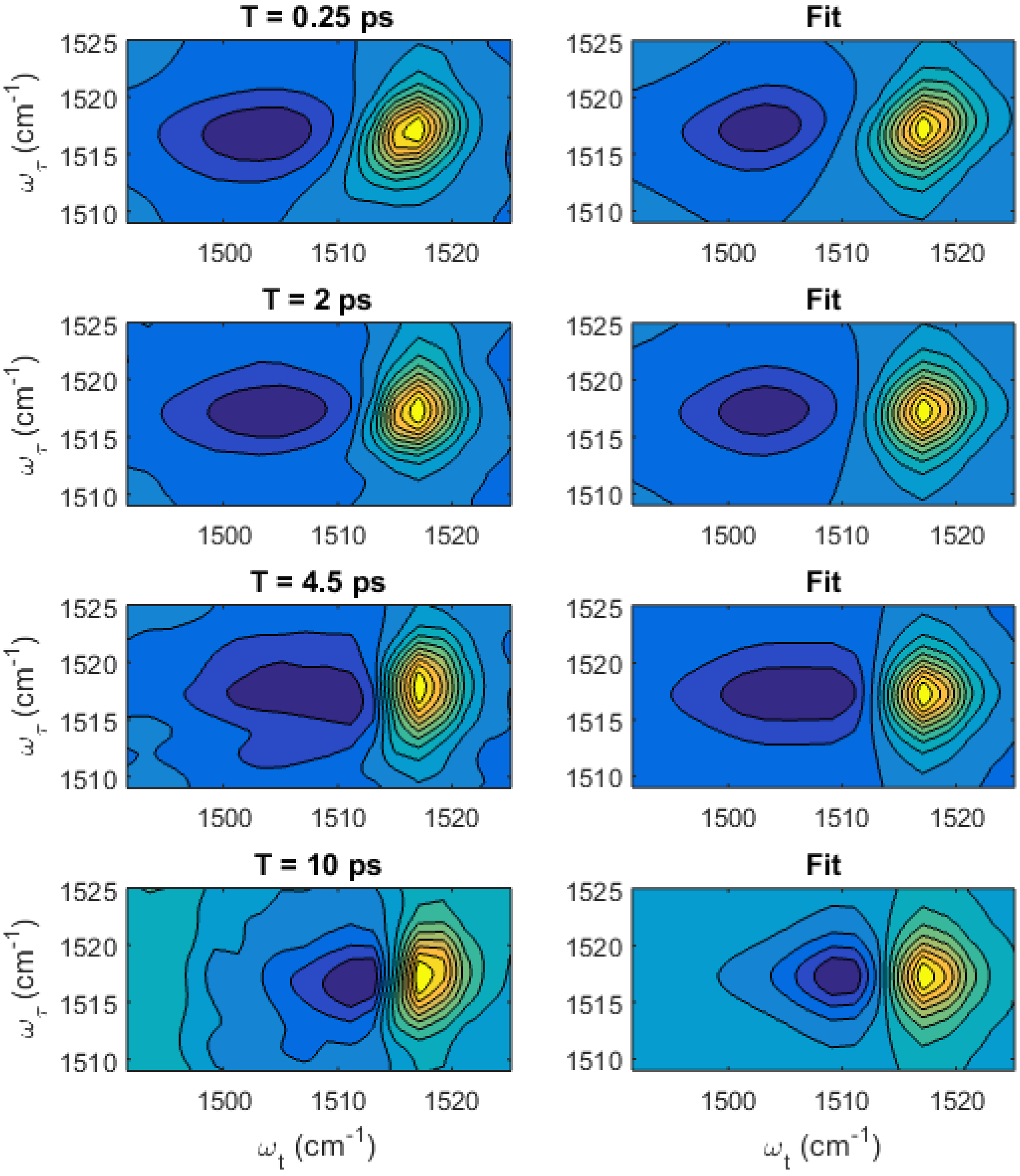

Figure 73. 2D IR spectra of Lenk in PS bicelles.

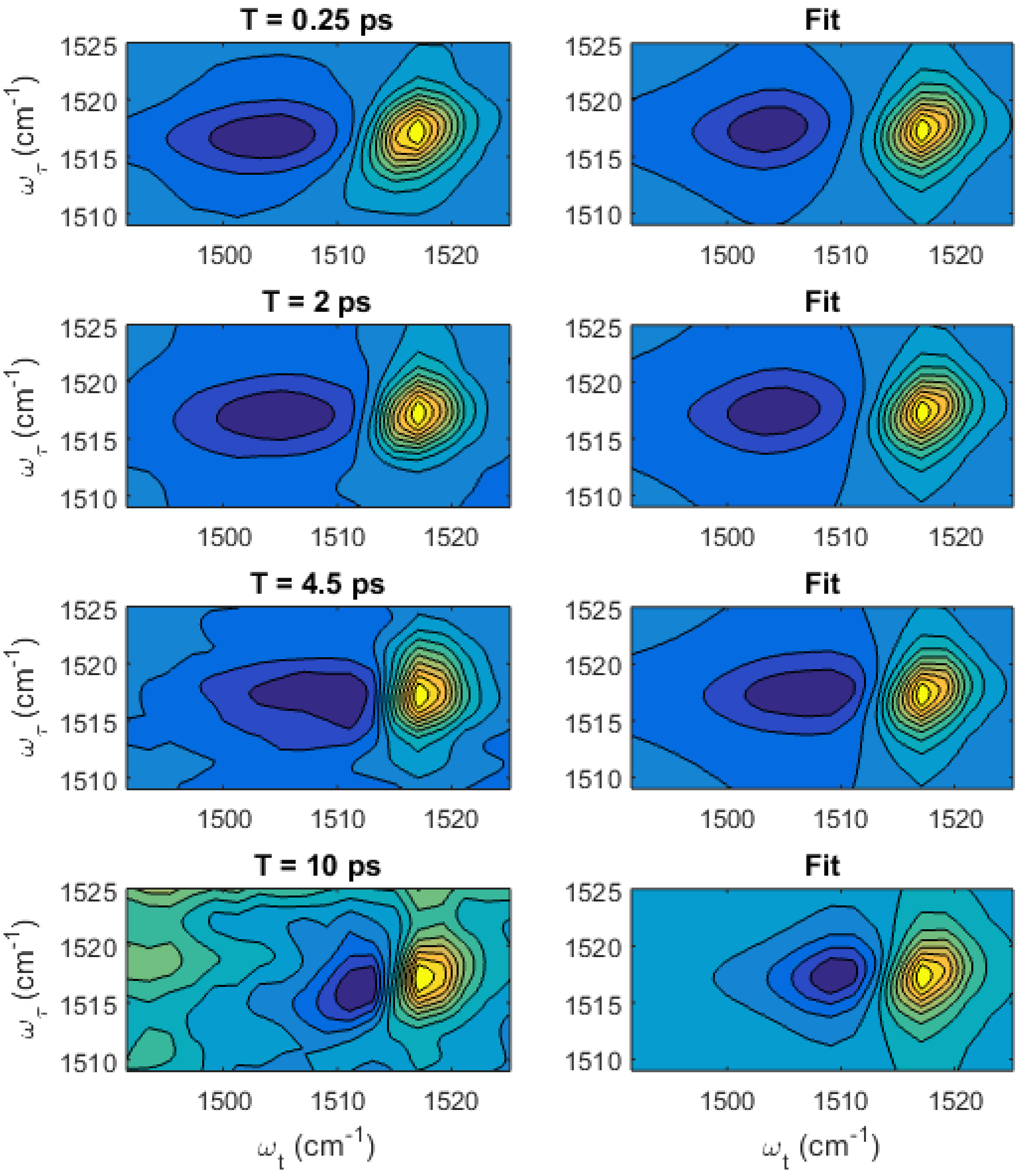

Figure 74. 2D IR spectra of Menk in PS bicelles.

Table 4. Summary of 2D IR fit parameters. Transition dipole moments are relative.

	μ_{01}	μ_{12}	ω_{01} cm^{-1}	ω_{12} cm^{-1}	ω_{IVR} cm^{-1}	t_1 ps	t_{IVR} ps	t_1' ps	τ ps	Δ_1 cm^{-1}	Δ_{inh} cm^{-1}	γ_0 cm^{-1}
p-Cresol/Buffer	0.28	0.25	1515.1	13	5.3	2.9	13.6	13.3	1	2.6	0	0.69
p-Cresol/DMSO	0.28	0.2	1516.7	16.9	5.7	3	3.6	15.2	1.1	1.9	0.27	1.84
Lenk/Buffer	0.25	0.22	1517.8	13.2	6	1.8	6.4	4.9	1	2.6	0	0.54
Lenk/PC	0.23	0.19	1517.5	14	6.7	1.8	9	5.8	2.1	2.4	0.16	0.2
Lenk/PE	0.23	0.2	1517.5	13.4	6.9	1.8	6.2	4.7	1.9	2.4	0	0.51
Lenk/PG	0.22	0.18	1517.4	13.7	6.5	1.8	9.6	6.3	1.8	2.5	0	0.07
Lenk/PS	0.22	0.18	1517.3	14.2	6.6	1.8	13	8.8	1.8	2.5	0.17	0.3
Menk/Buffer	0.25	0.21	1517.6	14.2	6.3	1.7	11.3	7	1	2.5	0.02	0.69
Menk/PC	0.23	0.19	1517.4	14.6	7	1.8	14	8	1.9	2.4	0.04	0.11
Menk/PE	0.23	0.19	1517.3	14.3	7.1	1.8	14.3	8.2	1.4	2.6	0	0.54
Menk/PG	0.21	0.16	1517.4	13.7	6	1.8	15	7.5	1.8	2.5	0.42	0.29
Menk/PS	0.2	0.17	1517.4	13.6	7.4	1.8	10.1	6.4	0	2	1.2	1.33

5.6 CLS Plots and Fit Results

Figure 75 and Figure 76 summarize the CLS results. In Figure 75, we include error bars which estimate the CLS error. To calculate this error, we subdivided each 2D data set into 10 subsets and calculated the CLS for each subset. The error bars represent the standard deviation in the resulting set of CLS values. Each error also has a circle indicating the mean CLS point calculated from the subsets. The solid line represents the CLS extracted from the full data set. Note that for p-cresol the error bars are very large, even though the 2D IR data has a high SNR. This is because width of the p-cresol peak is on the limit of our spectrometer's resolution. Therefore, the CLS value is extremely sensitive to small amounts of noise. For Lenk and Menk, the diagonal peak becomes narrower with longer waiting time (which is not predicted by the response function model). Therefore, the resolution problem is partially responsible for the large error bars at long waiting time, although the low SNR of the longer waiting times is the most important contributor.

In Figure 76, we present the CLS fits to the damped oscillation. Table 5 summarizes the full fit parameters. We used the standard deviations shown in Figure 75 as weights for the fitting. The fitting function is:

$$f(T) = {\Delta_1}^2 + \ {\Delta_2}^2 \cdot \cos\left(\frac{2\pi T}{\tau_1}\right) \cdot e^{-\frac{T}{\tau_2}} \qquad (112)$$

Note that this fitting function does not represent a physical correlation function. Instead, it is an attempt to extract the static inhomogeneous contribution to the correlation function given the peak interference present in the 2D data. As such, some of the fits may not have physically meaningful results. For example, Lenk and Menk in buffer have negative static inhomogeneities.

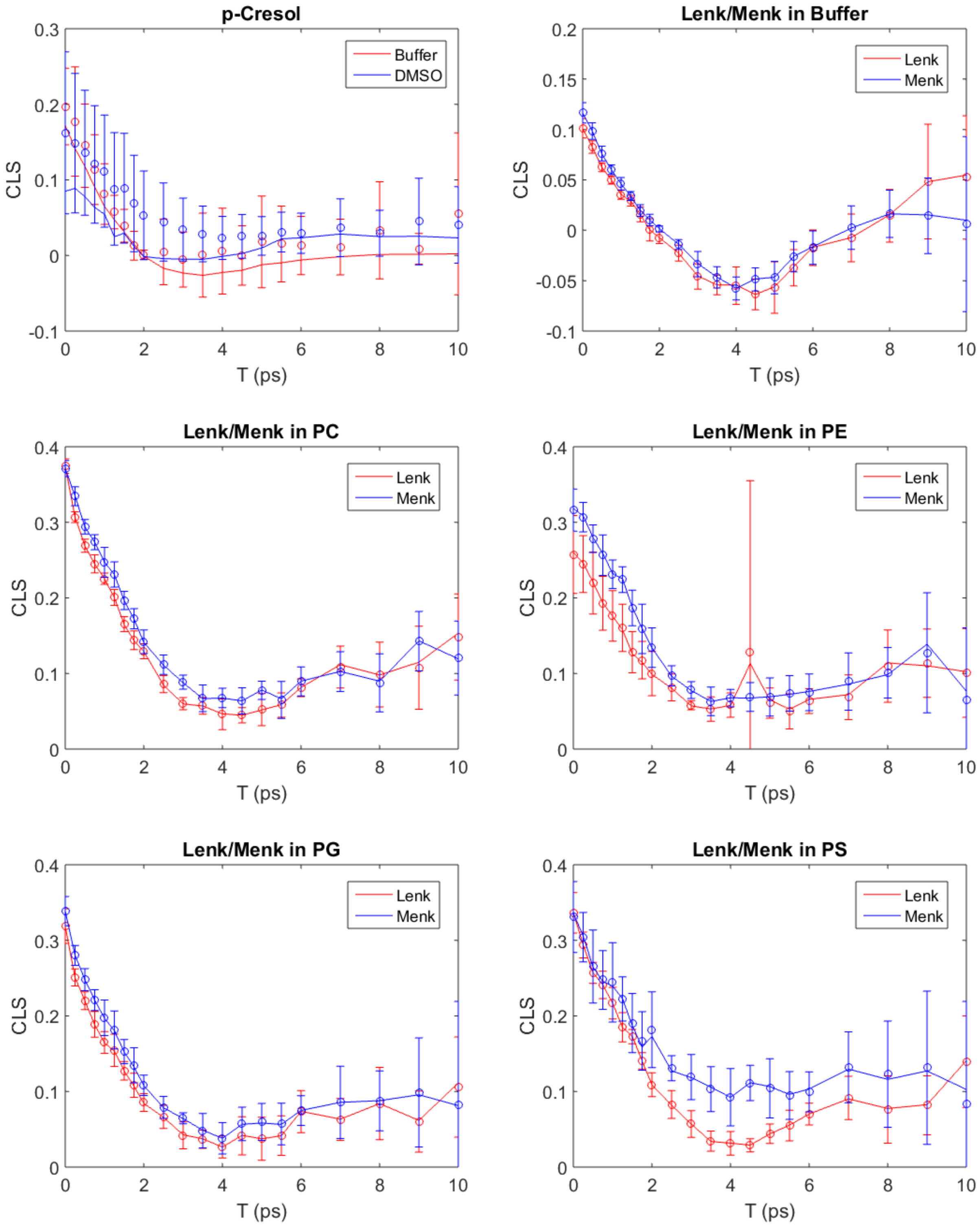

Figure 75. CLS results for all 2D data collected showing error bars.

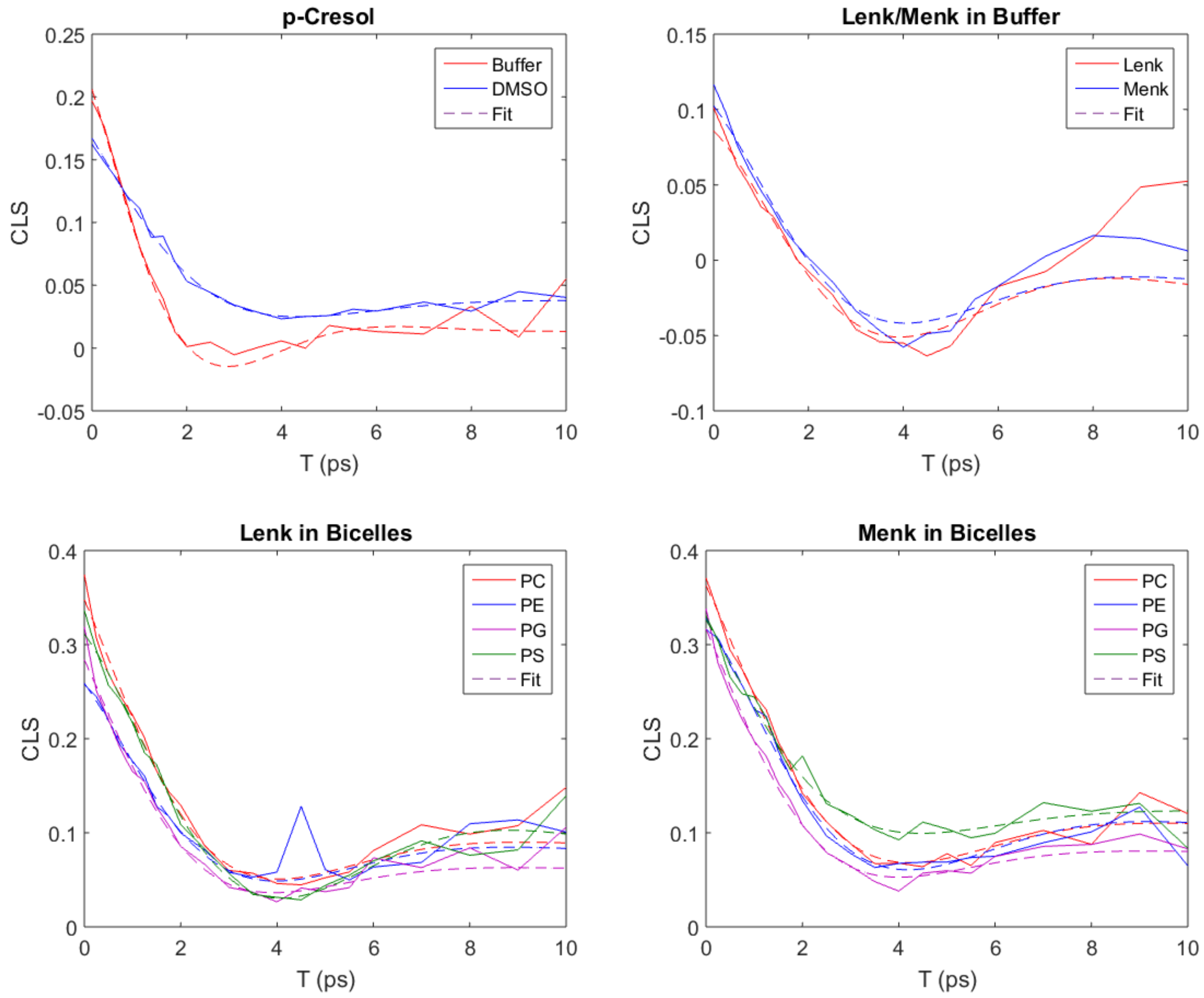

Figure 76. Plots of the CLS fit results.

Table 5. CLS fit results.

		Δ_1^2	Δ_2^2	τ_2	τ_1
p-Cresol	Buffer	0.01 ± 0.01	0.19 ± 0.04	1.7 ± 0.7	7.1 ± 0.9
	DMSO	0.04 ± 0.01	0.13 ± 0.03	2.1 ± 0.7	11.3 ± 2.0
Lenk	Buffer	-0.02 ± 0.02	0.11 ± 0.04	3.4 ± 2.8	9.0 ± 2.7
	PC	0.09 ± 0.03	0.26 ± 0.06	2.2 ± 1.0	10.0 ± 3.2
	PE	0.08 ± 0.02	0.18 ± 0.05	2.5 ± 1.3	9.6 ± 1.4
	PG	0.06 ± 0.03	0.22 ± 0.05	2.0 ± 0.9	10.0 ± 3.5
	PS	0.09 ± 0.02	0.22 ± 0.04	3.3 ± 1.2	9.5 ± 1.1
Menk	Buffer	-0.02 ± 0.02	0.12 ± 0.04	2.9 ± 2.0	9.6 ± 3.1
	PC	0.11 ± 0.02	0.26 ± 0.03	2.4 ± 0.7	10.4 ± 2.0
	PE	0.10 ± 0.02	0.22 ± 0.04	2.8 ± 1.1	10.0 ± 1.6
	PG	0.08 ± 0.02	0.24 ± 0.04	2.0 ± 0.7	10.2 ± 2.5
	PS	0.12 ± 0.03	0.21 ± 0.05	2.3 ± 1.2	11.4 ± 4.0

5.7 Computational detail for population exchange model

To calculate the response functions with an arbitrary kinetic model, we partition the problem into calculating the dephasing dynamics and calculating the population dynamics. The population dynamics are represented by a kinetic model, as described in the main text. When evaluated on a time grid, this method can be written in matrix notation:

$$\boldsymbol{R}(T) = \boldsymbol{G}(T) \circ \boldsymbol{Pr} \cdot \boldsymbol{M}(T) \cdot \boldsymbol{Pu} \tag{113}$$

here, $\boldsymbol{R}(T)$ is the total rephasing or non-rephasing response function on a $N_t \times N_\tau$ time grid; $\boldsymbol{Pu}$ is a $N_{Pu} \times N_\tau$ matrix; $\boldsymbol{Pr}$ is a $N_t \times N_{Pr}$ matrix; $\boldsymbol{G}(T)$ is a matrix containing the exponential of the line shape function which is responsible for spectral diffusion; the $\cdot$ product represents matrix multiplication; and the $\circ$ product represents the Hadamard product, or by-element multiplication. The matrices $\boldsymbol{Pu}$ and $\boldsymbol{Pr}$ represent the first and second half of all rephasing or non-rephasing Feynman diagrams evaluated on the τ and t time grid, respectively. N_{Pu} and N_{Pr} represent the number of populations after the second and last interaction, respectively. N_τ and N_t represent the number of τ and t grid points used in the calculation. The matrix $\boldsymbol{M}(T) = \exp(\boldsymbol{K}T)$, of dimensionality $N_{Pr} \times N_{Pu}$, is the T-dependent solution to the linear kinetic equations for each pump-generated population, where $\boldsymbol{K}$ is the kinetic matrix of first order rate constants. As an example, the solution for the hot-band kinetic model is shown in Figure 77. Note that the rephasing and non-rephasing response functions need to be calculated separately. Finally, assuming the semi-impulsive limit, the spectra are Fourier transformed, for each time T, along (t, τ) to $(\omega_t, -\omega_\tau)$ for rephasing and $(\omega_t, +\omega_\tau)$ for non-rephasing response functions.[140] The absorptive spectra are the real parts of the sum of the rephasing and non-rephasing spectra.

The matrices $\boldsymbol{Pr}$ and $\boldsymbol{Pu}$ are constructed directly from the Feynman pathways. As an example, the rephasing equations that involve the 1st excited state as a population are given by:

$$\boldsymbol{Pu}_{i1}^{R} = -\mu_{01}^{2} \cdot \exp\left(\tau_i \left(i\omega_{01} - \frac{1}{2T_1}\right)\right) \tag{114}$$

$$\boldsymbol{Pr}_{1i}^{R} = \mu_{01}^{2} \cdot \exp\left(t_i \left(-i\omega_{01} - \frac{1}{2T_1}\right)\right) - \mu_{12}^{2} \cdot \exp\left(t_i \left(-i\omega_{12} - \frac{2}{3T_1}\right)\right) \tag{115}$$

The indices i indicates the ith grid point on which the experimental times, t_i or τ_i, are evaluated on. The other index indicates the population (0 for ground state, 1 for excited state, etc.) and corresponds to a row or column in the matrices. The diagrams that involve the ground state are given by:

$$\boldsymbol{Pu}_{i0}^{R} = -\mu_{01}^{2} \cdot \exp\left(\tau_i \left(i\omega_{01} - \frac{1}{2T_1}\right)\right) \tag{116}$$

$$\boldsymbol{Pr}_{0i}^{R} = \mu_{01}^{2} \cdot \exp\left(t_i \left(-i\omega_{01} - \frac{1}{2T_1}\right)\right) \tag{117}$$

There is an additional probe pulse term involving the IVR peak:

$$\boldsymbol{Pr}_{1'i}^{R} = -\mu_{1,1+1'}^{2} \cdot \exp\left(t_i \left(-i\omega_{1,1+1'} - \frac{1}{2T_{1'}} - \frac{1}{T_1}\right)\right) \tag{118}$$

The spectral diffusion component, $\boldsymbol{G}(T)$, is given in the usual way:[5]

$$\boldsymbol{G}_{ij}^{R}(T) = \sin\left(-g(\tau_j) + g(T) - g(t_i) - g(\tau_j + T) - g(t_i + T) + g(\tau_j + T + t_i)\right) \tag{119}$$

$$\boldsymbol{G}_{ij}^{NR}(T) = \sin\left(-g(\tau_j) - g(T) - g(t_i) + g(\tau_j + T) + g(t_i + T) - g(\tau_j + T + t_i)\right) \tag{120}$$

$$g(t) = \int_0^t dt_1 \int_0^{t_1} dt_2 C(t_2) \tag{121}$$

where $C(t)$ is the FFCF, and indices i and j indicates the i and j^{th} grid-point on which t and τ are defined on. Finally, we note that when there is no spectral diffusion, this calculation can be directly performed in the frequency domain.

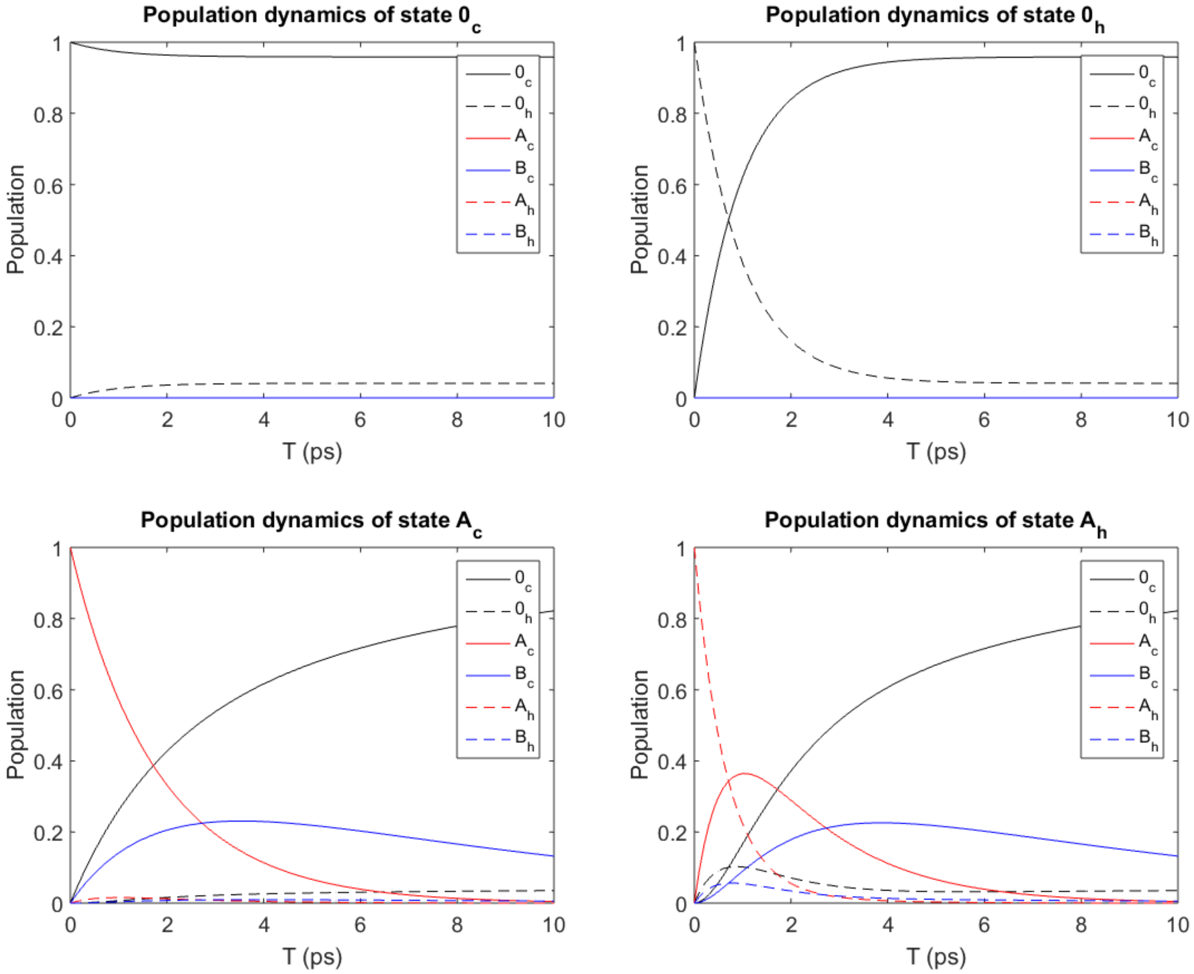

Figure 77. The population dynamics represented by the population transfer matrix for the hot-band model.

6. Summary and Conclusions

I will conclude this dissertation with a summary of the main results. Chapter 2 and 3 focused on improving the SNR so that we can perform more difficult 2D IR experiments on biomolecules. Chapter 4 applies these SNR enhancements on the enkephalin/bicelle system. Chapter 5 provides a comprehensive summary of the data acquired for Chapter 4.

In Chapter 2, we derived a method to optimally remove the local oscillator fluctuations from the signal. When applied to pump-probe spectroscopy, this removes the probe fluctuations. This "smart referencing" algorithm is a linear-regression based method that best fits, after chopping or phase cycling, all the reference detector pixels to any given signal pixel. The main result is given in Eq. (18) and Eq. (21). The fit coefficient given by Eq. (18) must be estimated either before or during data acquisition by inserting blank shots. For detectors with many reference pixels, many blank shots must be acquired (as a rule of thumb, shot pairs must be >15x the number of reference pixels) to avoid overfitting the noise. To reduce the time cost of acquiring many blank shots, pixel compression and expansion may be employed. For our MCT detectors, we found that this method typically increases the SNR by 10-30x. For visible detectors, we found that we can achieve shot-noise limited performance for both white light continuum and 800 nm light sources.

In Chapter 3, I provide an analysis of the key operatic principles of the mid IR pulse shaper and associated zero-dispersion line. The focus of the chapter was characterizing double pulse falloff, the use of the Littrow configuration zero-dispersion line as a pulse compressor, and the associated aberrations introduced at the pump-probe overlap. We found that conserving acoustic bandwidth is critical to minimizing double pulse falloff. Inserting the AOM into the zero-dispersion line introduces a substantial amount of chirp which should be compensated for by moving the first and second gratings. In addition, compensating for temporal chirp introduces spatial chirp, but does not introduces angular chirp. We found that the pump beam focus quality is poor and concluded that this can be caused by poor collimation of the probe and input into the pulse shaper. Poor collimation into the pulse shaper causes a mismatch between beam divergence and angular dispersion, which causes the pump focus to be horizontally dispersed. By understanding all of these considerations, the pulse shaper throughput and beam quality can be improved, thereby increasing the 2D IR signal.

Finally, Chapter 4 we characterize the tyrosine ring mode in the enkephalin/bicelle system using 2D IR spectroscopy. Using the unprecedented SNR of our 2D IR setup, we observed energy transfer to a dark state and a line-shape distortion that made it difficult to use routine data analysis methods. We proposed several models to explain the line-shape distortion. The coherence transfer model gave the best reproduction of the distortion, although the model lacks a compelling physical basis. One of the goals of the work was to quantify the ring mode’s sensitivity to local environment. Given the complex relaxation dynamics, we were only able to give a qualitative description. We found that the ring mode has sensitivity to very drastic changes in local environment.

References

1. Petti, M. K.; Lomont, J. P.; Maj, M.; Zanni, M. T. Two-Dimensional Spectroscopy Is Being Used to Address Core Scientific Questions in Biology and Materials Science. *The Journal of Physical Chemistry B.* **2018**, *122*, 1771.
2. Thielges, M. C.; Fayer, M. D. Protein Dynamics Studied with Ultrafast Two-Dimensional Infrared Vibrational Echo Spectroscopy. *Accounts of Chemical Research.* **2012**, *45*, 1866.
3. Maekawa, H.; Ge, N.-H. Comparative Study of Electrostatic Models for the Amide-I and -II Modes: Linear and Two-Dimensional Infrared Spectra. *The Journal of Physical Chemistry B.* **2010**, *114*, 1434.
4. Maekawa, H.; Toniolo, C.; Moretto, A.; Broxterman, Q. B.; Ge, N.-H. Different Spectral Signatures of Octapeptide 310- and α-Helices Revealed by Two-Dimensional Infrared Spectroscopy. *The Journal of Physical Chemistry B.* **2006**, *110*, 5834.
5. Hamm, P.; Zanni, M. *Concepts and Methods of 2D Infrared Spectroscopy*; Cambridge University Press: Cambridge, 2011.
6. Serrano, A. L.; Lomont, J. P.; Tu, L.-H.; Raleigh, D. P.; Zanni, M. T. A Free Energy Barrier Caused by the Refolding of an Oligomeric Intermediate Controls the Lag Time of Amyloid Formation by hIAPP. *Journal of the American Chemical Society.* **2017**, *139*, 16748.
7. Middleton, C. T.; Woys, A. M.; Mukherjee, S. S.; Zanni, M. T. Residue-specific structural kinetics of proteins through the union of isotope labeling, mid-IR pulse shaping, and coherent 2D IR spectroscopy. *Methods.* **2010**, *52*, 12.
8. Feng, Y.; Huang, J.; Kim, S.; Shim, J. H.; MacKerell, A. D.; Ge, N.-H. Structure of Penta-Alanine Investigated by Two-Dimensional Infrared Spectroscopy and Molecular Dynamics Simulation. *The Journal of Physical Chemistry B.* **2016**, *120*, 5325.
9. Waegele, M. M.; Culik, R. M.; Gai, F. Site-Specific Spectroscopic Reporters of the Local Electric Field, Hydration, Structure, and Dynamics of Biomolecules. *The Journal of Physical Chemistry Letters.* **2011**, *2*, 2598.
10. Ma, J.; Pazos, I. M.; Zhang, W.; Culik, R. M.; Gai, F. Site-Specific Infrared Probes of Proteins. *Annual Review of Physical Chemistry.* **2015**, *66*, 357.
11. Kim, H.; Cho, M. Infrared Probes for Studying the Structure and Dynamics of Biomolecules. *Chemical Reviews.* **2013**, *113*, 5817.
12. Błasiak, B.; Londergan, C. H.; Webb, L. J.; Cho, M. Vibrational Probes: From Small Molecule Solvatochromism Theory and Experiments to Applications in Complex Systems. *Accounts of Chemical Research.* **2017**, *50*, 968.
13. Backus, E. H. G.; Garrett-Roe, S.; Hamm, P. Phasing problem of heterodyne-detected two-dimensional infrared spectroscopy. *Optics Letters.* **2008**, *33*, 2665.
14. Shim, S.-H.; Zanni, M. T. How to turn your pump–probe instrument into a multidimensional spectrometer: 2D IR and Vis spectroscopiesvia pulse shaping. *Physical Chemistry Chemical Physics.* **2009**, *11*, 748.
15. Shim, S.-H.; Strasfeld, D. B.; Ling, Y. L.; Zanni, M. T. Automated 2D IR spectroscopy using a mid-IR pulse shaper and application of this technology to the human islet amyloid polypeptide. *Proceedings of the National Academy of Sciences.* **2007**, *104*, 14197.

16. Kanal, F.; Keiber, S.; Eck, R.; Brixner, T. 100-kHz shot-to-shot broadband data acquisition for high-repetition-rate pump–probe spectroscopy. *Optics Express.* **2014**, *22*, 16965.
17. Luther, B. M.; Tracy, K. M.; Gerrity, M.; Brown, S.; Krummel, A. T. 2D IR spectroscopy at 100 kHz utilizing a Mid-IR OPCPA laser source. *Optics Express.* **2016**, *24*, 4117.
18. Donaldson, P. M.; Greetham, G. M.; Shaw, D. J.; Parker, A. W.; Towrie, M. A 100 kHz Pulse Shaping 2D-IR Spectrometer Based on Dual Yb:KGW Amplifiers. *The Journal of Physical Chemistry A.* **2018**, *122*, 780.
19. Mukamel, S. *Principles of Nonlinear Optical Spectroscopy*; Oxford University Press: Oxford, U.K., 1999.
20. Roberts, S. T.; Loparo, J. J.; Tokmakoff, A. Characterization of spectral diffusion from two-dimensional line shapes. *The Journal of Chemical Physics.* **2006**, *125*, 084502.
21. Guo, Q.; Pagano, P.; Li, Y.-L.; Kohen, A.; Cheatum, C. M. Line shape analysis of two-dimensional infrared spectra. *The Journal of Chemical Physics.* **2015**, *142*, 212427.
22. Lazonder, K.; Pshenichnikov, M. S.; Wiersma, D. A. Easy interpretation of optical two-dimensional correlation spectra. *Optics Letters.* **2006**, *31*, 3354.
23. Kwak, K.; Park, S.; Finkelstein, I. J.; Fayer, M. D. Frequency-frequency correlation functions and apodization in two-dimensional infrared vibrational echo spectroscopy: A new approach. *The Journal of Chemical Physics.* **2007**, *127*, 124503.
24. Kwak, K.; Rosenfeld, D. E.; Fayer, M. D. Taking apart the two-dimensional infrared vibrational echo spectra: More information and elimination of distortions. *The Journal of Chemical Physics.* **2008**, *128*, 204505.
25. Feng, Y.; Vinogradov, I.; Ge, N.-H. General noise suppression scheme with reference detection in heterodyne nonlinear spectroscopy. *Optics Express.* **2017**, *25*, 26262.
26. Tan, H.-S.; Piletic, I. R.; Fayer, M. D. Polarization selective spectroscopy experiments: methodology and pitfalls. *Journal of the Optical Society of America B.* **2005**, *22*, 2009.
27. Feng, Y.; Vinogradov, I.; Ge, N.-H.; Innovation, U. A., Ed. 2018.
28. Bradler, M.; Riedle, E. Temporal and spectral correlations in bulk continua and improved use in transient spectroscopy. *Journal of the Optical Society of America B.* **2014**, *31*, 1465.
29. Brazard, J.; Bizimana, L. A.; Turner, D. B. Accurate convergence of transient-absorption spectra using pulsed lasers. *Review of Scientific Instruments.* **2015**, *86*, 053106.
30. Abbas, G. L.; Chan, V. W. S.; Yee, T. K. Local-oscillator excess-noise suppression for homodyne and heterodyne detection. *Optics Letters.* **1983**, *8*, 419.
31. Moon, J. A. Optimization of signal-to-noise ratios in pump-probe spectroscopy. *Review of Scientific Instruments.* **1993**, *64*, 1775.
32. Werley, C. A.; Teo, S. M.; Nelson, K. A. Pulsed laser noise analysis and pump-probe signal detection with a data acquisition card. *Review of Scientific Instruments.* **2011**, *82*, 123108.
33. Schriever, C.; Lochbrunner, S.; Riedle, E.; Nesbitt, D. J. Ultrasensitive ultraviolet-visible 20fs absorption spectroscopy of low vapor pressure molecules in the gas phase. *Review of Scientific Instruments.* **2008**, *79*, 013107.
34. Röttger, K.; Wang, S.; Renth, F.; Bahrenburg, J.; Temps, F. A femtosecond pump–probe spectrometer for dynamics in transmissive polymer films. *Applied Physics B.* **2015**, *118*, 185.

35. Reber, M. A. R.; Chen, Y.; Allison, T. K. Cavity-enhanced ultrafast spectroscopy: ultrafast meets ultrasensitive. *Optica.* **2016**, *3*, 311.
36. Bizimana, L. A.; Brazard, J.; Carbery, W. P.; Gellen, T.; Turner, D. B. Resolving molecular vibronic structure using high-sensitivity two-dimensional electronic spectroscopy. *The Journal of Chemical Physics.* **2015**, *143*, 164203.
37. McClure, S. D.; Turner, D. B.; Arpin, P. C.; Mirkovic, T.; Scholes, G. D. Coherent Oscillations in the PC577 Cryptophyte Antenna Occur in the Excited Electronic State. *The Journal of Physical Chemistry B.* **2014**, *118*, 1296.
38. Dobryakov, A. L.; Kovalenko, S. A.; Weigel, A.; Pérez-Lustres, J. L.; Lange, J.; Müller, A.; Ernsting, N. P. Femtosecond pump/supercontinuum-probe spectroscopy: Optimized setup and signal analysis for single-shot spectral referencing. *Review of Scientific Instruments.* **2010**, *81*, 113106.
39. Hamm, P.; Wiemann, S.; Zurek, M.; Zinth, W. Highly sensitive multichannel spectrometer for subpicosecond spectroscopy in the midinfrared. *Optics Letters.* **1994**, *19*, 1642.
40. Kaucikas, M.; Barber, J.; Van Thor, J. J. Polarization sensitive ultrafast mid-IR pump probe micro-spectrometer with diffraction limited spatial resolution. *Optics Express.* **2013**, *21*, 8357.
41. Ghosh, A.; Serrano, A. L.; Oudenhoven, T. A.; Ostrander, J. S.; Eklund, E. C.; Blair, A. F.; Zanni, M. T. Experimental implementations of 2D IR spectroscopy through a horizontal pulse shaper design and a focal plane array detector. *Optics Letters.* **2016**, *41*, 524.
42. McCamant, D. W.; Kukura, P.; Yoon, S.; Mathies, R. A. Femtosecond broadband stimulated Raman spectroscopy: Apparatus and methods. *Review of Scientific Instruments.* **2004**, *75*, 4971.
43. Auböck, G.; Consani, C.; Monni, R.; Cannizzo, A.; Mourik, F. v.; Chergui, M. Femtosecond pump/supercontinuum-probe setup with 20 kHz repetition rate. *Review of Scientific Instruments.* **2012**, *83*, 093105.
44. Megerle, U.; Pugliesi, I.; Schriever, C.; Sailer, C. F.; Riedle, E. Sub-50 fs broadband absorption spectroscopy with tunable excitation: putting the analysis of ultrafast molecular dynamics on solid ground. *Applied Physics B.* **2009**, *96*, 215.
45. Polli, D.; Lüer, L.; Cerullo, G. High-time-resolution pump-probe system with broadband detection for the study of time-domain vibrational dynamics. *Review of Scientific Instruments.* **2007**, *78*, 103108.
46. Anderson, K. E. H.; Sewall, S. L.; Cooney, R. R.; Kambhampati, P. Noise analysis and noise reduction methods in kilohertz pump-probe experiments. *Review of Scientific Instruments.* **2007**, *78*, 073101.
47. Hamm, P.; Kaindl, R. A.; Stenger, J. Noise suppression in femtosecond mid-infrared light sources. *Optics Letters.* **2000**, *25*, 1798.
48. Sul, S.; Karaiskaj, D.; Jiang, Y.; Ge, N.-H. Conformations of N-Acetyl-l-Prolinamide by Two-Dimensional Infrared Spectroscopy. *The Journal of Physical Chemistry B.* **2006**, *110*, 19891.
49. Shim, S.-H.; Strasfeld, D. B.; Zanni, M. T. Generation and characterization of phase and amplitude shaped femtosecond mid-IR pulses. *Optics Express.* **2006**, *14*, 13120.

50. Li, Y.-q.; Guzun, D.; Xiao, M. Sub-Shot-Noise-Limited Optical Heterodyne Detection Using an Amplitude-Squeezed Local Oscillator. *Physical Review Letters.* **1999**, *82*, 5225.
51. Holmes, J. F.; Rask, B. J. Optimum optical local-oscillator power levels for coherent detection with photodiodes. *Applied Optics.* **1995**, *34*, 927.
52. Weiner, A. M. Ultrafast optical pulse shaping: A tutorial review. *Optics Communications.* **2011**, *284*, 3669.
53. Monmayrant, A.; Weber, S.; Chatel, B. A newcomer's guide to ultrashort pulse shaping and characterization. *Journal of Physics B: Atomic, Molecular and Optical Physics.* **2010**, *43*, 103001.
54. Weiner, A. M. Femtosecond pulse shaping using spatial light modulators. *Review of Scientific Instruments.* **2000**, *71*, 1929.
55. Middleton, C. T.; Strasfeld, D. B.; Zanni, M. T. Polarization shaping in the mid-IR and polarization-based balanced heterodyne detection with application to 2D IR spectroscopy. *Optics Express.* **2009**, *17*, 14526.
56. Brixner, T.; Gerber, G. Femtosecond polarization pulse shaping. *Optics Letters.* **2001**, *26*, 557.
57. Hillegas, C. W.; Tull, J. X.; Goswami, D.; Strickland, D.; Warren, W. S. Femtosecond laser pulse shaping by use of microsecond radio-frequency pulses. *Optics Letters.* **1994**, *19*, 737.
58. Fetterman, M. R.; Goswami, D.; Keusters, D.; Yang, W.; Rhee, J. K.; Warren, W. S. Ultrafast pulse shaping: amplification and characterization. *Optics Express.* **1998**, *3*, 366.
59. Chang, I. C. I. Acoustooptic Devices and Applications. *IEEE Transactions on Sonics and Ultrasonics.* **1976**, *23*, 2.
60. Malitson, I. H. A Redetermination of Some Optical Properties of Calcium Fluoride. *Applied Optics.* **1963**, *2*, 1103.
61. Polyanskiy, M. N. https://refractiveindex.info, 2019; Vol. 2019.
62. Kumar, S. K. K.; Tamimi, A.; Fayer, M. D. Comparisons of 2D IR measured spectral diffusion in rotating frames using pulse shaping and in the stationary frame using the standard method. *The Journal of Chemical Physics.* **2012**, *137*, 184201.
63. *All About Bragg Angle Errors in AO Modulators and Deflectors*, ISOMET, 2007.
64. Thurston, R.; Heritage, J.; Weiner, A.; Tomlinson, W. Analysis of picosecond pulse shape synthesis by spectral masking in a grating pulse compressor. *IEEE Journal of Quantum Electronics.* **1986**, *22*, 682.
65. Barnes, N. P.; Piltch, M. S. Temperature-dependent Sellmeier coefficients and nonlinear optics average power limit for germanium. *Journal of the Optical Society of America.* **1979**, *69*, 178.
66. Akturk, S.; Gu, X.; Bowlan, P.; Trebino, R. Spatio-temporal couplings in ultrashort laser pulses. *Journal of Optics.* **2010**, *12*, 093001.
67. Brinks, D.; Hildner, R.; Stefani, F. D.; van Hulst, N. F. Beating spatio-temporal coupling: implications for pulse shaping and coherent control experiments. *Optics Express.* **2011**, *19*, 26486.
68. Kostenbauder, A. G. Ray-pulse matrices: a rational treatment for dispersive optical systems. *IEEE Journal of Quantum Electronics.* **1990**, *26*, 1148.

69. Duarte, F. J. Multiple-prism dispersion and 4×4 ray transfer matrices. *Optical and Quantum Electronics.* **1992**, *24*, 49.
70. Akturk, S.; Gu, X.; Gabolde, P.; Trebino, R. The general theory of first-order spatio-temporal distortions of Gaussian pulses and beams. *Optics Express.* **2005**, *13*, 8642.
71. Gorunski, N.; Dimitrov, N.; Dreischuh, A.; Paulus, G. G. Pulse-front tilt created in misaligned dispersionless optical systems and correct interferometric autocorrelation. *Optics Communications.* **2010**, *283*, 5192.
72. E. Popov, E. *Gratings: Theory and Numeric Applications*; 2nd ed.; Popov, Institut Fresnel, 2014
73. Nite, J. M.; Cyran, J. D.; Krummel, A. T. Active Bragg angle compensation for shaping ultrafast mid-infrared pulses. *Optics Express.* **2012**, *20*, 23912.
74. Woys, A. M.; Mukherjee, S. S.; Skoff, D. R.; Moran, S. D.; Zanni, M. T. A Strongly Absorbing Class of Non-Natural Labels for Probing Protein Electrostatics and Solvation with FTIR and 2D IR Spectroscopies. *The Journal of Physical Chemistry B.* **2013**, *117*, 5009.
75. Brinzer, T.; Berquist, E. J.; Ren, Z.; Dutta, S.; Johnson, C. A.; Krisher, C. S.; Lambrecht, D. S.; Garrett-Roe, S. Ultrafast vibrational spectroscopy (2D-IR) of CO2 in ionic liquids: Carbon capture from carbon dioxide's point of view. *The Journal of Chemical Physics.* **2015**, *142*, 212425.
76. Yamada, S. A.; Bailey, H. E.; Tamimi, A.; Li, C.; Fayer, M. D. Dynamics in a Room-Temperature Ionic Liquid from the Cation Perspective: 2D IR Vibrational Echo Spectroscopy. *Journal of the American Chemical Society.* **2017**, *139*, 2408.
77. Kramer, P. L.; Giammanco, C. H.; Fayer, M. D. Dynamics of water, methanol, and ethanol in a room temperature ionic liquid. *The Journal of Chemical Physics.* **2015**, *142*, 212408.
78. Tamimi, A.; Bailey, H. E.; Fayer, M. D. Alkyl Chain Length Dependence of the Dynamics and Structure in the Ionic Regions of Room-Temperature Ionic Liquids. *The Journal of Physical Chemistry B.* **2016**, *120*, 7488.
79. Ren, Z.; Brinzer, T.; Dutta, S.; Garrett-Roe, S. Thiocyanate as a Local Probe of Ultrafast Structure and Dynamics in Imidazolium-Based Ionic Liquids: Water-Induced Heterogeneity and Cation-Induced Ion Pairing. *The Journal of Physical Chemistry B.* **2015**, *119*, 4699.
80. Brinzer, T.; Daly, C. A.; Allison, C.; Garrett-Roe, S.; Corcelli, S. A. Modeling Carbon Dioxide Vibrational Frequencies in Ionic Liquids: III. Dynamics and Spectroscopy. *The Journal of Physical Chemistry B.* **2018**, *122*, 8931.
81. Fried, S. D.; Boxer, S. G. Measuring Electric Fields and Noncovalent Interactions Using the Vibrational Stark Effect. *Accounts of Chemical Research.* **2015**, *48*, 998.
82. Slocum, J. D.; Webb, L. J. Measuring Electric Fields in Biological Matter Using the Vibrational Stark Effect of Nitrile Probes. *Annual Review of Physical Chemistry.* **2018**, *69*, 253.
83. Ivanova, A. S.; Brinzer, T.; Roth, E. A.; Kusuma, V. A.; Watkins, J. D.; Zhou, X.; Luebke, D.; Hopkinson, D.; Washburn, N. R.; Garrett-Roe, S.; Nulwala, H. B. Eutectic ionic liquid mixtures and their effect on CO2 solubility and conductivity. *RSC Advances.* **2015**, *5*, 51407.

84. Ren, Z.; Ivanova, A. S.; Couchot-Vore, D.; Garrett-Roe, S. Ultrafast Structure and Dynamics in Ionic Liquids: 2D-IR Spectroscopy Probes the Molecular Origin of Viscosity. *The Journal of Physical Chemistry Letters.* **2014**, *5*, 1541.
85. Brinzer, T.; Garrett-Roe, S. Temperature and chain length dependence of ultrafast vibrational dynamics of thiocyanate in alkylimidazolium ionic liquids: A random walk on a rugged energy landscape. *The Journal of Chemical Physics.* **2017**, *147*, 194501.
86. Roy, V. P.; Kubarych, K. J. Interfacial Hydration Dynamics in Cationic Micelles Using 2D-IR and NMR. *The Journal of Physical Chemistry B.* **2017**, *121*, 9621.
87. Osborne, D. G.; Dunbar, J. A.; Lapping, J. G.; White, A. M.; Kubarych, K. J. Site-Specific Measurements of Lipid Membrane Interfacial Water Dynamics with Multidimensional Infrared Spectroscopy. *The Journal of Physical Chemistry B.* **2013**, *117*, 15407.
88. Yan, C.; Thomaz, J. E.; Wang, Y.-L.; Nishida, J.; Yuan, R.; Breen, J. P.; Fayer, M. D. Ultrafast to Ultraslow Dynamics of a Langmuir Monolayer at the Air/Water Interface Observed with Reflection Enhanced 2D IR Spectroscopy. *Journal of the American Chemical Society.* **2017**, *139*, 16518.
89. Maj, M.; Ahn, C.; Błasiak, B.; Kwak, K.; Han, H.; Cho, M. Isonitrile as an Ultrasensitive Infrared Reporter of Hydrogen-Bonding Structure and Dynamics. *The Journal of Physical Chemistry B.* **2016**, *120*, 10167.
90. Oh, K.-I.; Lee, J.-H.; Joo, C.; Han, H.; Cho, M. β-Azidoalanine as an IR Probe: Application to Amyloid Aβ(16-22) Aggregation. *The Journal of Physical Chemistry B.* **2008**, *112*, 10352.
91. Wolfshorndl, M. P.; Baskin, R.; Dhawan, I.; Londergan, C. H. Covalently Bound Azido Groups Are Very Specific Water Sensors, Even in Hydrogen-Bonding Environments. *The Journal of Physical Chemistry B.* **2012**, *116*, 1172.
92. Maj, M.; Ahn, C.; Kossowska, D.; Park, K.; Kwak, K.; Han, H.; Cho, M. β-Isocyanoalanine as an IR probe: comparison of vibrational dynamics between isonitrile and nitrile-derivatized IR probes. *Physical Chemistry Chemical Physics.* **2015**, *17*, 11770.
93. Zanobini, C.; Bozovic, O.; Jankovic, B.; Koziol, K. L.; Johnson, P. J. M.; Hamm, P.; Gulzar, A.; Wolf, S.; Stock, G. Azidohomoalanine: A Minimally Invasive, Versatile, and Sensitive Infrared Label in Proteins To Study Ligand Binding. *The Journal of Physical Chemistry B.* **2018**, *122*, 10118.
94. Lee, G.; Kossowska, D.; Lim, J.; Kim, S.; Han, H.; Kwak, K.; Cho, M. Cyanamide as an Infrared Reporter: Comparison of Vibrational Properties between Nitriles Bonded to N and C Atoms. *The Journal of Physical Chemistry B.* **2018**, *122*, 4035.
95. Smith, E. E.; Linderman, B. Y.; Luskin, A. C.; Brewer, S. H. Probing Local Environments with the Infrared Probe: l-4-Nitrophenylalanine. *The Journal of Physical Chemistry B.* **2011**, *115*, 2380.
96. Peran, I.; Oudenhoven, T.; Woys, A. M.; Watson, M. D.; Zhang, T. O.; Carrico, I.; Zanni, M. T.; Raleigh, D. P. General Strategy for the Bioorthogonal Incorporation of Strongly Absorbing, Solvation-Sensitive Infrared Probes into Proteins. *The Journal of Physical Chemistry B.* **2014**, *118*, 7946.
97. Ahmed, I. A.; Gai, F. Simple method to introduce an ester infrared probe into proteins. *Protein Science.* **2017**, *26*, 375.

98. Tookmanian, E. M.; Phillips-Piro, C. M.; Fenlon, E. E.; Brewer, S. H. Azidoethoxyphenylalanine as a Vibrational Reporter and Click Chemistry Partner in Proteins. *Chemistry – A European Journal.* **2015**, *21*, 19096.
99. Levin, D. E.; Schmitz, A. J.; Hines, S. M.; Hines, K. J.; Tucker, M. J.; Brewer, S. H.; Fenlon, E. E. Synthesis and evaluation of the sensitivity and vibrational lifetimes of thiocyanate and selenocyanate infrared reporters. *RSC Advances.* **2016**, *6*, 36231.
100. Tookmanian, E. M.; Fenlon, E. E.; Brewer, S. H. Synthesis and protein incorporation of azido-modified unnatural amino acids. *RSC Advances.* **2015**, *5*, 1274.
101. Chalyavi, F.; Gilmartin, P. H.; Schmitz, A. J.; Fennie, M. W.; Tucker, M. J. Synthesis of 5-Cyano-Tryptophan as a Two-Dimensional Infrared Spectroscopic Reporter of Structure. *Angewandte Chemie International Edition.* **2018**, *57*, 7528.
102. Sul, S.; Feng, Y.; Le, U.; Tobias, D. J.; Ge, N.-H. Interactions of Tyrosine in Leu-Enkephalin at a Membrane–Water Interface: An Ultrafast Two-Dimensional Infrared Study Combined with Density Functional Calculations and Molecular Dynamics Simulations. *The Journal of Physical Chemistry B.* **2010**, *114*, 1180.
103. Chalyavi, F.; Hogle, D. G.; Tucker, M. J. Tyrosine as a Non-perturbing Site-Specific Vibrational Reporter for Protein Dynamics. *The Journal of Physical Chemistry B.* **2017**, *121*, 6380.
104. Takahashi, R.; Noguchi, T. Criteria for Determining the Hydrogen-Bond Structures of a Tyrosine Side Chain by Fourier Transform Infrared Spectroscopy: Density Functional Theory Analyses of Model Hydrogen-Bonded Complexes of p-Cresol. *The Journal of Physical Chemistry B.* **2007**, *111*, 13833.
105. Hughes, J.; Smith, T. W.; Kosterlitz, H. W.; Fothergill, L. A.; Morgan, B. A.; Morris, H. R. Identification of two related pentapeptides from the brain with potent opiate agonist activity. *Nature.* **1975**, *258*, 577.
106. Sargent, D. F.; Schwyzer, R. Membrane lipid phase as catalyst for peptide-receptor interactions. *Proceedings of the National Academy of Sciences.* **1986**, *83*, 5774.
107. Takekiyo, T.; Kato, M.; Taniguchi, Y. FT-IR spectroscopic study on conformational equilibria of [Leu]^5-enkephalin in DMSO and 2H2O solutions. *Journal of Molecular Liquids.* **2005**, *119*, 147.
108. Han, S.-L.; Stimson, E. R.; Maxfield, F. R.; Scheraga, H. A. Conformationalstudy Of [Leu^5]-Enkephalin by Laser Raman Spectroscopy. *International Journal of Peptide and Protein Research.* **1980**, *16*, 173.
109. Aburi, M.; Smith, P. E. A conformational analysis of leucine enkephalin as a function of pH. *Biopolymers.* **2002**, *64*, 177.
110. Marcotte, I.; Dufourc, E. J.; Ouellet, M.; Auger, M. Interaction of the Neuropeptide Met-Enkephalin with Zwitterionic and Negatively Charged Bicelles as Viewed by ^{31}P and ^{2}H Solid-State NMR. *Biophysical Journal.* **2003**, *85*, 328.
111. Marcotte, I.; Separovic, F.; Auger, M.; Gagné, S. M. A Multidimensional ^{1}H NMR Investigation of the Conformation of Methionine-Enkephalin in Fast-Tumbling Bicelles. *Biophysical Journal.* **2004**, *86*, 1587.
112. Mosberg, H. I.; Hurst, R.; Hruby, V. J.; Gee, K.; Yamamura, H. I.; Galligan, J. J.; Burks, T. F. Bis-penicillamine enkephalins possess highly improved specificity toward delta opioid receptors. *Proceedings of the National Academy of Sciences.* **1983**, *80*, 5871.

113. Hruby, V. J.; Kao, L. F.; Pettitt, B. M.; Karplus, M. The conformational properties of the delta opioid peptide [cyclic] [D-pen2,D-pen5]enkephalin in aqueous solution determined by NMR and energy minimization calculations. *Journal of the American Chemical Society.* **1988**, *110*, 3351.
114. Kosterlitz, H. W.; Lord, J. A. H.; Paterson, S. J.; Waterfield, A. A. Effects of changes in the structure of enkephalins and of narcotic analgesic drugs on their interactions with μ and δ-receptors. *British Journal of Pharmacology.* **1980**, *68*, 333.
115. Milon, A.; Miyazawa, T.; Higashijima, T. Transferred nuclear Overhauser effect analyses of membrane-bound enkephalin analogs by proton nuclear magnetic resonance: correlation between activities and membrane-bound conformations. *Biochemistry.* **1990**, *29*, 65.
116. Lee, K.-K.; Park, K.-H.; Choi, J.-H.; Ha, J.-H.; Jeon, S.-J.; Cho, M. Ultrafast Vibrational Spectroscopy of Cyanophenols. *The Journal of Physical Chemistry A.* **2010**, *114*, 2757.
117. Frisch, M. J.; Trucks, G. W.; Schlegel, H. B.; Scuseria, G. E.; Robb, M. A.; Cheeseman, J. R.; Montgomery, J. A.; Vreven, T.; Kudin, K. N.; Burant, J. C.; Millam, J. M.; Iyengar, S. S.; Tomasi, J.; Barone, V.; Mennucci, B.; Cossi, M.; Scalmani, G.; Rega, N.; Petersson, G. A.; Nakatsuji, H.; Hada, M.; Ehara, M.; Toyota, K.; Fukuda, R.; Hasegawa, J.; Ishida, M.; Nakajima, T.; Honda, Y.; Kitao, O.; Nakai, H.; Klene, M.; Li, X.; Knox, J. E.; Hratchian, H. P.; Cross, J. B.; Bakken, V.; Adamo, C.; Jaramillo, J.; Gomperts, R.; Stratmann, R. E.; Yazyev, O.; Austin, A. J.; Cammi, R.; Pomelli, C.; Ochterski, J. W.; Ayala, P. Y.; Morokuma, K.; Voth, G. A.; Salvador, P.; Dannenberg, J. J.; Zakrzewski, V. G.; Dapprich, S.; Daniels, A. D.; Strain, M. C.; Farkas, O.; Malick, D. K.; Rabuck, A. D.; Raghavachari, K.; Foresman, J. B.; Ortiz, J. V.; Cui, Q.; Baboul, A. G.; Clifford, S.; Cioslowski, J.; Stefanov, B. B.; Liu, G.; Liashenko, A.; Piskorz, P.; Komaromi, I.; Martin, R. L.; Fox, D. J.; Keith, T.; Laham, A.; Peng, C. Y.; Nanayakkara, A.; Challacombe, M.; Gill, P. M. W.; Johnson, B.; Chen, W.; Wong, M. W.; Gonzalez, C.; Pople, J. A. 2003.
118. Rodgers, J. M.; Zhang, W.; Bazewicz, C. G.; Chen, J.; Brewer, S. H.; Gai, F. Kinetic Isotope Effect Provides Insight into the Vibrational Relaxation Mechanism of Aromatic Molecules: Application to Cyano-phenylalanine. *The Journal of Physical Chemistry Letters.* **2016**, *7*, 1281.
119. Park, K.-H.; Jeon, J.; Park, Y.; Lee, S.; Kwon, H.-J.; Joo, C.; Park, S.; Han, H.; Cho, M. Infrared Probes Based on Nitrile-Derivatized Prolines: Thermal Insulation Effect and Enhanced Dynamic Range. *The Journal of Physical Chemistry Letters.* **2013**, *4*, 2105.
120. Zhang, W.; Markiewicz, B. N.; Doerksen, R. S.; Smith, I. I. I. A. B.; Gai, F. C≡N stretching vibration of 5-cyanotryptophan as an infrared probe of protein local environment: what determines its frequency? *Physical Chemistry Chemical Physics.* **2016**, *18*, 7027.
121. Rodgers, J. M.; Abaskharon, R. M.; Ding, B.; Chen, J.; Zhang, W.; Gai, F. Fermi resonance as a means to determine the hydrogen-bonding status of two infrared probes. *Physical Chemistry Chemical Physics.* **2017**, *19*, 16144.
122. Maekawa, H.; Ge, N.-H. Picosecond Rotational Interconversion Adjacent to a C═O Bond Studied by Two-Dimensional Infrared Spectroscopy. *The Journal of Physical Chemistry B.* **2012**, *116*, 11292.

123. Giammanco, C. H.; Kramer, P. L.; Yamada, S. A.; Nishida, J.; Tamimi, A.; Fayer, M. D. Coupling of Carbon Dioxide Stretch and Bend Vibrations Reveals Thermal Population Dynamics in an Ionic Liquid. *The Journal of Physical Chemistry B.* **2016**, *120*, 549.
124. Ramesh, P.; Loring, R. F. Thermal Population Fluctuations in Two-Dimensional Infrared Spectroscopy Captured with Semiclassical Mechanics. *The Journal of Physical Chemistry B.* **2018**, *122*, 3647.
125. Khalil, M.; Demirdöven, N.; Tokmakoff, A. Vibrational coherence transfer characterized with Fourier-transform 2D IR spectroscopy. *The Journal of Chemical Physics.* **2004**, *121*, 362.
126. Kenkre, V. M.; Tokmakoff, A.; Fayer, M. D. Theory of vibrational relaxation of polyatomic molecules in liquids. *The Journal of Chemical Physics.* **1994**, *101*, 10618.
127. Stratt, R. M. The Instantaneous Normal Modes of Liquids. *Accounts of Chemical Research.* **1995**, *28*, 201.
128. Hazra, M. K.; Bagchi, B. Collective excitations in liquid dimethyl sulfoxide (DMSO): FIR spectrum, low frequency vibrational density of states, and ultrafast dipolar solvation dynamics. *The Journal of Chemical Physics.* **2017**, *146*, 024505.
129. Wiewiór, P. P.; Shirota, H.; Jr., E. W. C. Aqueous dimethyl sulfoxide solutions: Inter- and intra-molecular dynamics. *The Journal of Chemical Physics.* **2002**, *116*, 4643.
130. Frank, H. S.; Evans, M. W. Free Volume and Entropy in Condensed Systems III. Entropy in Binary Liquid Mixtures; Partial Molal Entropy in Dilute Solutions; Structure and Thermodynamics in Aqueous Electrolytes. *The Journal of Chemical Physics.* **1945**, *13*, 507.
131. Rezus, Y. L. A.; Bakker, H. J. Observation of Immobilized Water Molecules around Hydrophobic Groups. *Physical Review Letters.* **2007**, *99*, 148301.
132. Raschke, T. M.; Levitt, M. Detailed Hydration Maps of Benzene and Cyclohexane Reveal Distinct Water Structures. *The Journal of Physical Chemistry B.* **2004**, *108*, 13492.
133. Raschke, T. M.; Levitt, M. Nonpolar solutes enhance water structure within hydration shells while reducing interactions between them. *Proceedings of the National Academy of Sciences of the United States of America.* **2005**, *102*, 6777.
134. Gierszal, K. P.; Davis, J. G.; Hands, M. D.; Wilcox, D. S.; Slipchenko, L. V.; Ben-Amotz, D. π-Hydrogen Bonding in Liquid Water. *The Journal of Physical Chemistry Letters.* **2011**, *2*, 2930.
135. Choudhary, A.; Chandra, A. Anisotropic structure and dynamics of the solvation shell of a benzene solute in liquid water from ab initio molecular dynamics simulations. *Physical Chemistry Chemical Physics.* **2016**, *18*, 6132.
136. Steiner, T.; Koellner, G. Hydrogen bonds with π-acceptors in proteins: frequencies and role in stabilizing local 3D structures11Edited by R. Huber. *Journal of Molecular Biology.* **2001**, *305*, 535.
137. Baiz, C. R.; Kubarych, K. J.; Geva, E. Molecular Theory and Simulation of Coherence Transfer in Metal Carbonyls and Its Signature on Multidimensional Infrared Spectra. *The Journal of Physical Chemistry B.* **2011**, *115*, 5322.
138. King, J. T.; Anna, J. M.; Kubarych, K. J. Solvent-hindered intramolecular vibrational redistribution. *Physical Chemistry Chemical Physics.* **2011**, *13*, 5579.

139. Yang, C.; Peng, S.; Xie, Q.; Peng, J.; Wei, J.; Hu, Y. In *2011 4th International Conference on Biomedical Engineering and Informatics (BMEI)* 2011; Vol. 3, p 1724.
140. Ge, N.-H.; M. Hochstrasser, R. Femtosecond two-dimensional infrared spectroscopy: IR-COSY and THIRSTY. *PhysChemComm.* **2002**, *5*, 17.